RANGE OPTIMIZATION OF LIFTING REENTRY VEHICLES

by

THOMAS C. BETTERTON, Lieutenant Commander, U.S. Navy
B.S., University of Notre Dame (1957)

DENNY B. CARGILL, Lieutenant Commander, U.S. Navy
B.S., University of Washington (1958)

THOMAS J. MAGUIRE, Lieutenant Commander, U.S. Navy
B.S., United States Naval Academy (1957)

SUBMITTED IN PARTIAL FULFILLMENT

OF THE REQUIREMENTS FOR THE DEGREES

OF MASTER OF SCIENCE AND ENGINEER

OF AERONAUTICS AND ASTRONAUTICS

at the

MASSACHUSETTS INSTITUTE OF TECHNOLOGY

August, 1966

RANGE OPTIMIZATION OF LIFTING REENTRY VEHICLES

by

THOMAS C. BETTERTON, Lieutenant Commander, U.S. Navy
B.S., University of Notre Dame (1957)

DENNY B. CARGILL, Lieutenant Commander, U.S. Navy
B.S., University of Washington (1958)

THOMAS J. MAGUIRE, Lieutenant Commander, U.S. Navy
B.S., United States Naval Academy (1957)

SUBMITTED IN PARTIAL FULFILLMENT

OF THE REQUIREMENTS FOR THE DEGREES

OF MASTER OF SCIENCE AND ENGINEER

OF AERONAUTICS AND ASTRONAUTICS

at the

MASSACHUSETTS INSTITUTE OF TECHNOLOGY

August, 1966

RANGE OPTIMIZATION OF LIFTING REENTRY VEHICLES

by

Thomas C. Betterton, Lieutenant Commander, U.S. Navy

Denny B. Cargill, Lieutenant Commander, U.S. Navy

Thomas J. Maguire, Lieutenant Commander, U.S. Navy

Submitted to the Department of Aeronautics and Astronautics on August 22, 1966, in partial fulfillment of the requirements for the Degrees of Master of Science and Engineer of Aeronautics and Astronautics.

ABSTRACT

The optimization of range, with respect to thermal protection system weight, was investigated for a lifting reentry vehicle with an $(L/D)_{max}$ of 2.4. Two-phase angle of attack modulation and bank modulation were used in an effort to improve results of constant angle of attack trajectories. The resulting straight-ahead trajectories were optimized based on an all-ablative Teflon heat shield. A set of bank angles was introduced to provide extensive landing site coverage, and the variation of both thermal protection system weight and payload fraction with attainable landing area were examined.

The optimized straight-ahead trajectories were also used to generate thermal protection system weights for other vaporizing ablators, a charring ablator, and a combination ablation-radiation system using various high temperature metals. The charring ablator heat shield was found to require the least thermal protection system weight over the entire range capability of the vehicle.

The effect of variations in initial entry angle and wing loading on landing site coverage were also examined. The resulting thermal protection system weights and payload fractions were compared to those for the nominal footprint.

A comparison, based on total stagnation heating, between the two-phase angle of attack modulation and a "steepest descent" formal optimization procedure was made for one trajectory. Using a constant angle of attack trajectory as a basis, the reduction in total stagnation heating possible through the use of two-phase angle of attack modulation compared favorably with that attainable through the formal optimization procedure.

Thesis Supervisor: René H. Miller

Title: H. N. Slater Professor of Flight Transportation

ACKNOWLEDGMENTS

TABLE OF CONTENTS

4

TABLE OF CONTENTS (Continued)

5

NOMENCLATURE

A	Bank modulation factor
C_A	Axial force coefficient
C_N	Normal force coefficient
C_D	Drag coefficient
C_L	Lift coefficient
C_P	Newtonian pressure coefficient or specific heat (BTU/lb-°F)
CR	Cross range (nautical miles)
D	Drag
DR	Down range (nautical miles)
DYNP	Dynamic pressure
GW	Gross weight (lbs)
H	Altitude (feet)
L	Lift
L/D	Lift/drag ratio
M	Mach number
PW	Payload weight
Q	Total heat (BTU/ft^2)
$\overset{*}{Q}$	Effective heat of ablation (BTU/lb)
R	Radius (feet)
R,θ	Spherical coordinates
R_{LE}	Leading edge radius (feet)

R_N	Nose radius (feet)
R_B	Base radius (feet)
RPA	Resultant physiological acceleration
S	Surface area (square feet)
T	Temperature ($^\circ$F)
TF	Time of flight
V	Velocity (ft/sec)
W/S	Wing loading (lbs/ft^2)
WT	Thermal protection system weight (lbs)
W_N	Nose ablator weight (lbs)
W_B	Body ablator weight (lbs)
W_{LE}	Leading edge ablator weight (lbs)
W_{TOP}	Top ablator weight (lbs)
W_A	Total ablator weight (lbs)
W_I	Insulation weight-total (lbs)
$\vec{a}$	Inertial acceleration
g	Gravitational acceleration
h	Enthalpy (BTU/lb)
k	Thermal conductivity (BTU/ft-sec$^\circ$F)
m	Mass
p	Pressure
q	Heating rate (BTU/ft^2-sec) or dynamic pressure
x_i, y_i, z_i	Cartesian coordinates

Greek Letters

α	Angle of attack
α_1	Phase I angle of attack
α_2	Phase II angle of attack
β	Body angular coordinate
γ	Flight path angle or ratio of specific heats
η	Angle between velocity vector and body normal vector
θ	Angular distance from stagnation point
θ_v	Cone semi-vertex angle
Λ	Angle of sweep
ρ	Density
ϕ	Bank angle
ω	Angular velocity (rad/sec)

Subscripts

A	Sublimation
c	Convective
r	Radiative
S	Stagnation
S.L.	Sea level
w	Wall
0	Initial conditions
∞	Free stream conditions

LIST OF TABLES

LIST OF FIGURES

13

INTRODUCTION

As the complexity and scope of this country's manned orbital and lunar exploratory flights increase throughout the next few decades, it becomes readily apparent that vehicles with much improved operational capability will be utilized. In this context, operational capability denotes the overall mission ability to react quickly, perform the assigned task and return to any of a wide range of landing points on the earth in the most expeditious manner with a minimum of external support.

It can be seen that this type of mission involves numerous parameters which must be examined in order to design an effective system. This study examines one phase of the mission, the reentry, and the effect of variations in the associated parameters on the size of the attainable landing area. This leads to a better understanding of some of the design trade-offs involved in determining the most suitable vehicle configuration and reentry flight path for a particular mission.

There are three basic types of reentry vehicles presently under consideration. These are the ballistic (and near ballistic) capsules such as Gemini, the lifting bodies such as NASA's M2 development vehicle and the winged glider such as the Dyna Soar. Subcatagories of these types are manned or unmanned vehicles and each configuration has advantages and disadvantages in application to a given mission.

The ballistic and near ballistic vehicles and their reentry trajectories are characterized by moderately high decelerations,

critical entry corridor requirements, relatively low thermal protection system weights and a very small operational footprint.

Lifting bodies show marked improved over ballistic vehicles in several areas. The criticality of initial entry conditions is greatly relieved by a much larger allowable entry corridor. Decelerations can be reduced well below human tolerances in entries from both circular and supercircular orbits. Of primary interest to the military viewpoint is the increase in footprint size over the ballistic capsule footprint. The attainable landing area for lifting bodies can approach global in many cases. A disadvantage of this configuration is its somewhat reduced volumetric efficiency which directly relates to the overall system efficiency through a reduction in mission payload.

The gliding vehicles obtain a marked increase in range capability and an apparent reduction in thermal protection system weight through use of light wing loadings. This allows a gradual reentry through the earth's atmosphere which maintains the convective heating rate at or below the re-radiation rate at an allowable surface temperature. The need for large amounts of ablative heat shielding is thereby eliminated. However, the large structural weight of the wings incurs a severe penalty on volumetric efficiency which reduces the overall system payload. In effect, the large wing structure becomes the thermal protection system.

In the time period of this writing, the major area of interest is in lifting body vehicles. Current projects with vehicles such as the M2, HL-10 and the SV-5 are providing detailed information on the configuration, aerodynamics and structural problems involved. As the requirement for flexibility increases, the problem of design tradeoffs is greatly

expanded. It becomes essential to appreciate the increase (or decrease) in performance of the entire system obtained by a unit expenditure in some given area. A system trade-off of this kind is the increase in available landing area which results from increasing the size of the thermal protection system a given amount (which in turn reduces the payload weight). The payload fraction is a good measure of this system tradeoff, and it will be of primary concern in this study. Also, the effect on the specific operational capability (i.e., size of landing area), of changes in other design parameters such as wing loading and general vehicle configuration will be examined to provide basic guide lines in these areas.

The results obtained are presented with a view toward indicating trends and sensitivities involved in the overall design of a space vehicle system, rather than handbook data on particular vehicles.

CHAPTER 1

FORMULATION OF THE PROBLEM

In order to indicate the effect and the sensitivity of several parameters on one operational capability, i.e., size of landing area, the problem was formulated in such a way that a single parameter, such as wing loading, could be varied and the effect linearized to indicate a general trend. There are undoubtedly cross-coupling effects and second order effects which should be considered in a specific vehicle design.

A typical reentry situation and a basic vehicle configuration were assumed as fixed initial conditions. An iterative procedure was used to develop a set of trajectories, each of which provides a near optimum (lowest) thermal protection system weight for a given range. Lift and bank modulation were used in the optimizing procedure. The set of straight-line, down-range trajectories was expanded into a footprint by introducing a set of nominal bank angles in addition to the bank modulation. This resulted in the desired crossrange capability.

Contour lines were connected through landing points of equal thermal protection system weight and a conformal map was developed which indicates the desired design tradeoff, that is, the amount of ablator weight required to increase the size of the landing area.

18

This procedure was repeated after making gross variations in several design parameters and further comparisons were made.

This brief description of the general procedure will be expanded in detail in subsequent sections.

1.1 Vehicle Description

The basic vehicle chosen for this study is a blunted, half circular cone with a 10 degree semi-vertex angle. Sizing the vehicle begins with a mission definition, i.e., duration and specific tasks to be accomplished during the flight. This study is pointed toward a general military mission with the following assumptions:

a) Crew size - 6 men

b) Mission duration - 15 days

The volume requirements, based on aerospace and submarine experience and confinement tests, are presented in Ref. 1 for different mission definitions. Assuming a volume requirement of 250 cu.ft. per man gives a personnel volume requirement of 1500 cu.ft. With a factor to provide equipment and cargo space, the total volume requirement of the vehicle is 2580 cu.ft. With an assumed nose blunting by a spherical cap of two foot radius, the length of a 10 degree half-circular cone body is 36 feet. From Ref. 2 , the weight of this vehicle was estimated to be 18,000 lbs. with a weight breakdown as follows:

19

Component	Weight Fraction	Weight
Structure (less insulation)	0.29	5220
Guidance and Control	0.07	1260
Auxiliary Power	0.08	1440
Life Support	0.04	720
Propulsion System	0.23	4500
Thermal Protection System Payload	0.27	4860
		18,000

For the purposes of this analysis, all the weights shown above will be considered constant. The thermal protection system and payload weights were combined in this manner to more readily show the tradeoff between payload fraction and thermal protection system fraction. The effect of varying thermal protection system weight requirements will be reflected directly in the payload fraction. The relation between payload fraction and ranging capability will be discussed in Chapters 5 and 6. The aerodynamic characteristics of this shape are developed in Appendix A. Fig. 1 shows a schematic of the vehicle.

1.2 Initial Entry Conditions

As a hypothesis, the mission requirement is assumed to establish the point of retro-fire from a circular, near earth orbit and the magnitude of retro-fire (i.e., the ΔV expended) which establishes the initial entry angle. The entry angle was found to be a sensitive parameter and a study was made to determine its influence on time of flight, range, deceleration and dynamic pressure.

The effect of entry angle, γ, on the trajectory is very pronounced. The vehicle may initially accelerate or decelerate depending on the

magnitude of γ and, for large positive γ's, may skip out to very high altitudes (700,000 feet). The maximum range is also a direct function of entry angle. Fig. 2 indicates this dependence where range is seen to increase for lower γ's. This additional range could be converted to lateral range to expand the footprint.

Another consideration is the guidance problem associated with maintaining the nominal trajectory. Lees, Hartwig and Cohen[3] suggest that high entry angles (4 degrees and higher) tend to reduce inaccuracies in location of the landing point and allow less complex guidance schemes.

Load factor and dynamic pressure are influenced by the entry angle also since they are functions, primarily, of the depth to which the vehicle dives into the atmosphere before the velocity decreases appreciably. Lifting capability can greatly relieve problems in this area and allow much higher entry angles with the same load factor and dynamic pressure. For L/D = 1.0, the load factor can be maintained below 4 g's for entry angles up to 5°.[4] The allowable deceleration limit is considered to be 10 g's in this study and will be discussed further in a later section.

The same considerations which determine load factor and dynamic pressure also influence heating rates. Since heating is dependent primarily on the velocity and the density, a deeper initial dig into the atmosphere will cause an increase in heating rate. As mentioned above, lifting bodies have advantages in this respect also.

The time of flight is generally longer for lower γ's and, although not of particular interest in itself, has a large effect on the total heat absorbed by the vehicle. For example, the time of flight for an entry angle of 2 degrees and an angle of attack for maximum L/D is 3978 seconds

21

with an associated total stagnation heating of 188,408 BTU/ft^2 while, for an entry angle of 1 degree, the time of flight is 4202 seconds and the total stagnation heating is 213,603 BTU/ft^2.

Further effects on aerodynamic heating and, ultimately, thermal protection systems weight will be examined in later sections to indicate design trade-off trends in respect to overall mission capability.

Table 1 presents additional data for four entry angles and seven constant angle of attack trajectories. Fig. 2 shows the effect of entry angle on a particular trajectory, in this case a constant angle of attack of 5 degrees corresponding to the maximum L/D of 2.4.

These considerations, supported by a survey of the literature, indicate that an entry angle of 2 degrees is suitable to represent the problem as formulated. This angle provides realistic decelerations for piloted vehicles and realistic thermal protection system weights for the wide variety of trajectories necessary to reach all landing points within the desired footprint.

The initial velocity and altitude were assumed to be 25,500 feet per second and 400,000 feet respectively.

22

1.3 Equations of Motion

The derivation of the three dimensional equations of motion for a vehicle entering the earth's atmosphere is presented in detail in Appendix A. The equations are derived assuming the vehicle to be a point mass moving over a spherical, non-rotating earth fixed in inertial space. Perturbational forces such as non-homogeniety of the earth, the Sun's radiation pressure, Solar wind and gravitational fields from other bodies have been neglected. The final equations provide a description of the motion of a reentry vehicle, relative to the earth, with only two restrictions. The equations are not valid when the vehicle is either at the "poles" of the coordinate system, or in a vertical dive. Neither of these conditions were encountered in the present study.

1.4   Computational Procedure

The earth's atmosphere, as used in the calculation of trajectories and heating data, is assumed to be the ARDC model atmosphere described in ref. 32 . It is characterized by an exponential density variation as follows:

$$\rho = .003 \, e^{-\left(\frac{H}{23000}\right)}$$

and very closely approximates the IGY interim model atmosphere of Sterne, et. al. [33] in the altitude range of interest. The limit of the sensible atmosphere, in regard to aerodynamic and aerothermodynamic effects, is considered to be 400,000 feet. All trajectories were assumed to be essentially completed at 50,000 feet since no appreciable convective heating or range is generated below this altitude.

The use of a computer for numerical integration of the equations of motion allows a very accurate determination of the resulting trajectory. There are three general methods for the integration of the equations: Cowell's method, Encke's method and the Variation of Parameters method[34]. Cowell's method involves direct numerical integration of the total acceleration of the vehicle and provides a straightforward physical picture of the trajectory. This method assumes a straight-line trajectory during each time increment, although a higher order curve may be assumed to give better accuracy for large time increments. Encke's method differs in that a reference trajectory is assumed and only perturbational accelerations are integrated. This results in the change of the actual trajectory from the assumed. The variation of parameters method also assumes a reference trajectory, but the reference varies continuously due to the perturbing forces. This leads to an assumed conic section trajectory during each time increment, with the conic section parameters dependent on the values of

24

velocity, altitude and flight path angle at that time.

The trajectories for this study were calculated from the equations of motion using Cowell's method on an IBM 7094 high speed, digital computer. The program used, and its associated flow diagram are included in Appendix E.

It became apparent that, in computing a trajectory by this method, the step size is extremely critical in certain areas but can be very coarse in others with little loss in accuracy. The critical areas are those in which the flight path angle, γ, is changing rapidly. This occurs primarily at the bottom of each oscillation in the flight path and is concurrent with increased values of dynamic pressure and convective heating rate. The basic step size of five seconds was refined to one second in these areas through the use of a sensing technique in the computer program. Since the magnitude of the deceleration was also found to increase appreciably with a rapidly changing flight path angle, this parameter was used to signal the need for a reduction in step size.

It was also noted that the dynamics involved in a trajectory with lift modulation are extremely sensitive to the rate at which the angle of attack is changed. An angle of attack rate of .007 rads/sec was introduced into the calculation with a corresponding reduction in maximum deceleration by a factor of seven over the same trajectory with instantaneous lift modulation. The amplitude of the flight path oscillations was also reduced appreciably in the critical area. This technique provides a more realistic mathematical model since an actual vehicle would necessarily be controlled in this manner. The angle of attack modulation rate was determined from an analysis of its incremental effect on deceleration rate and a fixed value of 0.007 rads/sec was used for all trajectories.

The values of deceleration force which were encountered during the calculation of a trajectory varied over a wide range depending on many

25

factors. Entry angle, wing loading and L/D were the principal determining factors on this parameter. For this study, a maximum allowable limit on RPA was taken as 10 g's (see chap 4). Provisions were made in the modulation technique to constrain the deceleration at or below this value. It was found that this constraint was necessary only during preliminary investigations which involved relatively high entry angles and, for the trajectories which were ultimately used for the heating analysis, the decelerations remained in the tolerable range.

The numerical computation procedure was divided into several basic sections which were, for the most part, self-contained. These sections are Initial Conditions, Aerodynamic Characteristics, Trajectory, and Heating and Ablator Weight. The Trajectory section includes the sub-sections for acceleration constraint, gradual angle of attack modulation and time incrementing and the Heating section has subsections for nose, bottom, leading edges, top and insulation weight computations. A complete treatment of the method of determining the aerodynamic characteristics for the vehicle shape used is found in the succeeding chapter and in Appendix B. The development of the methods used to determine the heating and thermal protection system weight is presented in Chapter 3 and Appendices C and D.
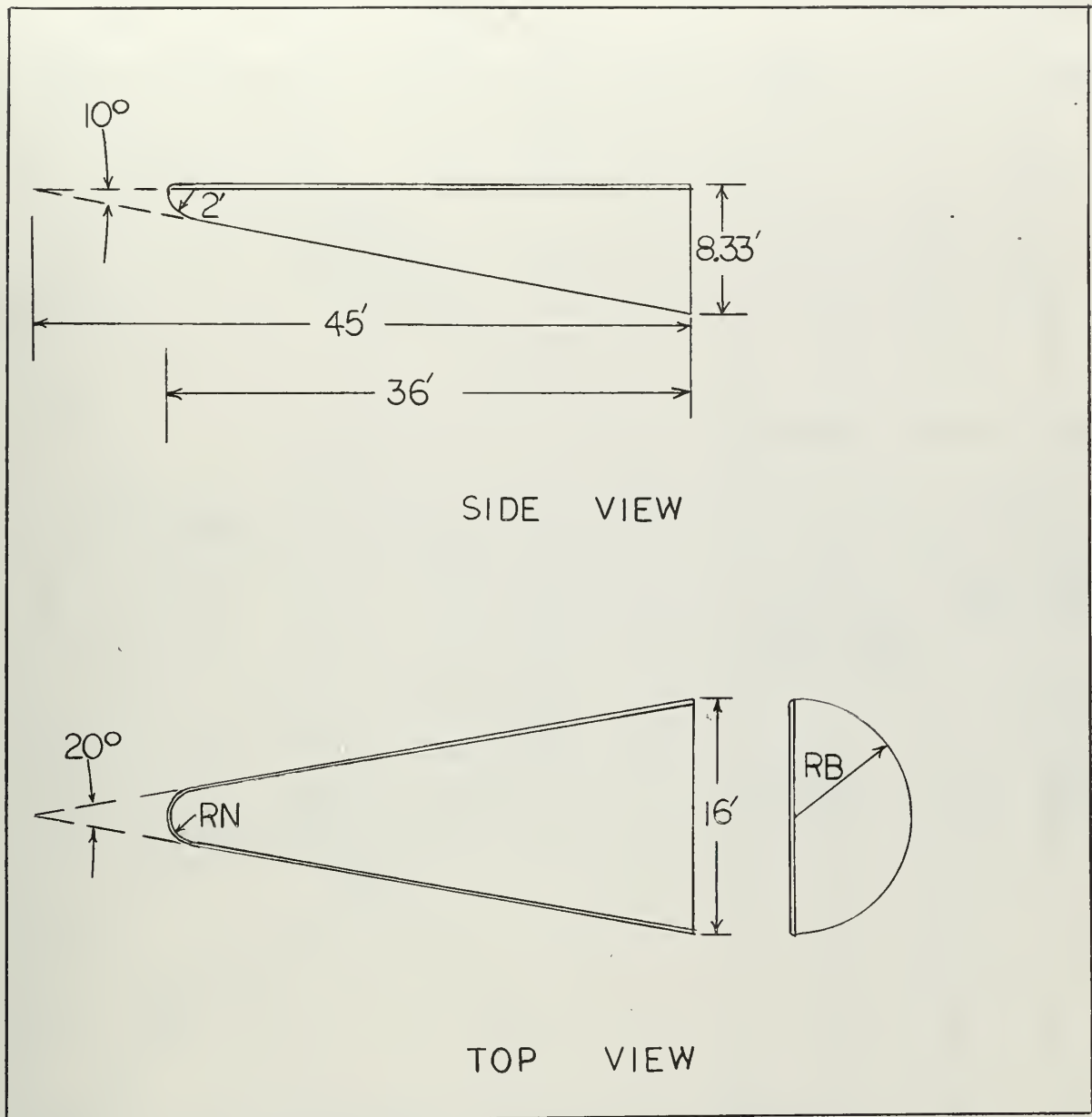
Fig. 1 Vehicle Schematics

27
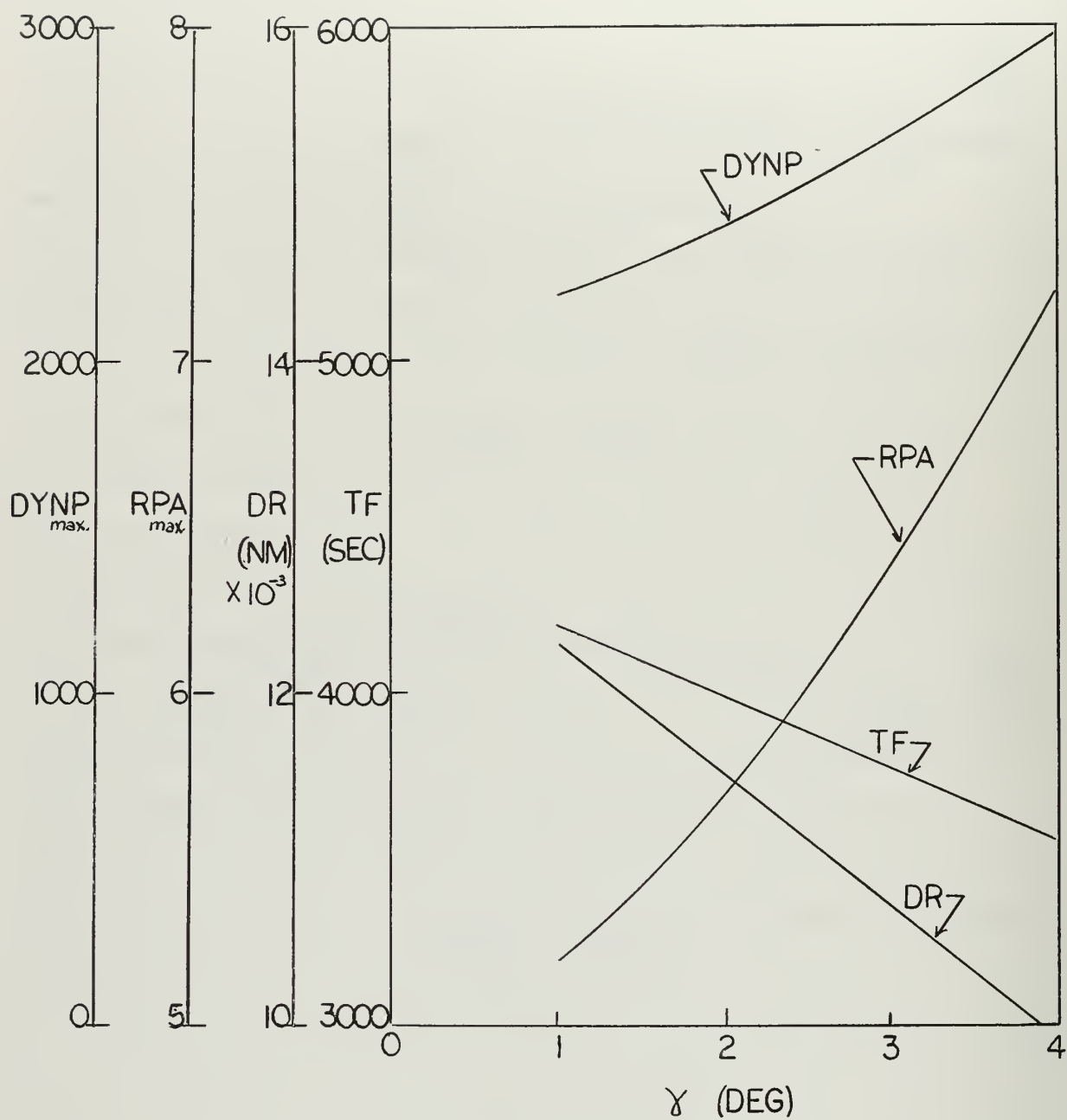
Fig. 2 Variation of Dynamic Pressure, RPA, Down Range, and Time of Flight with Initial Entry Angle

α	γ = 1°				γ = 2°			
	TF(SEC)	DR(NM)	RPA$_{max}$	DYNP$_{max}$	TF(SEC)	DR(NM)	RPA$_{max}$	DYNP$_{max}$
-5°	544	1887	4.09	4800	438	1446	5.18	6100
-2°	1958	5893	2.47	2100	1818	5280	2.73	2400
1°	2974	8807	3.43	2300	2764	8083	3.74	2500
5°	4202	12360	5.23	2200	3978	11532	5.74	2400
20°	--	--	--	--	2366	6471	3.05	380
40°	1250	3433	2.12	110	1130	2927	2.41	130
50°	--	--	--	--	896	2293	2.64	120

α	γ = 3°				γ = 4°			
	TF(SEC)	DR(NM)	RPA$_{max}$	DYNP$_{max}$	TF(SEC)	DR(NM)	RPA$_{max}$	DYNP$_{max}$
-5°	364	1145	6.9	8100	312	935	9.0	11000
-2°	1666	4744	3.3	2900	1584	4311	4.0	3600
1°	2650	7460	4.3	2900	2486	6882	5.0	3300
5°	3768	10773	6.3	2700	3678	10077	7.2	3000
20°	2290	5914	3.5	430	2114	5430	4.2	510
40°	1040	2538	3.2	170	952	2230	4.5	240
50°	812	1945	3.6	160	756	1679	5.2	230

TABLE 1

Constant Angle of Attack Trajectories

(variable entry angle)

CHAPTER 2

AERODYNAMICS

The aerodynamic design of a lifting body reentry vehicle is complicated by the wide range of flight conditions it encounters; from hypersonic flight at the limit of the earth's atmosphere to subsonic flight in the landing configuration. The requirement is to obtain a high L/D to provide range capability in the hypersonic regime and to provide maneuverability and landing capability in the subsonic regime. The basic tradeoff is the fact that, in hypersonic flight, blunt based vehicles are more efficient, while in subsonic flight, the additional base drag from such vehicles reduces the L/D.

Since this study is concerned with the ranging capability of a lifting reentry vehicle, only the hypersonic aerodynamic characteristics of the vehicle will be considered.

The first difficulty encountered in the study of hypersonic flow is the presence of extremely high temperatures downstream of a shock wave and the resulting changes in the properties of the fluid (e.g. air). With these high temperatures, it becomes necessary to consider the excitation of the three internal degrees of freedom of the air molecules; vibration, dissociation and ionization in addition to the normal translational and rotational modes.

Also, at hypersonic speeds, the shock wave tends to conform to the surface of the body to form a very thin "supersonic boundary layer." In this boundary layer, the interaction of compressible and viscous

30

forces greatly influence the pressure distribution over the body.

Finally, as the operating regime of the reentry vehicle approaches the limit of the earth's atmosphere, analysis based on continuum dynamics is no longer valid. In this region, the kinetic theory of rarefied gases must be used.

There are several basic analytical methods for determining the pressure distribution around a body moving at hypersonic speed. These, of course, vary in accuracy and complexity depending on the inclusion of effects such as those outlined above. These methods are fully described in the literature [5,6].

As pointed out by Corning [4], it becomes readily apparent that the single method which gives the best agreement between theory and experiment is based on Newtonian impact theory. The basis of Newtonian theory is the assumption that the fluid striking a body loses all momentum in the normal direction, while the tangential momentum is unchanged. The normal force on the body may then be expressed as the time rate of change of the normal momentum and a Newtonian pressure coefficient may be derived. This pressure coefficient is integrated over the body to obtain the lift and drag coefficients (see Appendix A).

It is shown in ref. 7 that the Newtonian theory, as presented in Appendix A, agrees closely with experimental data for the reentry configuration chosen. Closer correlation between theory and experiment could be expected for configurations having larger blunted noses and steeper body slopes. Also, the theory may be improved by using the stagnation pressure coefficient, $C_{P_{STAG.}} = \dfrac{\gamma+3}{\gamma+1} - \left(\dfrac{2}{\gamma+1}\right)\dfrac{1}{M_\infty^2}$ in place of the factor 2 in the expression for Newtonian pressure coefficient. In addition, there are several other normally neglected

31

factors which greatly influence the correlation between Newtonian theory and experimental results. Real gas effects (such as viscosity), centrifugal effects, leading edge pressure losses and leeward surface pressures may have a sizable effect on the aerodynamic characteristics of a given configuration. These considerations should be kept in mind when assessing the accuracy of results obtained by the simplified theory. Ref. 7 shows the comparison of theory and experiment for configurations where these neglected factors are noticeable. These various refinements were not considered germane to this study and were not included in the determination of the aerodynamic characteristics presented in Fig. B-2.

CHAPTER 3

AERODYNAMIC HEATING

During reentry from orbital altitude, the space vehicle will be
subject to severe aerodynamic heating while its kinetic energy is being
dissipated. The severity of the heating encountered will depend on many
parameters such as L/D, wing loading, entry angle, angle of attack and lift
or bank modulation scheme. Two heating parameters which are of prime
importance are the heating rate, q, which is the instantaneous heating
rate at any point on the body in BTU/ft^{2}sec, and the total heat input, Q,
in BTU/ft^2. High heating rates produce high temperatures which require
special thermal protection systems to prevent the structure of the reentry
vehicle from losing its strength, or in extreme cases, from melting. The
total heat input represents the amount of energy that must be dissipated
by the thermal protection system and, as such, has a direct influence on
the weight of thermal protection required for the vehicle. This chapter
will deal with the problem of determining the heating rates on the entire
surface of a representative lifting body vehicle. The total heat input
is a function of the resulting heating rate history and the time of flight
of the reentry. Analytical expressions are given for the heating rates
on the various parts of the vehicle as a function of the trajectory
parameters of velocity and altitude.

The heating analysis is based on the following two primary assumptions.
The first assumption is that the individual components of the vehicle can
be analyzed separately, thus allowing application of known empirical formulas to

33

standard geometric shapes such as hemispheres, cones, cylinders, etc.,
which can be joined together to form the complete vehicle. This assumption
assumes shock patterns on the composite vehicle will be unchanged from
those of the individual components. The effect of blunting the conical
body is considered in the analysis used. The second assumption
is that the effects of ablation, convective heating and radiation can be
uncoupled and treated individually

Aerodynamic heating will be assumed only on those surfaces that are
in direct contact with the flow field and the resulting heating determined
from empirical heating formulas based on Newtonian flow theory. At positive
angles of attack, the top will not be subject to impact heating and will
be in a vacuum of extremely low pressure with separated flow. The heating
rates in this region will be low enough that ablation cooling will not be
necessary and reradiation cooling and insulation will maintain the desired
internal temperature. Numerical integration methods were used on an IBM
7094 digital computer to solve the resulting non-analytical equations for
the total heating on the body and the required heat protection system.

Since heat is transferred through the boundary layer, it is first
necessary to determine if the flow over the vehicle is laminar or turbulent
because the heat transfer properties of the boundary layer will differ
greatly. The transition between laminar and turbulent flow in the boundary
layer is a function of many complex variables such as Reynolds number,
surface roughness, pressure gradient, wall temperature, Mach number and
altitude. This transition does not take place at any one point, but
rather over a large range of Reynolds numbers, ranging between approximately
0.5×10^6 and 20×10^6 (see ref. 8). Using a transition Reynolds
number of 5×10^6, it can be shown that the flow will be entirely laminar

above 140,000 feet for a vehicle 36 feet long. Since most of the heating will take place above this altitude for the type of lifting reentry being considered, laminar flow will be assumed throughout the entries being analyzed.

In order to determine the instantaneous heating rates over the body, it is necessary to know the velocity and altitude history of the vehicle during reentry. This is treated in detail earlier in this paper and, at this point, it is sufficient to state that the heating rates were computed in the same computer program as the trajectories and use the trajectory data calculated to determine the heating rate history. This heating rate history is then used to determine the required amount of heat protection as described in Appendix D. apter.

Appendix C contains a detailed description of the heating equations used for the various components of the body. The nose, which is assumed to be a quarter sphere, will encounter the most severe heating at the stagnation point. This heating rate is given as

$$
\dot{q}_s = 865 \left(\frac{V_\infty}{10^4} \right)^{3.15} \frac{e^{-\frac{H}{47,000}}}{\sqrt{R_N}}
\tag{3.1}
$$

The position of the stagnation point on the nose will be a function of the angle of attack. The heating rate distribution over the nose is a function of the heating rate at the stagnation point and the angular distance from the stagnation point and is given by the relationship:

$$
\frac{\dot{q}(\theta)}{\dot{q}_s} = \frac{\cos^{1.5}\theta}{\frac{\sin 2\theta}{2\theta}\left[\cos\theta\left\{1 + \left(\frac{\frac{2\theta}{\sin 2\theta} - \cos 2\theta}{\sin 2\theta}\right)^2\right\}\right]^{0.5}}
\tag{3.2}
$$

35

where θ is the angle measured from the stagnation point to the position

on the nose being considered. See Fig. (C-2A).

The next most severe heating will be encountered on the swept

leading edge. The heating rate along the leading edge is a function of the

stagnation heating rate, the angle of sweep and the angle of attack and

is given as:

$$\dot{q} = 610 \left(\frac{V_\infty}{10^4} \right)^{3.15} \frac{e^{-\frac{H}{47,000}}}{\sqrt{R_{LE}}} \left[1 - \sin^2 \Lambda \cos^2 \alpha \right]^{0.6}$$

(3.3)

It can be seen in both equations (3.1) and (3.3), the heating rates

are reduced by a factor of $1/\sqrt{R}$ as the radius of curvature of the surface

is increased. This leads to the conclusion that the heating rates will be

lower on blunter noses and leading edges. However, as will be shown later,

this does not necessarily mean a decrease in the weight of heat protection

needed since the area to be protected increases at a greater rate than the

decrease   in heating rate and material ablated.

The local heating rates over the underside of the body are dependent

on the angle of attack and position on the body. The underside is

assumed to be a half, right circular cylinder with a vertex angle, θ_v.

Using the method for compensating for non-axisymmetric flow caused by an

angle of attack as shown in reference 9, and discussed in Appendix C, the

local instantaneous heating rate on the underside of the vehicle is given

by:

$$\dot{q} = 750 \left(\frac{V_\infty}{10^4} \right)^{3.15} \frac{e^{-\frac{H}{47,000}}}{R_N^{1.5}} \frac{\sqrt{\frac{\pi}{2} - \theta_{EFF}} \; x' \; \sin \theta_{EFF}}{\left[\beta(\theta_v) + \left(x'/R_N \right)^3 \right]^{0.5}}$$

(3.4)

36

where θ_{EFF} is the effective vertex angle. This is the angle an element makes with the free stream velocity vector as shown in Fig. C-4 and is given by the relationship:

$$\theta_{EFF} = TAN^{-1} \left\{ TAN^2 \left[TAN^{-1}(TAN\,\theta_v\,SIN\beta) + \alpha \right] + TAN^2\theta_v\,COS^2\beta \right\}^{.5}$$

(3.5)

where β is the anglular position on the cone as shown in Fig. C-3. The blunt nose on the body creates an overpressure that persists for several nose diameters back along the cone and is compensated for by the factor $\beta(\theta_v)$ in equation (3.4). This factor is a function of the vertex angle θ_v and is tabulated in Table C-1 for various values of vertex angle. The distance measured along the body from the virtual apex is x' as described in Appendix C and shown in Fig. C-3.

The top surface will be subjected to impact heating when the vehicle is being flown at negative angles of attack. The top is assumed to be a delta shaped flat plate on which the heating rates can be found from the relationship:

$$\dot{q} = 25.3 \left(\frac{V_\infty}{10^4} \right)^{3.15} \frac{e^{-\frac{H}{47,000}}}{\sqrt{x'}} \alpha^{2/3}$$

(3.6)

where α is the angle of attack in degrees.

In addition to convective heat input to the system, there is also a radiative heat input to be considered. This heat transfer is due to radiation to the surface from the high temperature air in the shock layer near the stagnation point. This radiative heat transfer is usually negligible for subcircular velocities, but may be predominant at higher speeds. The gas cap radiation transfer rate is given as:

37

$$q_r = 7.5 \left(\frac{\rho_\infty}{\rho_{SL}} \right)^{1.5} \left(\frac{V_\infty}{10^4} \right)^{12.5} R_N \tag{3.7}$$

for $V_\infty > V_T$ and by

$$q_r = 100 \left(\frac{\rho_\infty}{\rho_{SL}} \right)^{1.6} \left(\frac{V_\infty}{10^4} \right)^{8.5} R_N \tag{3.8}$$

for $V_\infty < V_T$ where the transition velocity obtained by equating (3.7) and (3.8) is given by:

$$V_T = 1.91 \times 10^4 \, e^{-\frac{H}{94,000}} \tag{3.9}$$

In order to determine the magnitude of the gas cap radiation as compared to the convective heat input, several lifting body trajectories were examined to determine the ratio q_r/q_c. The results showed that for subcircular velocities, the maximum value of q_r found was $q_r/q_c = .2$ which existed for a period of less than 10 sec. The average value of the ratio was of the order of 10^{-3} and, as a result, the radiative heat input was neglected for the remainder of the heat analysis.

CHAPTER 4

VEHICLE DESIGN CONSIDERATIONS

The flight regime of a hypersonic lifting reentry vehicle is such
that severe aerodynamic loading and structural heating environments are
encountered. Some factors that must be considered in the design of such
a vehicle are aerodynamic efficiency, payload fraction, fuel containment,
crew safety and comfort, and integration of boost and cruise (if applicable)
propulsion systems. Materials having high temperature strength, and an
efficient means of fabrication, must be developed. The requirements of
guidance and control, communications, and navigation during the launch,
orbit, and reentry phases demand the development of improved avionics
equipment. Errors in guidance and navigation, and performance restrictions
during the reentry phase often impose additional requirements on the structure.

Underlying the specific requirements listed above is the choice
of the type of system; reusable or expendable. As space operations increase
in frequency, requirements for frequent transportation of personnel and
cargo to and from earth orbit become apparent. As the number of launches
increase, the cost of expendable boosters and reentry vehicles tends to
dominate the overall cost. This provides the motivation for development
of a completely reusable system, and studies[10] have shown that the launch
rate at which the reusable system (booster and reentry vehicle) pays for
its development is between one and two launches per month. In addition
to the cost reduction for increased launch rates, another advantage is
the greatly improved operational capability of such a system.

Along with the economic considerations, the mission requirements are also reflected in structural design criteria. For example, a reusable vehicle returning to a prepared landing site simplifies the problems of landing, refurbishment, search, and retrieval. This gain, however, comes at the cost of a more complex vehicle and control system, and the addition of an auxiliary propulsion system for subsonic ranging and landing. On the other hand, an expendable system, while not as complex, introduces the problems of landing on unknown surfaces, and providing shelter and food for perhaps an extended period of time during retrieval.

Since the present study is concerned primarily with the reentry phase of a manned vehicle, the design considerations will be based on this phase of the mission. There are, of course, requirements generated in other phases of the mission which must be considered in the overall system design. For example, components designed for high dynamic pressure during the launch phase will be able to withstand the lower dynamic pressures during lifting reentry. Other components of the vehicle may be designed from considerations of launch phase accelerations, meteoroid penetrations, bending moments, internal pressurization, or other loading conditions. Therefore, the criteria presented here for the reentry phase must be considered not as firm requirements, but rather only a portion of the overall system criteria.

4.1 Human Tolerances

The consideration of a human tolerance limit is a necessity when specifying thermal protection and structural design limits for a manned reentry vehicle. The deceleration tolerance limit is defined as the maximum amount of time the crew is able to endure a given deceleration force with a preselected level of pain or performance degradation. The most vulnerable items on board the vehicle in regard to deceleration forces are the human occupants and their tolerance limit was taken to be the upper boundary on the system.

40

A considerable amount of effort has been expended in the area of human tolerance to deceleration loads[11,12,13] and it has been found that the ability to tolerate these loads depends on a variety of interrelated effects. Most significant of these are body position, peak force level, duration of exposure, and time rate of change of forces. Also, the requirement to perform complex control functions while under deceleration loads reduces the allowable limit. A function involving precise hand or finger positioning imposes a lower allowable limit than does an "on-off" switch function.

The body position which allows the highest decelerations is the transverse supine. In this position, g forces are transmitted from chest to back and a large surface area of the body may be supported by a couch or seat. Hydrostatic blood circulation problems are small and the unconsciousness limit is determined by ability of the chest muscles to expand against the g load during respiration.

The effect of duration of loading is seen in Fig. 3 . Based on the transverse supine body position, the ability to withstand high g loads is greatly degraded by increasing the time duration a small amount. The area of physical discomfort in Fig. 3 may be used under certain circumstances such as physically trained personnel with simple control functions, however, the pulse peak limit is reduced drastically while in this region. Bryson[28] uses a weighted function based on both peak force and duration to determine the effective deceleration limit.

The direction of the force is seen to be an important factor and must be determined from a vector summation of the applied aerodynamic forces.

41

This vector sum is termed the "Resultant Physiological Acceleration (RPA)". It is important that the transverse supine body position must be aligned with the RPA vector direction to obtain the greatest capacity to withstand deceleration. The RPA is found from: (See Appendix A)

$$RPA = \frac{1}{gm} \left\{ \left(L\cos\phi\cos\gamma + D\sin\gamma\right)^2 + \left[\left(-D\cos\epsilon + L\cos\phi\sin\gamma\right)\cos\theta_3 + L\sin\phi\sin\theta_3\right]^2 \right.$$

$$\left. + \left[\left(D\cos\gamma - L\cos\phi\sin\gamma\right)\sin\theta_3 + L\sin\phi\cos\theta_3\right]^2 \right\}^{1/2}$$

Deceleration due to drag and normal g's due to the curvature of the flight path are the predominant effects in RPA.

An additional human tolerance limit is that caused by aerodynamic heating. Fig. 4 shows the results of experimental data presented by Webb[14]. The maximum levels indicated do not represent the ultimate in tolerances for high transient heating. Protection improvements such as air-ventilated reflective clothing and cooling the body prior to exposure can be used to improve tolerances. The tolerance levels presented were difficult to set specifically because of the variation in reactions of different individuals. Selected tolerance limits will depend both on the individual and on the required performance during the time of exposure.

4.2 Control and Guidance System Requirements

The calculation of the reentry trajectories in this study is based on fixed initial conditions. In actual practice, however, there are many factors which influence the conditions at the initiation of the reentry phase. Also, the accuracy of the retro-firing, both magnitude and direction, has a great influence on the resulting reentry trajectory. Each of these varying parameters affects the location of the landing point or, for a given landing site, the severity of the maneuvers required to reach it. Thus the design of a reentry control system must consider encountering all possible variations in the trajectory parameters, the response of the vehicle to orientation commands, and the ability of the structure to withstand the resultant loading conditions.

The guidance process involves the measurement of the trajectory parameters, the computation of the control actions necessary to correct the trajectory parameters, and the delivery of such command signals to the vehicle control system.

The combination of these two concepts gives rise to the force-vector control system; i.e., a system which controls the magnitude and direction of the resultant force such that the vehicle arrives safely at the desired destination. Various techniques for implementing force-vector control are presented in the literature[15,16]. The determination of guidance requirements for a specific mission involves a complicated analysis of trajectories, uncertainties in the specification of parameters, vehicle aerodynamic properties, control and guidance system capabilities, propulsion system, payload requirements, heating and deceleration constraints, and system cost. For the present study, however, the specific instrumentation and guidance scheme necessary to fly the final nominal trajectory was not considered.

43

4.3 Structural Design

The structural design of a reentry vehicle is influenced directly
by two effects in the high speed flight regime: a) increased surface
temperatures caused by aerodynamic heating and b) increased surface pressure
loads. The former dictates the type of materials that must be used for
exterior surfaces while the latter requires a generally heavier structure
to resist the forces that are generated.

Since both of these effects are functions of velocity and air
density, the structural advantage of the lifting body becomes apparent since
the use of aerodynamic lift gives some control over the operating portion
of the flight envelope.

It follows then, that the structural design of a vehicle must
integrate the results of two separate considerations; the environment
to which the vehicle will be exposed, and the "state-of-the-art" for
material usage and fabrication techniques.

4.3.1 Environmental Considerations

Generally, the structural design criteria for the vehicle must be
combined with the criteria for heat shield design since the heat shield
is normally attached directly to the structure. The prime requirement for
an efficient heat shield is that it minimizes the heat that reaches the
primary structure. This, of course, is necessary so that structural problems,
such as reduced strength, thermal deformations, thermal fatigue and creep,
and thermal stresses due to temperature gradients, are reduced. A more
detailed examination of the thermal protection system concept and use is
presented in Section 4.4.

The major source of heating is that which is generated aerodynamically,
and is associated with both the ascent and descent of the vehicle through

44

the atmosphere at high speeds. In general, the heating associated with reentry is two to three times greater than that encountered during the ascent[17]. It is this phase which imposes the design condition for the external surfaces of the vehicle.

Another source of structural heating is solar heating while in orbit. The surface temperature of a material undergoing this type of heating is a function of the absorptivity/emissivity ratio of the surface. Since both the absorptivity and emissivity can be varied by surface finishing and painting, solar heating is not considered as a primary design criterion.

Also radiation heating, which was mentioned briefly in Chapter 3, is not considered to be a primary design criterion for a vehicle entering the earth's atmosphere from orbital velocity under the conditions of this study.

The loading environment of the vehicle may be considered to consist of two general types of loading, dynamic loads and quasi-steady state loads.

The primary dynamic loading consideration is acoustic fatigue resulting from intense noise levels associated with both the ascent and reentry of a vehicle. The acoustic inputs are fluctuating pressures on the surface of the vehicle. These, as well as vibrations and aerodynamic buffeting, are transmitted into the vehicle structure and equipment. It is shown in Fig. 5 that the noise level is less during the reentry phase, but the duration of the noise environment is longer. The noise sources which may be present are booster exhaust, boundary layer noise, base pressure fluctuations, cavity resonances, oscillating and moving shocks, atmospheric turbulence, retro-rocket turbulences, and internal equipment.

The source of boundary layer noise is the pressure fluctuations in a fluid along the surface of a vehicle moving at high speed in the

atmosphere. The strength of the pressure fluctuations is proportional to the free stream dynamic pressure. This noise is a major source of skin vibration for most vehicles, although its importance in relation to total noise is a function of the type of reentry trajectory.

Base pressure fluctuations are primarily a function of vehicle configuration and can contribute to the overall noise level at both subsonic and supersonic speeds. It should be noted that this noise source is only present during the reentry phase since the base is normally shielded by the booster or the interstage fairing during the launch and ascent phases.

The noise and vibration attributable to atmosphere turbulence, retro-rockets and internal equipment is of secondary importance in relation to the other noise sources.

Quasi steady state loads are associated with both the ascent and reentry phase. The launch and ascent phase generates the greatest dynamic pressure which, when combined with the accelerations imposed by the launch vehicle, specifies the design criteria for the major portion of the vehicle structure in the context of vehicle stiffness and separation fitting strength.

During the orbital phase, the primary loading consideration is the steady state internal cabin pressurization. The design criteria for this portion of the flight are a shell that can withstand long periods of pressurization with negligible leakage, and materials that can be fabricated and joined with minimum weight.

The primary loads during the reentry phase are low compared to those during the ascent phase. With the proper heat protection system, the inner structure temperatures can be kept low enough so that the design criteria

are not specified by reentry loads. Now, however, the external thermal protection system has imposed upon it the requirements to withstand combinations of high temperature and pressures, to maintain sufficient stiffness to resist flutter, and to provide sufficient fatigue strength.

Meltzer, et. al.[18] present some structural and material design considerations of the PRIME flight test vehicle. An iterative computer program was used to determine where to add or subtract strength, area, or stiffness and still maintain an efficient structure from the standpoint of total vehicle weight. The structural elements, such as stringers, frames, and skin panels were ultimately defined in terms based on local loads, thermal stress buckling criteria, stiffness requirements, and minimum gauges. Overall bending was not a contributing factor in the sizing of structural members. However, thermal stresses did serve as the basis for the design of the skin panels. The substructure thermal stress is a function of both the particular reentry trajectory and the external thermal protection system design. Due to thermal lag, structural requirements based on resulting temperature gradient calculations lag the requirement for establishing skin gauges and structure based on loading conditions. As the result of a study of the effect of temperature gradients on thermal stresses, 10,000 psi longitudinal thermal plus static stress was established as a basis for panel buckling. The maximum thermal stress was calculated near the end of heating as 8000 psi while the maximum bending stress at this time was less than 2000 psi.

There is a serious design problem that follows directly from the discussion in the two preceeding paragraphas, and that is the problem of panel flutter. As the operating dynamic pressure increases at higher speeds,

47

the effect of panel flutter becomes greater. It should be noted that panel flutter is, technically, a dynamic loading problem and, as such, is difficult to distinguish from acoustic effects since the failure modes are similar. The analysis of panel flutter is complicated by the number of factors which influence its presence, such as material properties, pressure differences, panel thickness and boundary conditions.

Consideration also should be given to the effects on panel flutter of aerodynamic heating and flow direction. Two other parameters which are related to the panel flutter problem are panel mid-plane stress and pressure difference across the panel[19].

As previously mentioned, the severity of panel flutter, which is proportional to the dynamic pressure, suggests that the ascent phase may determine the design conditions for panel flutter. However, it should be noted that flutter during reentry may be critical for some sections of the vehicle because of a more severe attitude, and longer exposure time than during the ascent phase.

Neglected to this point in the consideration of structural design, but perhaps of primary importance, are the landing loads absorbed by the vehicle at impact. Due to the thermal lag of the structure, the materials chosen to absorb the landing loads must do so at elevated temperature under the constraint of minimum weight.

The design of the heat protection system and structure of a reentry vehicle must consider both deviations in assumed constant parameters such as entry conditions, and also the validity of basic assumptions such as the atmospheric model and planetary rotation. The effect of changes in several of these parameters on aerodynamic heating and loading will be examined.

48

The effect of variations in the initial flight path angle will be examined for two cases. One is the Apollo lunar return[20], and the other is the return from near earth orbit of the basic vehicle used for this study.

For the Apollo return mission (L/D = 0.5), the initial flight path angle upon entering the earth's atmosphere is the controlling parameter which determines the subsequent aero-thermodynamic loading. The expected velocity variation of $\pm$ 200 feet per second around the nominal velocity of 36,000 feet per second produces little variation in the aero-thermodynamic loads. The deviation in the initial flight path angle is set by the tolerance of the guidance system. A variation of $\pm$ 1 degree about the nominal entry angle of five degrees results in a variation of + 70 percent and -60 percent in the maximum dynamic pressure. The corresponding deviations in the stagnation point convective heating rate are +20 percent and -30 percent. The stagnation point heating rate, integrated to the first pull up, shows a deviation of + 7 and - 20 percent.

The deviation in the aero-thermodynamic loading of a vehicle returning from a near-earth orbit are not as great as those described above for the Apollo mission. For a representative angle of attack modulated trajectory as described in Chapter 5, a variation in initial entry angle of $\pm$ 1 degree from the nominal angle of two degrees results in a variation of + 12 percent and - 12 percent in the maximum dynamic pressure. The variation in the stagnation heating rate and the total stagnation heating are + 21 percent, - 21 percent and - 11 percent, + 13 percent respectively. The corresponding variations in the peak deceleration loads are + 18 percent and - 12 percent. These and other effects of varying initial entry angle are

presented in more detail in Chapter 6.

The variation of the atmospheric model and its effect on deceleration loads and stagnation point heating has been investigated by Rute[21]. Two trajectories were examined; one a ballistic reentry and the other a super-circular skip-out trajectory. Two atmospheric models were considered and the effect of variations in each of the two trajectories was examined. The first model was an exponential isothermal layer atmosphere and variations were introduced through both the reference density and the density decay parameter (scale height). The second model was a multi-layer, multi-temperature model with variations introduced by means of the Hot and Cold days defined in ref. 11. The study concludes that the choice of atmospheric model has considerable influence on the aero-thermodynamic loading parameters with a supercircular reentry. For the subcircular reentry considered in this study, the aero-thermodynamic loading parameters are relatively insensitive to changes in the atmospheric model. The actual model used is described in Chapter 1.

Another effect, normally neglected in the analysis of loading on a reentry vehicle, is that of wind. The maximum wind velocity normally exists in the altitude range in which maximum dynamic pressure and maximum stagnation heating rates occur. A study has been conducted[20] in which assumed velocity perturbations of $\pm$ 600 feet per second around a nominal velocity of 20,000 feet per second were introduced. The maximum deviation in dynamic pressure and stagnation point heating rate was $\pm$ 6 percent and $\pm$ 9 percent respectively. These are maximum deviations since the analysis did not consider the direction of the wind.

The final assumption to be examined is that of a non-rotating earth. Since the atmosphere is rotating with the earth, the relative

50

velocity vector of the wind should be included in the basic equations of motion. This would alter the trajectory and hence, the parameters affecting aero-thermodynamic loads would change. This is a small effect and was neglected for the present study.

4.3.2 Material and Fabrication Techniques

The two factors which, more than any others, place design limits on space vehicles are the lack of suitable materials and the lack of adequate processing and fabrication techniques. The first considerations in selecting materials are their physical and mechanical properties. However, as explained in the previous section, the adaptability of the material to changing environments and its ability to maintain the design criteria are the deciding factors in the final selection. Some of the environmental considerations in material selection are:

a) Corrosion

b) Lubrication

c) Chemical compatibility

d) Vacuum welding

e) Oxygen exposure

f) Meteoroid penetration

g) Radiation

h) Vacuum instability of nonmetals

Corrosion - Corrosion, which is the deterioration of a material through reaction with its environment, may occur either by direct chemical reaction or by an electrochemical reaction. Some factors which effect the rate at which corrosion occurs are temperature, stress levels, oxygen concentration and hydrogen-ion activity. The corrosion problem is

51

especially important in space vehicle design because of the large scale use of lighter, more active alloys such as titanium, aluminum and magnesium.

Lubrication - Lubrication of moving parts in a space vehicle poses a problem since the majority of the common petroleum and synthetic base lubricants are subject to rapid evaporation in a high vacuum environment. Another lubricant commonly used on earth, graphite, tends to act as an abrasive after a short exposure to a near vacuum environment. Acceptable lubrication characteristics in space have been obtained by use of disulfide types of dry film lubricants.

Chemical Compatibility - Chemical compatibility is primarily a problem in the vehicle's fuel storage and transfer system and the fuel cell system. The compatibility of materials in such cases is normally verified experimentally under simulated environmental conditions, if possible, prior to final design.

Vacuum welding - Metals subjected to a high vacuum environment are affected in two ways: the "boiling off" of the layer of absorbed gases on the surface of the material and/or the evaporation of the material. The removal of the layer of gases results in an ultraclean surface which may lead to the fusion of two contacting metals which have no surface protection from normal metallic oxidation. The rate and severity of this vacuum welding is a function of the bearing pressure, temperature, and metal similarity. The consideration of vacuum welding imposes restrictions on material selection and/or requires surface coating with a stable protective film.

Oxygen Exposure - The reaction of certain metals, exposed to a pure oxygen environment, is of primary concern in the design of the spacecraft cabin and oxygen system. Experimental evidence has shown that an impact or exposure of a fresh metallic surface to a pure oxygen environment, under certain conditions of pressure and temperature, may cause a pyrophoric reaction.

Tests on the Gemini cabin, which is constructed basically of titanium, have shown that, under normal cabin pressure levels, spontaneous combustion phenomenon of this type will not be a problem.

Meteoroid Penetration - Considerable research is presently being conducted to determine the resistance of materials to meteoroid penetration. It appears, however, that meteoroid penetration will not pose a problem for vehicles in a near earth orbit.

Radiation - Materials exposed to radiation generally exhibit some degradation in mechanical or physical properties. This degradation is primarily experienced by organic materials such as paints, fabrics and lubricants. Near earth orbits are below the serious radiation zone but, for interplanetary missions or synchronous orbits, radiation effects could specify certain material design requirements.

Vacuum Instability of Non-metals.- Certain non-metals, in particular fabrics such as nylon and dacron, exhibit a loss in strength after exposure to a vacuum environment. This instability appears to be associated with dehydration since the strength is restored to varying degrees when the materials are exposed to a humid environment.

While all the above mentioned factors must be considered, the most obvious influence on material selection for hypersonic flight is

53

temperature. Fig. 6 shows the general thermal classification of common structural materials. It should be noted that the time of exposure has an appreciable affect on the maximum temperature at which the material possesses useful structural properties.

In addition to the metals shown here, another general class of material has useful high temperature applications in space vehicle design. The theory and application of ablative materials are presented in the following section and in Appendix D.

High temperature characteristics of several super-alloy sheet materials are tabulated in Table D-2 and presented in Fig. 7 [23].

Another important consideration that influences the choice of a particular material is its oxidation resistance. Although most superalloys and considered to be oxidation resistant for temperatures below 2000°F, the nickel-base super-alloy René 41 exhibits intergranular oxidation at lower temperatures. The extent of this oxidation is shown in Fig. 8 as a function of temperature and exposure time.

The problem of oxidation of the refractory metals is also one of major concern since these materials begin to oxidize at temperatures in the neighborhood of 800°F. It then becomes necessary to set temperature limits for these materials based on the ability of a protective surface coating to retard oxidation. The present state-of-the-art in protective coatings of this type sets the upper temperature limit at approximately 2500°F for a relatively long time duration.

Up to this point, the actual structural design of the vehicle has not been examined. However, the cross-coupling between material characteristics and vehicle design is such that neither can be considered without the other.

54

The structural concept chosen for a given mission must satisfy the structural integrity requirement and do so with minimum weight. As an example of the tradeoffs present in the structural design of a spacecraft, reference is again made to the PRIME test vehicle[18]. The basic structure of the vehicle is of 2014-T6 aluminum with an expected maximum temperature of 300°F. This design allowed use of present fabrication techniques and involved little expenditure for additional development. In addition, studies were made to determine the feasibility of setting the structure temperature limit at 800°F. Titanium was selected as the basic structural material. The resulting vehicle structure showed an increased weight over the aluminum structure due to three factors: a) steeper thermal gradients on titanium, b) the lower buckling efficiency of titanium and c) the increase in environmental control system weight due to the increased wall temperature. On the credit side, however, is the reduction in heat shield weight made possible by allowing a higher back wall temperature. The net result was a weight saving of two percent over the vehicle with aluminum sub-structure. However, other considerations such as increased development costs and a more complex fabrication technique for the titanium vehicle resulted in a compromise. The basic vehicle was designed for a 300°F maximum structure temperature, with the fins and flaps designed for an 800°F temperature. Another by-product of this high temperature sub-structure on the fins and flaps is that the thinner heat shield allows the composite structure to remain within aerodynamic thickness limitations. For this vehicle, stiffness requirements to prevent cracking of the ablator, and the high density of the vehicle lead to a composite heat shield and structure weight fraction of .44.

55

The next consideration in the structural design of a vehicle is the actual structural configuration. There are two basic choices for the load carrying sub-structure: a) carry the primary bending loads in longerons running lengthwise along the vehicle, or b) by carrying the primary bending loads in a semi-monocoque surface structure. In the first case, the primary function of the surface is to support shear loads and to transmit pressure loads to the longerons and supporting stiffness rings. In the latter case, the heavy members are eliminated and the surface structure is stiffened to carry the compressive, shear, and pressure loads. There are three general types of surface structures which may be used: a) stiffener-skin surfaces, b) corrugation-skin surfaces, or c) sandwich structure.

The stiffener-skin surface has the advantage of simplicity over the other two types, but is less rigid. The stiffeners generally run in one direction and are integrated with the surface skin through rivets or spotwelds.

The corrugation-skin structure is a relatively efficient method for applications in which the loading is predominately in one direction. As in the stiffener-skin structure, the corrugation is attached to the surface by riveting or spot welding.

The sandwich structure is composed of two flat sheets separated by either honeycomb semi-structure or a corrugated structural core. This construction is the most rigid of the three types and is able to withstand the highest stresses.

4.4   Thermal Protection System

Chapter 3 and Appendix C describe the methods used to determine the heating rates which occur on the body during the reentry. These heating rates will result in temperatures well above those that can be tolerated by occupants of the spacecraft, equipment and even the structural material used in the spacecraft. It is the purpose of the thermal protection system to dissipate this heat input and to restrict the temperature behind the protection system to a specified maximum value. There are several heat protection schemes that can be used to accomplish this end. These are the use of a heat sink, ablation cooling and re-radiation cooling. These methods will be discussed in light of their relative advantages and disadvantages and their applicability to the type of reentry being considered.

The heat sink is a heat absorption system operating below the melting point of the material. It employs the principle of absorbing heat by conduction and works effectively only if the heating rates are low. Since the surface temperature must, by necessity, be low to avoid melting the material, re-radiation is negligible and all the heat input is absorbed by the material. The weight of the heat protection system is directly proportional to the amount of heat to be absorbed. Since lifting body reentries are primarily being considered here, the time of flight will generally be long, approximately 2000 - 3000 secs., which leads to a large total heat input to the system. This large total heat input makes a heat sink protection system impractical from a weight standpoint due to the large mass of absorbing material that would be required.

The longer the duration of hypervelocity flight, the more attractive it is to cool by radiating the heat into the surrounding space. This is

57

especially true for high L/D and low wing loading vehicles where the long

time of flight and the low heating rates produce maximum equilibrium

temperatures of approximately $2000°F$ or less. These equilibrium temperatures

are within the capability of many present day materials. In this type of

system the structure of the vehicle would be covered with a thin shell of

high temperature re-radiation metal with a layer of insulation between the

shell and the main structure to maintain the desired inner wall temperatures.

The radiation cooled structure has the advantage of reuseability if designed

correctly. After each flight, inspection procedures would be necessary to

ensure the radiation structure was not damaged during reentry. Due to

the wide variation of temperatures involved, the design must allow a margin

of safety for the allowable stresses determined from the analysis of the

expected heating. Failure of the radiation cooled structure may be more

subject to small imperfections in the material (through manufacturing

techniques or through reuse) than the ablation cooled structure. One

consideration in choosing a radiation system is the higher guidance accuracy

required over that of the other systems. A single trajectory error causing a

momentarily excessive heating rate could be disasterous.

Another method of cooling regions of high heating rates, such as

near the stagnation point, is transpiration cooling[24]. In this system

evaporative fluid is forced through porous metals or screens into the

boundary layer in the stagnation region forming a very thin film, some

1/1000 of an inch thick. The evaporation of the fluid absorbs the heat as

the fluid is forced away from the region of high heating rates. Water is

a good candidate for the evaporative coolant fluid, especially since it may

58

be produced aboard the spacecraft during its time in orbit as a
by-product of an energy production process such as a fuel cell. This
is especially attractive since the weight of the coolant would not now
be charged against the weight of the thermal protection system.
Reference 24 shows that the effective heat of evaporation of water is a
function of the velocity. For small velocities it is approximately 1100
BTU/lb, while at reentry velocities it increased by a factor of 10 to 11,000
BTU/lb. This value of the effective heat of evaporation is in the velocity
range of 10,000 ft/sec to 25,000 ft/sec. It is in this velocity range
that most of the heating takes place. The effective heat of evaporation
is used in the same way as effective heat of ablation is used for ablating
materials and is a measure of the effectiveness of the material. The value
of 11,000 BTU/lb given above for water is about twice the value of many
ablating materials, including Teflon. The primary problem associated with
transpiration cooling is bridging the gap between test/theory and
practice in a full scale reentry vehicle. This is partially due to the
large amount of plumbing needed to distribute the coolant over any
substantial area of the vehicle. This problem would tend to restrict
the use of transpiration cooling to small areas such as the nose and leading
edges of a glider type vehicle.

The absorption of aerodynamic heating by the ablation process is,
at this time, the most powerful method of heat protection for reentry
vehicles. This method of protection is not restricted by high heating
rates since the rate of ablation will automatically adjust to the
heating rates. This is in contrast to the possible disasterous results
which might occur under the similar circumstances with a radiation cooling

59

system. In the ablation process, there are several mechanisms of heat absorption which are controlled by the properties of the ablating material[25]. These are a) heat absorption by the body through thermal conduction in which absorption is dependent on the thermal diffusivity of the material, b) heat is absorbed by melting and/or vaporization depending upon the latent heats of fusion and vaporization of the material, c) heat transfer from the boundary layer can be effectively blocked by the injection of the vaporized mass into the boundary layer, d) heat is radiated away from high temperature ablation materials that have high emissivity, and e) heat can be absorbed or released by chemical reactions between the air and the ablating material. Blocking heat transfer by injection into the boundary layer depends upon the flight velocity of the ablating body, the type of boundary layer (laminar or turbulent) and the molecular weight of the ablating material.

When calculating the weight of an ablation system, the weight of insulation must be considered. Since the surface of the ablating material will be at the vaporization temperature during the ablation process, it is necessary to provide an insulation between the surface and the structural wall if the desired wall temperature is less than the vaporization temperature of the ablating material. The insulation weight required will depend on the energy diffused into the heat shield during the reentry. In order to minimize the amount of energy conducted into the body, it is desirable to use a material with a low thermal conductivity. An ablator such as Teflon has a low conductivity and can be used as both ablator and insulation. This makes heat shield fabrication easier since bonding problems caused by one material being used for ablator and another for

60

insulation are eliminated. The vaporization temperatures of the material must also be considered. Although a high temperature ablator will dissipate more heat by re-radiation and thus reduce the weight of ablation material needed, it will also require more insulation weight to maintain a desired back wall temperature. The type of trajectory being considered will determine whether a high or low temperature ablator will provide the desired protection for the least combined ablator and insulation weight. For a nonlifting vehicle whose dimensions are such that the heating rates are too high to be balanced by radiation cooling, it is better to use a material with a low ablation temperature in order to reduce the insulation problem. For lifting vehicles which experience lower heating rates over most of the surface, the primary means of cooling would be radiative except at the leading edges where high temperature ablation material would be used.

Another type of material is the charring ablator. This material is characterized by the formation of a char layer on the surface of the material as shown in Figure D-5. The charring ablation materials are generally composed of thermosetting resins (epoxy or phenolic) usually reinforced with either organic or inorganic fillers (nylon or quartz fibers). The important features of the charring ablator concept are:

a) A highly cross-linked carbonaceous char residue results from the thermal degradation of the resin.

b) The depolymerization temperature associated with the breaking up of the organic polymer is low, resulting in approximately $500^{\circ}- 600^{\circ}F$ in the reaction layer.

c) The surface temperature of the char can be high, resulting in reradiation to space of a large percentage of the convective heat input during lifting reentry.

d) At low heating rates, and consequently low surface temperatures, the rate of char removal is low and results from combustion of the char with active species within the boundary layer.

d) As the char builds up, it acts as a self-generated insulation layer of low thermal conductivity.

The charring ablator combines the advantages of high surface temperature (allowing a high percentage of re-radiation) with a lower internal temperature in the reaction zone due to the insulation effect of the char (reducing the amount of additional insulation required to maintain a desired back wall temperature). Due to the complex chemical reaction taking place during the formation of the moving char layer, the analysis of a charring ablator is very difficult, as will be shown later.

The final heat protection scheme to be mentioned is the combination ablation-radiation cooling. Here ablation cooling is used on parts of the vehicle which will be subjected to high heating rates such as the nose and leading edge. The remainder of the underside may be radiation cooled, if the predicted heat flux permit, or partially cooled with ablator with the remainder protected by a high temperature metal or ceramic coated material.

The type of trajectories being examined in this thesis are lifting reentries for a vehicle of relatively high wing loadings (W/S = 50 lb/ft^2). An examination of the trajectories shows that high heating rates exist during the pull-up maneuvers encountered during the reentry and that these pull-ups last throughout a large percentage of the reentry time of flight. A typical temperature distribution over the body for one of the trajectories examined is shown in Figure 9.   Although some of the trajectories considered have peak heating rates low enough to allow reradiation cooling

over at least a portion of the underside, the weight of the thermal
protection system was determined using ablative cooling over the entire
vehicle, including the top when at negative angles of attack. The weight
of insulation required to maintain 200°F at the inner structural wall was
also determined and the sum of these weights represents the weight of the
entire thermal protection system. Teflon was assumed to be both the
ablative and insulating material. This approach allowed a common basis for
comparing the weights of the thermal protection system for a large variety
of reentry schemes.

Appendix D gives a description of the ablation cooling analysis.
It was assumed that the vehicle entered originally at 400,000 feet with a
uniform temperature of -100 F. After comparing the schemes of reentry
that provided the desired range capability for the least weight of thermal
protection utilizing Teflon, the same trajectories were again examined
using all ablative protection with various other materials, including both
vaporizing and charring ablators. The properties of the materials used
are tabulated in Appendix D and results compared in Figure 61. A
combination radiation ablative system was also examined and compared with
the all ablative protection system.

The preceeding sections have described briefly some of the factors
which must be considered when specifying the structural design criteria for
a reentry vehicle. The basis for all of these factors is the fundamental
requirement on any flight vehicle not to fail below ultimate loading
conditions, nor deform below limit loads so as to prevent satisfactory
completion of the specified mission.

It has been shown that the structural design of an entry vehicle is

63

primarily dependent on the aero-thermodynamic loading associated with a particular flight profile. High L/D vehicles with low wing loadings entering from a near earth orbit may most efficiently use a radiation type thermal protection system. On the other hand, low L/D vehicles with high wing loadings must use an ablative type thermal protection scheme, regardless of entry velocity. It is between these two extremes that the design of the vehicle must consider all possible factors in order to optimize the overall system.

The effect of perturbations in the initial entry conditions and the reentry environment have also been discussed. However, at the present time, deviations in the aero-thermodynamic loads caused by guidance errors are greater than those caused by the simplification of certain analytical methods. Perturbations generated by atmospheric variations and neglect of high altitude winds are generally of less importance than are those caused by deviations in initial entry conditions.

The most feasible method for establishing thermodynamic design criteria is to base the thermal protection system requirements on the most severe thermal environment expected for the specific mission. The reduction in strength and rigidity of the structure subjected to thermal stresses will depend to a large extent on the design details of the structure. Thermal stresses may be reduced by increasing deformation, reducing temperature gradients, or by cooling the structure. Cumulative changes in the capability of the structure to sustain loads must also be considered. The useful life of a vehicle may be limited by any number of effects such as fatigue, creep, corrosion, aging, and changes in aeroelastic response due to permanent deformations. In addition to thermal considerations and

aerodynamic loading, the loads associated with ground impact must also be considered. These may be the most severe design restrictions due to the time lag between the maximum heating and the loss in strength associated with the thermal response of the structure.

Due to the wide range of loading conditions and structural requirements for the large class of reentry vehicles, it is obvious that meaningful and useful design criteria may be established only after a particular vehicle or mission has been specified. One method which is useful in showing the design requirements of a particular reentry vehicle is through the use of a design envelope such as that shown in Fig. 10. This particular envelope is for the reentry and recovery phase of the Dyna-Soar[27]. The upper boundary is set by the aerodynamic capability of the vehicle and the lower boundary is set by the structural capability to withstand the aero-thermodynamic loads.

The safety factors normally applied to limit loads to obtain ultimate loads are 1.5 for factors which are hazardous to personnel and 1.25 for factors which are non-hazardous to personnel. These margins are applied to both boundaries and the resulting performance envelope is the basis for structural design criteria.
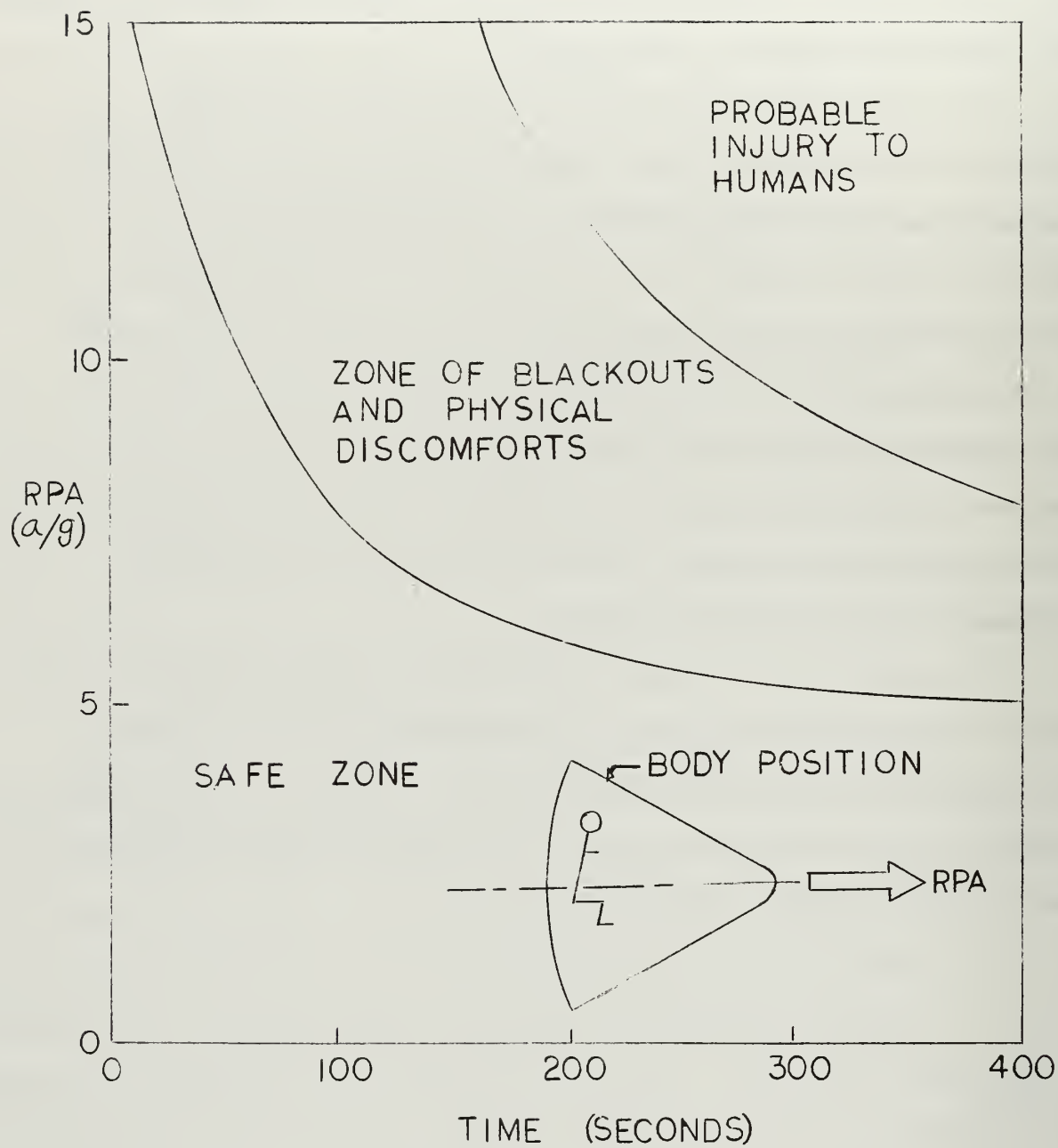
Fig. 3 Acceleration Tolerances

66
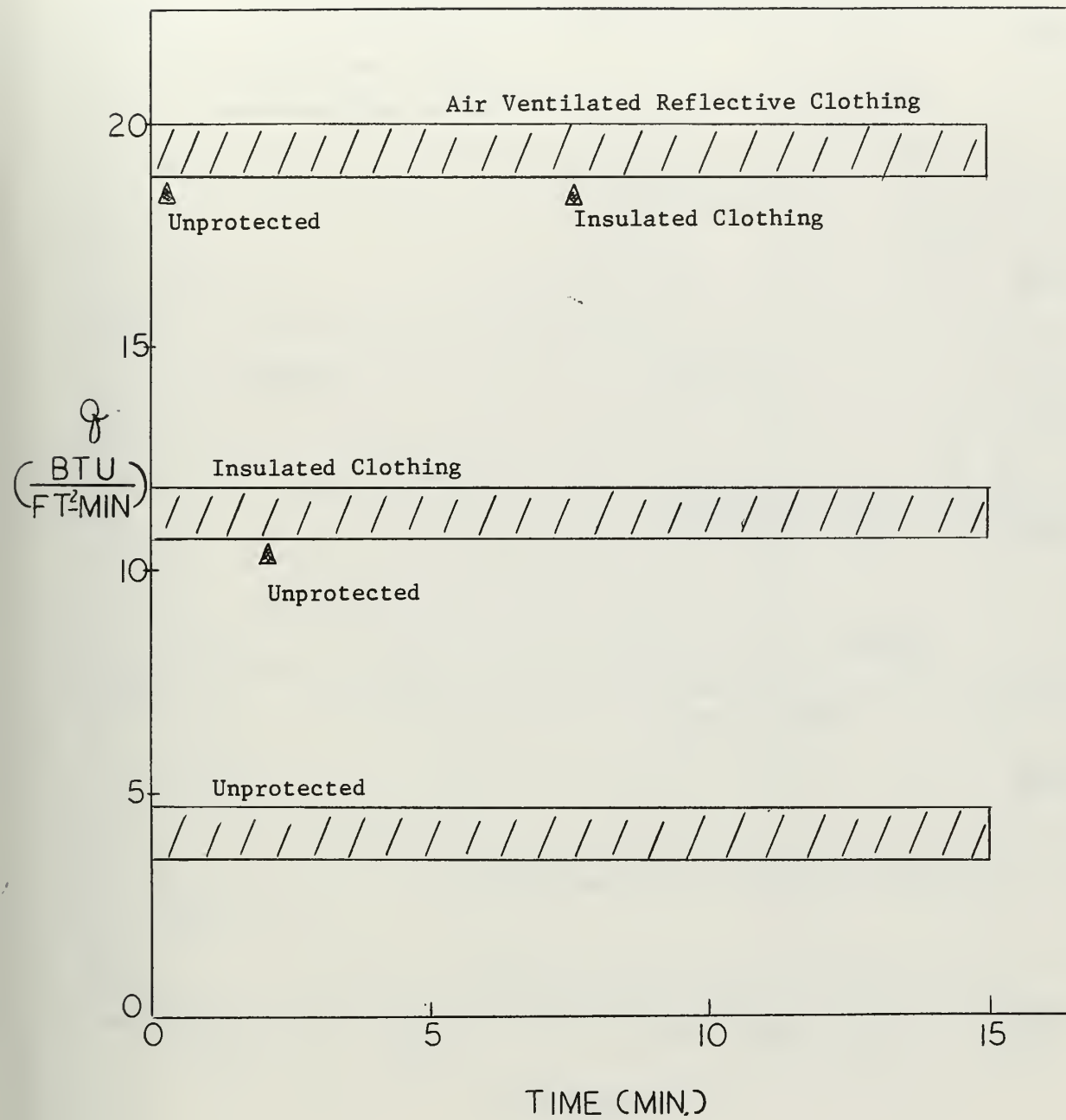
Fig. 4 Human Tolerances to Aerodynamic Heating
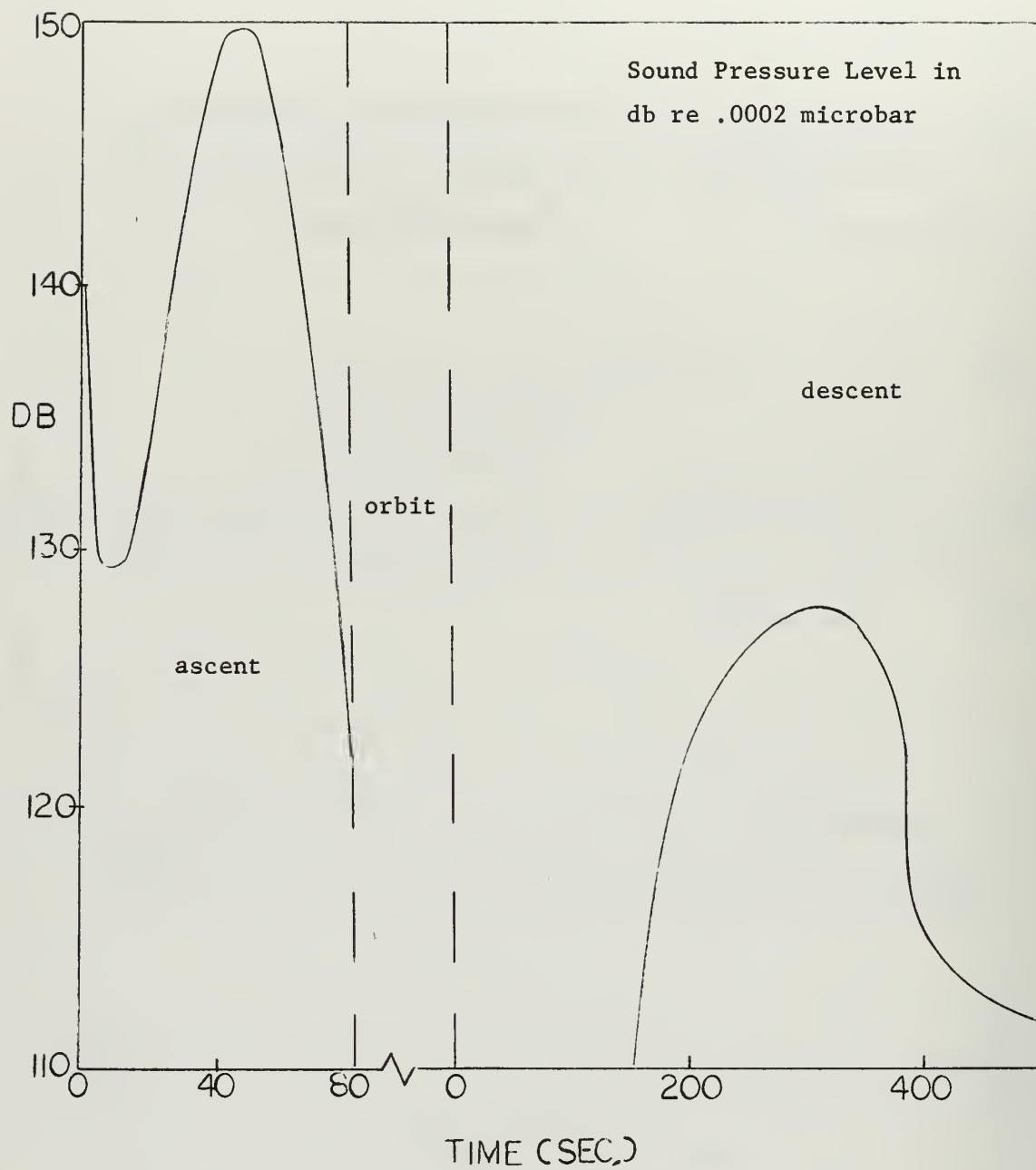
Fig. 5 Vehicle Noise Levels During Ascent and Descent
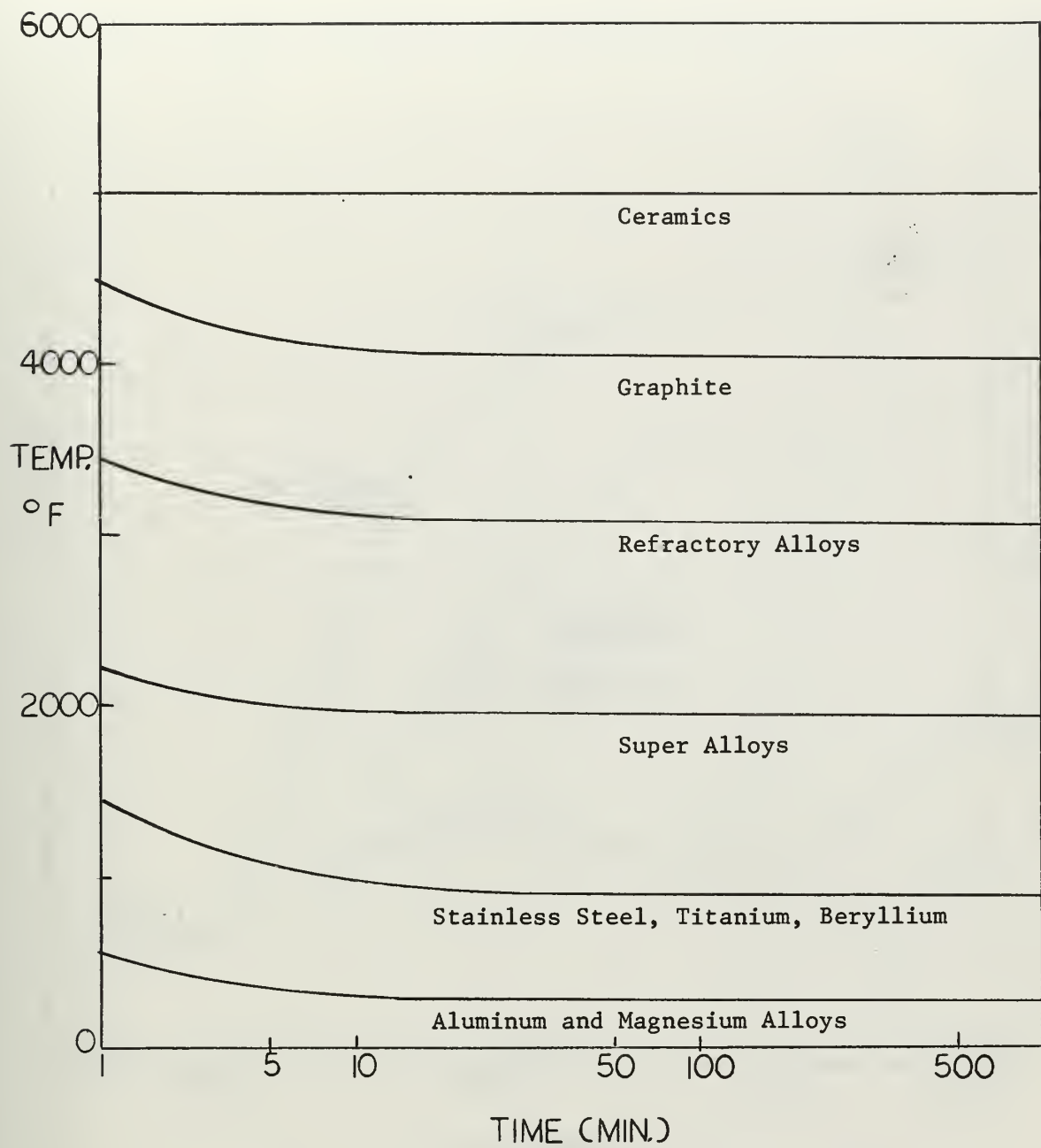
Fig. 6 Potential Temperature Capabilities for Various Structural Materials
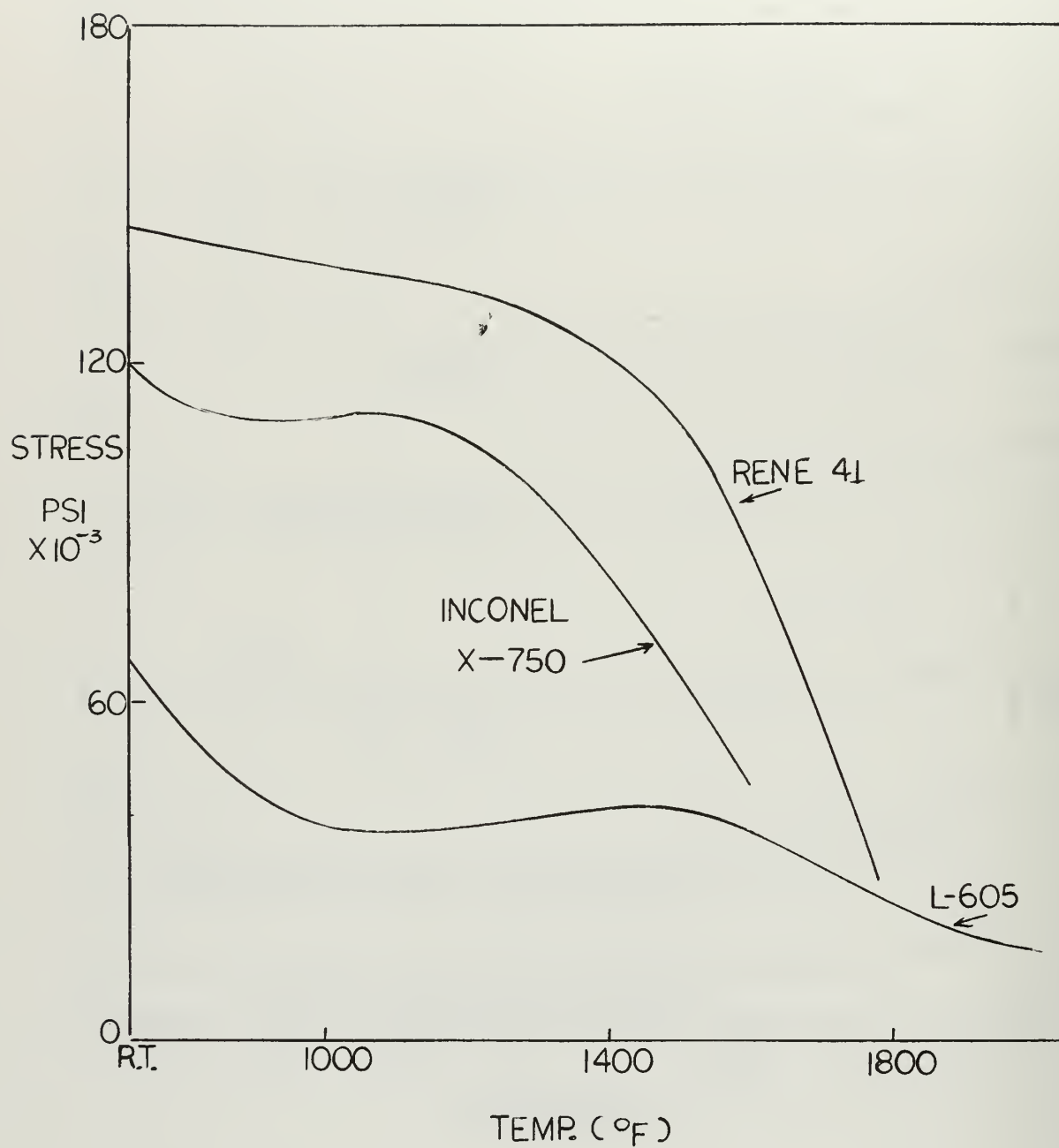
Fig. 7 Sheet Materials - Yield Strength

70
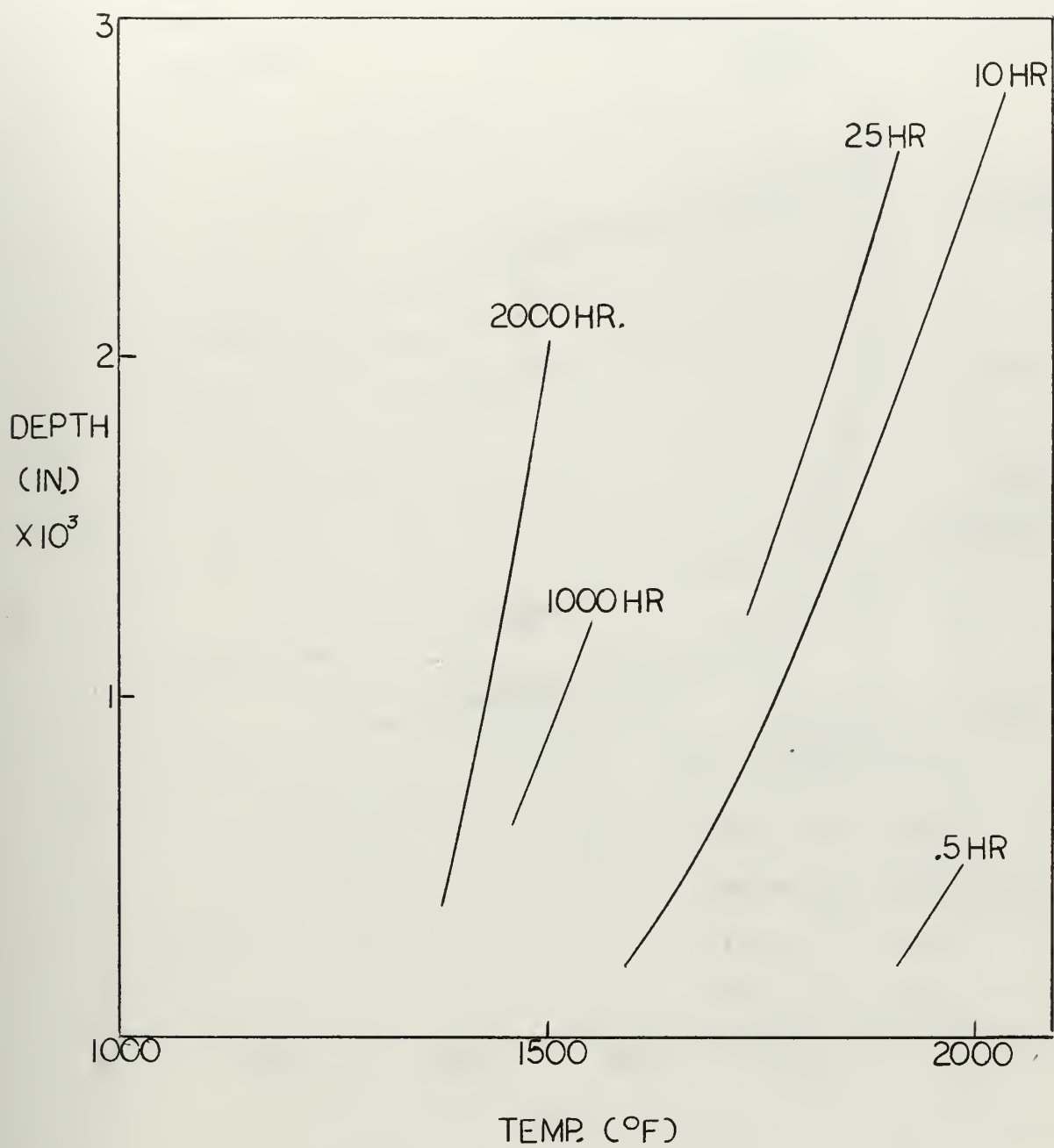
Fig. 8 Depth of Intergranular Oxidation as a Function of Exposure Temperature
for René 41
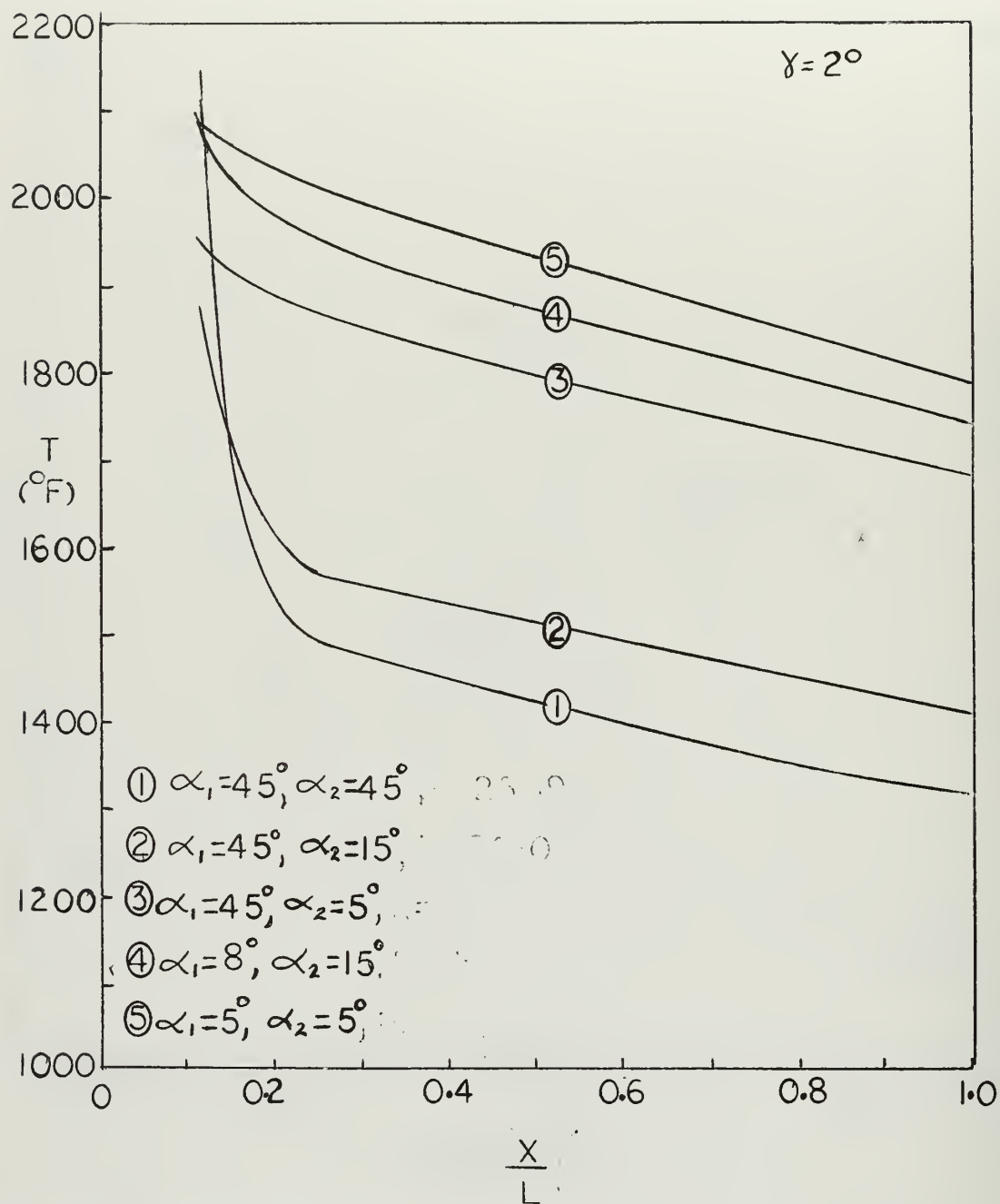
Fig. 9 Maximum Body Centerline Equilibrium Temperature

72
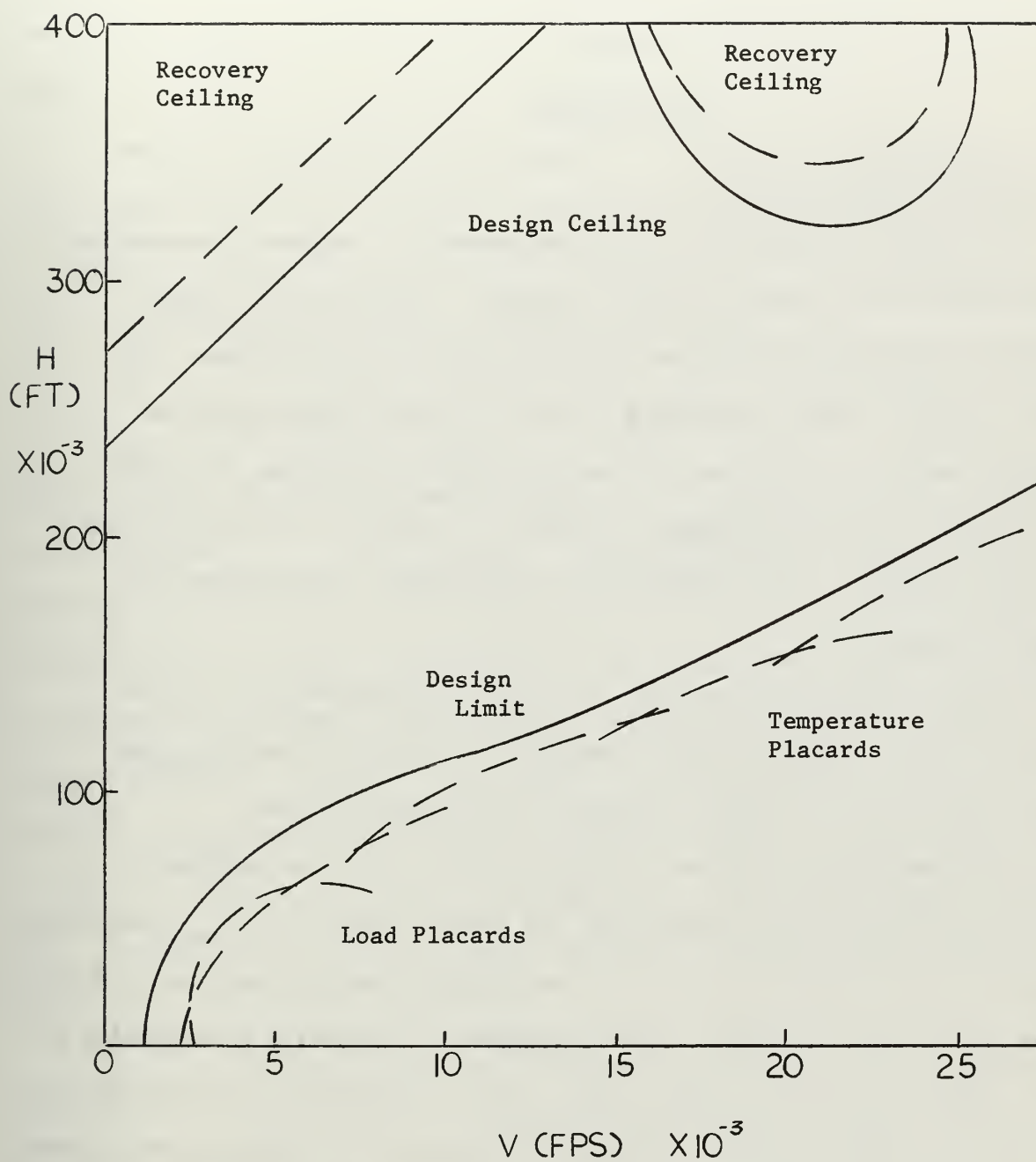
Fig. 10 Performance/Design Envelope

73

CHAPTER 5

TRAJECTORIES

5.1 Constant Angle of Attack

In order to establish a basis for comparison, several trajectories were computed using constant angle of attack. The associated thermal protection system weight for each trajectory was also determined. The angles of attack used in computing these trajectories range from the ballistic angle of -5 degrees, through the angle for maximum L/D which is 10 degrees, up to the maximum C_L angle of 45 degrees. Resulting data is shown in Table 2 and representative trajectories are presented in Figs. 11 through 22.

The longitudinal ranges are seen to vary from 1446 N.M. at the ballistic angle of attack, up to a maximum of 11,532 N.M. at L/D_{max} and then to decrease as the angle of attack is increased further.

The deceleration reaches a value of 5.18 g's in the ballistic trajectory and is generally lower for all others except the L/D_{max} trajectory in which deceleration builds up with each oscillation to a maximum of 5.74 g's in the last few oscillations. This phenomena of increasing deceleration is due to gradual steepening of the flight path in successive oscillations and could easily be eliminated by a simple lift modulation technique, which shows the inadequacy of using fixed parameters for anything more than preliminary investigations. In practice, all of the available means of controlling the trajectory would undoubtedly be used.

The stagnation heating rate, q_s, is generally seen to be greatest

74

at the bottom of the first pull-out, although in some trajectories it occurred during the second or third oscillation. The maximum heating rate of 693 BTU/ft^2sec occurs during the ballistic trajectory and is markedly above the next highest rate which occurs in the -2 degree angle of attack trajectory (See Fig. 17).

The total stagnation heating generally increases as the angle of attack approaches that for maximum L/D although the peak value is not exactly at L/D maximum. The peak value is 193,185 BTU/ft^2 and occurs in the 1 degree angle of attack trajectory. (See Fig. 14)

The weight of ablator and insulation required for each body section, i.e., nose, bottom, leading edges, etc. is shown in Fig. 19 for each angle of attack and a percentage breakdown of the weight for these sections is shown in Fig. 20 . The top ablator weight requirement disappears at angles of attack greater than zero due to shielding although considerable insulation weight is still required due to its relatively large surface area. The nose weight percentage remains nearly constant throughout the flight regime. The trade-off between body ablator weight percentage and total insulation weight percentage is readily apparent and, also, the consequence of neglecting insulation weight as negligible in a first approximation can be seen. Insulation contributes a weight equal to the total ablator weight in trajectories at high angles of attack.

A plot of the variation of total thermal protection system weight with range (Fig. 22) indicates two distinct branches for; (a) angles of attack less than that for maximum L/D and for (b) angles of attack greater than that for maximum L/D. The high angles of attack trajectories show a large weight saving over the low angle trajectories throughout the attainable flight regime. The difference in weight between branches varies from a few percent up to approximately 35 percent.

75

The variation of total stagnation heating is plotted versus range in Fig. 21 and also shows two branches with considerably lower heating for high angles of attack.

Other plots, including dynamic pressure and time of flight versus angle of attack, are presented for use in later comparisons.

5.2 Angle of Attack Modulation

A first approximation to continuous angle of attack modulation was made by dividing the trajectory into two phases as shown in Fig. 23 This allowed a considerable simplification in the analysis but retained the basic character of the problem since the trajectories have two natural and reasonably distinct regions. The first region is the initial descent into the atmosphere and the succeeding pull-up with its associated large heating pulse, and the second region is the remaining trajectory during which lateral and longitudinal range is achieved and during which the heating rate is diminished.

The differences between this simplified analysis and a more rigorous approach, such as formal optimization using variational techniques, is felt to be in degree rather than in kind since both would converge on the same solution if taken in sufficient detail. The relative complexity of the variational technique when applied to a problem of this scope makes it less desirable than simplified methods for preliminary work. Existing variational methods, such as those used by Bryson[28] to determine the total stagnation heating, are lengthy and involve several non-linear and adjoint differential equations. There may also be terminal constraints imposed on the problem. To expand from optimization of total stagnation heating to optimization of total thermal protection system weight requires consideration of body shape, three dimensional thermodynamics, and of the variation of ablator and insulation material characteristics throughout the heating range. These additional requirements complicate the differential equations and influence functions to such a degree that the determination of a solution would be difficult and would involve the use of

77

a considerable amount of computer time.

A separate study was made to obtain a relative comparison between the variational methods and the method used in this work. It is based on existing solutions to the problem of optimizing the total stagnation heating and is discussed in detail in a later section.

Angle of attack modulation as a means of reducing convective heating has been of interest for several years[2,3,9], and has shown considerable promise in the medium L/D type of vehicle. It allows the best utilization of the vehicle as an aerodynamic body in each of the differing flight regimes and indicates the direction to follow in an optimization scheme. From a systems analysis viewpoint, optimization with respect to heating pertains specifically to a reduction in total thermal protection system weight. This viewpoint requires a composite analysis of heating on all of the various sections of the body in which surface area of the section, angle of attack of the vehicle, and time of flight become major considerations. Insulation thickness and the corresponding area over which it is required are also of primary importance.

With this objective in mind, the basic modulation technique used here incorporates low angles of attack during the first phase of the trajectory in order to take the large heating pulse on the relatively small area of the nose cap. Then the angle of attack is increased to obtain atmospheric braking and reduced heating loads. During the second phase, the large surface area of the bottom of the vehicle is necessarily presented to the flow and a tradeoff between reduced heating and increased surface area is introduced.

An iterative computer survey was used to determine the optimum (as

denoted in this analysis) combinations of Phase I and Phase II angles of attack for a large number of longitudinal ranges. The results of this survey are shown in Table 3 and Figs. 24 through 33.

In Fig. 24, the longitudinal range is seen to increase markedly as the Phase I angle of attack varies from ballistic to that for maximum L/D. The ranges obtained at constant angle of attack are also shown (dashed curve) for comparison. As expected, the range deteriorates as the angle of attack in Phase II is increased above that for L/D maximum.

Similar effects were obtained when examining total stagnation heating (see Fig. 25). However, the total heating at large Phase II angles is greatest for a ballistic Phase I angle of attack rather than for a L/D maximum Phase I angle of attack. This was again apparent in Fig. 26 in which total stagnation heating is plotted versus range. Of importance in this comparison is the reduction in stagnation heating for a given range over constant angle of attack trajectories, which is achieved through angle of attack modulation. This occurs to the greatest degree where the first phase is flown at L/D maximum and the second phase is flown at high angles of attack. The improvement is as high as 18 percent and is fairly consistant throughout the major part of the attainable range. It will be shown later, however, that percentage improvements in total stagnation heating are misleading in regard to improvement in overall thermal protection system weight.

It is also significant that combinations of flight attitudes using low angles of attack in both phases are uniformly less effective than are the low to high angle combinations to give the same range. Each comparison of effects, such as total stagnation heating and weight versus range,

79

resulted in two branches as before in the constant angle of attack

trajectories and severe penalties in both dynamic pressure and heating

rate occur in the upper branch. The maximum dynamic pressure is increased

by a factor of approximately 4 to 8 and would impose a secondary adverse

effect by requiring an increase in the vehicle structure weight. The

increased heating rate also causes increased thermal protection system

weight for each range.

The trajectories were then used to generate the ablator weight

required for protection of the nose, bottom, top and leading edge, and

the insulation weight required for the entire body for each trajectory.

These weight requirements are shown in Figs. 27 through 30 and the

total thermal protection system weight requirement for the various

trajectories is presented in Fig. 31.

To illustrate the weight for each section in relation to the total

weight, results for a representative set of trajectories with a phase I

angle of attack of 5° degrees are included in Fig. 32.

Since a reduction in total weight for given range capability is the

desired result, the weight requirement for each trajectory is compared

with the constant angle of attack trajectory weights as a standard. Fig. 33

illustrates this comparison and also shows the effect on weight and range

of variations in Phase I and Phase II angle of attack.

The trajectories using the angle of attack for maximum L/D in Phase I

and higher angles in Phase II have lower weight requirements than the

standard in all cases although, at the higher ranges, the improvement is

small. It is here that the fallacy of using total stagnation heating as

a basis for optimization is apparent. At a range of 9000 N.M., the improvement

80

in stagnation heating is 16 percent, but the reduction in total weight is less than 1 $^1/2$ percent. As bank modulation is introduced (in the next section), this condition becomes even more pronounced, ultimately reaching a point where the weight continues to decrease even though the total stagnation heating increases. The maximum gain in weight saving occurs in the mid ranges and is approximately 14 percent. This corresponds to a 16 percent saving in total stagnation heating.

5.3 Bank Modulation

A further refinement in trajectory control was made by introducing bank modulation. As suggested by Brekka[29] and Baradell[30], bank modulation is an available means of varying the lift to drag ratio in a particularly useful manner. In addition to providing lateral range, it provides more flexible control over the trajectory by allowing independent variation of lift and drag in the manner of a variable geometry vehicle.

Banking the vehicle while maintaining the angle of attack constant reduces the vertical lift vector without changing the drag. The effective L/D is reduced and a modified trajectory results. The deceleration and heating profiles are also altered according to the new trajectory and the longitudinal range is reduced. The resulting cross range can either be utilized, if desired, or must be cancelled out by bank reversals if not desired. In this study, the cross range due to bank modulation was cancelled out and, when cross range was desired later, it was generated using a different technique.

Bank modulation was used in conjunction with angle of attack modulation in the iterative computer survey described above and the resulting

81

range, total stagnation heating, and ablator and insulation weight

relationships shown in Figs. 34 through 39 and presented in Table 4.

The degree of bank modulation is indicated by the parameter A, the factor

by which the effective lift is reduced.

The effect of bank modulation on range (Fig. 34) shows the expected

decrease as the amount of bank is increased. This occurs because the major

range producing effect, lift, is being reduced directly by the

modulation and the degradation in range at extreme values of bank

modulation (A = .3) is as high as 85 percent.

A similar effect occurs with total stagnation heating except in

the high angle of attack ranges where large values of bank modulation cause

an increase in heating. This is comparable to the results obtained when

examining the effect of angle of attack modulation.

The effect of bank modulation on the thermal protection system

weights for various sections of the vehicle is shown in Figs. 36 through 38.

The weights are, for the most part, reduced by bank modulation with a

small area of reversed effect at high angles of attack for the nose and the

bottom of the body. Fig. 39   gives total ablator weight in comparison

with the total insulator weight for several amounts of bank modulation

as well as a comparison of the resulting total thermal protection system

weight at the same values of bank modulation.

Figure 40   indicates the variation of total stagnation heating with

longitudinal range and gives a comparison with the constant angle of attack

trajectories and with angle of attack modulation only trajectories. The

stagnation heating is seen to increase to values well above those for constant

angle of attack in the lower longitudinal ranges.

82

However, Fig. 41 indicates that the corresponding thermal protection system weights are considerably less than those for constant angle of attack trajectories in this region. For example, at a down range of 3000 N.M., the total stagnation heating is 50 percent higher for bank modulation trajectories yet the thermal protection system weight is 10% lower than the constant angle of attack trajectories. It is evident that, although stagnation heating may indicate trends under certain conditions, its use is not a reliable shortcut to optimization of a space reeentry system and serious design errors could result if a composite type of weight study is not made.

Although bank modulation shows an improvement in weight when applied to a given trajectory, it is the weight variation at a particular down range (and later, cross range) that is of interest here. In this respect, Fig. 41 shows that combined angle of attack and bank modulation is better in the low longitudinal ranges while angle of attack modulation only is better in the higher ranges. In addition, in the bank modulation region, the best results are obtained using the same angle of attack modulation scheme, i.e., angle of attack for L/D maximum in Phase I and angle of attack for maximum lift in Phase II. The trajectory is controlled by varying the amount of bank modulation only. Using this method, the variation of weight with range is nearly linear and varies at approximately the same rate as in the higher ranges using angle of attack modulation only.

The minimum possible range is obtained by using the ballistic angle of attack in both phases and is 1445 N.M. This trajectory also results in the lowest total weight requirement which is 990 lb.

Based on the indicated minimum weights in Fig. 41 , a set of seven

83

trajectories was established as representative of the complete aggregate
of optimized trajectories from the lowest to the highest longitudinal
range.   Each trajectory is described by the angle of attack in each phase
and by the factor, A, by which the lift vector was multiplied to produce
the effect of bank modulation.   These trajectories are:

Phase I Angle of Attack	Phase II Angle of Attack	Bank Mod. Factor-A	Range (N.M.)	
-5	-5	1.0	1446	(Ballistic)
5	45	.3	2181	
5	45	.7	3743	
5	45	1.0	4776	
5	30	1.0	5712	
5	15	1.0	8840	
5	5	1.0	11,532	(Maximum L/D)

5.4   Lateral Range Capability

The set of optimized straight line trajectories was used to generate
a two dimensional footprint by introducing a series of nominal bank
angles into each trajectory.   The resulting footprint is shown in Fig. 42
and the associated data is presented in Tables 5 and 6.   The bank angle, ϕ,
ranged from 0 degrees up to the maximum allowed by the acceleration
constraint of 10 g's.   The maximum allowable ϕ varied depending on the
particular trajectory, but was above 75 degrees in all cases and the
acceleration constraint did not restrict the size of the footprint to any
great degree.

84

The physical description of superimposing bank modulation on
a nominal bank angle is given as follows: the vehicle is rolled to a
nominal bank angle, for example 30 degrees. Then it is rolled further
to, say, 45 degrees for a period of time after which the bank is reduced
to 15 degrees for a corresponding period. This achieves continuous bank
modulation while maintaining a constant average bank.

An overall limit of 90 degrees was put on the bank angle, and the
bank modulation was reduced as required in order to respect this limit.
To illustrate, if the nominal bank angle is 60 degrees, then the bank
modulation must be maintained at or below $\pm$ 30 degrees. It can be seen
that, inherent in this approach, are several linearizations and superpositions
which do not take second order effects into account, however, the
inaccuracies are found to be small and do not alter the ultimate trends
and comparisons which are presented.

It is desired that the path over the ground be the same as for a
constant bank angle without modulation, and it is not rigorously correct to
assume that this is accomplished by using equal time increments for the
banks to the right and to the left of the nominal angle since the vehicle
experiences different velocity, density and acceleration conditions during
each successive time increment.

An investigation into the effect of this approximation was made
and it was determined that the reduction in longitudinal range due to
the zig zag nature of the track over the ground could be maintained below
three percent if the bank reversals were made every two minutes and no
effort was made to correct for this small discrepancy.

In order to utilize bank modulation in the manner described, the

vehicle must, of course, have an attitude control system of adequate size. A further investigation into the effect on the weight of a control system of this type compared with the reduction in thermal protection system weight would be appropriate before the overall design task is complete.

The footprint shown in Fig. 42 has a maximum width of 5300 N.M. and a total area of about 42 million square miles. For comparison, the area of the North American continent is approximately 7 million square miles. The versatility of this vehicle is readily apparent and presents a new and interesting strategic problem to military mission planners.

The grid which appears on the footprint indicates the trajectory control parameters which would be required to reach a given landing point. The lines of constant ϕ should not be confused with tracks over the ground although they have roughly similar shapes. The tracks over the ground are not shown, only the landing point of each trajectory.

Sector A in the footprint is the region encompassing points which are reached using angle of attack modulation only in which the Phase I angle of attack is that for maximum L/D. Sector B is the area in which combined bank and angle of attack modulation provides optimum trajectories. The relative size of this area is about 9 percent of the total footprint.

In addition, there is a relatively small area, Sector C, which is reached by changing the Phase I angle of attack to values other than that for L/D maximum and using bank modulation as above. Since this area is small no attempt was made to analyze the associated trajectories due to the inordinate amount of computer effort required.

In examining the effects of trajectory control parameters, it can

be seen from this figure that bank modulation introduces an additional

advantage in that control sensitivities are greatly reduced. In the

higher range regions, small angle of attack errors will cause large

dispersions in landing point while, in Sector B, the use of bank as the

primary control mechanism reduces these errors considerably. This effect

was investigated by Brekka[29] and Lecat[31] and it was noted that the

permissable bank error is four times greater than the permissable pitch

error. For example, a 20 percent bank error causes a corresponding lift

variation of six percent. This same lift variation would be caused by

only five degrees of error in pitch.

The total weight of the thermal protection system which is required

to reach a particular landing point in the footprint is shown in Fig. 43

The weight is seen to increase continuously from the minimum of 990

pounds at the minimum achievable range up to a maximum value of 2810 pounds

which occurs at the maximum longitudinal range. The increase in weight

is relatively uniform as the distance down range is increased and

illustrates the large weight penalty which is incurred as the operational

capability of the vehicle is increased. In order to obtain the maximum

utility from the system, an increase in thermal protection system weight

of 183 percent over the minimum allowable is required.

This raises the thermal protection system weight from 5.5 percent

of the total vehicle weight to 15.5 percent and is definitely a factor

to be examined carefully in a mission analysis.

A non-dimensionalized presentation of these results is given in

Fig. 44. Since the most useful means of indicating tradeoffs involving

space systems must necessarily use payload weight as a basis, the ratio

of payload to vehicle gross weight is shown versus landing area. The vehicle gross weight is 18,000 pounds and the weight breakdown given in section 1.2 indicates that all systems and components other than payload and thermal protection system require a weight of 13,140 pounds. The remaining 4860 pounds may be traded off between payload and thermal protection system based on the size of the desired landing area. Therefore, the payload is considered to be the weight remaining after the thermal protection system weight required for a desired area is subtracted from 4860 pounds. The range of values of this payload fraction is seen to be from .215 for the ballistic trajectory down to .114 for the maximum range trajectory.

Fig. 45 clearly illustrates the variation in the size of the landing area with both thermal protection system weight and payload fraction. With this particular vehicle, a payload fraction of .195 would be available if the vehicle was required to be able to land at any point within the United States (area of 2,780,000 N.M.^{2}).

5.5 Comparison with "Steepest Descent" Optimization Procedure

Bryson, in reference 29, describes a "steepest descent" computation procedure for solving variational problems, and gives, as an example, the trajectory to minimize the total stagnation heat for a hypersonic glider. The glider is injected into a reentry condition at 300,000 feet with a velocity of 25,920 ft/sec and an initial flight path angle of .18 degrees upward. The range is constrained to 21,600 NM, and the optimized trajectory gives a 39 percent reduction in total stagnation heating over that generated in the nominal constant angle of attack trajectory.

To establish a bssis of comparison, the same vehicle parameters and initial conditions were used in the digital computer program described in Appendix E, and a constant angle of attack trajectory was computed. Because of the different initial conditions for this trajectory, it was necessary to re-examine one of the basic assumptions made in the deviation of the trajectory equations of motion. It was assumed previously that the distance from the center of the inertial coordinate system to the vehicle, R, was constant and equal to the radius of the earth. The effect of this assumption was to increase the velocity required for a circular orbit at an altitude of 300,000 ft from 25,930 ft/sec to an apparent velocity of 26,075 ft/sec. The large down range obtained by Bryson during the initial ballistic skip is due to the combination of initial injection velocity, initial entry angle, and actual circular velocity. The increase in apparent circular velocity due to the assumption of constant R, in conjunction with these initial conditions, is such that an erroneous reduction in down range (by a factor of approximately 1/2) results. With the inclusion of both variable R and variable gravitation force, the computation of down

range was corrected and was then found to also be extremely sensitive to the time increment between calculations. The basic time interval of 5 seconds was found to be too large and orbital velocity was attained during the initial portion of the reentry. In an effort to conserve computer time, the initial ballistic portion of Bryson's trajectory was omitted, and new initial conditions of altitude (300,000 ft), velocity (28,880 FPS) and flight path angle (-1°) were assumed. This modification is valid when examining the total stagnation heating and thermal protection system weights since the heating rate during the initial ballistic phase is extremely low. The resulting down range was 22,217 NM and the total stagnation heating was 122,000 BTU/ft^2. These results compare closely with Bryson's constant angle of attack trajectory values.

Two-phase angle of attack modulation was introduced into this trajectory and the total stagnation heating and thermal protection system weight, based on Teflon, were calculated. The reduction in total stagnation heating using this method of angle of attack modulation is 28 percent, with a corresponding reduction in thermal protection system weight of 12 percent. These results illustrate the relative effectiveness of this method in comparison with the formal optimization method.
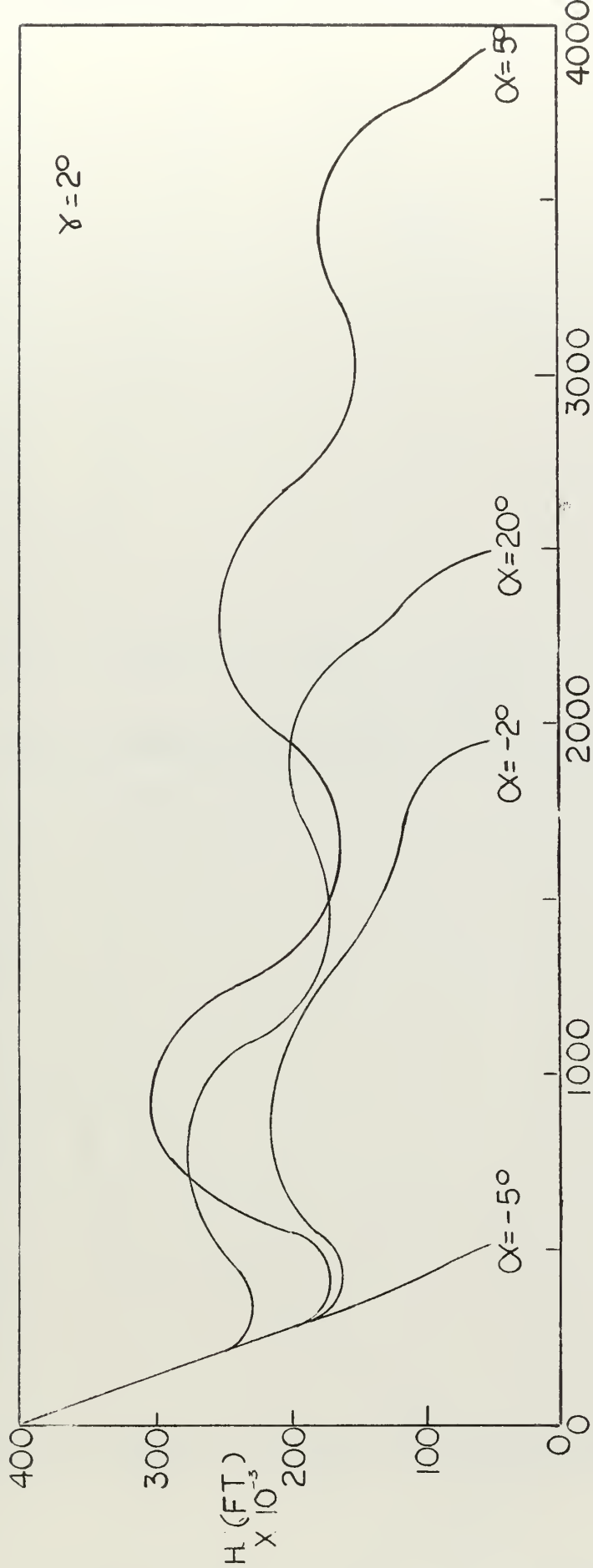
Fig. 11 Variation of Altitude with Time of Flight
(Constant Angle of Attack)

90
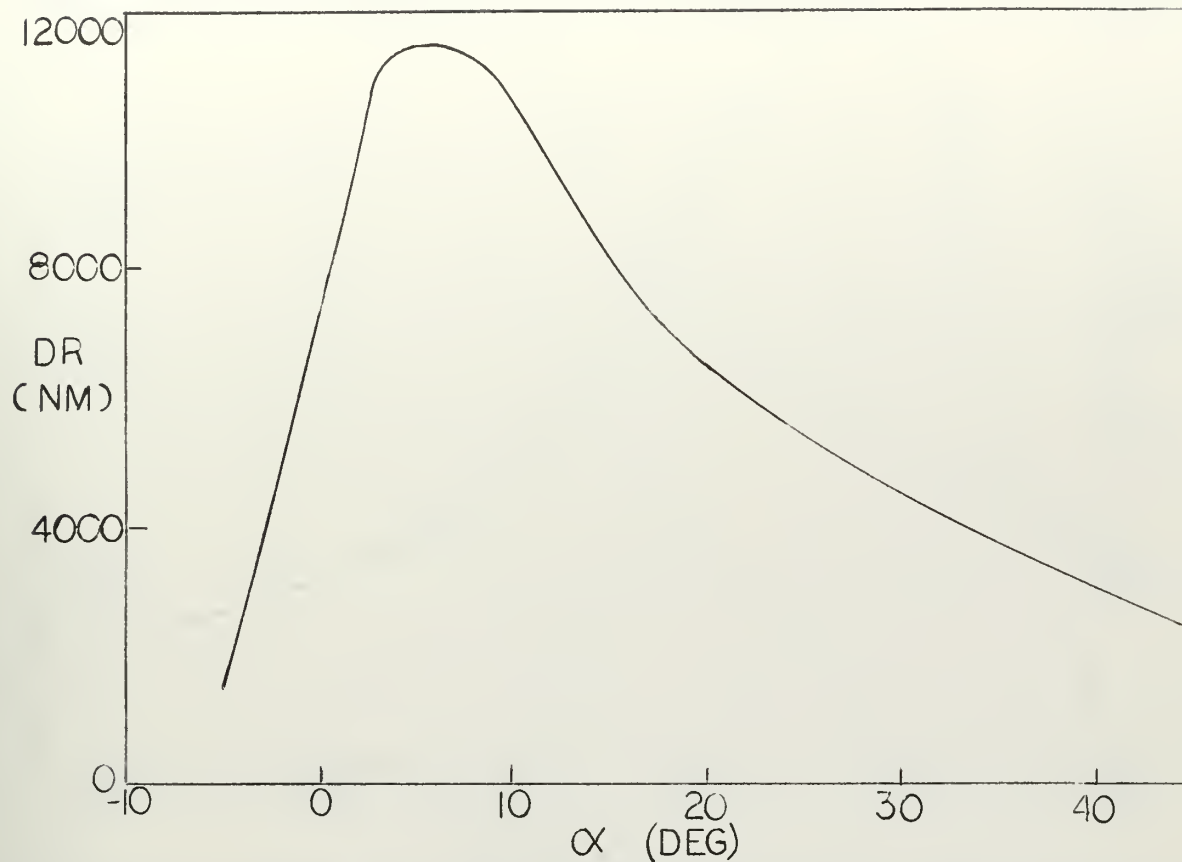
Fig. 12 Variation of Down Range with α (Constant Angle of Attack)
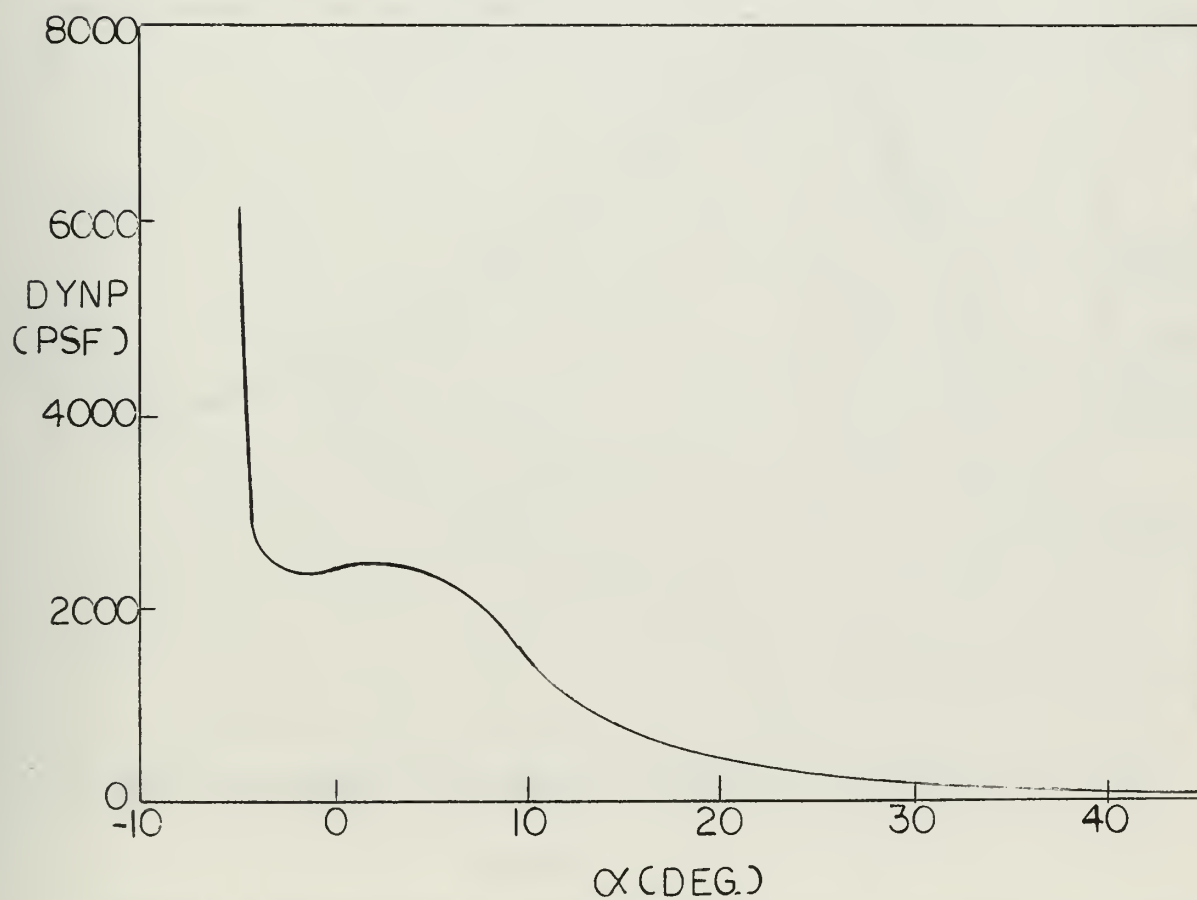
Fig. 13 Variation of Dynamic Pressure with α (Constant Angle of Attack)
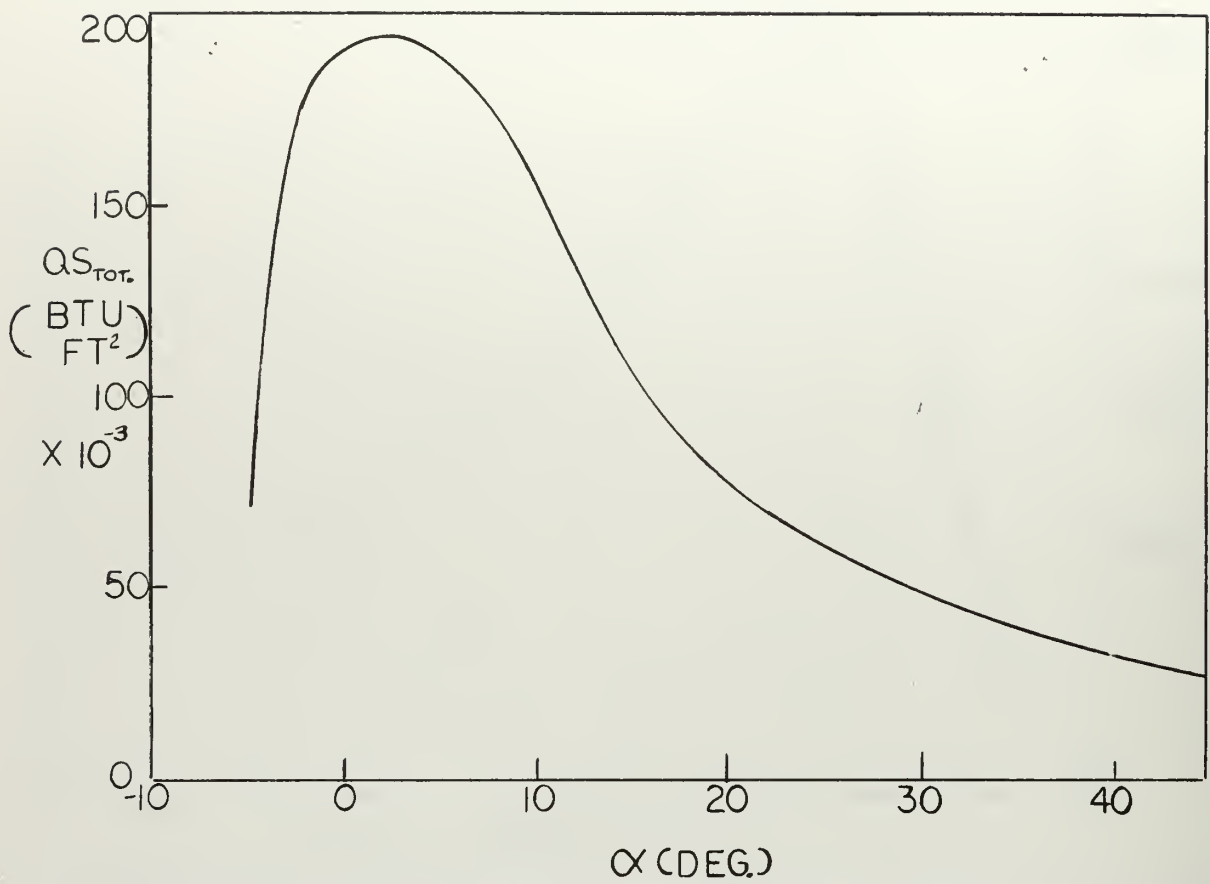
Fig. 14   Variation of Total Stagnation Heating with α (Constant Angle of Attack)
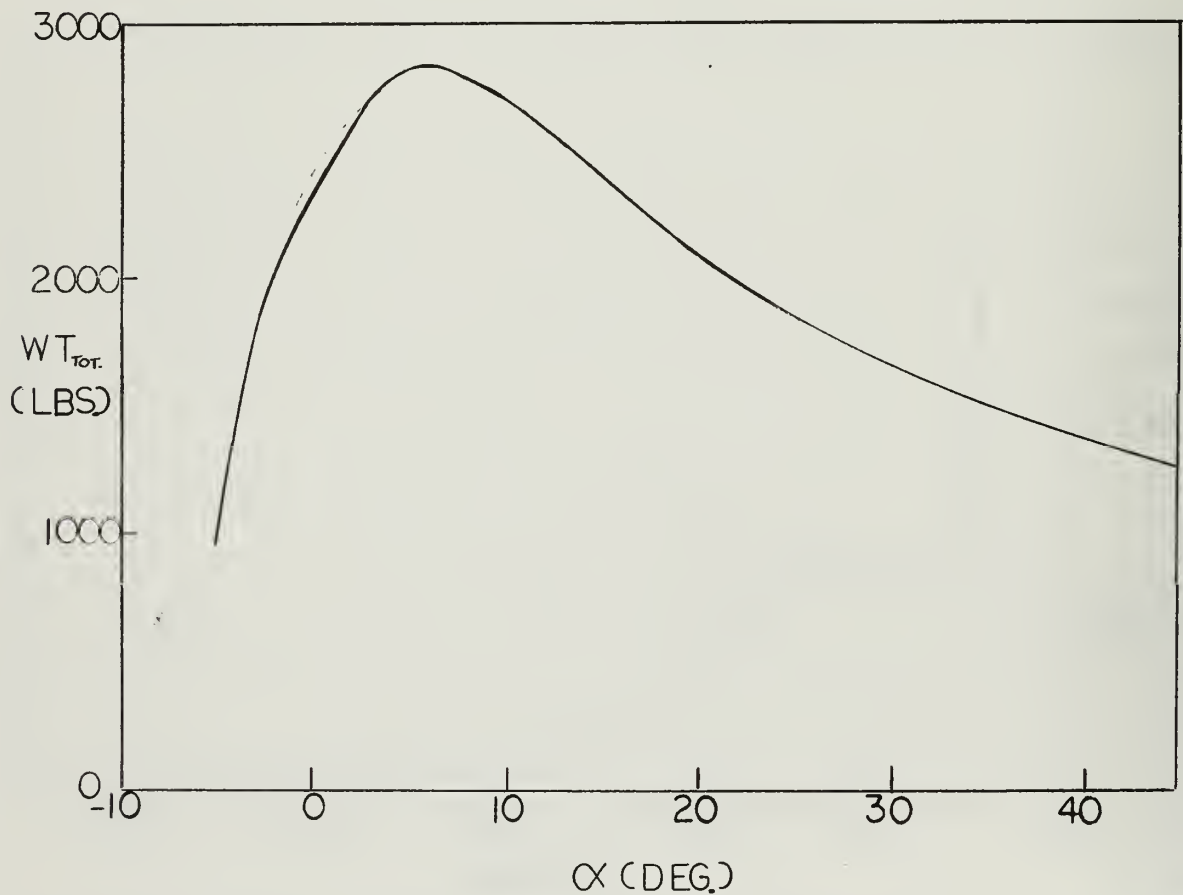
Fig. 15   Variation of Thermal Protection System Weight with α (Constant
Angle of Attack)

92
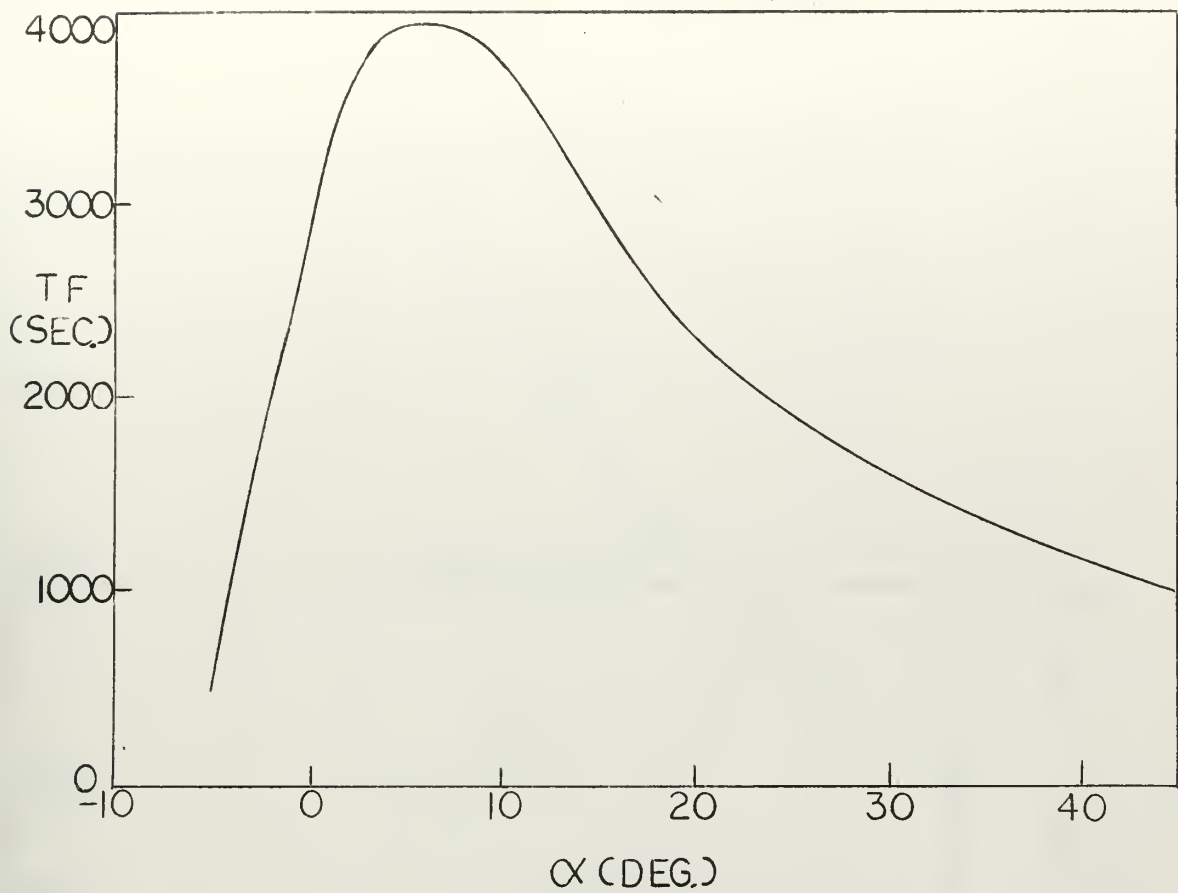
Fig. 16   Variation of Time of Flight with α (Constant Angle of Attack)
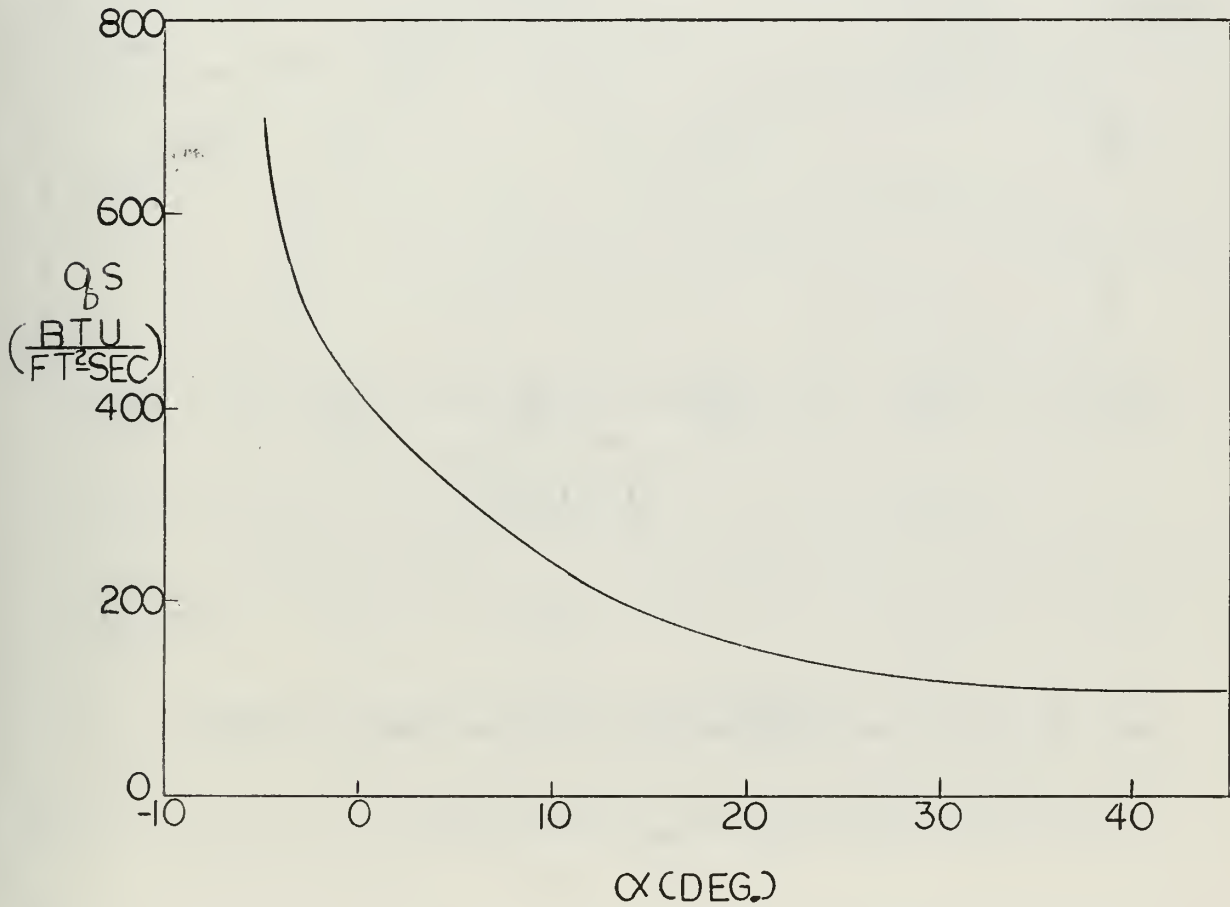
Fig. 17   Variation of Stagnation Heating Rate with α (Constant Angle of Attack)

93
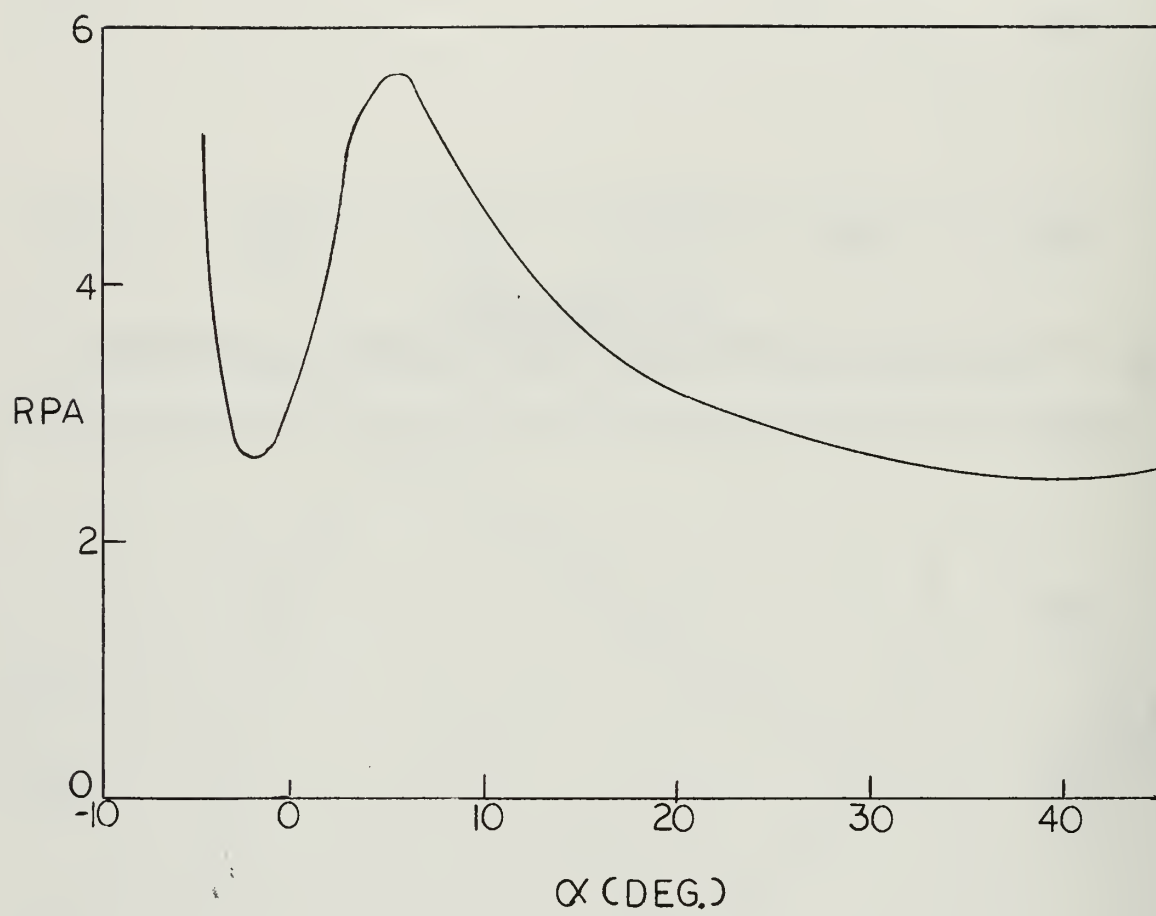
Fig. 18 Variation of RPA with α   (Constant Angle of Attack)

94
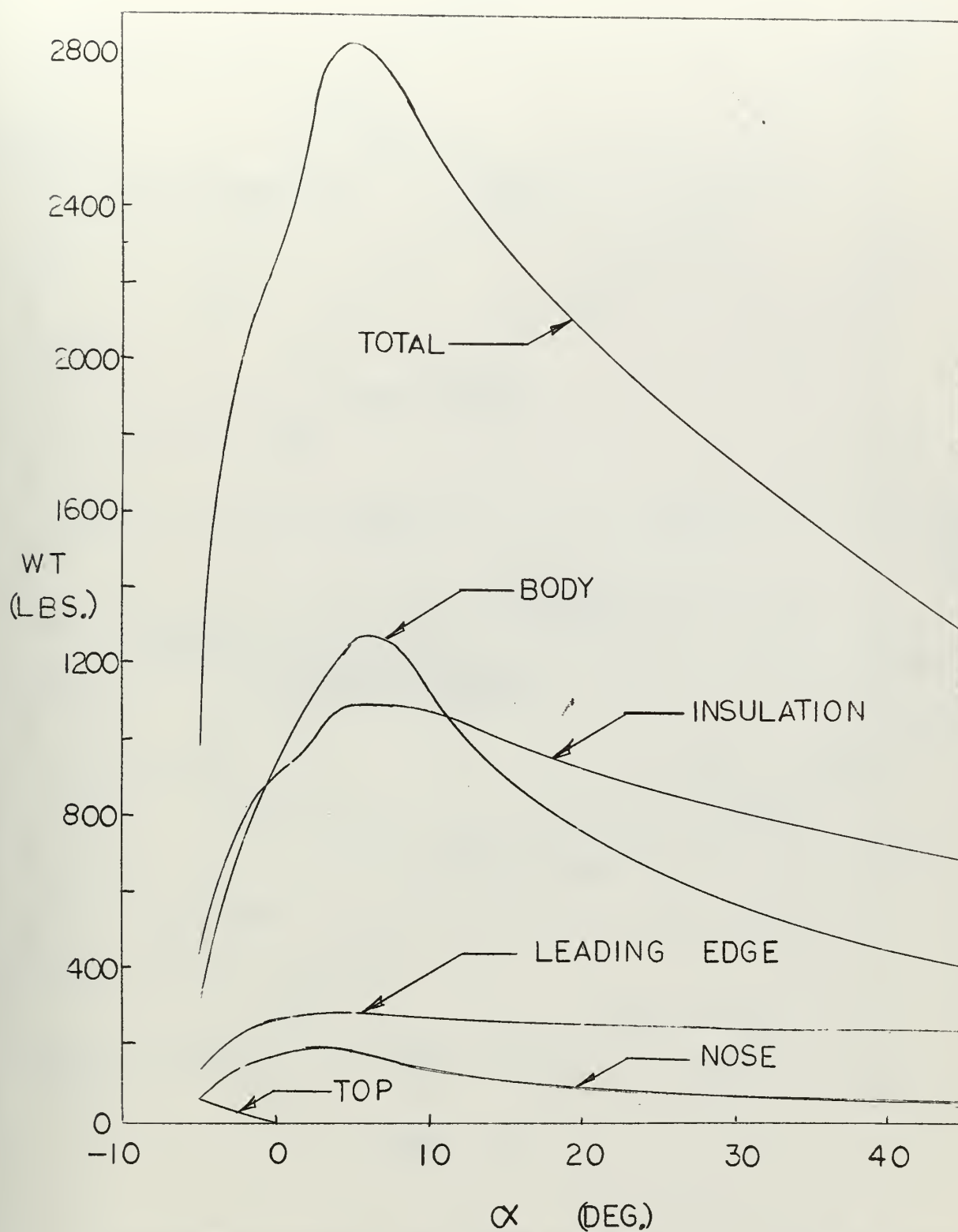
Fig. 19 Variation of Component Ablator and Insulation Weight with α
(Constant Angle of Attack)
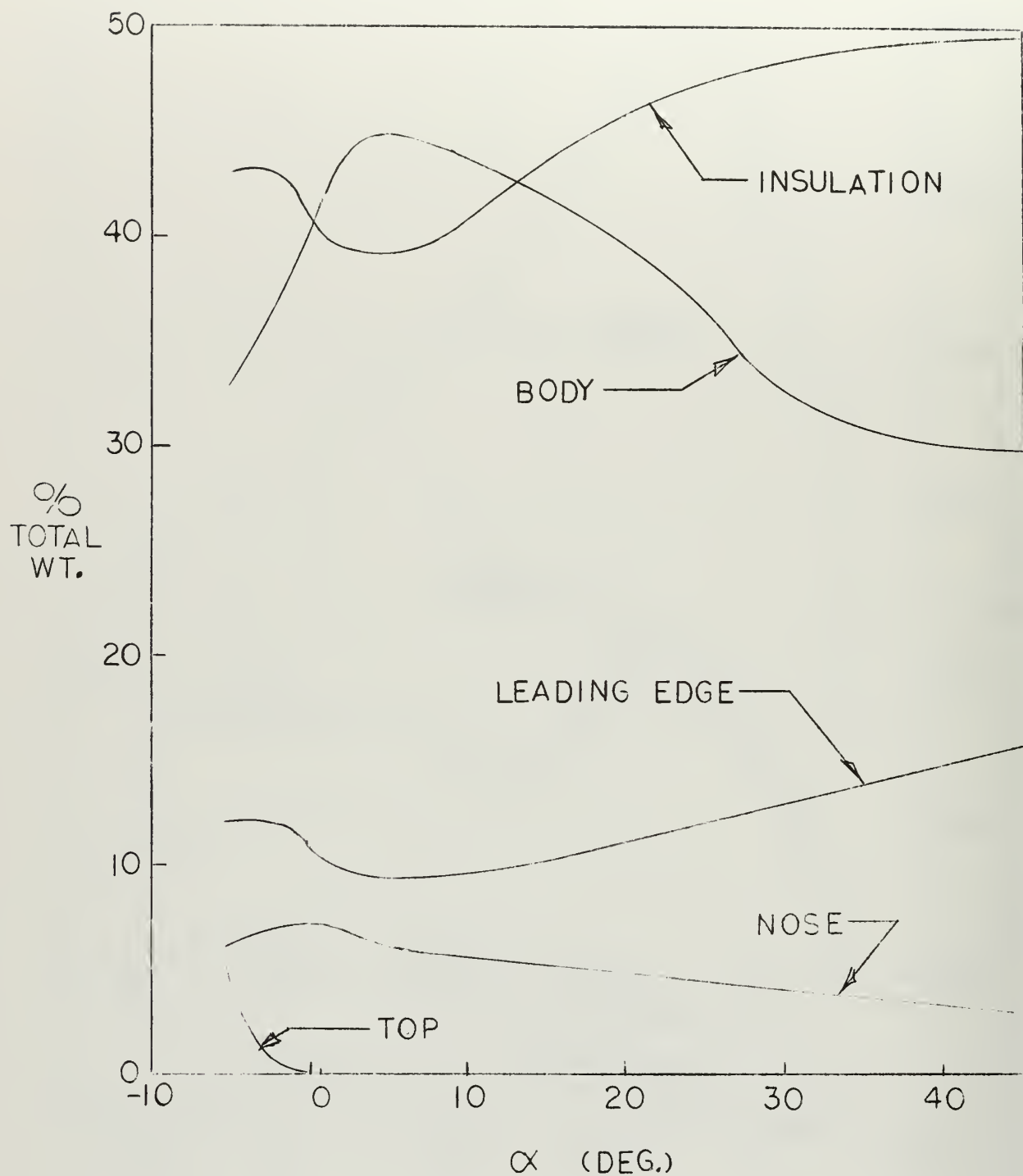
Fig. 20 Variation of Component Ablator and Insulation Percentage of
Weight with α   (Constant Angle of Attack)
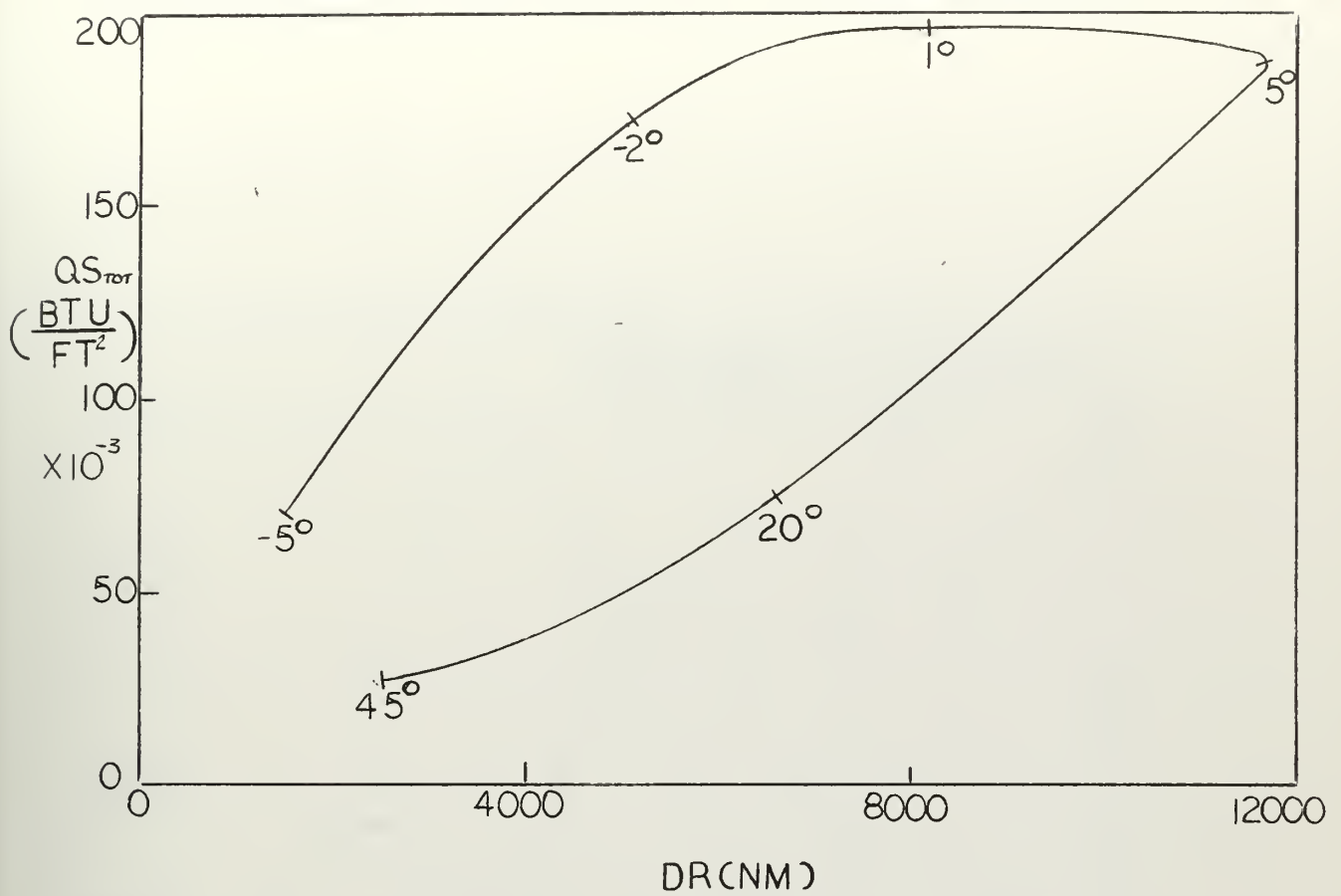
Fig. 21 Variation of Total Stagnation Heating with Down Range
(Constant Angle of Attack)
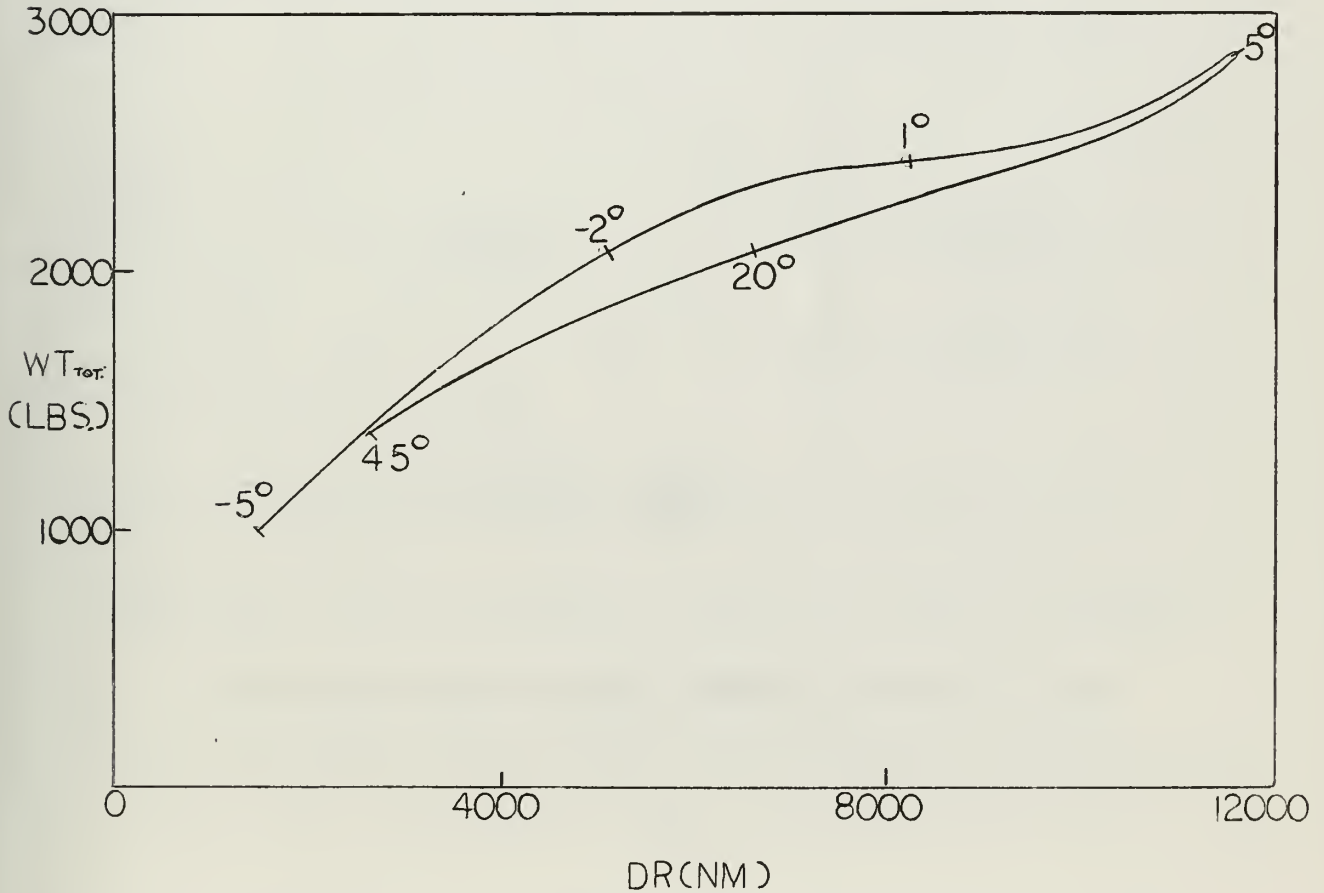
Fig. 22 Variation of Thermal Protection System Weight with Down Range
(Constant Angle of Attack)
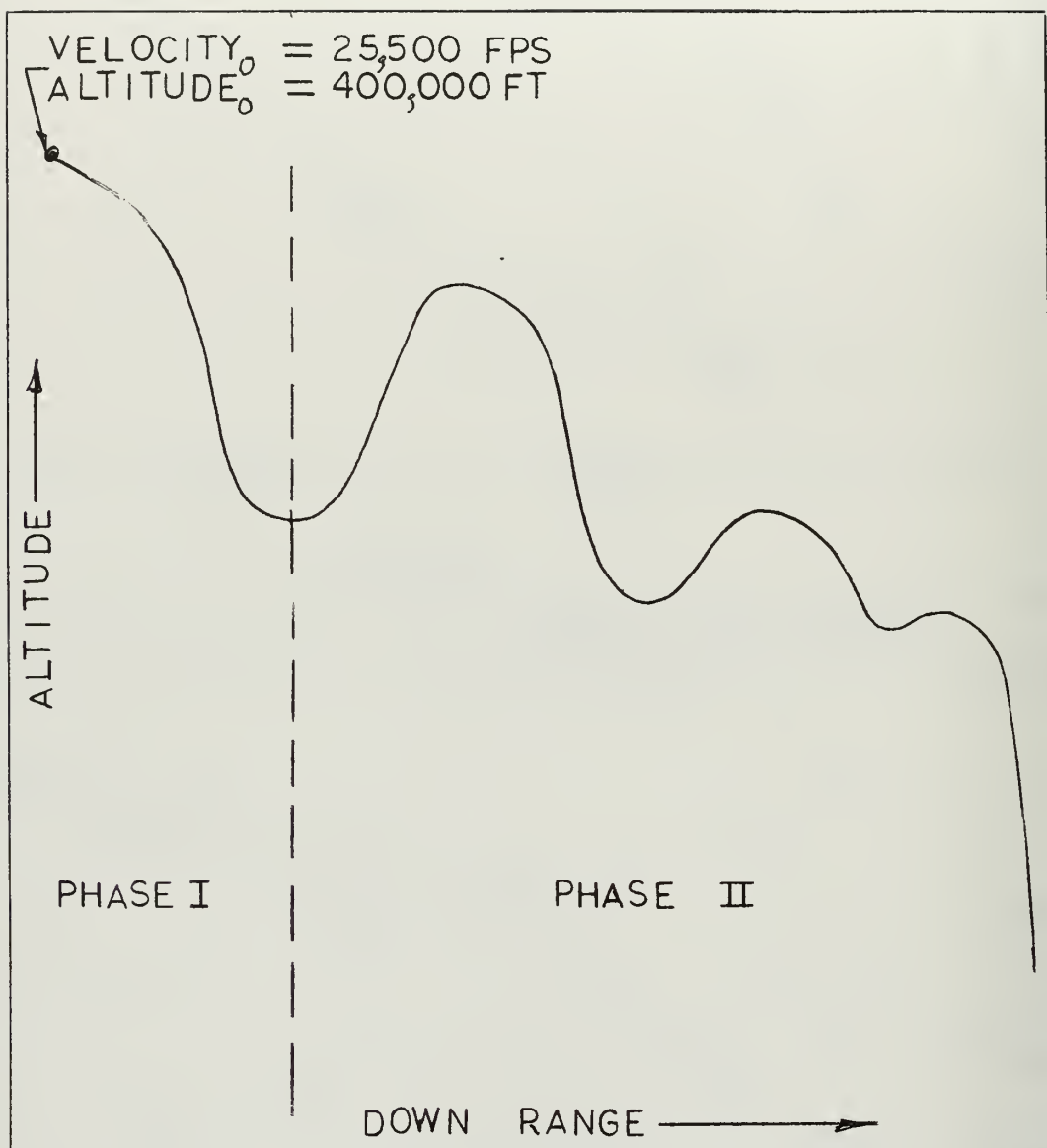
Fig. 23 Trajectory Profile (Angle of Attack Modulation)
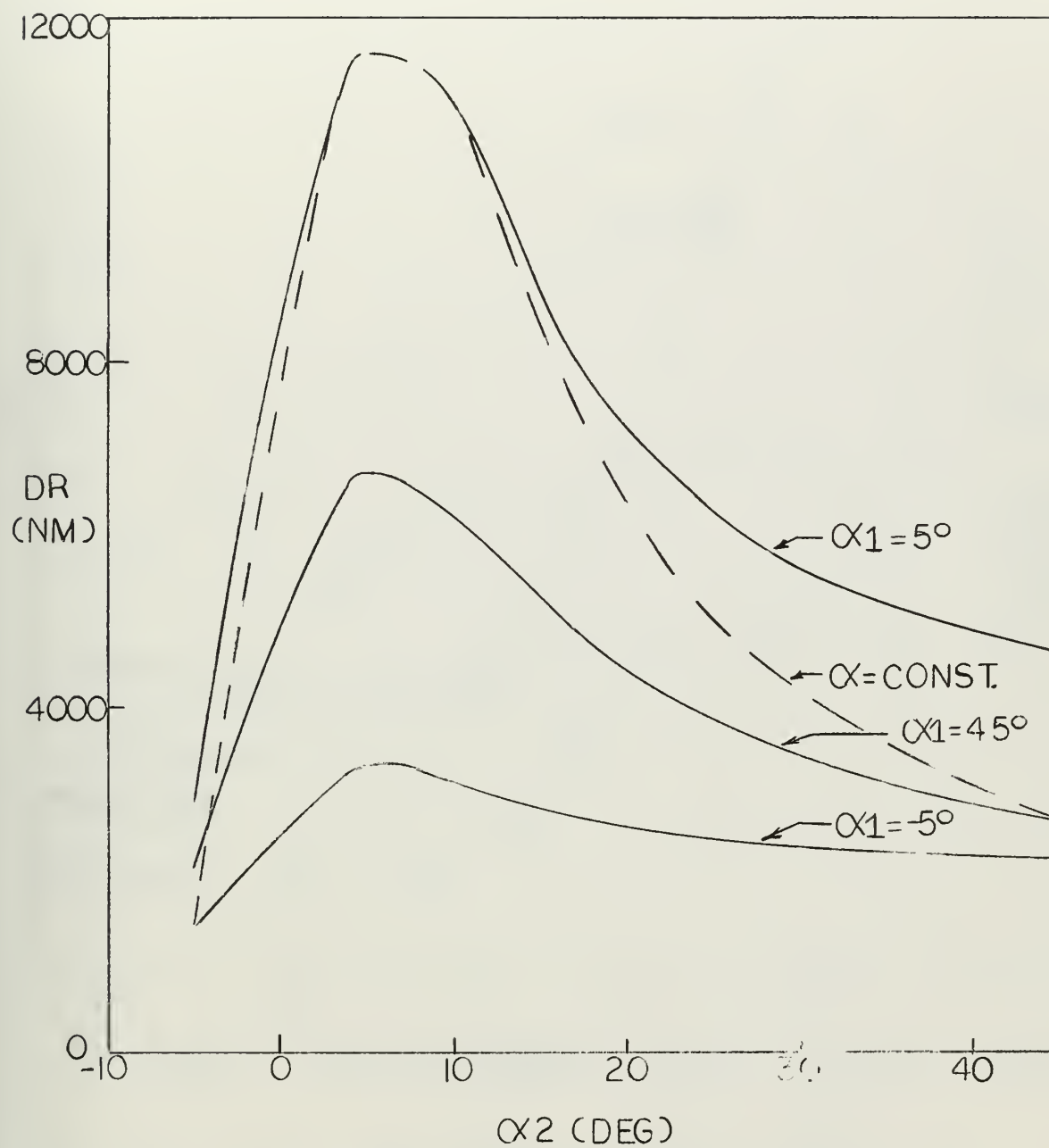
Fig. 24   Variation of Down Range with α2   (Angle of Attack Modulation)
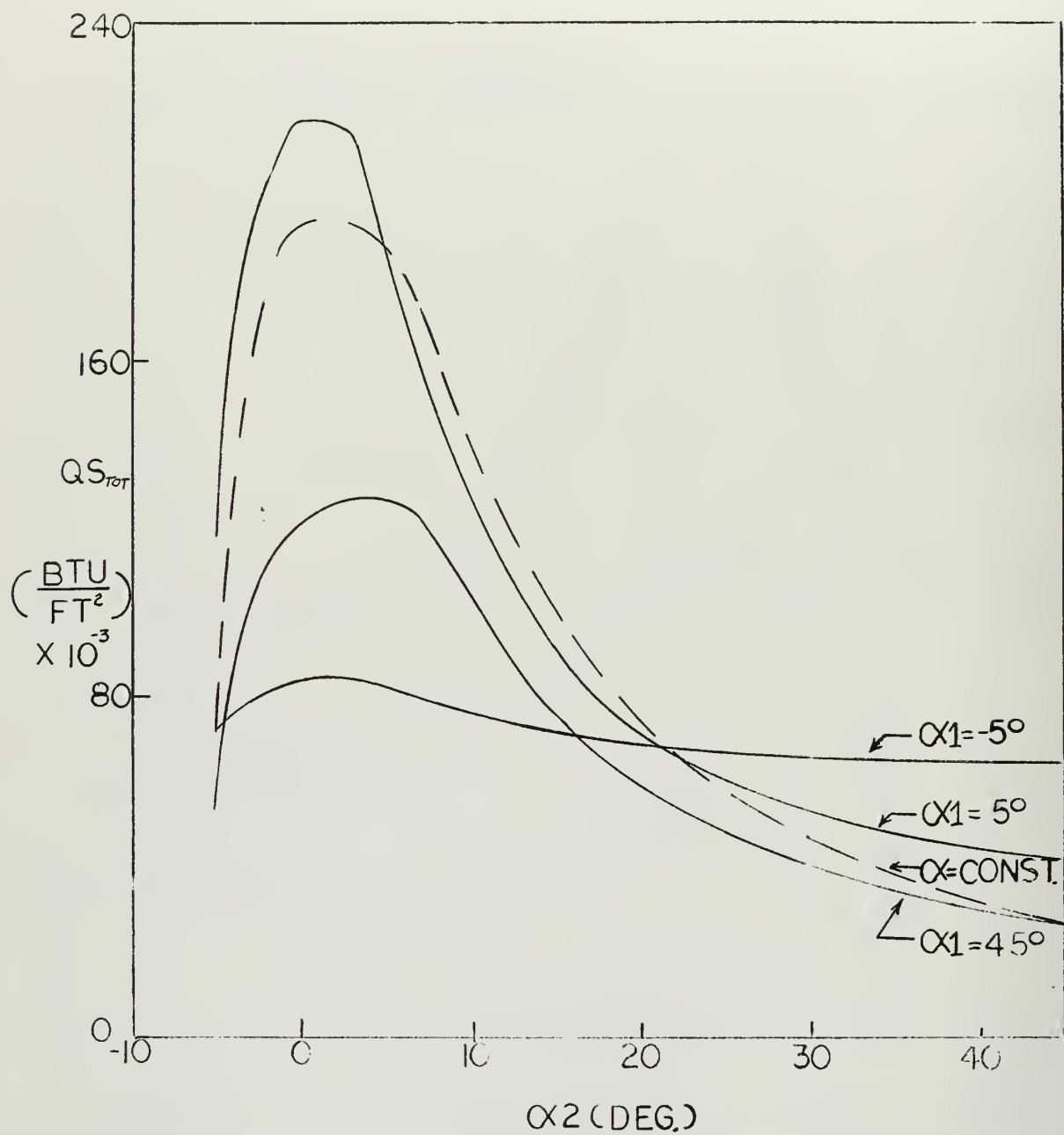
Fig. 25 Variation of Total Stagnation Heating with α2   (Angle of
Attack Modulation)

100
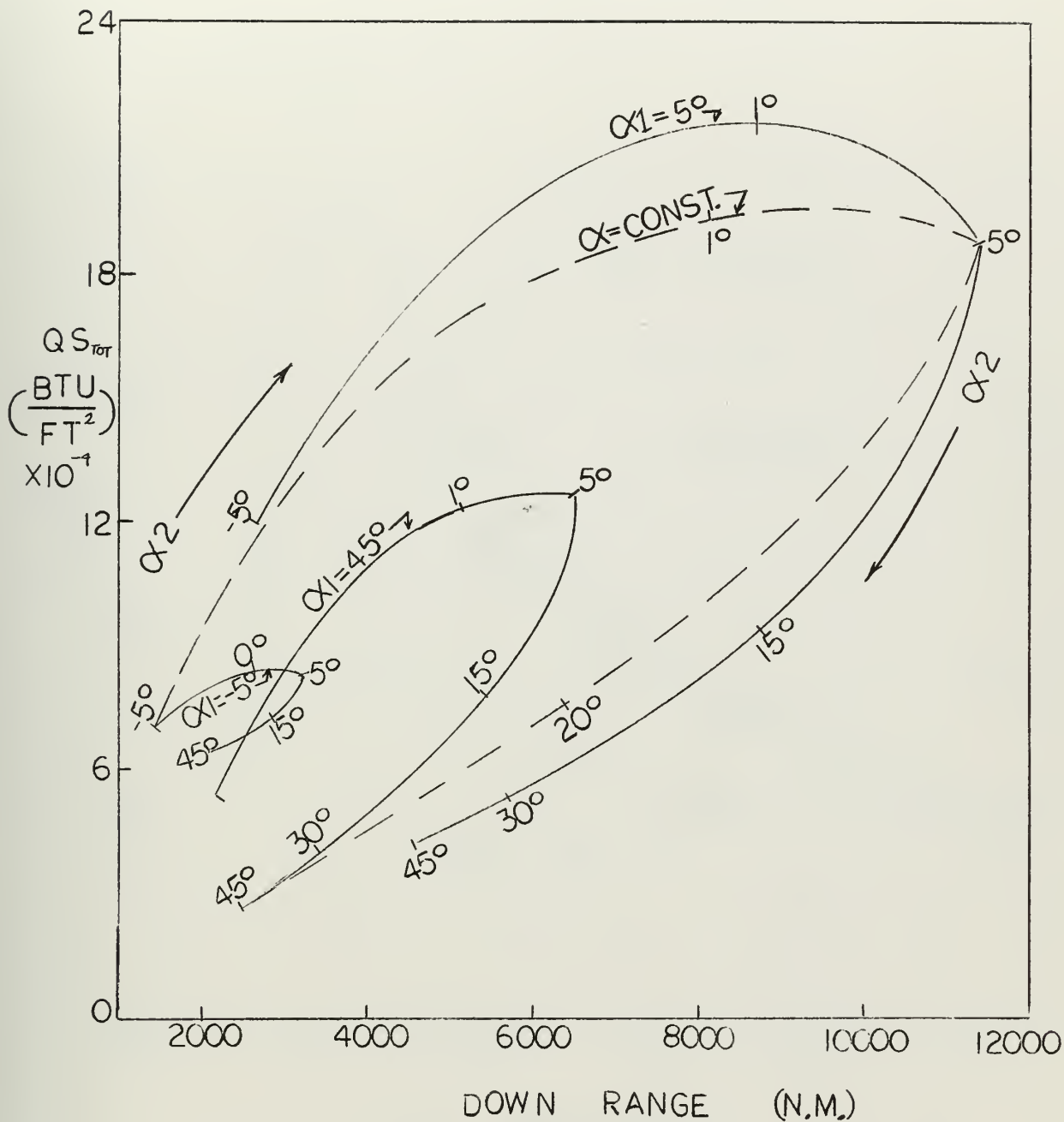
Fig. 26   Variation of Total Stagnation Heating with Down Range
(Angle of Attack Modulation)

101
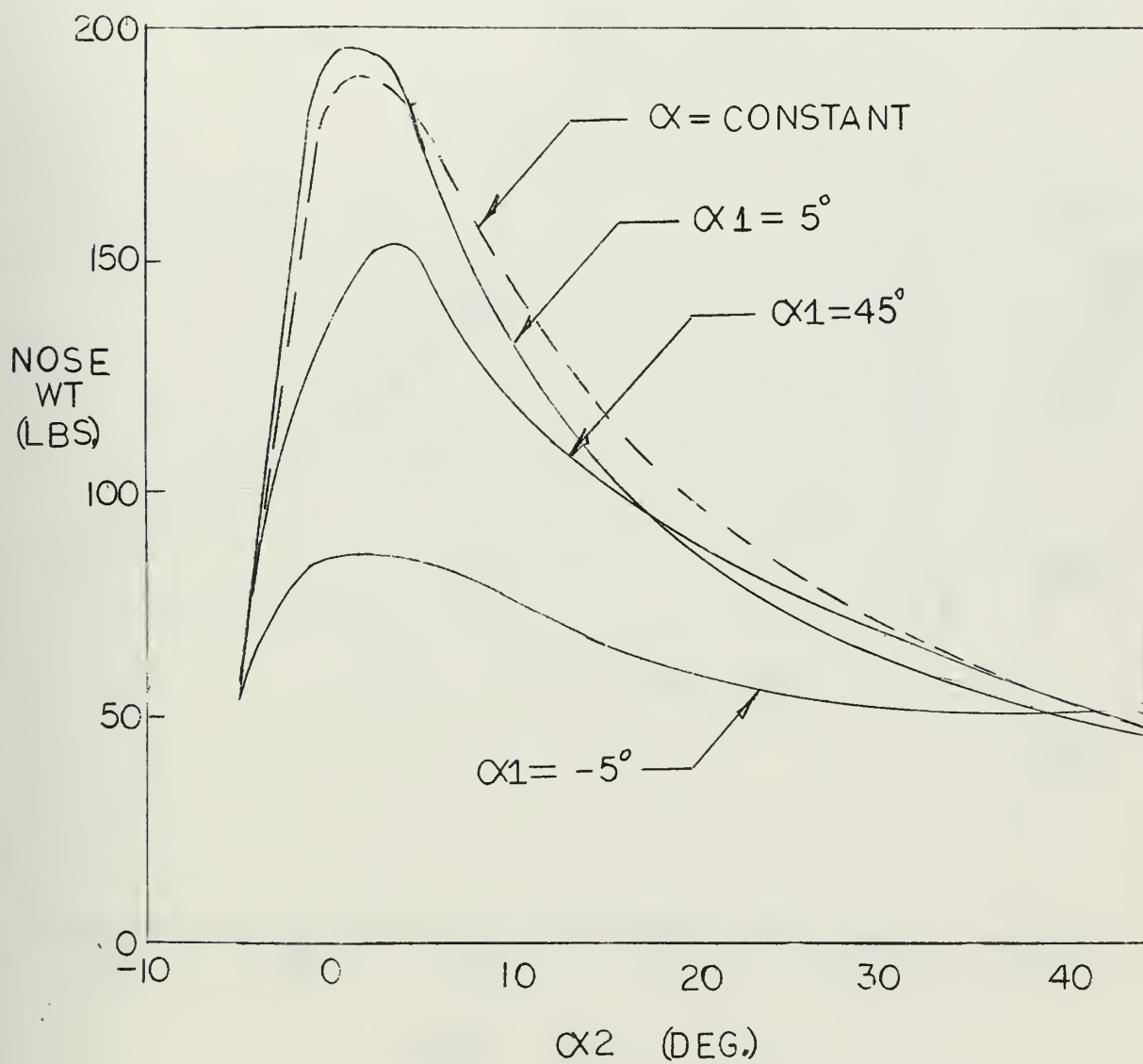
Fig. 27   Variation of Nose Ablator Weight with $\alpha 2$
(Angle of Attack Modulation)

101
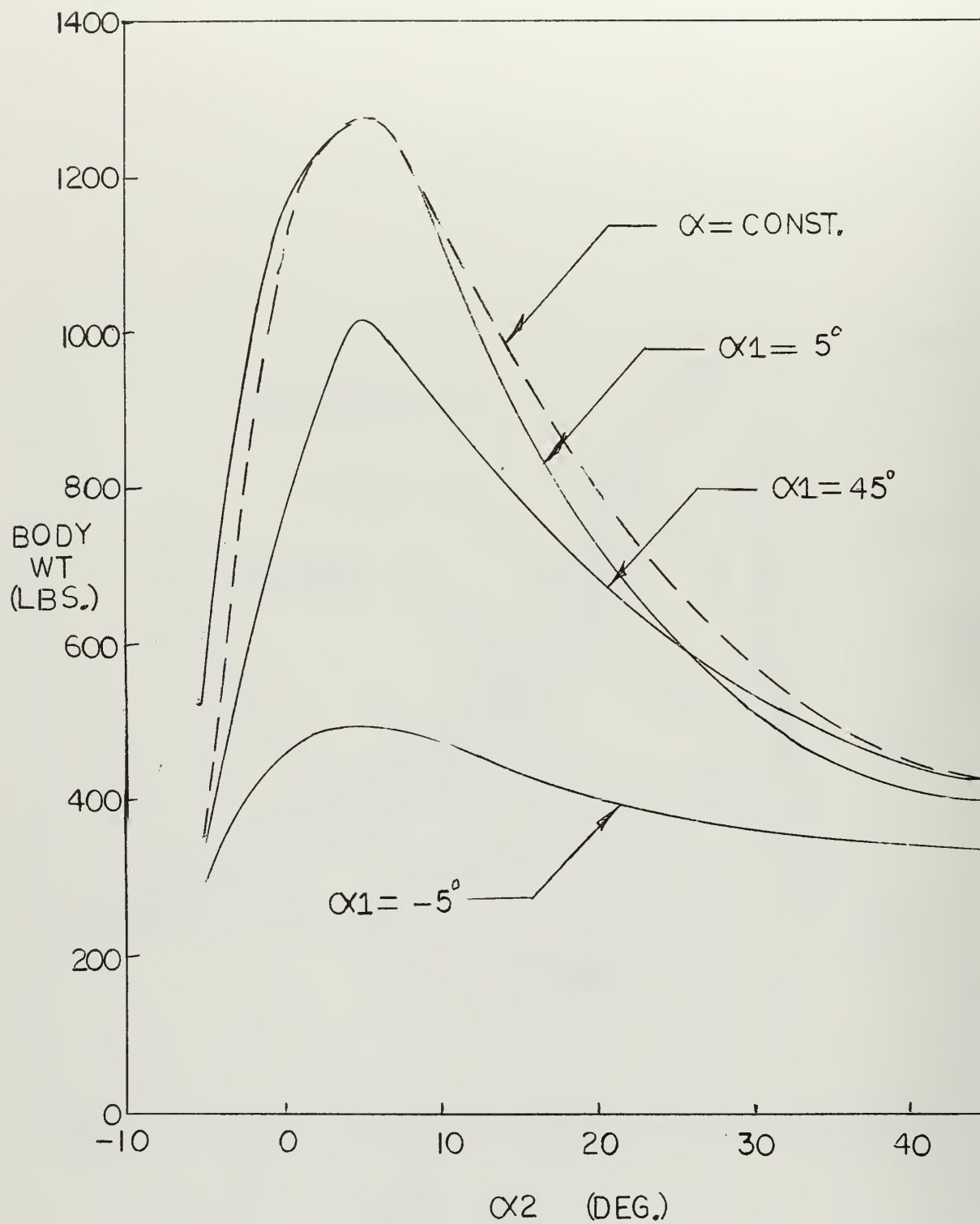
Fig. 28 Variation of Body Ablator Weight with α2 (Angle of Attack
Modulation)

102
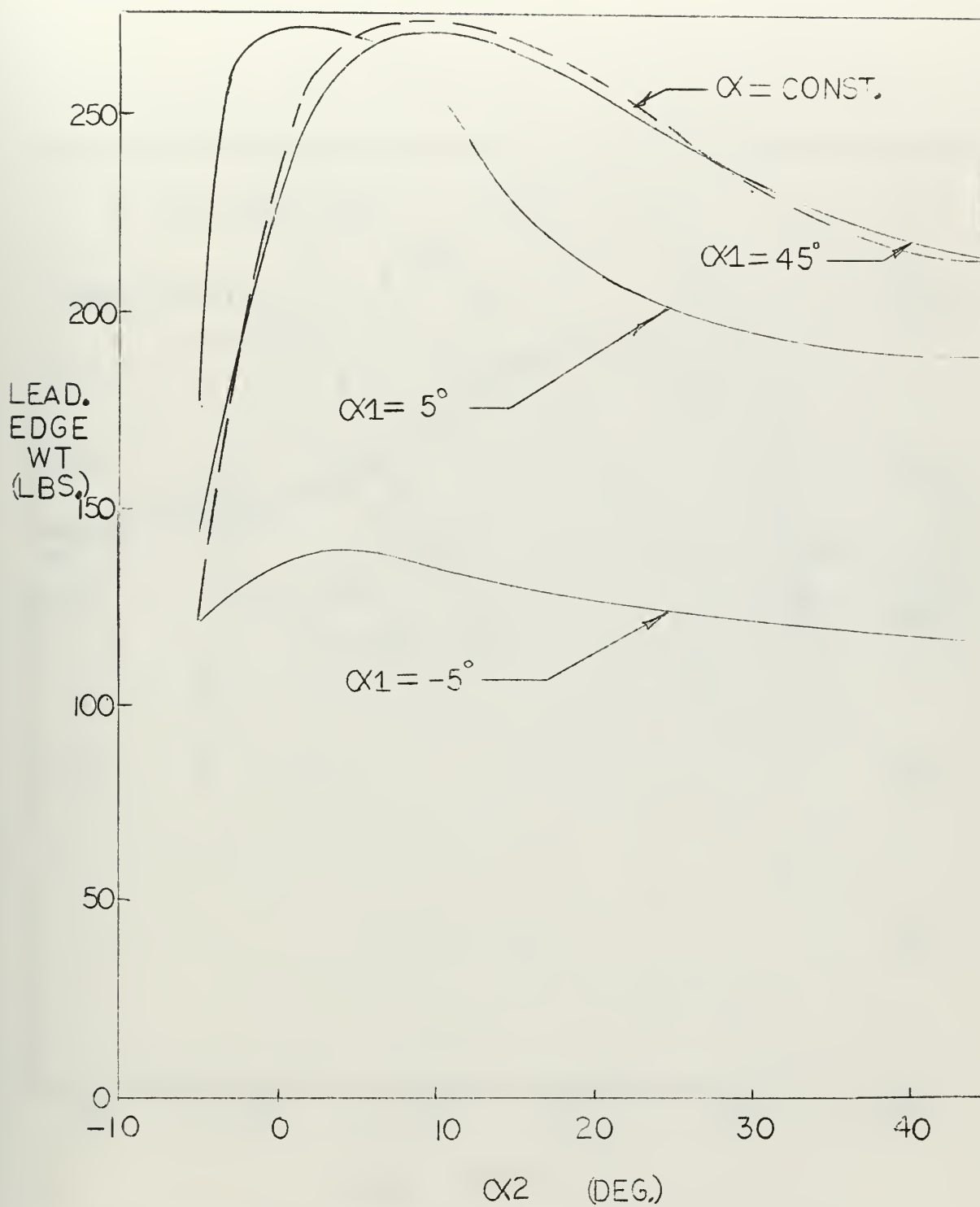
Fig. 29   Variation of Leading Edge Ablator Weight with α2
(Angle of Attack Modulation)

103
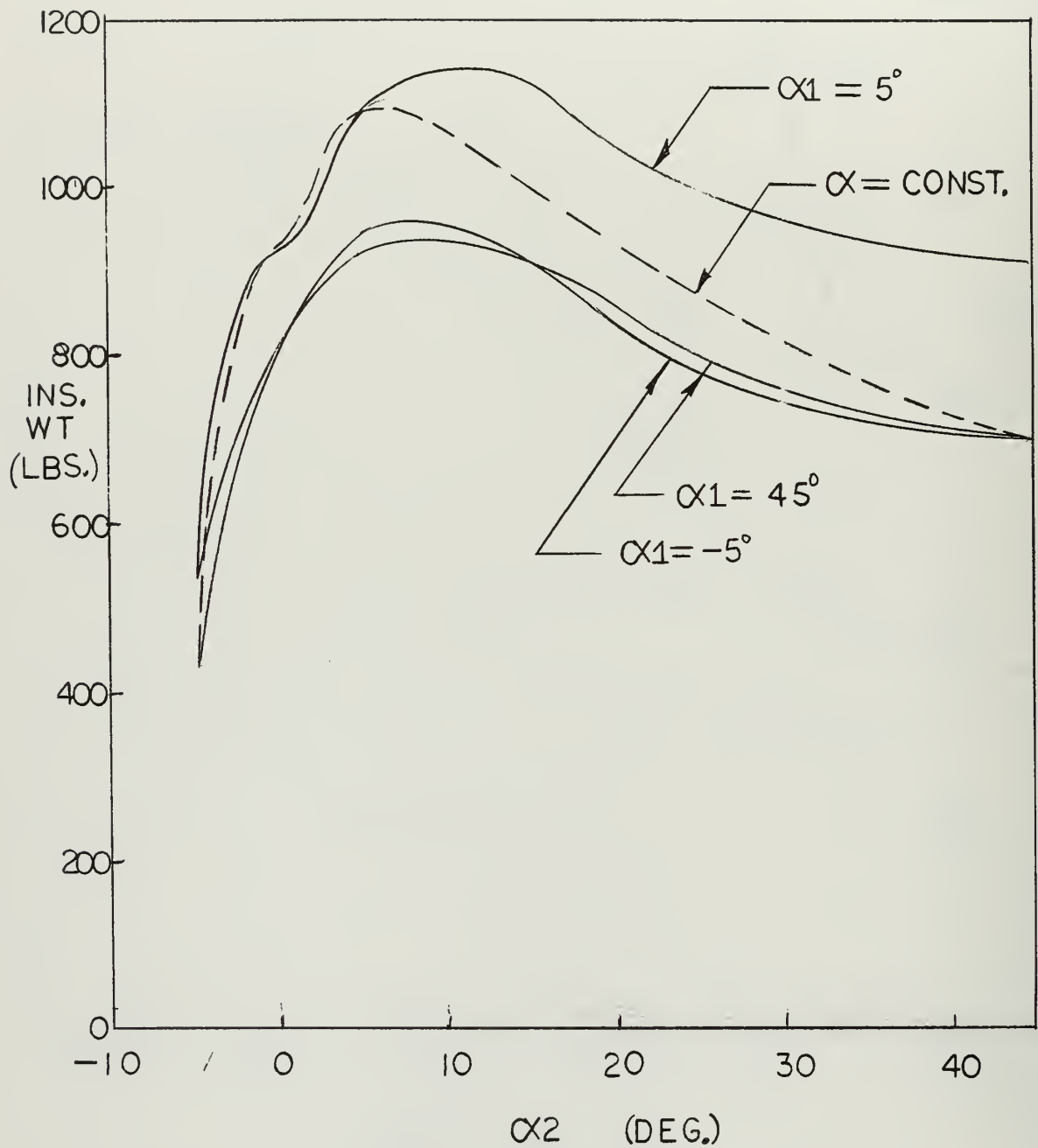
Fig. 30 Variation of Insulation Weight with α2 (Angle of Attack Modulation)
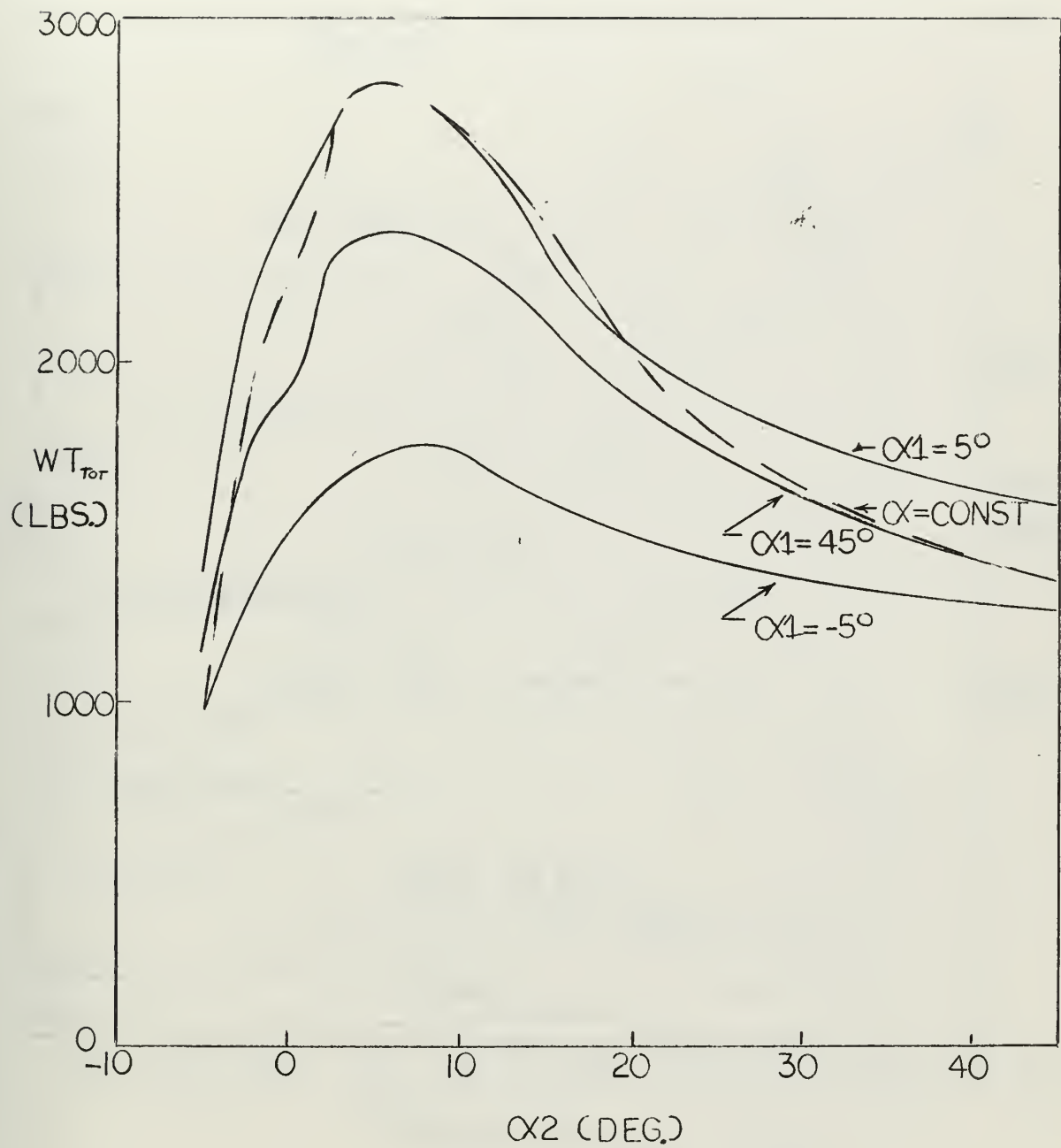
Fig. 31 Variation of Thermal Protection System Weight with α2
(Angle of Attack Modulation)
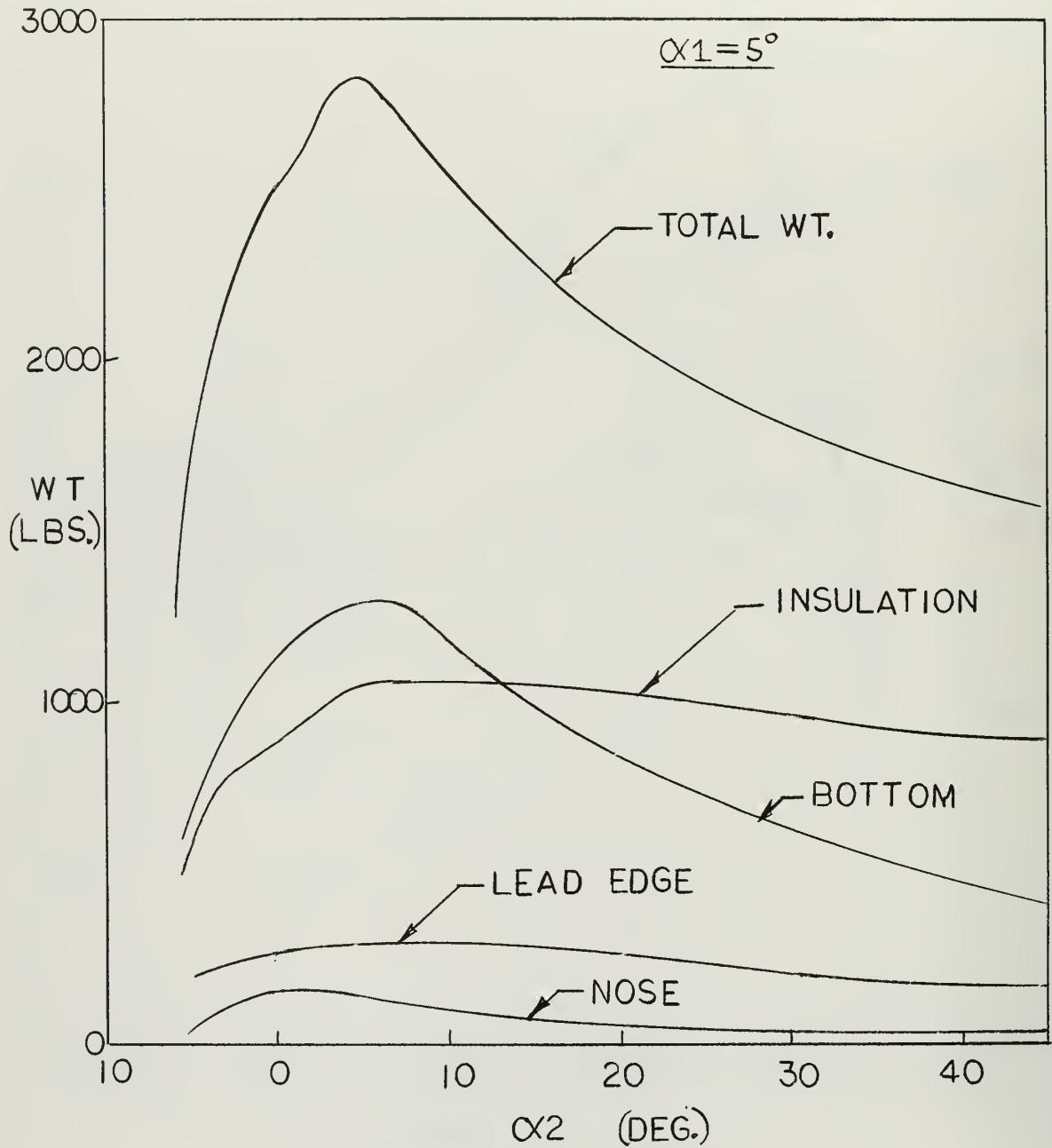
Fig. 32   Variation of Component Ablator and Insulation Weight
with α2   (Angle of Attack Modulation)

106

Fig. 33 Variation of Thermal Protection System Weight with Down Range (Angle of Attack Modulation)
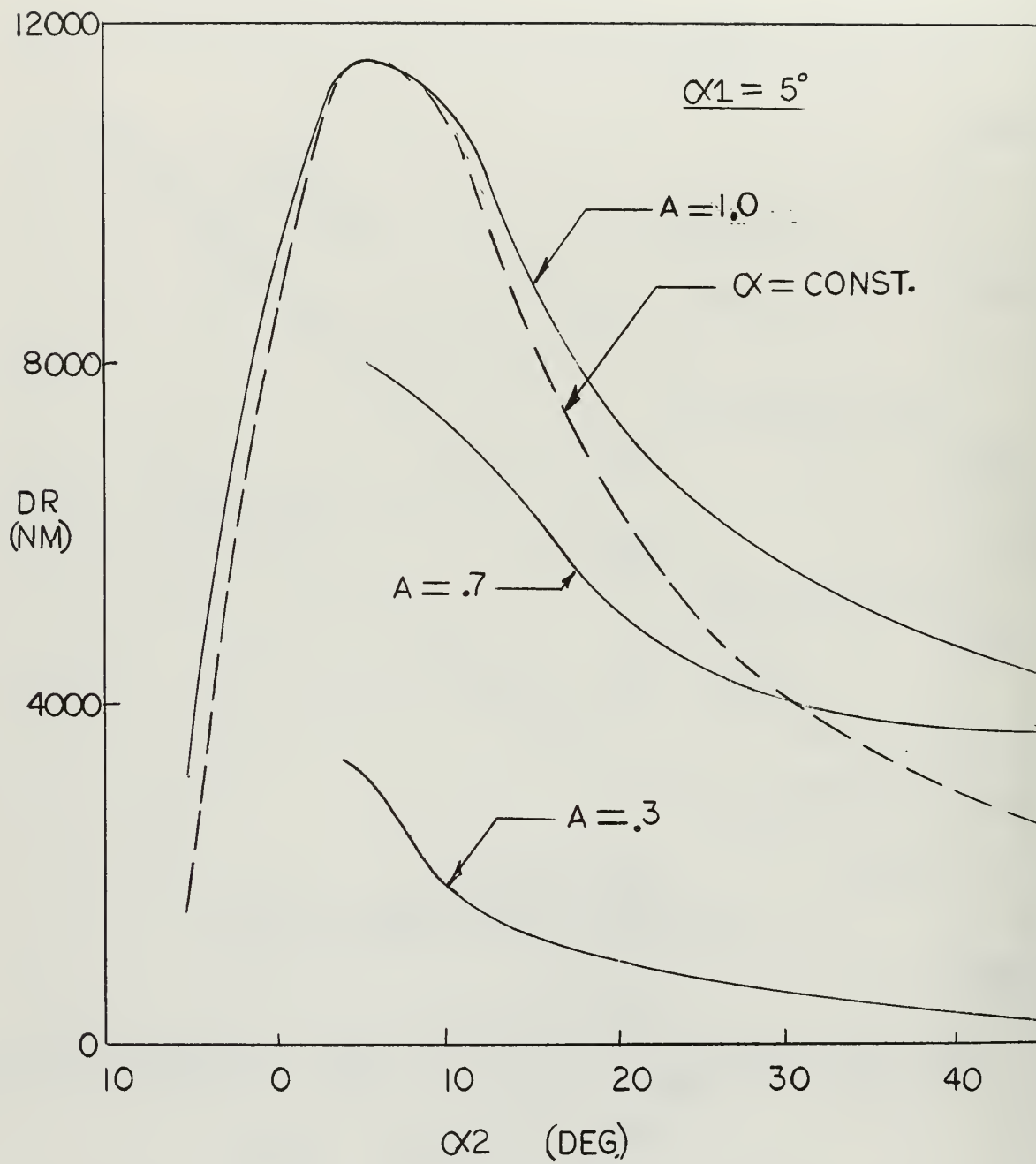
Fig. 34 Variation of Down Range with α2 (Bank Modulation)
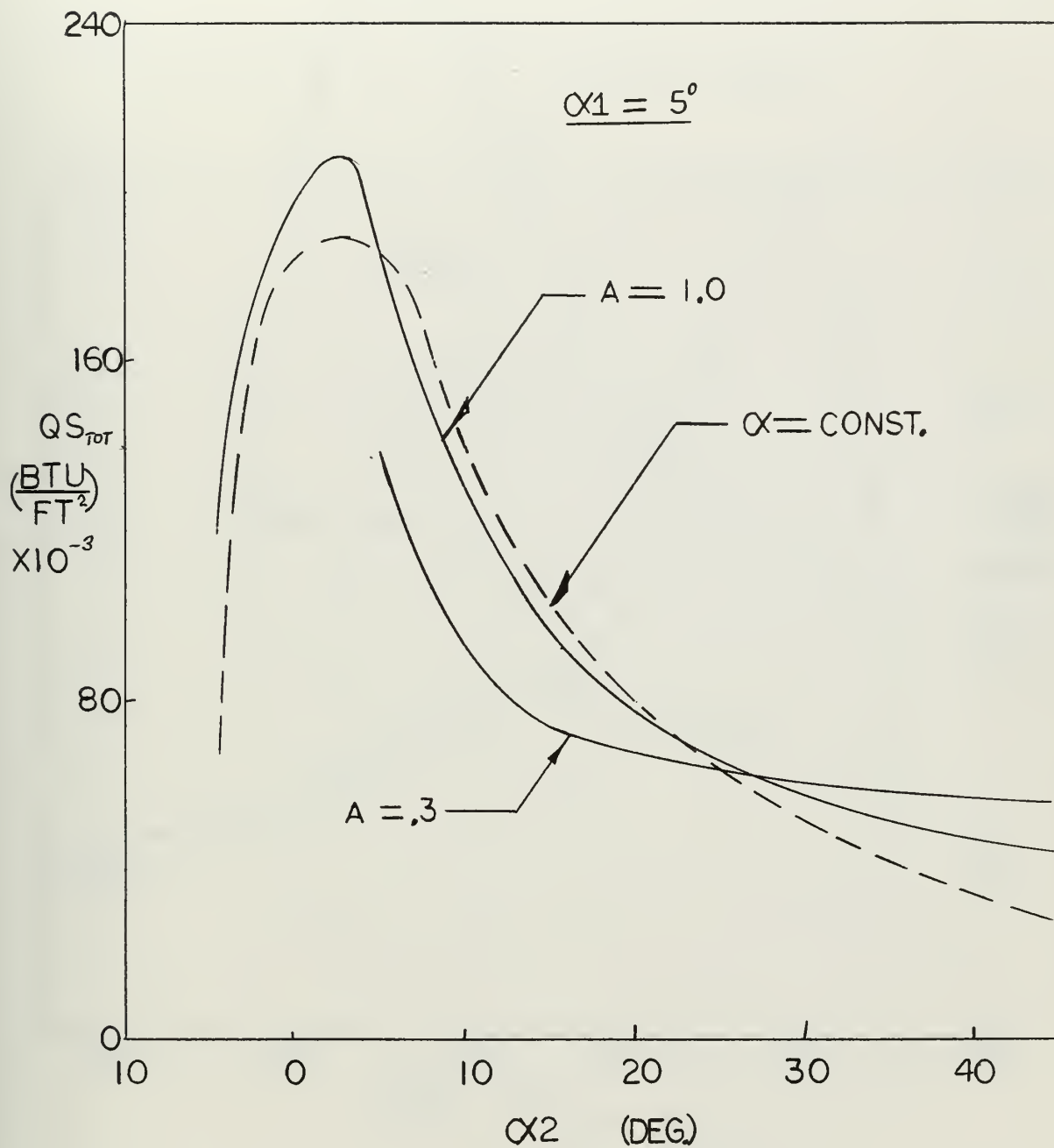
Fig. 35   Variation of Total Stagnation Heating with α2
(Bank Modulation)
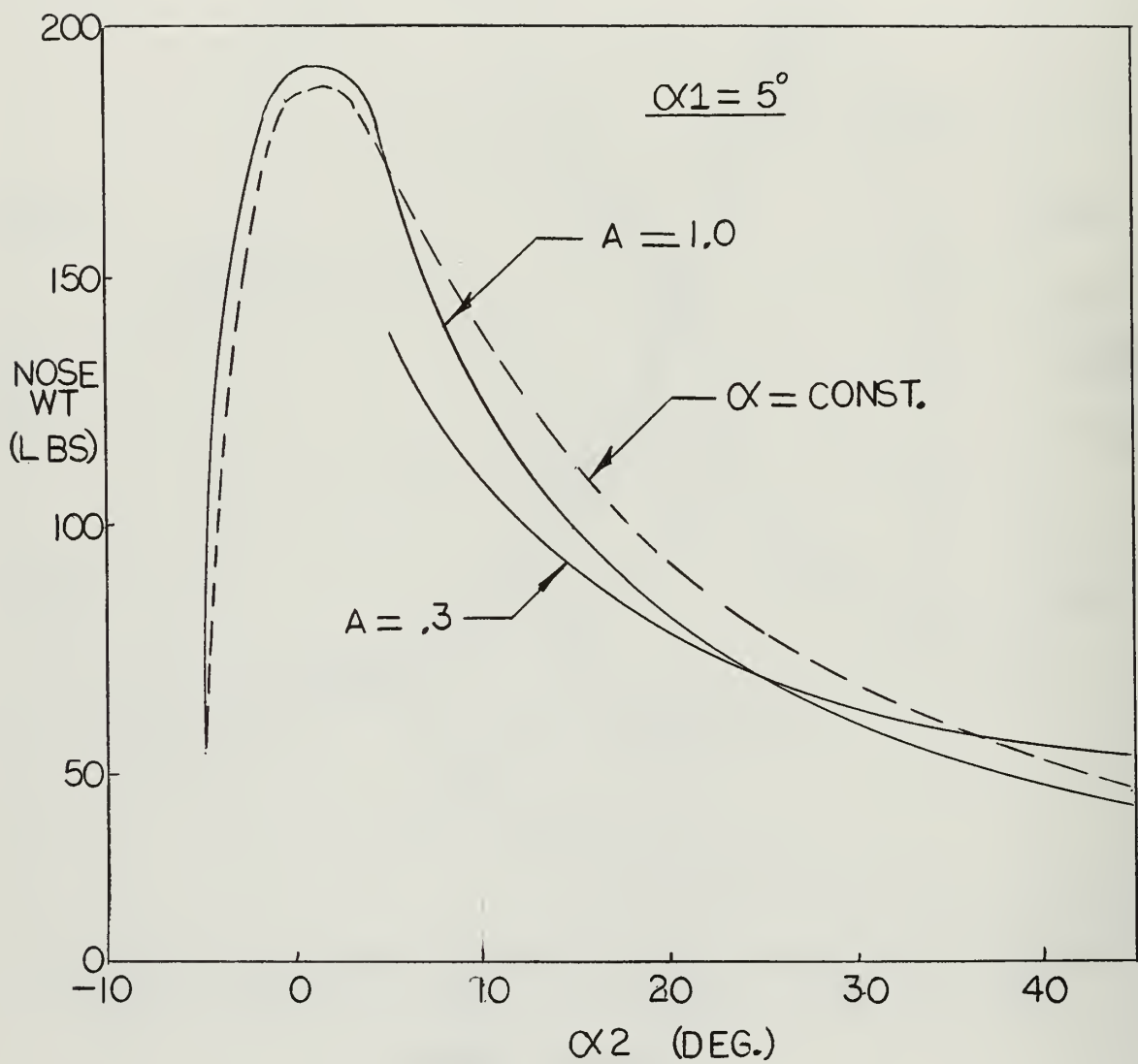
Fig. 36 Variation of Nose Ablator Weight with α2 (Bank Modulation)
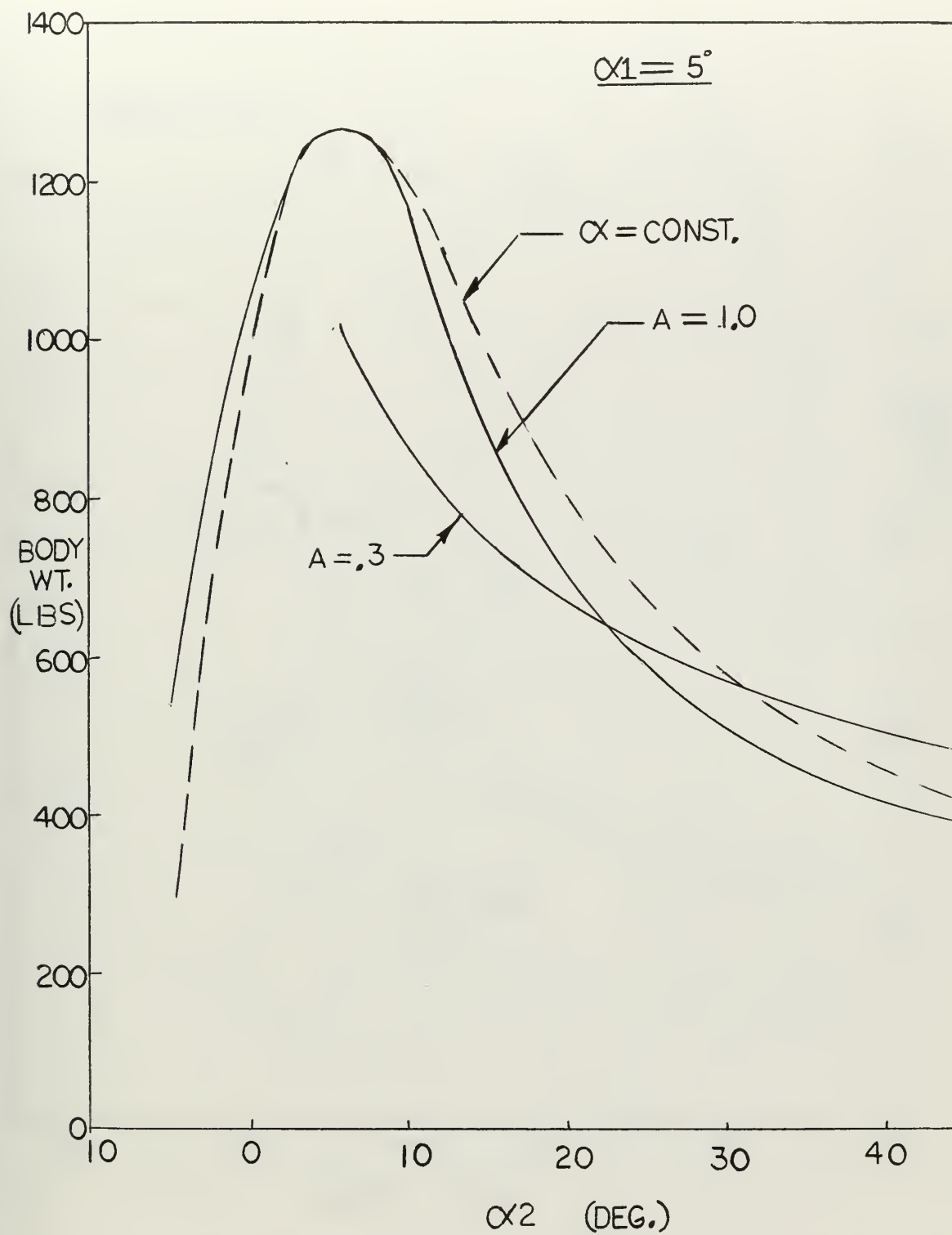
Fig. 37   Variation of Body Ablator Weight with α2   (Bank
          Modulation)

111
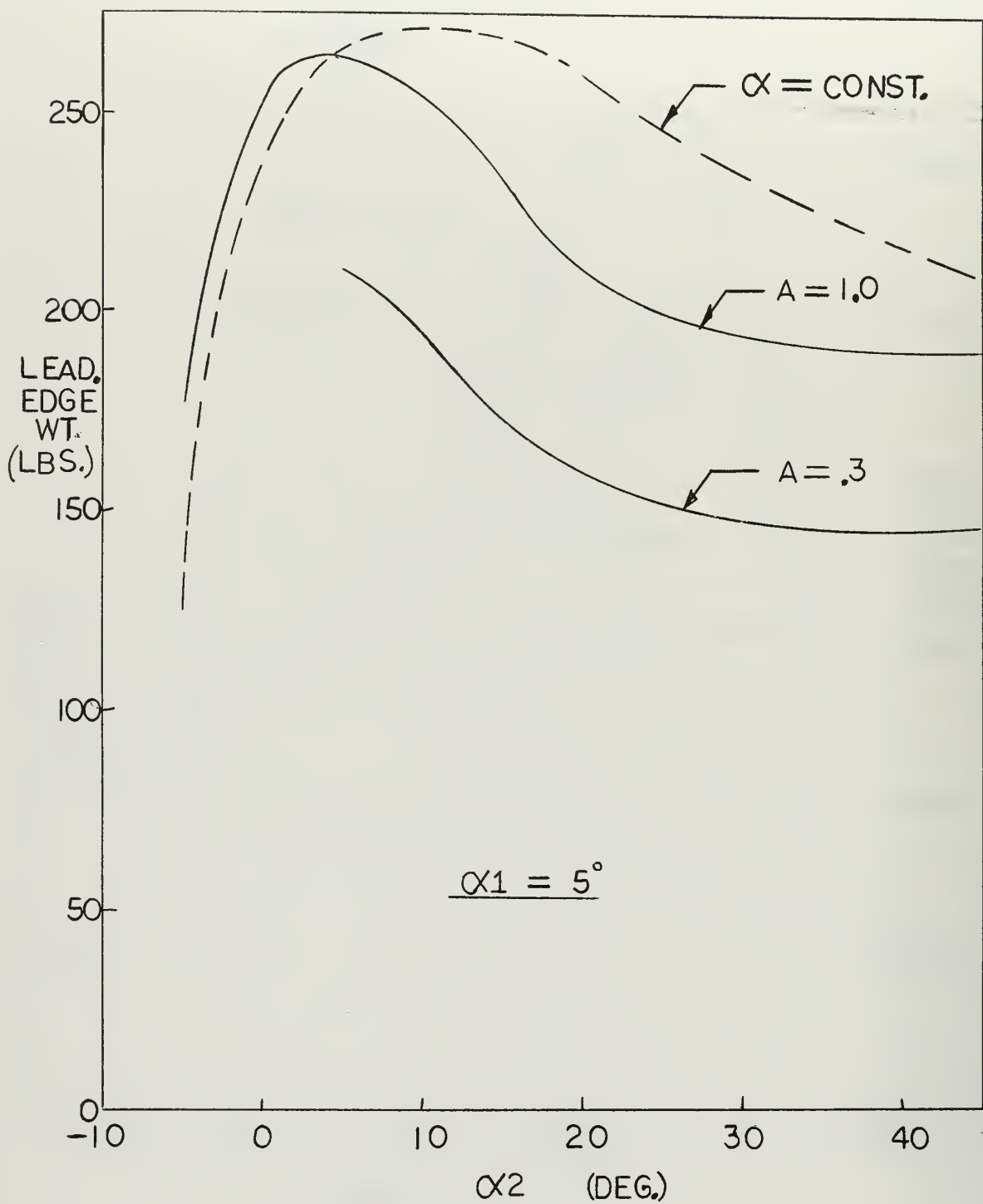
Fig. 38   Variation of Leading Edge Ablator Weight with α2
(Bank Modulation)

112
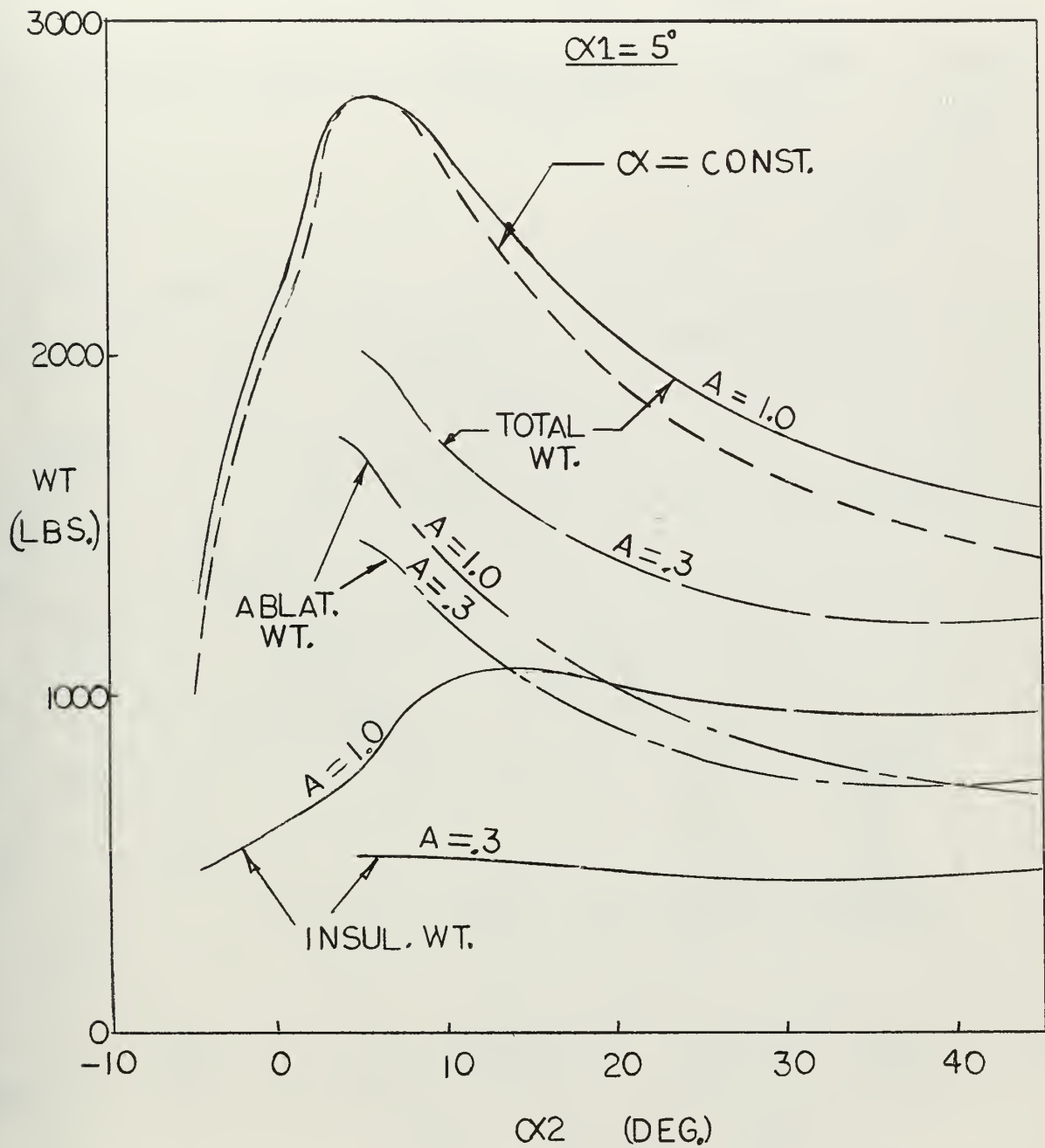
Fig. 39 Variation of Total Ablator, Insulation, and Thermal Protection System
Weight with α2   (Bank Modulation)

113

Fig. 40   Variation of Total Stagnation Heating with Down Range
(Bank Modulation)
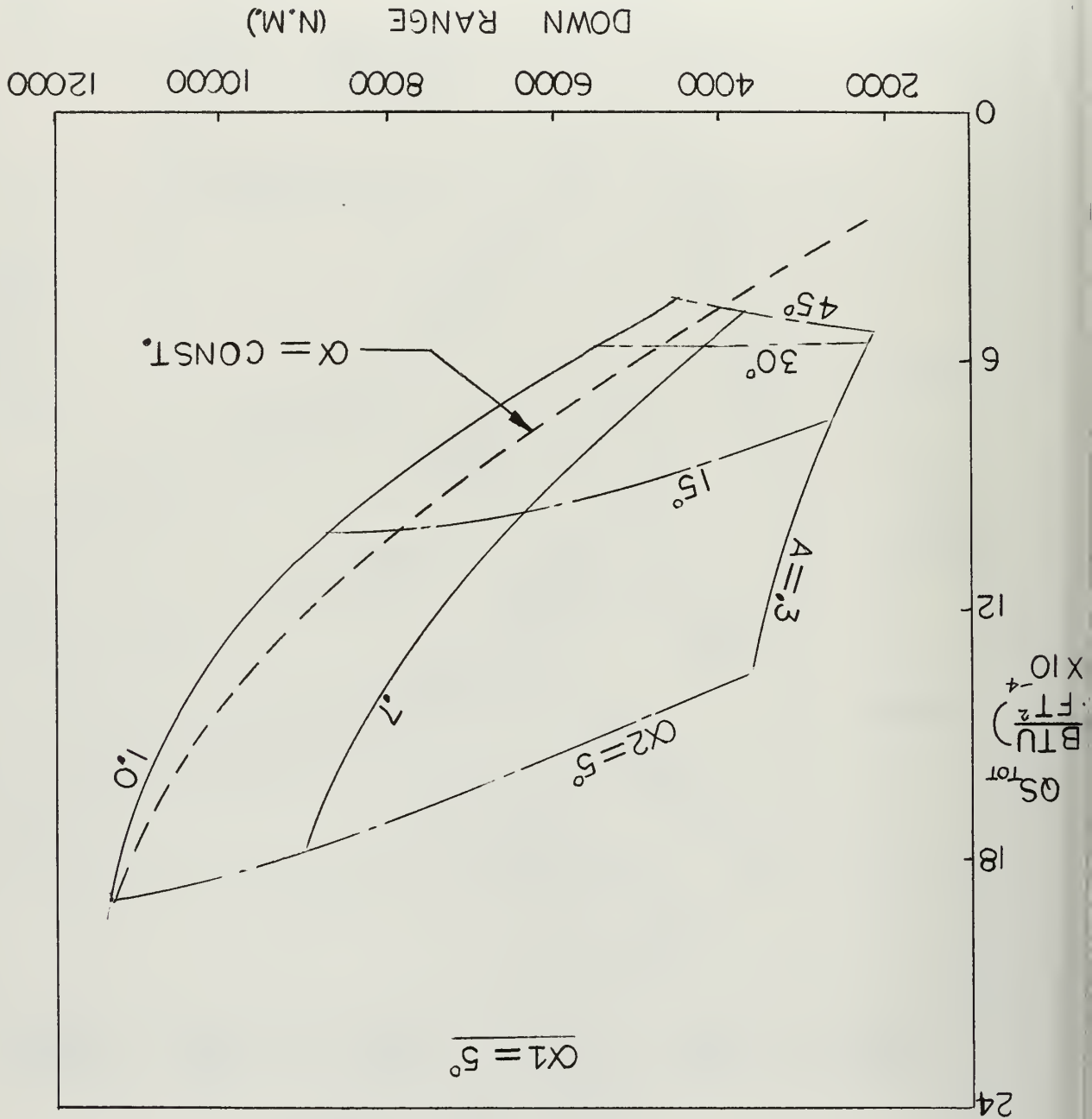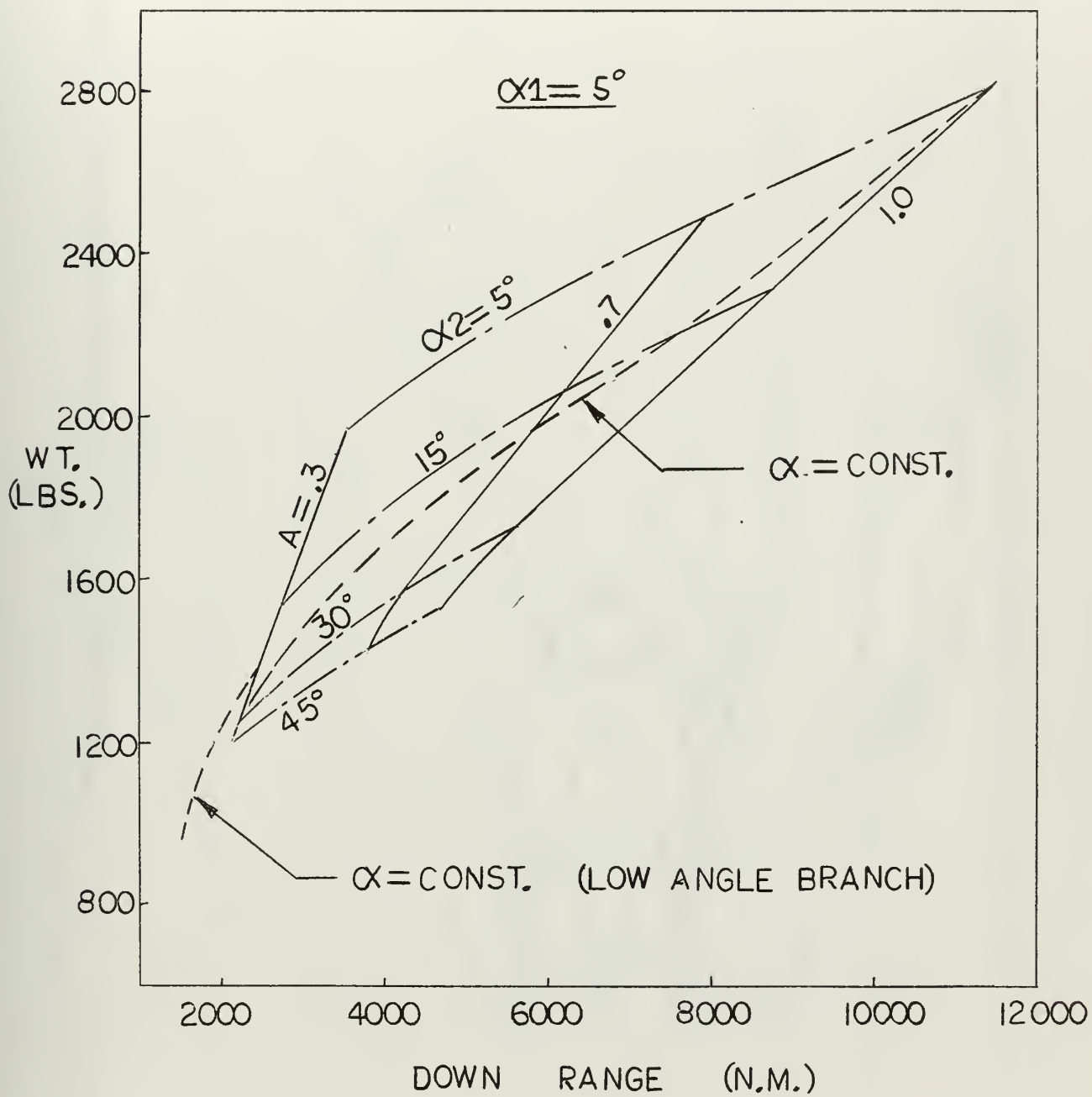
Fig. 41 Variation of Thermal Protection System Weight with Down
Range (Bank Modulation)

115
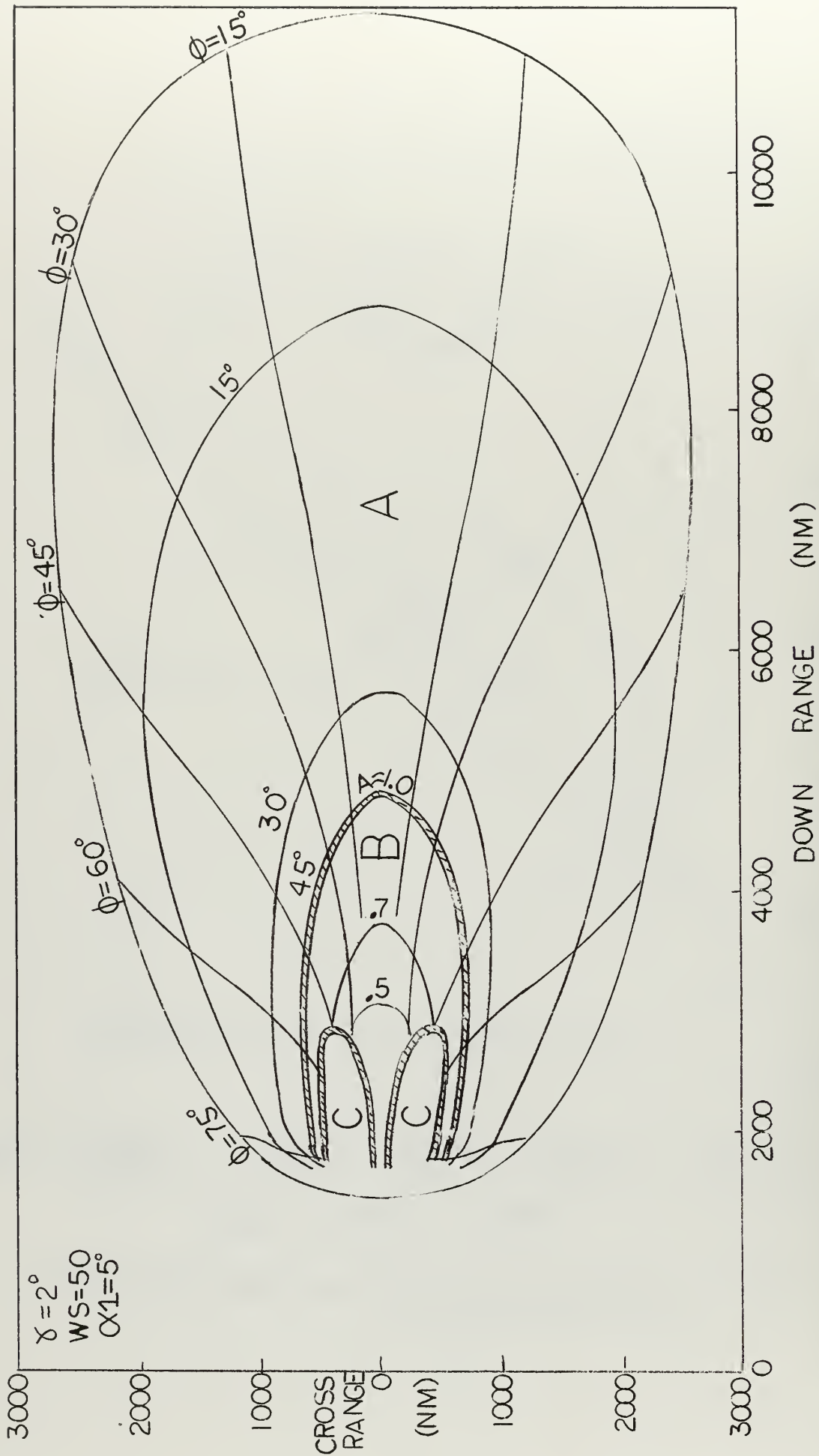
Fig. 42 Trajectory Control Parameters (Lateral Range Capability)
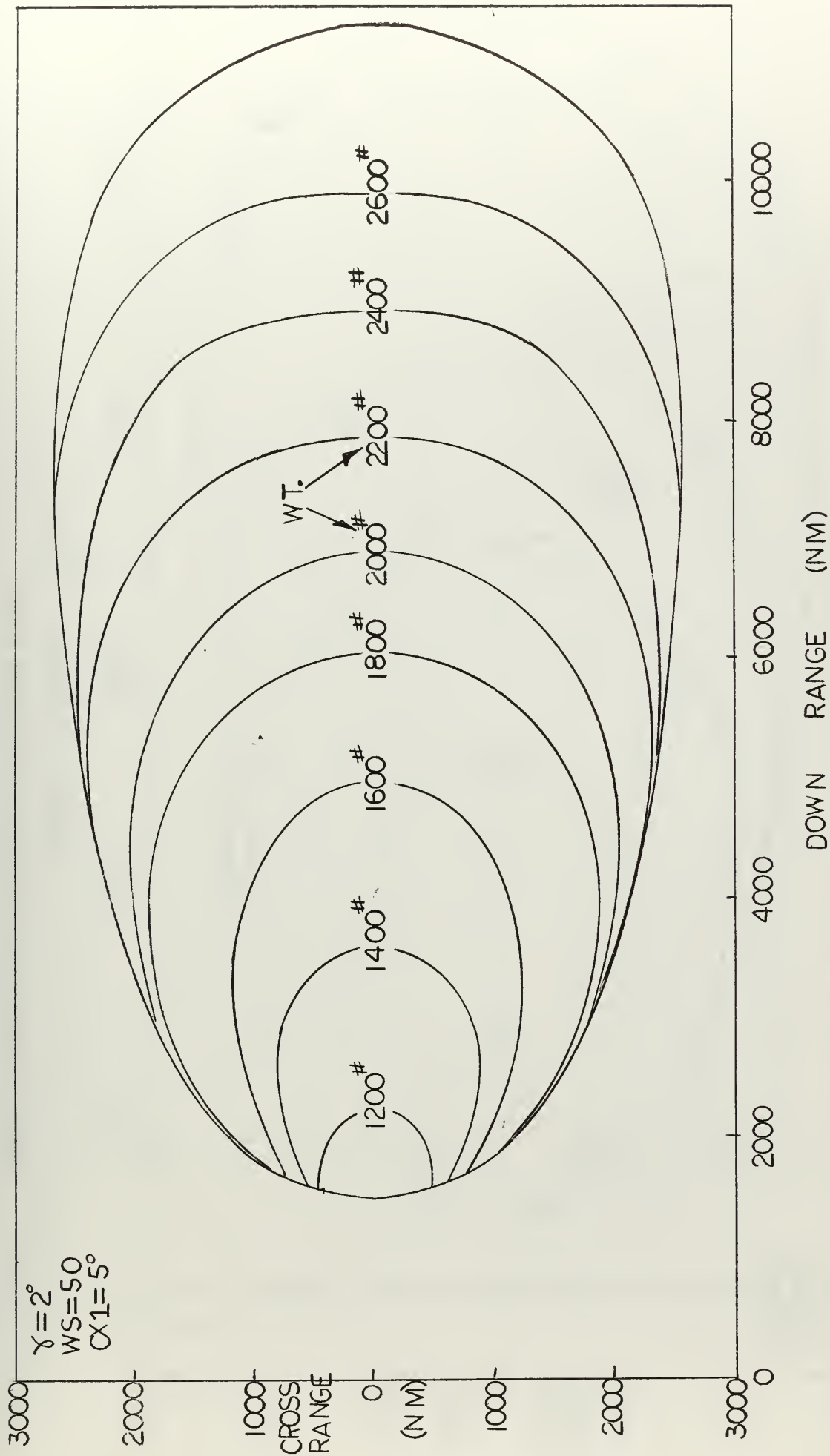
Fig. 43 Variation of Thermal Protection System Weight with Landing Point

117
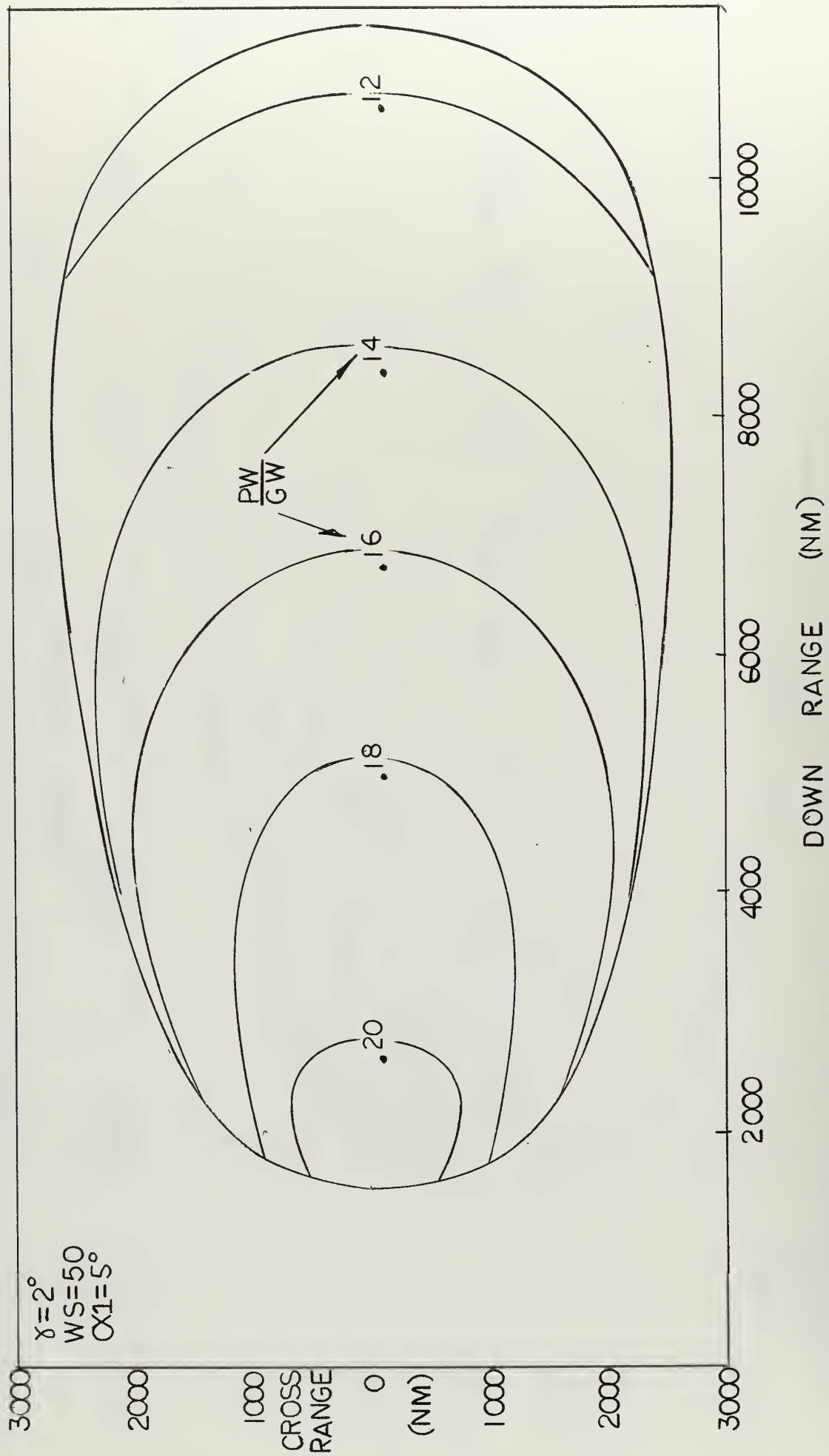
Fig. 44 Variation of Payload with Landing Point
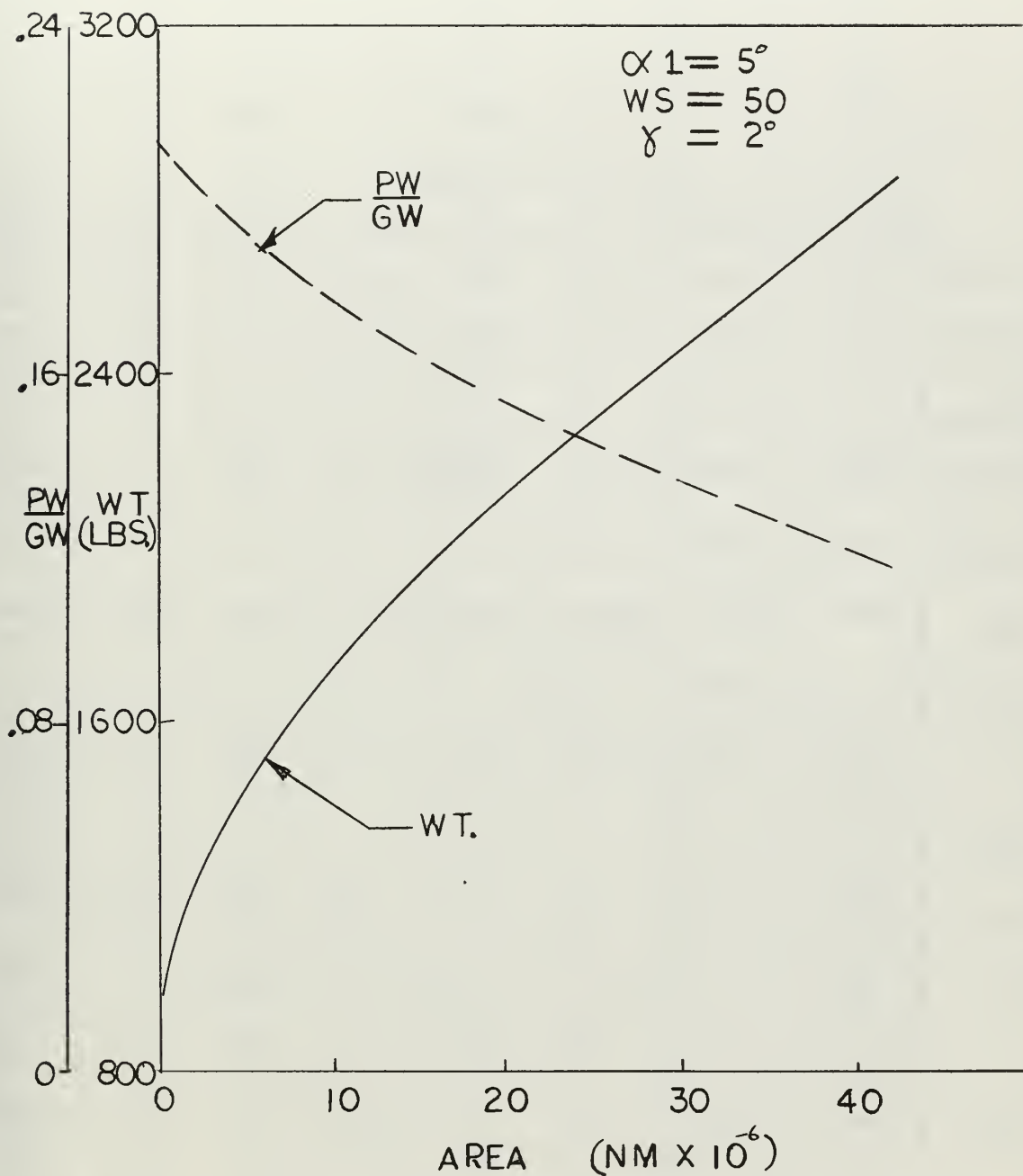
Fig. 45 Variation of Thermal Protection System Weight and Payload Fraction
with Area

	α ($\gamma = 2°$, WS = 50 PSF)							
	-5°	-2°	1°	5°	20°	40°	45°	50°
TF(SEC)	438	1818	2764	3978	2366	1130	998	896
DR(NM)	1446	5280	8083	11532	6471	2927	2569	2293
RPA_{max}	5.2	2.8	3.8	5.8	3.0	2.4	2.5	2.6
$DYNP_{max}$	6100	2400	2500	2400	380	130	120	120
$q_{s\ max}$	693	476	407	334	173	120	115	113
Q_{STOT}	70826	170876	193185	188408	75819	30866	26985	24064
W_N	55	141	170	177	97	49	43	39
W_B	331	750	1003	1260	793	436	401	371
W_{TOP}	57	21	0	0	0	0	0	0
W_{LE}	121	240	250	266	258	220	216	214
W_A	563	1152	1423	1703	1148	705	660	624
W_I	427	882	948	1107	951	728	690	659
W_{TOT}	990	2034	2371	2810	2099	1433	1350	1283

TABLE 2

Constant Angle of Attack Trajectories

α_2 ($\gamma= 2°$, $\alpha_1 = -5°$, WS = 50 PSF)				
-5°	**5°**	**15°**	**30°**	**45°**
TF(SEC)				
438	1664	1482	1030	886
DR(NM)				
1446	3220	2847	2290	2109
RPA_{max}				
5.2	7.8	8.8	8.5	8.6
$DYNP_{max}$				
6100	6100	6100	6100	6100
$q_{s\ max}$				
693	693	693	693	693
Q_{STOT}				
70826	83111	72001	66505	65026
W_N				
55	80	63	53	49
W_B				
331	497	442	369	356
W_{TOP}				
57	46	46	46	46
W_{LE}				
121	139	133	125	122
W_A				
563	762	683	593	572
W_I				
427	954	914	756	690
W_{TOT}				
990	1716	1597	1349	1262

	-5°	5°	15°	30°	45°
TF(SEC)	438	1664	1482	1030	886
DR(NM)	1446	3220	2847	2290	2109
RPA_{max}	5.2	7.8	8.8	8.5	8.6
$DYNP_{max}$	6100	6100	6100	6100	6100
$q_{s\ max}$	693	693	693	693	693
Q_{STOT}	70826	83111	72001	66505	65026
W_N	55	80	63	53	49
W_B	331	497	442	369	356
W_{TOP}	57	46	46	46	46
W_{LE}	121	139	133	125	122
W_A	563	762	683	593	572
W_I	427	954	914	756	690
W_{TOT}	990	1716	1597	1349	1262

α_2 ($\gamma= 2°$, $\alpha_1 = -2°$, WS = 50 PSF)

	-2°	5°	15°	30°	45°
TF(SEC)	1818	3422	2826	1814	1476
DR(NM)	5280	9395	7562	5164	4378
RPA_{max}	2.7	6.8	6.5	6.8	7.9
$DYNP_{max}$	2400	2900	1600	1600	1600
$q_{s\ max}$	476	481	476	481	481
Q_{STOT}	170876	150524	90640	61653	53754
W_N	141	145	91	60	48
W_B	750	1038	774	504	409
W_{TOP}	21	4	4	4	4
W_{LE}	240	222	196	174	166
W_A	1152	1409	1065	743	627
W_I	882	1214	1201	1023	949
W_{TOT}	2034	2623	2266	1766	1576

TABLE 3
Angle of Attack Modulated Trajectories

	α2						
	(γ = 2°, α1 = 5°, WS = 50 PSF)						
	–5°	–2°	1°	5°	15°	30°	45°
TF(SEC)	794	2072	2954	3978	3150	1930	1562
DR(NM)	2882	6403	8764	11532	8840	5712	4776
RPA_{max}	3.7	2.3	3.4	5.7	5.2	5.1	6.0
$DYNP_{max}$	4300	1800	2200	2400	890	660	660
$q_{s\ max}$	476	345	334	334	323ˆ	323	323
Q_{STOT}	118368	204992	217243	188408	93492	53873	43806
W_N	82	164	189	177	102	62	48
W_B	518	908	1105	1260	881	541	428
W_{TOP}	58	12	0	0	0	0	0
W_{LE}	172	278	279	266	222	194	183
W_A	830	1363	1573	1703	1205	797	659
W_I	545	886	938	1107	1128	963	900
W_{TOT}	1375	2249	2511	2810	2333	1760	1559

	α2						
	(γ = 2°, α1 = 45°, WS = 50 PSF)						
	–5°	–2°	1°	5°	15°	30°	45°
TF(SEC)	642	1470	2030	2768	2268	1374	998
DR(NM)	2177	3932	5173	6697	5430	3407	2569
RPA_{max}	7.1	2.9	3.3	4.5	3.1	2.2	2.5
$DYNP_{max}$	8400	2500	2200	1900	550	160	120
$q_{s\ max}$	515	377	317	243	140	115	115
Q_{STOT}	53810	104304	123240	127645	76985	39012	26985
W_N	52	110	138	152	106	61	43
W_B	368	615	808	1006	833	535	401
W_{TOP}	34	8	0	0	0	0	0
W_{LE}	145	223	243	264	268	235	216
W_A	600	956	1188	1422	1207	831	660
W_I	557	834	838	947	914	776	690
W_{TOT}	1157	1790	2026	2369	2121	1607	1350

TABLE 3 (Continued)

Angle of Attack Modulated Trajectories

| | α2 (γ = 2°, α1 = 5°, WS = 50 PSF) | | | | | | |
| | (A = 0.7) | | | | (A = 0.3) | | |
	15°	30°	45°	5°	15°	30°	45°
TF(SEC)	2222	1434	1204	1178	1006	778	722
DR(NM)	6282	4290	3743	3441	2869	2298	2181
RPA_{max}	5.2	6.2	7.1	5.0	8.1	8.5	8.5
$DYNP_{max}$	920	920	920	2100	2000	2000	2000
$q_{s\,max}$	370	370	370	506	506	506	506
Q_{STOT}	90271	53931	45557	134122	76525	56915	53484
W_N	101	60	47	139	83	57	51
W_B	847	533	438	1086	753	537	497
W_{TOP}	0	0	0	0	0	0	0
W_{LE}	219	181	168	219	177	151	154
W_A	1167	774	652	1445	1013	745	702
W_I	882	793	753	526	517	499	500
W_{TOT}	2049	1567	1405	1971	1530	1244	1202

| | α2 (γ = 2°, α1 = -2°, WS = 50, A = 0.7) | | | |
	5°	15°	30°	45°
TF(SEC)	2360	1946	1330	1134
DR(NM)	6355	5221	3820	3397
RPA_{max}	5.9	7.3	8.1	8.9
$DYNP_{max}$	2500	2300	2300	2300
$q_{s\,max}$	541	541	541	541
Q_{STOT}	142737	87793	63455	57199
W_N	143	90	60	49
W_B	969	729	496	407
W_{TOP}	6	6	6	6
W_{LE}	216	188	164	153
W_A	1334	1013	725	615
W_I	941	942	839	800
W_{TOT}	2275	1955	1564	1415

TABLE 4

Bank Modulated Trajectories

123

	$\alpha 2$ ($\gamma = 2°$, $\alpha 1 = 5°$, WS = 50 PSF)							
	$\phi = 30°$				$\phi = 60°$			
	5°	15°	30°	45°	5°	15°	30°	45°
TF(SEC)	3442	2726	1720	1396	1976	1604	1098	954
DR(NM)	9182	7176	4966	4279	4063	3561	3017	2844
CR(NM)	2440	1704	694	427	2098	1571	843	632
RPA_{max}	4.8	4.9	5.4	6.3	4.0	6.1	7.2	7.9
$DYNP_{max}$	2000	840	740	740	1700	1200	1200	1200
$q_{s\ max}$	340	340	340	340	421	421	421	421
Q_{STOT}	191969	93275	54497	44944	167876	85513	54627	48209
W_N	185	103	62	48	170	95	58	47
W_B	1271	874	545	440	1229	818	541	443
W_{TOP}	0	0	0	0	0	0	0	0
W_{LE}	275	223	191	178	263	207	167	155
W_A	1731	1200	798	666	1662	1121	766	645
W_I	973	1016	891	829	703	690	650	641
W_{TOT}	2704	2216	1689	1495	2365	1811	1415	1286

TABLE 5

Lateral Range Capability

(Angle of Attack Modulated Trajectories)

	$\alpha 2$ (γ = 2, $\alpha 1$ = 5°, WS = 50 PSF)						
	ϕ = 75°				ϕ= 15°	ϕ= 45°	ϕ= 90°
	5°	15°	30°	45°	5°	5°	5°
TF(SEC)	1030	886	714	656	3860	2844	290
DR(NM)	1947	1836	1781	1779	10941	6628	1087
CR(NM)	1101	903	646	584	1478	2612	108
RPA_{max}	5.6	8.7	8.5	8.2	5.4	4.1	33.3
$DYNP_{max}$	2400	2300	2300	2300	2300	1700	14000
$q_{s\ max}$	529	529	528	528	335	368	790
Q_{STOT}	124914	75065	57821	55244	189300	187290	56125
W_N	130	81	58	53	179	185	49
W_B	1031	738	551	515	1261	1264	458
W_{TOP}	0	0	0	0	0	0	0
W_{LE}	207	171	150	154	267	280	82
W_A	1368	990	759	722	1707	1729	590
W_I	490	481	464	453	1082	855	267
W_{TOT}	1857	1472	1223	1175	2789	2585	857

TABLE 5 (Continued)

LATERAL RANGE CAPABILITY

(Angle of Attack Modulated Trajectories)

125

	$\phi = 30°$ $A = 0.5$	$\phi = 45°$ $A = 0.7$	$\phi = 60°$ $A = 0.866$	$\phi = 75°$ $A = 0.965$
TF (SEC)	886	954	886	650
DR (NM)	2711	2915	2609	1752
CR (NM)	188	375	538	562
RPA_{max}	8.2	8.0	8.2	8.1
$DYNP_{max}$	1400	1200	1400	2400
$q_{s\ max}$	444	422	444	534
Q_{STOT}	50016	48160	49821	55293
W_N	48	47	48	53
W_B	459	442	458	517
W_{TOP}	0	0	0	0
W_{LE}	153	154	153	154
W_A	660	642	659	724
W_I	598	642	599	448
W_{TOT}	1259	1284	1258	1172

$\alpha 2 = 45°$

$(\gamma = 2°, \alpha 1 = 5°, \text{WS} = 50 \text{ PSF})$

TABLE 6

Lateral Range Capability

(Angle of Attack Modulated Trajectories
with Bank Modulation)

126

CHAPTER 6

DESIGN PARAMETER TRADE-OFFS

Several design parameters were found to be of particular interest
and an analysis of the effect of variations in these parameters was made.
The parameters which were considered are entry angle, wing loading, nose
radius, and heat protection methods and materials.

6.1 Entry Angle

The effect of varying the entry angle on some of the aero-
thermodynamic loading factors was mentioned briefly in Chapters 1 and 4.
Additional effects are shown in more detail in Figs. 46 through 48
as functions of the Phase II angle of attack. The comparison here is
restricted to the optimized trajectories with angle of attack modulation
only. It can be seen that the effect of increasing the entry angle is to
reduce the longitudinal range, the total stagnation heating, and the thermal
protection system weight.

Fig. 49 shows the relation between down range and thermal protection
system weight for several values of initial entry angle. It is seen that
although the actual weight required for a given range is relatively
insensitive to changes in initial entry angle, the maximum and minimum
ranges attainable are affected. For a nominal Phase II angle of attack
of 15 degrees, a $\pm$ 1 degree change in entry angle causes a $\pm$ 4
percent change in weight. The corresponding change in range is -7

percent and + 8 percent.

An initial entry angle of four degrees was assumed and, following the development in Section 5.4, the optimized straight line trajectories were expanded into a footprint through the introduction of nominal bank angles. The resulting footprint is shown in Fig. 50 and the associated data is presented in Table 7.

It can be seen that, for this larger entry angle, the limit on nominal bank angle imposed by the acceleration constraint of 10 g's does affect the attainable area of the footprint. However, as mentioned earlier, additional areas of the footprint may be reached, under the acceleration constraint, by employing a somewhat different angle of attack and bank modulation scheme and varying the nominal bank angle.

The three sectors, A, B, and C are defined by the same factors as were described in Section 5.4

The thermal protection system weight requirements to reach a particular landing site within the footprint are shown in the lower half of Fig. 50. Fig. 50 also shows the penalty on payload fraction associated with changes in the desired landing site within the footprint.

The thermal protection system weights for a landing area capability with the higher entry angle are compared to those required for the nominal entry angle in Fig. 51.

The reduction in payload fraction with increased ranging capability for each of the two entry angles is also compared in Fig. 51.

It can be seen from Fig. 51 that although the total area attainable is greater for the lower entry angle of two degrees, the payload fraction is less over the entire range of comparable areas.

128

6.2 Wing Loading

The wing loading, as applied to a lifting body, is somewhat of a misnomer since the reference surface area is that of the body only. Volumetric efficiency is a more descriptive term for this type of reentry vehicle since total surface area is of greater interest than planform area. However, when considering the same vehicle at different gross weights, wing loading is an adequate basis for comparison.

Vehicle weight is of fundamental importance in design efforts since it relates directly to payload capability. Its effect on operational capability is also of primary interest and should be considered carefully during the mission planning stage.

In this study, a large variation in vehicle weight was made to illustrate the effect on the thermal protection system weight versus landing area trade-off as developed in the preceeding chapter. The wing loading was reduced from 50 psf to 25 psf with all other characteristics of the vehicle and the initial entry conditions remaining unchanged. It is not entirely realistic to use this vehicle configuration, i.e., 10 degree half cone at a wing loading as low as 25 psf since this loading borders on the region in which winged vehicles with equilibrium reradiation thermal protection systems are more desirable. However, a large variation provides a relatively wide range of information without the need for a highly detailed study and is adequate from a preliminary analysis viewpoint.

The representative set of optimized trajectories was used as before to generate the thermal protection system weight requirements, and the effect of wing loading on various parameters was determined. Figs. 52 through 59 and Table 8 contain these results.

129

Since changing the weight of the vehicle does not alter its aerodynamic characteristics and since the initial entry conditions are unchanged, the footprint and the associated trajectory control parameters do not change. This is the same effect which occurs when gliding an aircraft at various gross weights. The range is a function of L/D only and, if L/D is kept constant, the only variation is that the heavier aircraft flys to the same range at a higher airspeed with a shorter time of flight.

This phenomenon has no serious disadvantage for the heavier aircraft but, when considering a reentry vehicle, a new and important factor is introduced. This factor is aerodynamic heating and, since velocity and time of flight directly influence total heating, the thermal protection system weights will vary considerably as the velocity and time of flight change for a variation in vehicle weight. Generally speaking, the thermal protection weight requirement increases as the vehicle weight increases.

Total stagnation heating at each wing loading is shown in Fig. 52 for a series of trajectories. A definite reduction in this factor is seen for lighter wing loadings. The same result also occurs for the dynamic pressure as shown in Fig. 53.

As expected, the ablator weights for various sections of the body are also reduced uniformly as the wing loading is reduced. These results are shown in Figs. 54 through 57. It is interesting to note that the insulation requirement is greater for the lighter wing loadings but, when combined with ablator weight, the total thermal protection system weight is very close to that for higher wing loadings. This again indicates the danger in neglecting insulation when making spacecraft weight estimates.

130

The trajectories were expanded into a conformal map as before (Fig. 58) to indicate the weight tradeoff against increase in landing point area. The associated trajectory grid and the payload fraction are also included in this figure.

The increase in weight and decrease in payload fraction against area for each wing loading are shown in Fig. 59.

6.3 Variation of Nose Radius

The variation of nose thermal protection system (including insulation) weight and stagnation heating rate with change of nose radius were examined and the results are plotted in Fig. 60. It was assumed that the nose radius change did not effect the geometry of the remainder of the body nor the aerodynamics of the composite body. This resulted in the same heating rates and thermal protection system weights for the other sections of the body. Since the stagnation heating rate is a function of $1/\sqrt{R_N}$, it decreases with an increase in radius. The heating rate over the remainder of the nose is a function of the stagnation heating rate and the angular distance from the stagnation point, and, therefore, decreases with the increase in radius. The rate of ablation, and therefore, the total mass/ft^2 of ablator required, decreases with increased radius. However, the area to be protected increases by a greater amount, thus requiring a greater total weight of thermal protection for the nose as the radius is increased. For a representative trajectory as described in Chapter 5, doubling the nose radius to four feet results in a seven percent increase in total thermal system weight of the vehicle.

6.4 Variation of Thermal Protection Materials and Methods

After completing the analysis of various trajectories with Teflon
as the ablator material, a group of optimized trajectories, using Teflon,
resulting in ranges from 2,000 to 12,000 N.M. was chosen to be analyzed
utilizing various other thermal protection materials. The ablation materials
chosen and their physical properties are listed in Table D-1. The effective
heats of ablation, of these materials, are shown in Fig. D-2. In addition
to those mentioned above, phenolic nylon was analyzed as a charring ablator
as outlined in Appendix D. The properties for this material are given in
Appendix D with the effective heat of ablation given by equation D-40. The
results are plotted in Fig. 61. The results show that phenolic nylon gives
the lowest weight for all ranges considered. This is because of its low
density, high surface temperature resulting in a large amount of re-radiation,
and the insulation effect of the char formed during ablation. The payload
fraction, which varies from 0.232 to 0.195, is better than that for Teflon
over the ranges considered.

A comparison between ablation and re-radiation protection was also
made. Several trajectories with low maximum stagnation heating and the same
ranges, approximately, as those used for the ablation analysis were chosen as
representative, and the thermal protection weight was determined using Teflon
ablation on the nose and leading edges and re-radiation protection over a
layer of insulation on the underside from 8 feet aft of the nose to the base of
the vehicle. The properties of the high temperature metals considered are
listed in Table D-2, and the properties of the insulation, which was low
density Q felt, are listed in Table D-1. The heating associated with the ranges
less than 5,500 N.M. permits use of René 41 nickel alloy protection shield over
Q felt insulation. Above these ranges, the maximum temperatures are above the

132

of René 41. Two refractory materials and one high temperature nickel
alloy were compared with the results shown in Fig. 62. The results show
that the lowest weight of metal re-radiation shielding is obtained by using
René 41 for ranges less than 5,500 N.M. and UDIMET 700 nickel alloy for
ranges up to 12,000 N.M.

The resulting weight comparision between all ablation and combination
ablation-radiation systems shows that the ablation system is lighter for the
lower ranges with the radiation protection system gaining the advantage at
high ranges over all but phenolic nylon. This is primarily due to the high
wing loading and medium L/D of this type of vehicle which places it in
the performance region between ballistic and glider. The radiation protection
scheme would easily become the lighest for a glider type vehicle with its
lower heating, longer time of flight and longer range. The vehicle used in
this analysis is just approaching this region at the high ranges where
the long time of flight increases the ablation and insulation requirements
making the ablation weight increase sharply.

6.5 Winged Vehicle Configuration

A complete thermal protection system weight analysis of the winged vehicle (or glider) was not attempted in this study, but general trajectory profile and heating trends for this type of vehicle can be inferred from the results obtained from the lifting body analysis. For example, the same L/D capability, range and footprint area could also be obtained with a winged glider type vehicle. However, a winged vehicle has a lower volumetric efficiency than the lifting body vehicle due to the large amount of unusable space in the wings. In order to obtain the same usable volume for passenger and storage space, the winged vehicle has to be larger than the lifting body configuration examined. This larger vehicle has a greater gross weight due to the structural weight requirements of the wings. The winged vehicle has a higher maximum lift coefficient and is able to fly a lower heating trajectory, thus allowing a radiation cooling scheme.

Due to its compactness, the entire lifting body must be protected so that the internal temperatures are kept low to protect the passengers and temperature sensitive cargo and equipment. This imposes a larger insulation weight requirement on the lifting body. On the winged vehicle, such components as wings, fins and controls, which compose a large percentage of the surface area, could operate at higher internal temperatures limited only by material strength degradation considerations, thus limiting the insulation requirements to the area around the passenger and storage areas. Ablation protection would be required only in the immediate vicinity of the nose and possibly wing leading edges. The remainder of the vehicle could be cooled by radiation.

A complete analysis of this type of vehicle with various construction

schemes and materials would have to be made to determine exactly how the weight of such a vehicle would compare with the lifting body with the same operational capability.
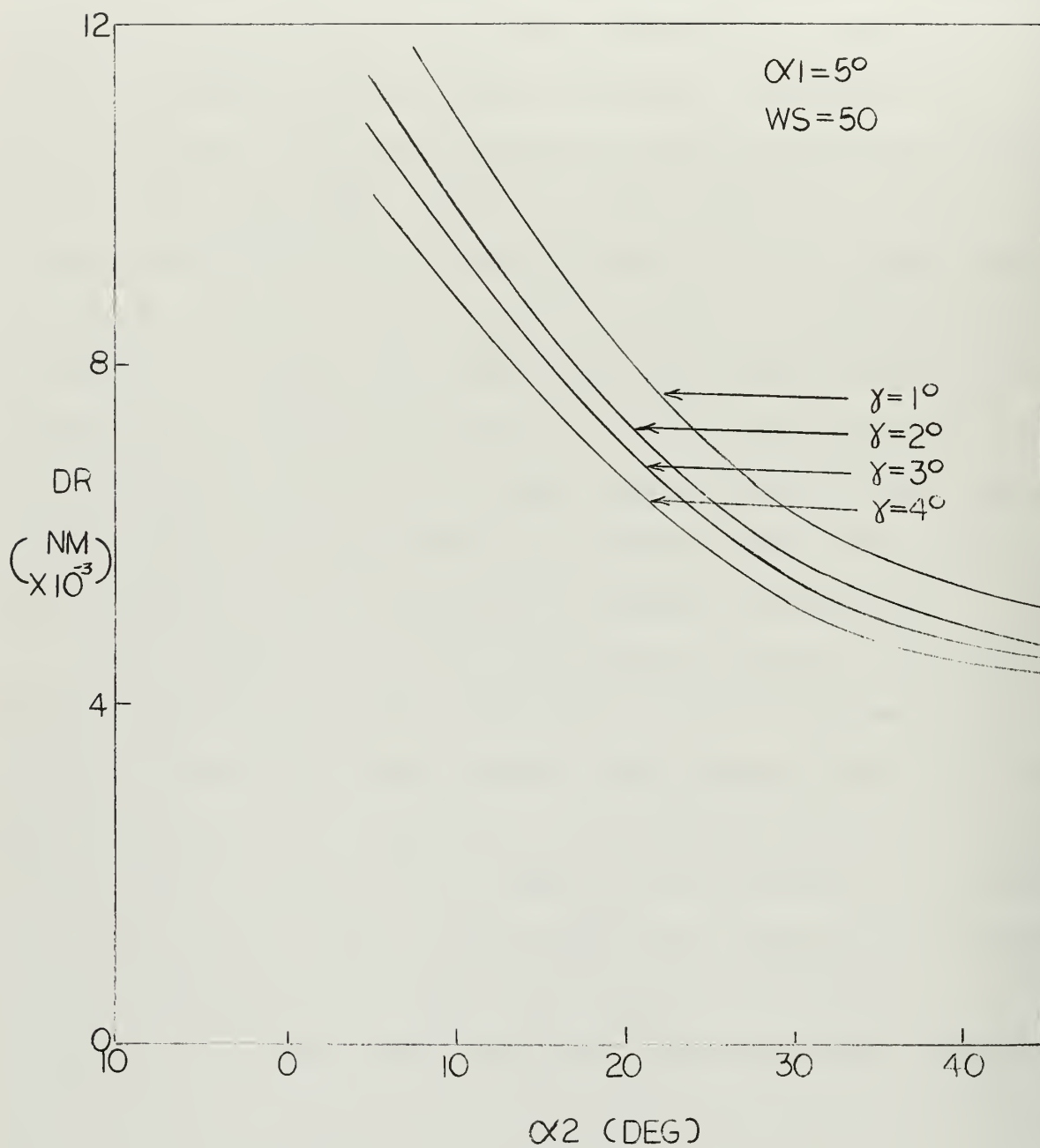
Fig. 46   Variation of Down Range with α2   (Variable Entry Angle)

136
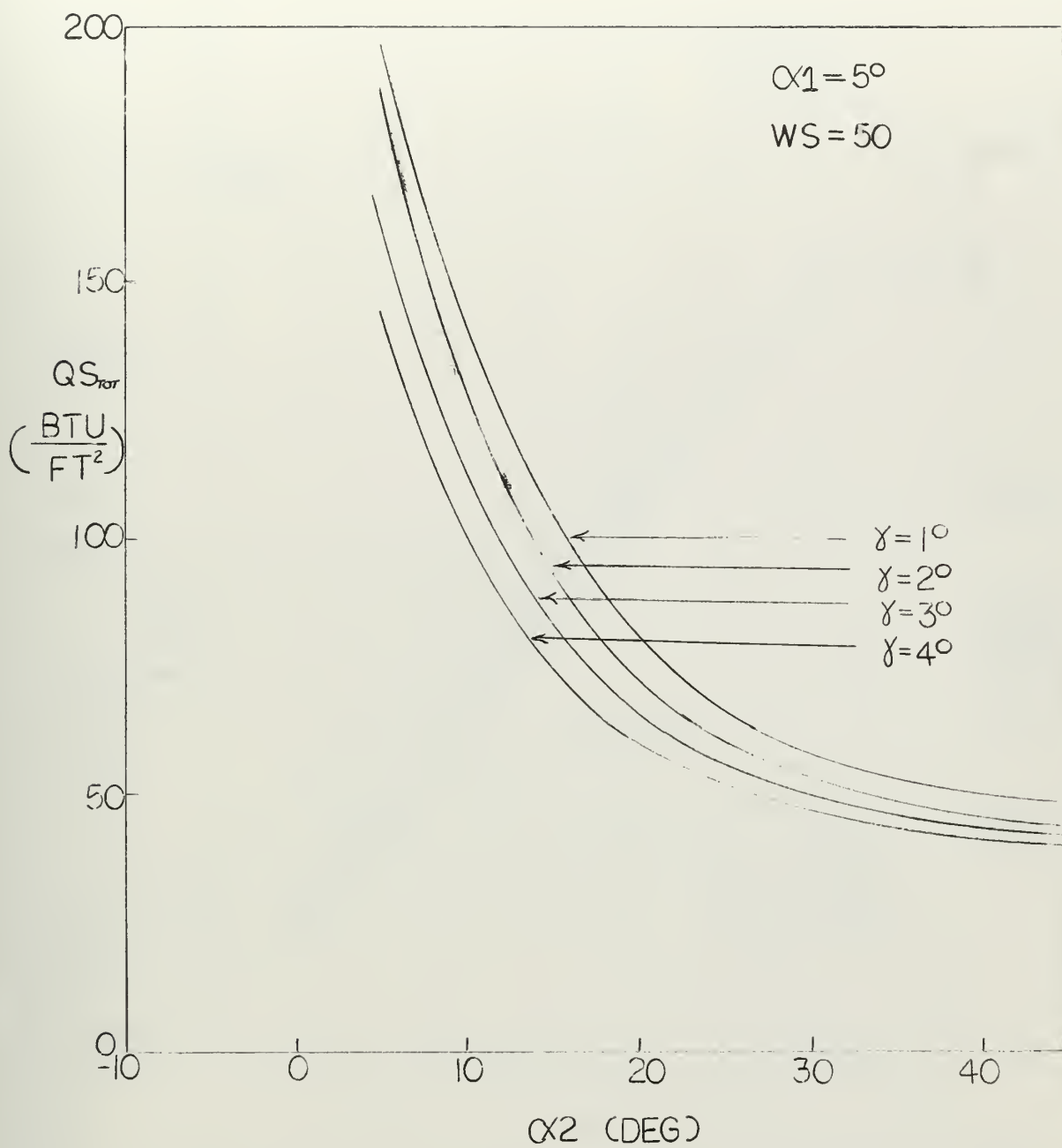
Fig. 47 Variation of Total Stagnation Heating with α2 (Variable
Entry Angle)

137
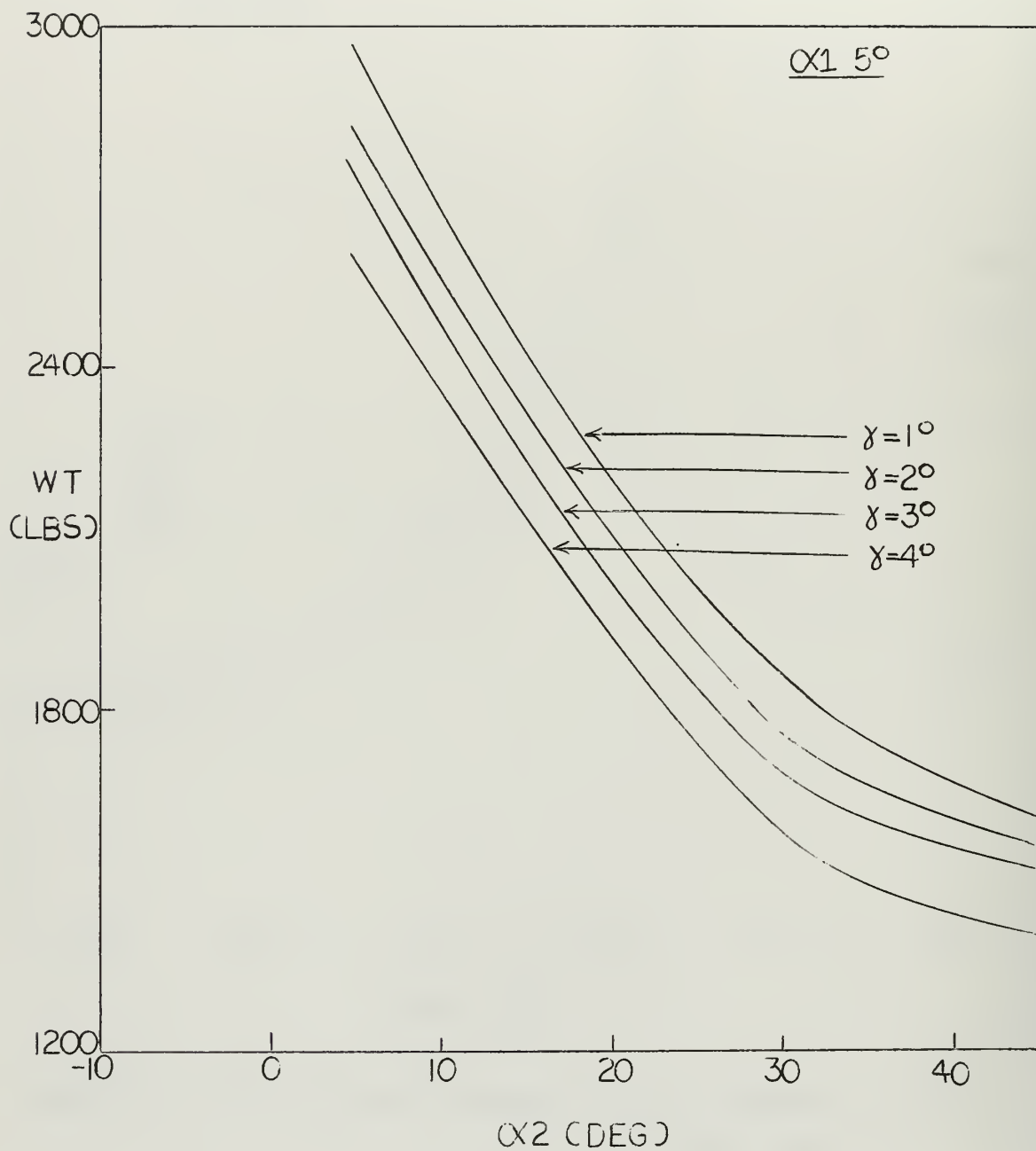
Fig. 48 Variation of Thermal Protection System Weight with α2
(Variable Entry Angle)
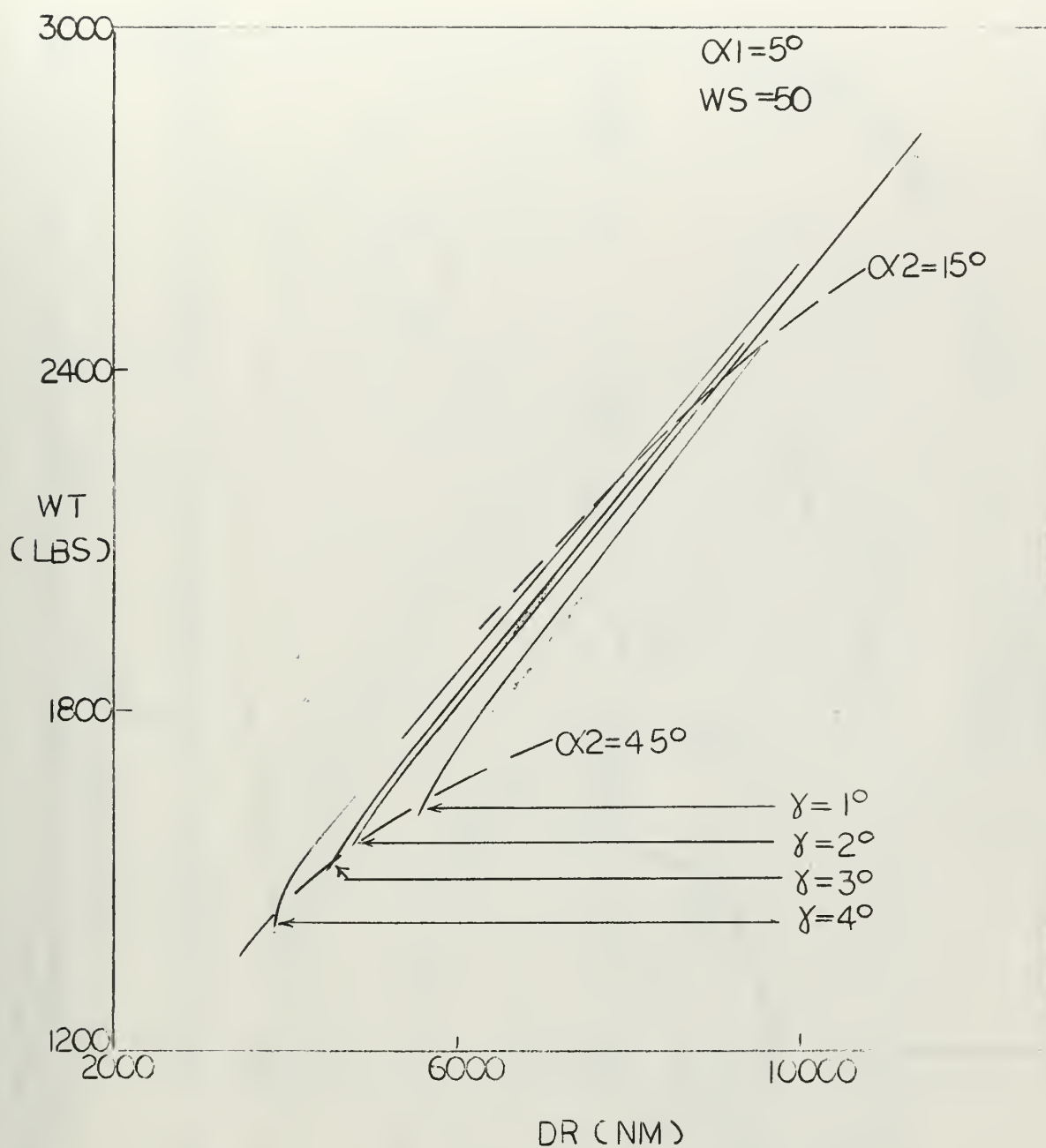
Fig. 49   Variation of Thermal Protection System Weight with Down
Range (Variable Entry Angle)

139
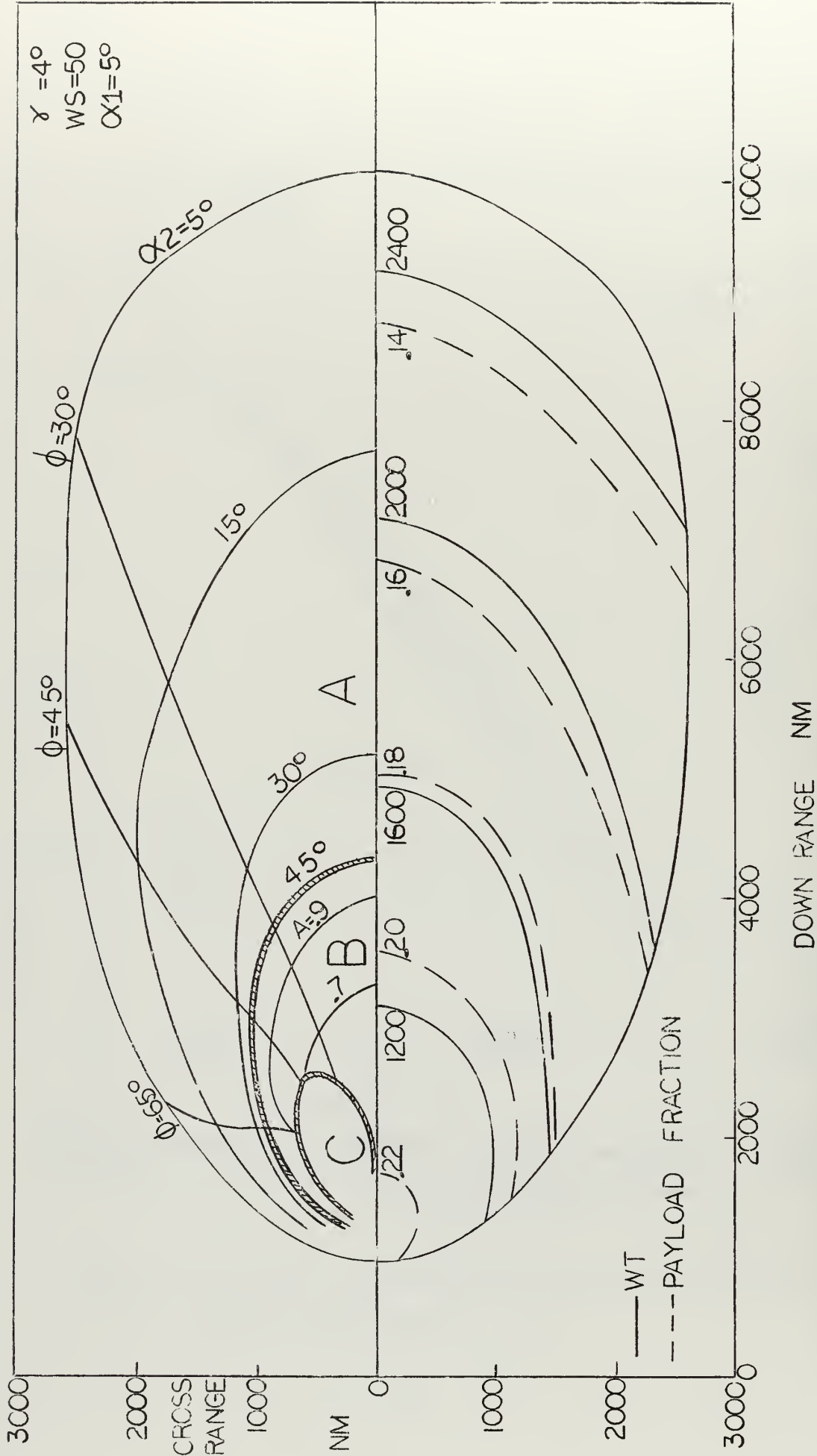
Fig. 50 Trajectory Control Parameters and Variation of Thermal Protection System Weight and Payload Fraction with Landing Point
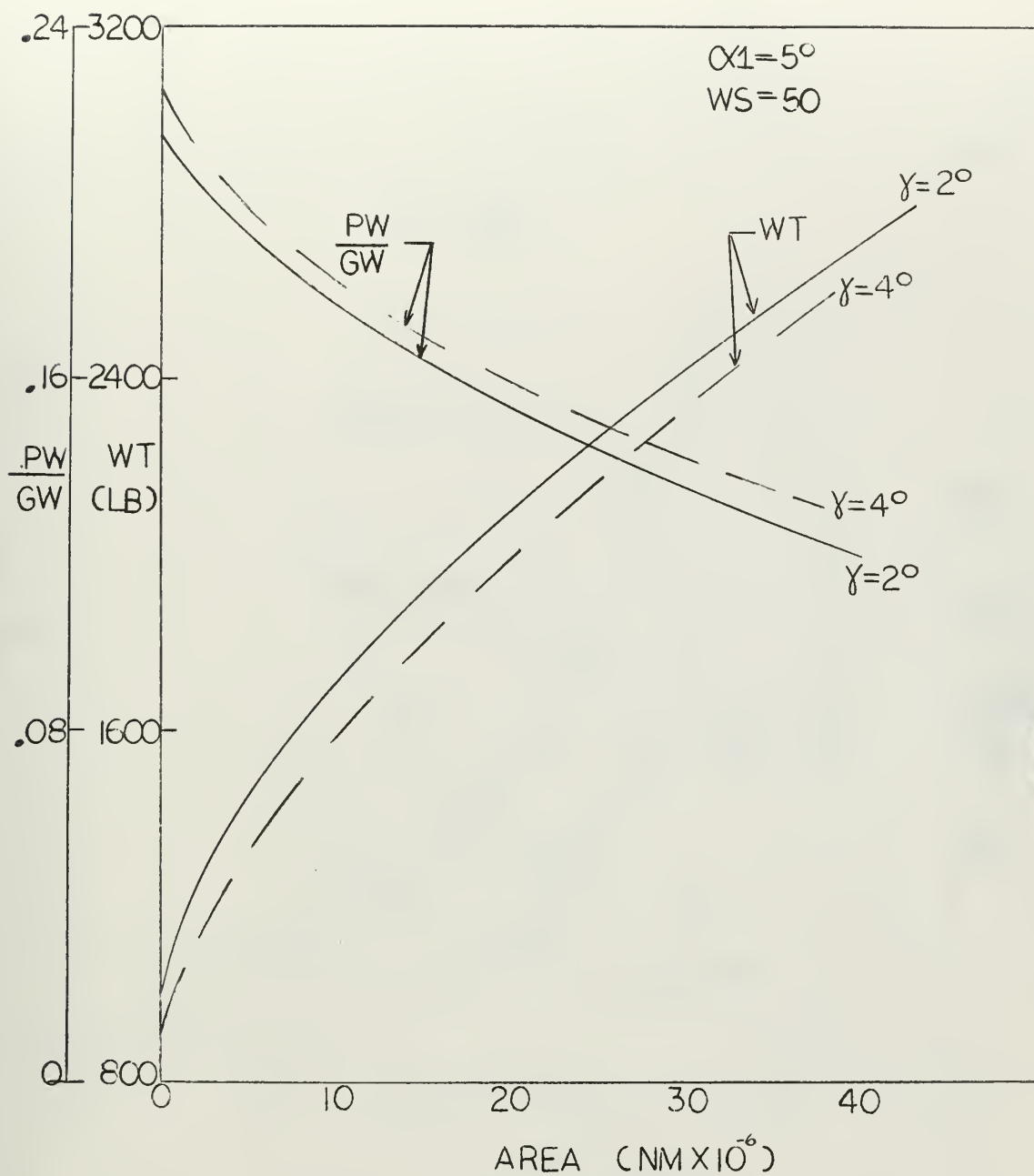
Fig. 51 Variation of Payload Fraction and Thermal Protection System Weight with Area (Variable Entry Angle)
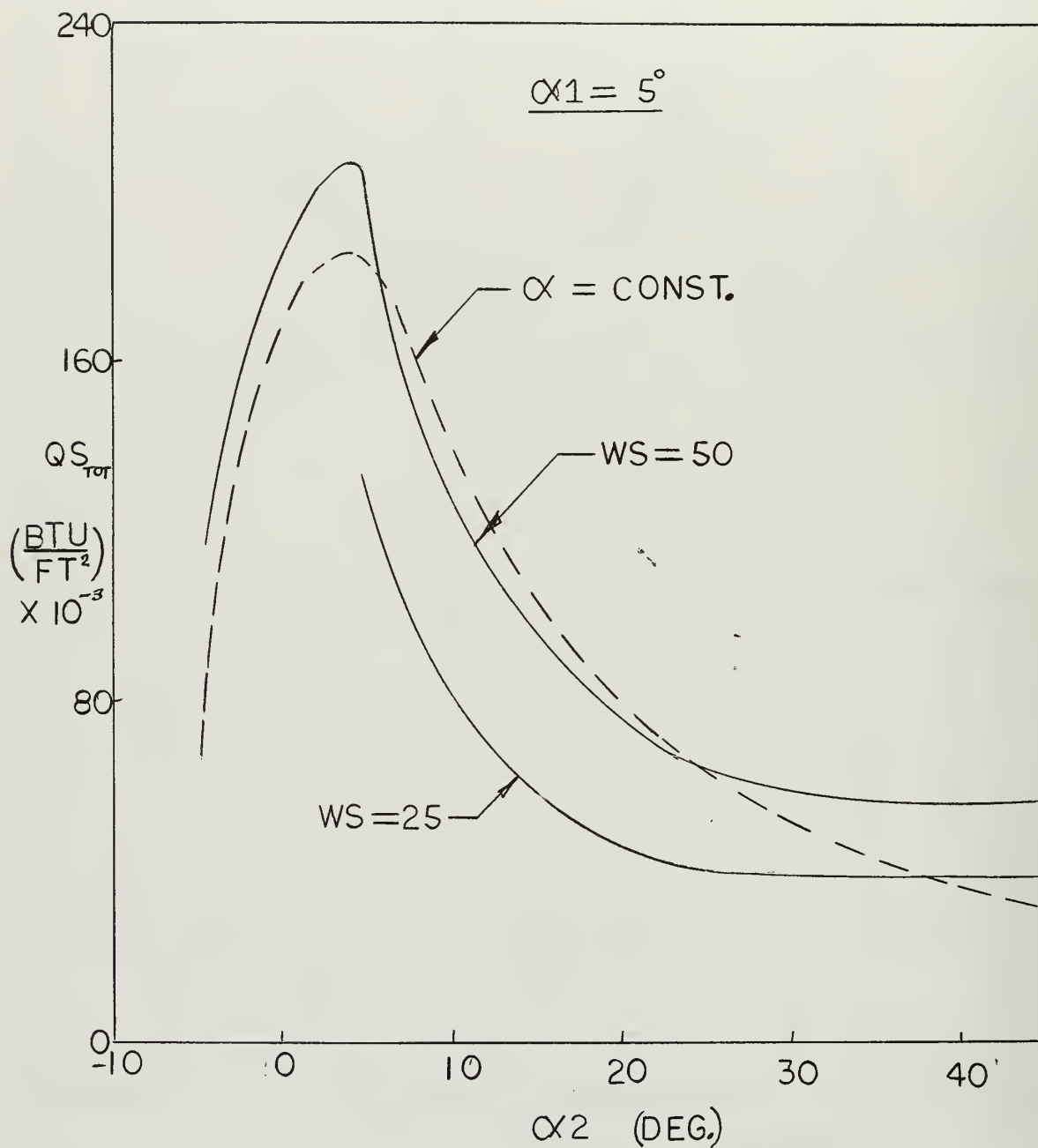
Fig. 52 Variation of Total Stagnation Heating with α2   (Variable
Wing Loading)
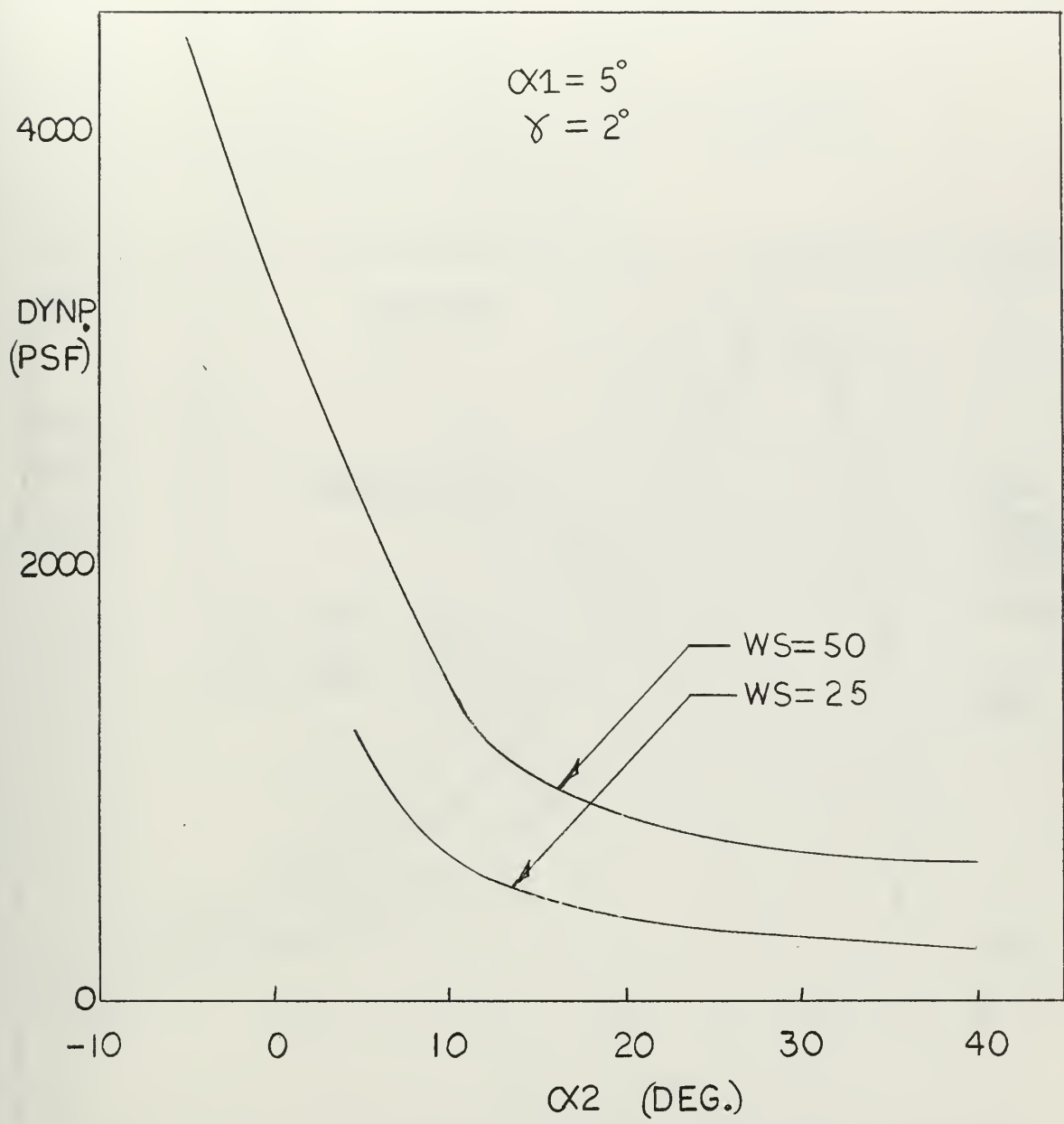
Fig. 53 Variation of Dynamic Pressure with α2 (Variable Wing
        Loading)

143
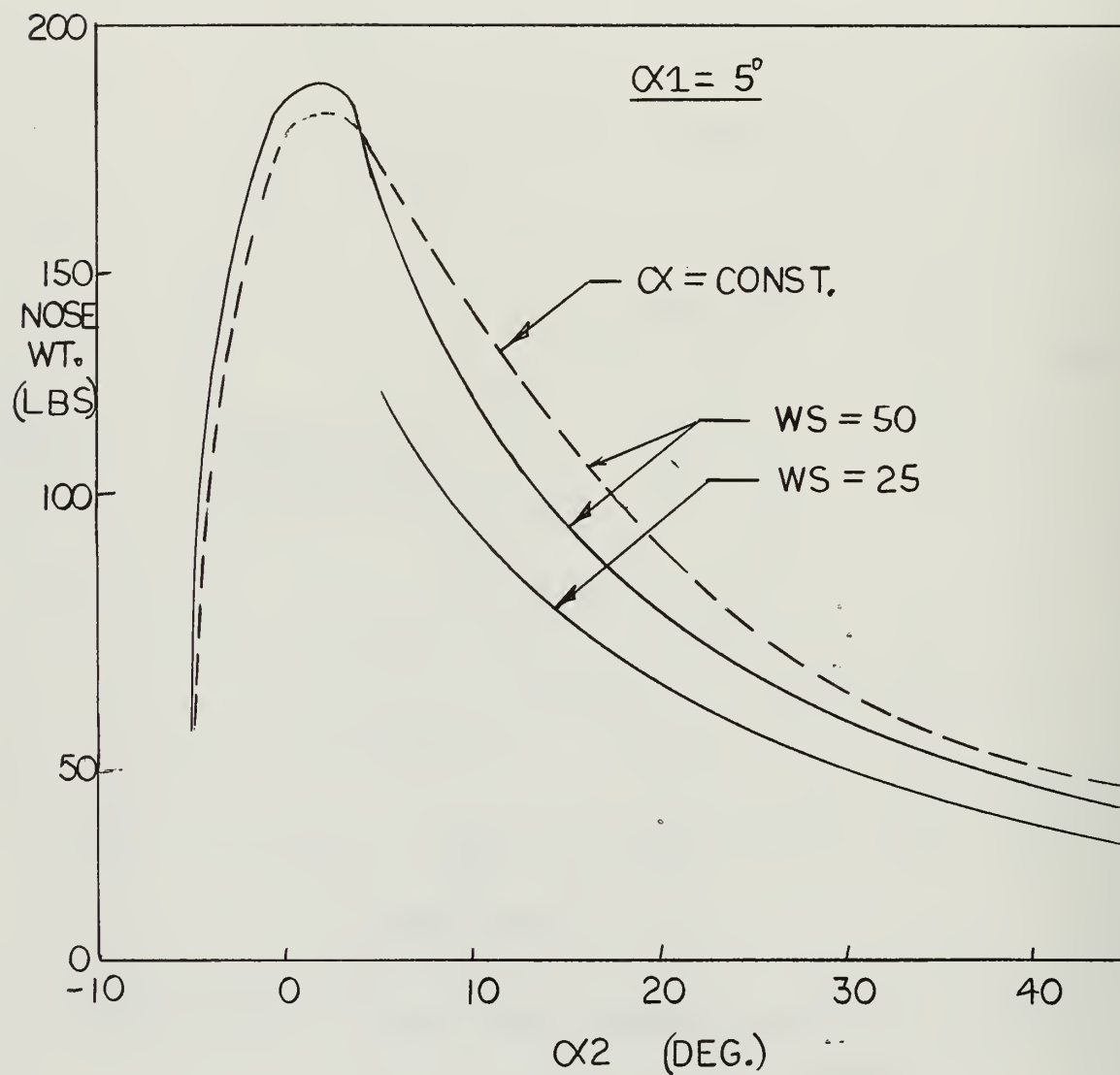
Fig. 54 Variation of Nose Ablator Weight with α2 (Variable Wing Loading)

Fig. 55 Variation of Body Ablator Weight with $\alpha2$ (Variable Wing Loading)
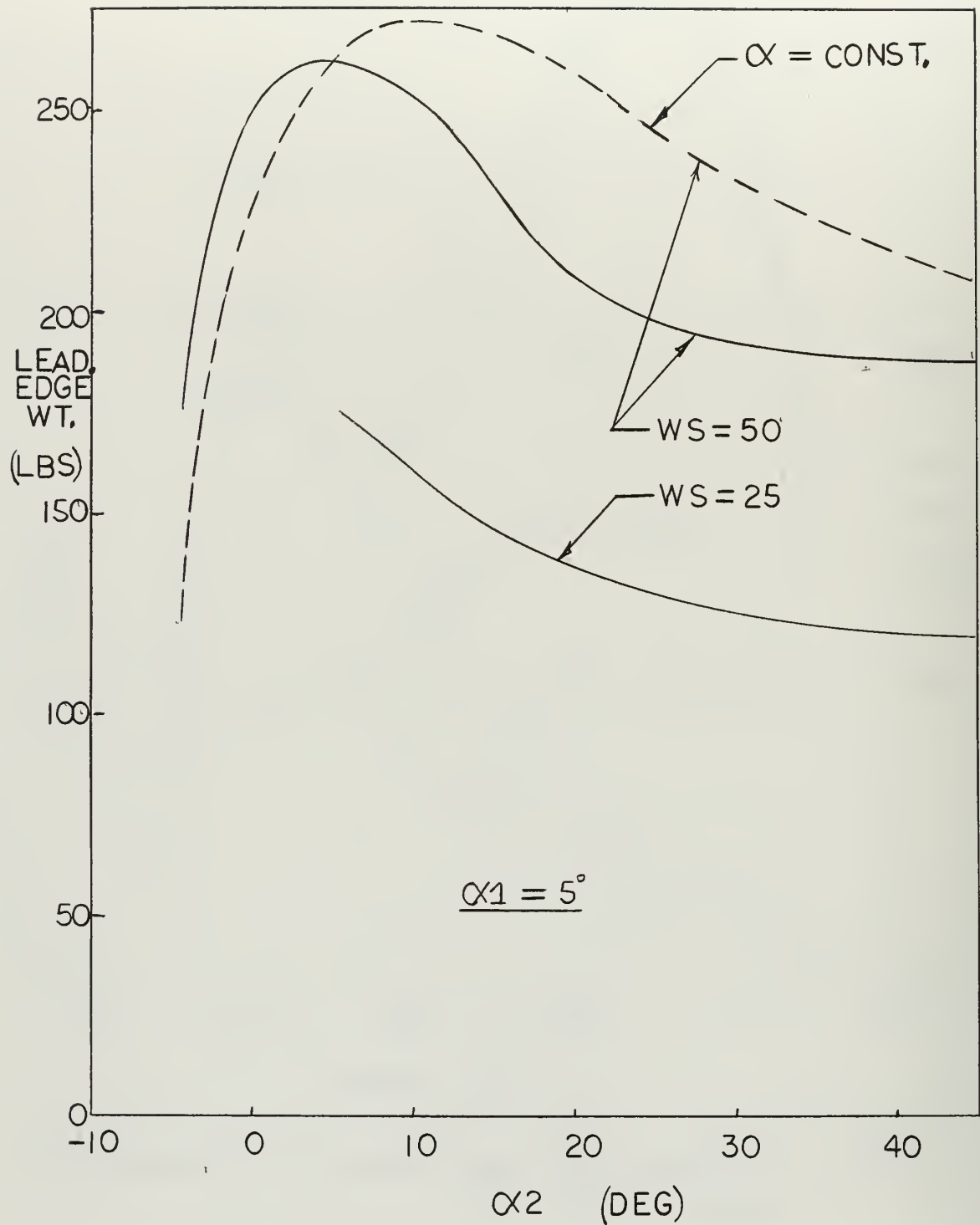
Fig. 56 Variation of Leading Edge Ablator Weight with α2
(Variable Wing Loading)
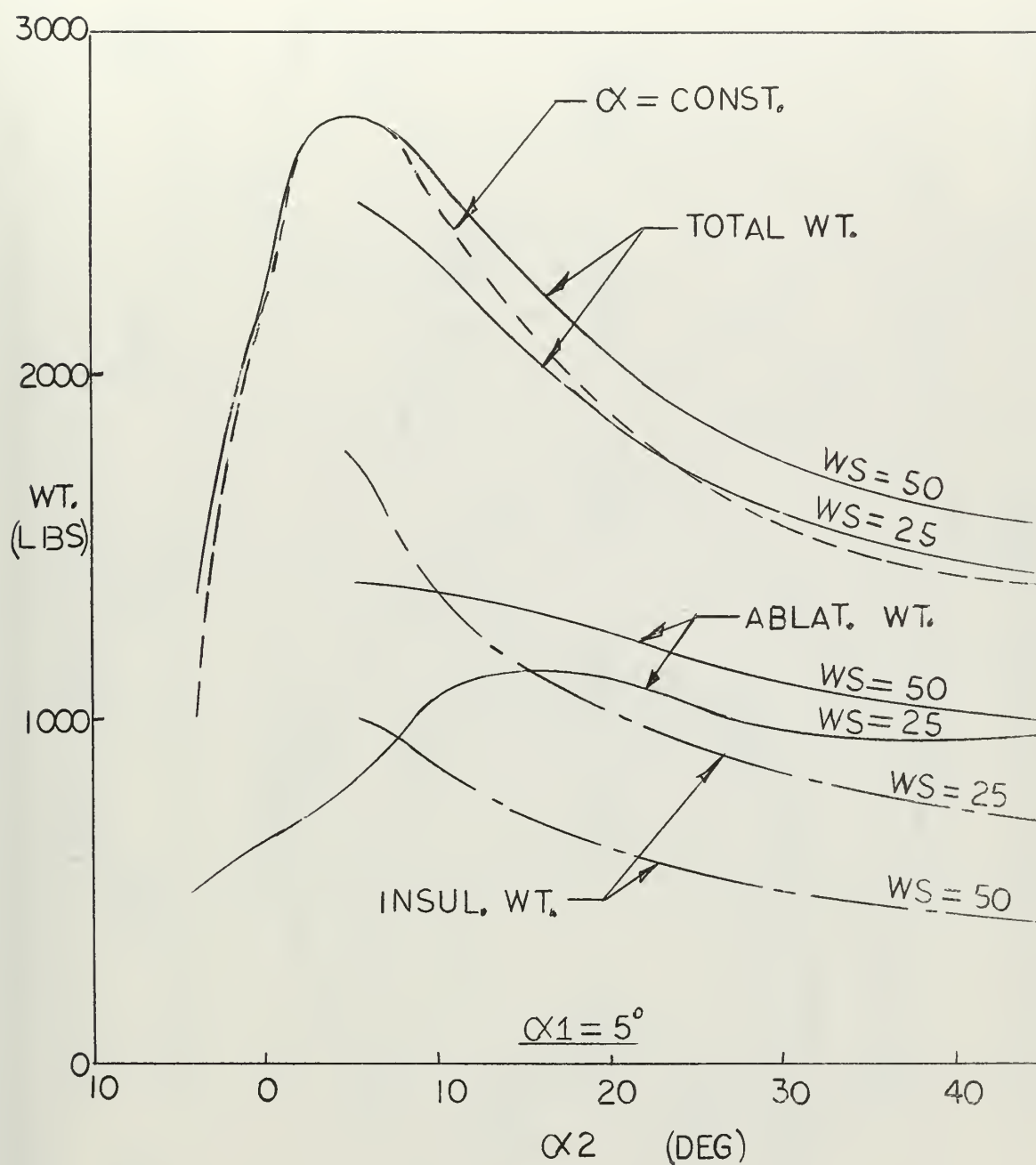
Fig. 57   Variation of Total Ablator, Insulation, and Thermal
Protection System Weight with α2   (Variable Wing Loading)

147
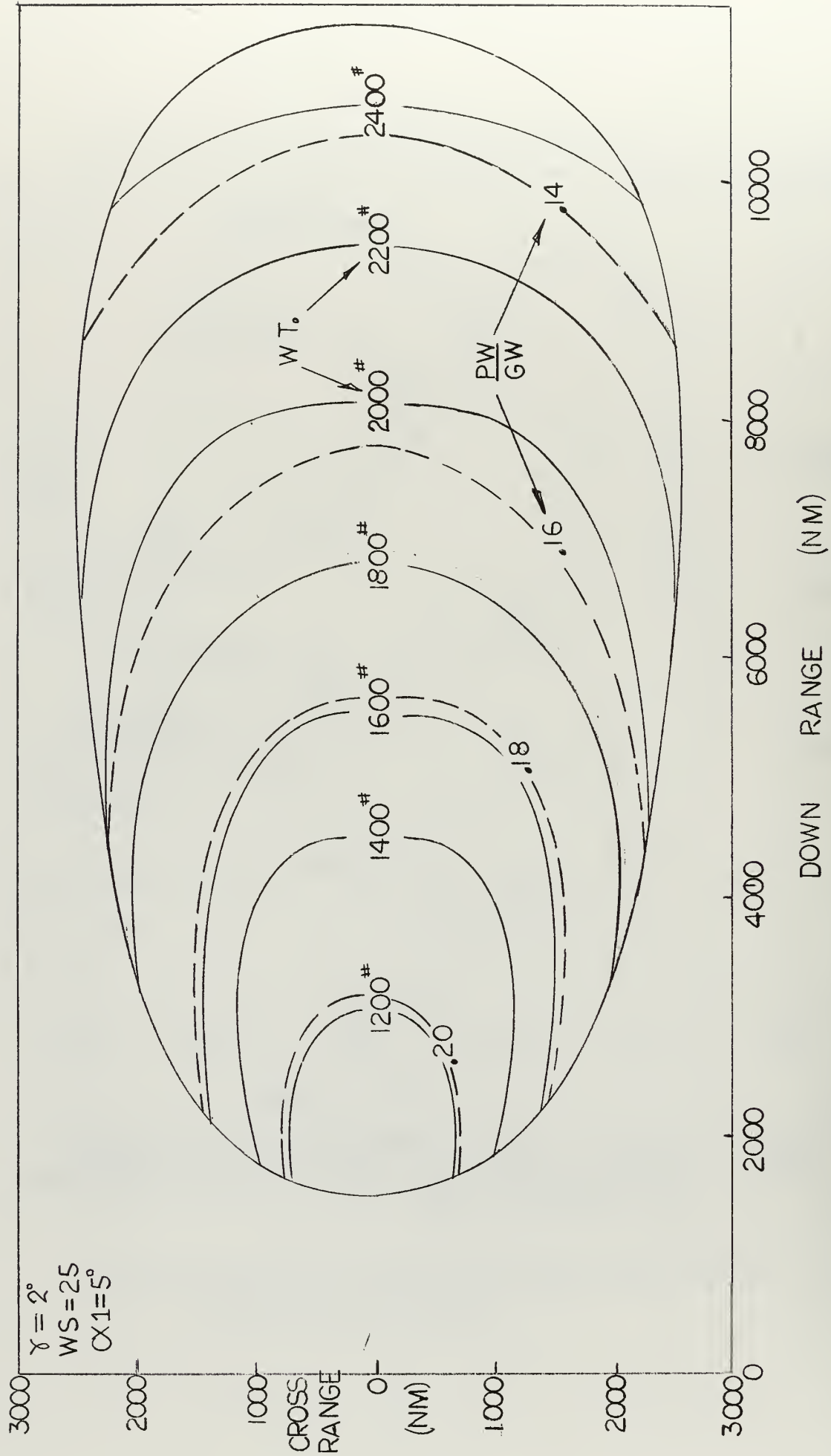
Fig. 58 Variation of Thermal Protection System Weight and Payload Fraction with Landing Points
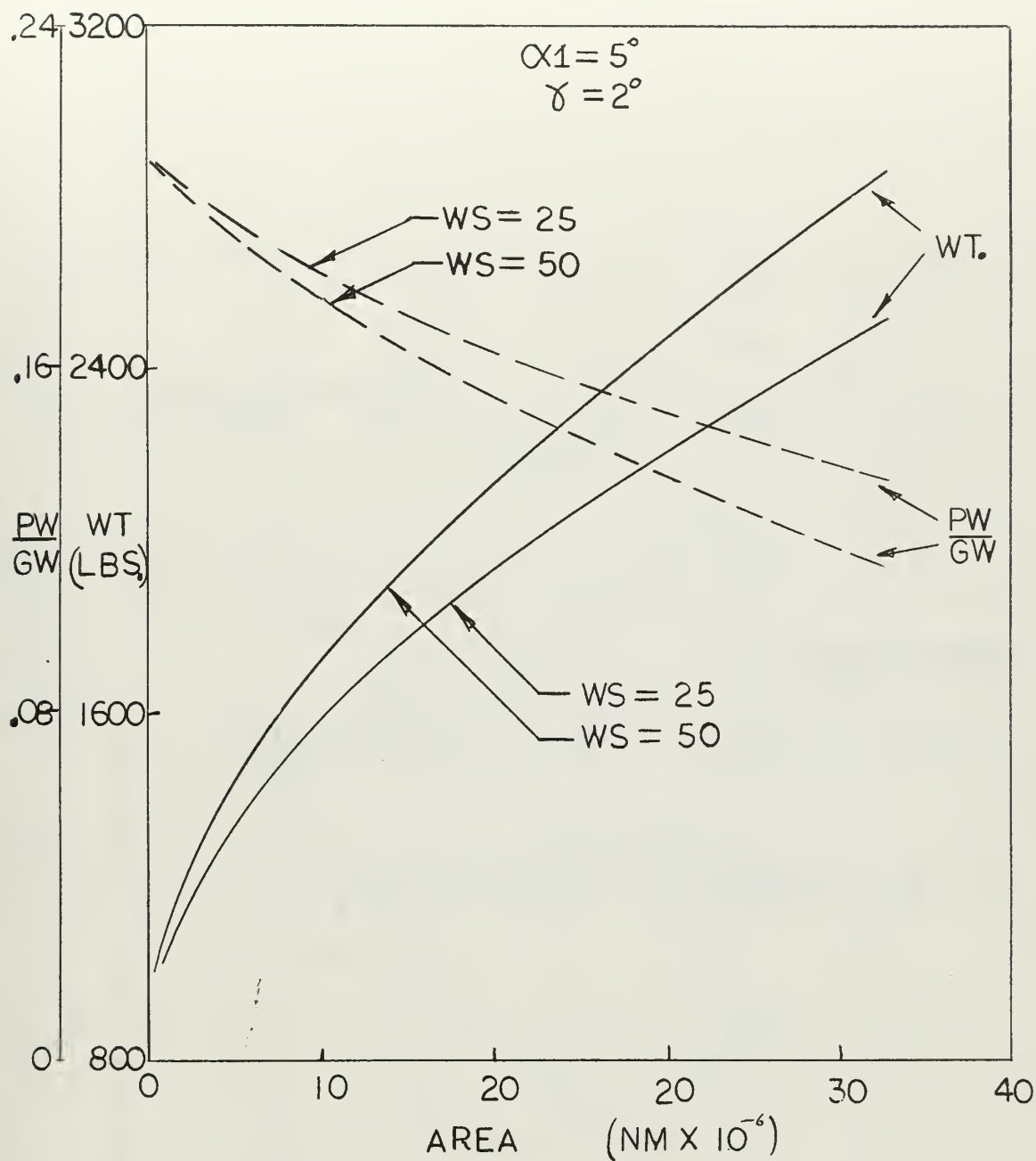
Fig. 59 Variation of Thermal Protection System Weight and Payload Fraction
with Area (Variable Wing Loading)

149
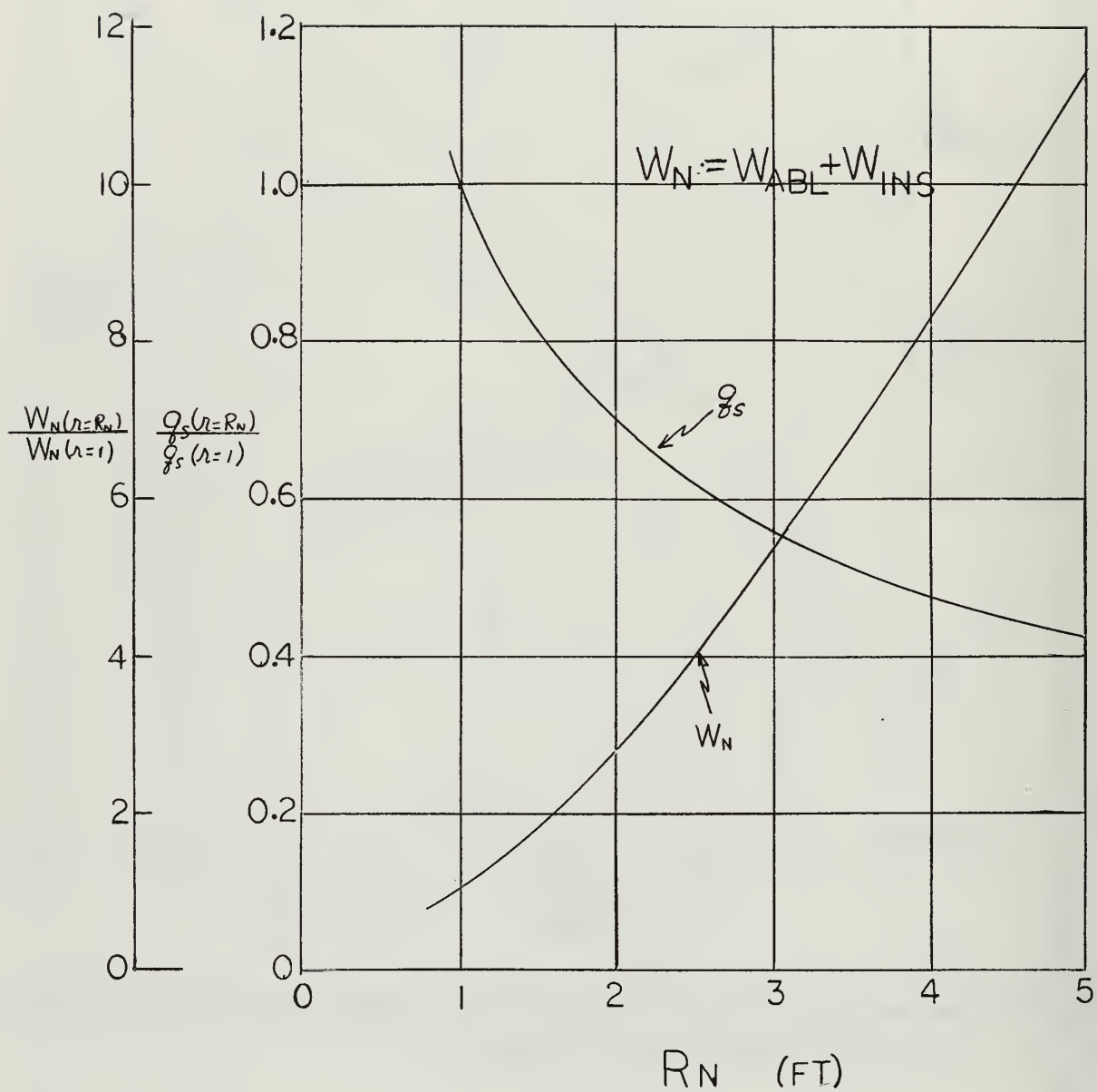
Fig. 60   Variation of Nose Thermal Protection Weight and Stagnation
Heating Rate with Nose Radius

150
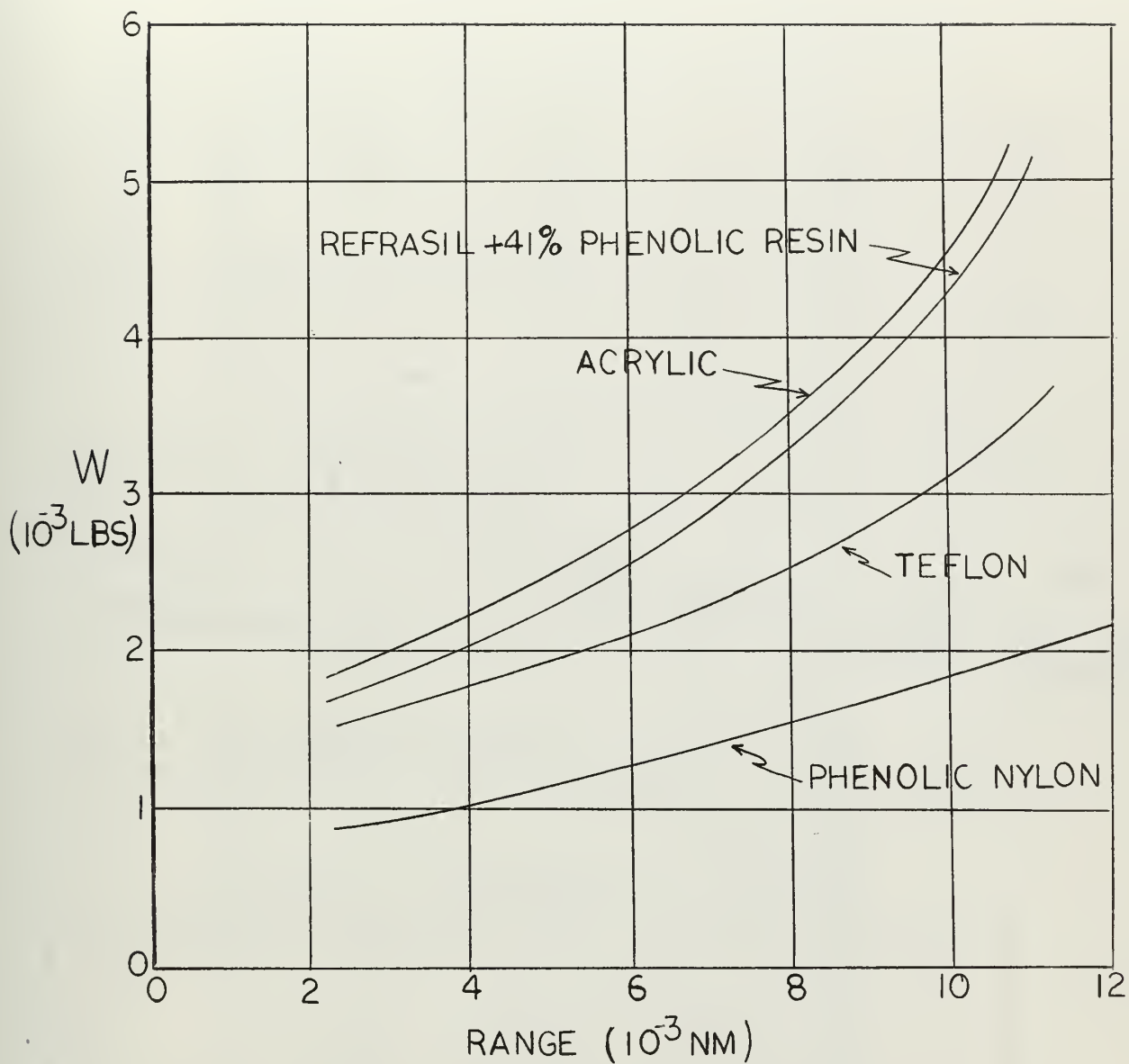
Fig. 61 Variation of Thermal Protection System Weight with Down Range
(Variable Ablation Material)

151
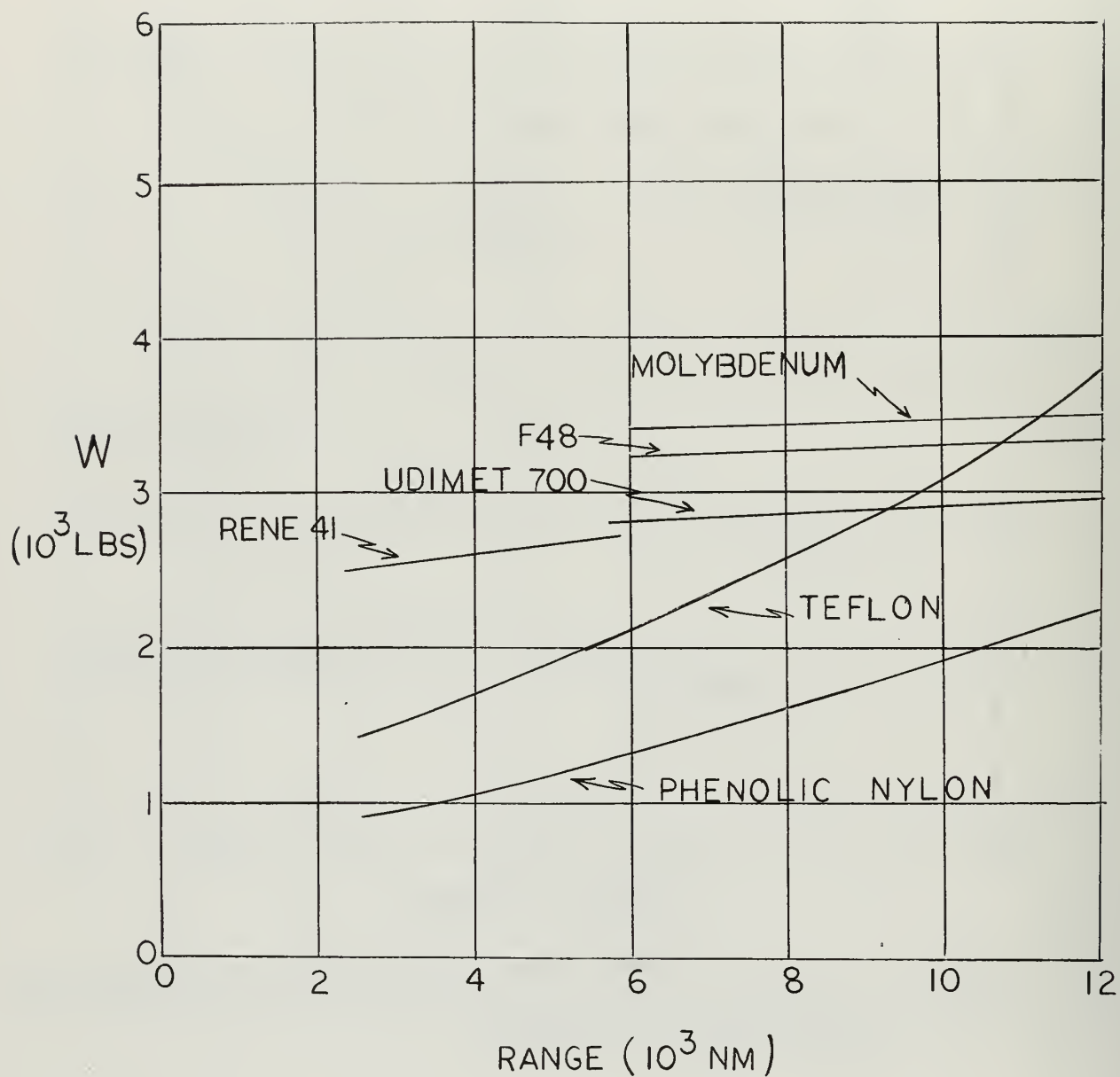
Fig. 62   Variation of Thermal Protection System Weight with Down Range
(Combination Ablation-Radiation Systems)

$$\frac{\alpha 2}{}$$

$(\gamma = 4°, \alpha 1 = 5°, WS = 50 \text{ PSF})$

	$\phi = 0°$, A = 1.0				$\phi = 30°$, A = 1.0			
	5°	15°	30°	45°	5°	15°	30°	45°
TF(SEC)	3666	2880	1808	1464	3152	2486	1616	1310
DR(NM)	10080	7717	5177	4388	7782	6115	4438	3886
CR(NM)	0	0	0	0	2430	1713	766	512
RPA_{max}	7.2	8.0	8.5	9.5	6.5	8.1	9.2	10.2
$DYNP_{max}$	3000	1500	1500	1500	2800	1700	1700	1700
$q_{s\ max}$	469	469	469	469	495	495	495	495
Q_{STOT}	145780	74453	47390	40012	144102	73993	46959	40049
W_N	144	83	53	42	145	82	52	41
W_B	1074	747	487	393	1047	737	472	386
W_{TOP}	0	0	0	0	0	0	0	0
W_{LE}	220	181	158	151	218	178	153	145
W_A	1437	1011	693	585	1410	998	677	572
W_I	1149	1137	958	887	1034	1031	898	831
W_{TOT}	2586	2148	1655	1473	2444	2029	1575	1403

TABLE 7

Lateral Range Capability ($\gamma = 4°$)

153

$$\frac{\alpha2}{}$$

$$(\gamma = 4°, \ \alpha1 = 5°, \ WS = 50 \ PSF)$$

| | $\phi = 65°$, A=1.0 | | | | $\phi=0°$ A=0.7 | $\phi=0°$ A=0.4 | $\phi=30°$ A=0.5 | $\phi=45°$ A=1.0 | $\phi=65°$ A=.905 |
	5°	15°	30°	45°	45°	45°	45°	5°	45°
TF(SEC)	1438	1188	882	798	1124	748	806	2548	742
DR(NM)	2359	2165	2070	2037	3363	2184	2303	5381	1899
CR(NM)	1723	1381	929	788	0	0	236	2577	708
RPA_{max}	7.5	11.3	11.2	11.4	10.8	11.3	11.5	6.0	11.5
$DYNP_{max}$	3100	3100	3100	3100	2000	3300	3100	2500	3400
q_s max	632	627	627	627	531	642	627	530	650
Q_{STOT}	120334	66990	49298	45872	41625	46185	45282	141258	46406
W_N	130	75	51	43	42	44	43	146	44
W_B	939	652	466	427	386	432	421	1029	434
W_{TOP}	0	0	0	0	0	0	0	0	0
W_{LE}	200	159	133	126	140	126	125	218	125
W_A	1269	887	650	596	568	601	589	1393	603
W_I	603	626	595	576	752	546	583	876	542
W_{TOT}	1872	1513	1245	1171	1319	1147	1172	2270	1145

TABLE 7 (Continued)

Lateral Range Capability ($\gamma = 4°$)

154

	α2 ($\gamma = 2°$, $\alpha 1 = 5°$, WS = 25 PSF)							
	5°	$\phi=0°$, 15°	A=1.0 30°	45°	5°	$\phi=30°$, 15°	A=1.0 30°	45°
TF(SEC)	4074	3178	1976	1580	3524	2754	1732	1408
DR(NM)	11493	8792	5657	4714	9086	7108	4894	4207
CR(NM)	0	0	0	0	2426	1697	692	425
RPA_{max}	5.4	5.3	5.0	5.9	4.9	4.9	5.3	6.3
$DYNP_{max}$	1100	450	320	320	1000	420	360	360
$q_{s\ max}$	237	225	225	225	240	238	238	238
Q_{STOT}	135386	66538	38281	31268	136618	66798	38605	31750
W_N	122	69	42	33	126	70	42	32
W_B	797	555	336	270	790	553	338	273
W_{TOP}	0	0	0	0	0	0	0	0
W_{LE}	179	149	130	129	181	149	128	121
W_A	1099	773	508	428	1097	772	508	426
W_I	1410	1329	1106	1006	1282	1214	1021	939
W_{TOT}	2508	2102	1614	1434	2379	1987	1530	1365

TABLE 8

Lateral Range Capability (WS = 25 PSF)

155

	$\alpha2$ ($\gamma = 2°$, $\alpha1 = 5°$, WS = 25 PSF)							
	5°	$\phi=60°$, 15°	A=1.0 30°	45°	$\phi=0°$ A=0.7 45°	$\phi=0°$ A=0.4 45°	$\phi=15°$ A=1.0 5°	$\phi=30°$ A=0.5 45°
TF(SEC)	2018	1632	1128	974	1224	724	3948	902
DR(NM)	4035	3518	2956	2783	3678	2124	10871	2651
CR(NM)	2096	1556	832	625	0	0	1502	187
RPA_{max}	3.9	6.1	7.1	7.9	7.0	8.4	5.3	8.2
$DYNP_{max}$	830	600	600	600	4400	970	1100	690
$q_{s\ max}$	295	295	295	295	260	354	235	312
Q_{STOT}	121116	60609	38862	34410	32349	38707	137028	35476
W_N	119	65	40	32	32	36	125	33
W_B	763	507	339	289	272	328	800	298
W_{TOP}	0	0	0	0	0	0	0	0
W_{LE}	178	139	114	107	115	108	181	105
W_A	1060	711	493	428	420	472	1106	436
W_I	869	888	784	744	865	593	1378	704
W_{TOT}	1930	1599	1277	1172	1284	1065	2484	1140

TABLE 8 (Continued 2)

Lateral Range Capability (WS = 25 PSF)

156

	$\phi=45°$ A=1.0	$\phi=60°$ A=.866	$\phi=75°$ A=1.0	$\phi=75°$ A=1.0
			$\alpha2$ ($\gamma = 2°$, $\alpha1 = 5°$, WS = 25 PSF)		

	$\phi=45°$ A=1.0	$\phi=60°$ A=.866	$\phi=75°$ A=1.0	$\phi=75°$ A=1.0
	45°	45°	5°	45°
TF(SEC)	2868	902	1050	670
DR(NM)	6579	2550	1917	1732
CR(NM)	2600	532	1103	579
RPA_{max}	4.1	8.2	5.5	8.1
$DYNP_{max}$	870	690	1200	1100
$q_{s\ max}$	259	312	370	370
Q_{STOT}	133749	35476	90120	38693
W_N	128	33	92	37
W_B	779	298	665	337
W_{TOP}	0	0	0	0
W_{LE}	186	105	142	108
W_A	1092	436	899	482
W_I	1115	704	560	558
W_{TOT}	2207	1140	1459	1039

TABLE 8 (Continued 3)

Lateral Range Capability (WS = 25 PSF)

157

CHAPTER 7

CONCLUSIONS

The constant angle of attack trajectories, which were used as a standard of comparison, increase in range as the angle of attack increases from ballistic to that for maximum L/D and then decrease as the angle of attack increases further. The maximum range is 11,532 NM for this vehicle.

The total stagnation heating increases primarily with time of flight and secondarily with heating rate, and the time of flight varies generally as a function of range. The peak value of total stagnation heating occurs at an angle of attack slightly less than that for L/D maximum and is about 194,000 BTU/ft^2.

The dynamic pressure, total stagnation heating and thermal protection system weight variations with range have two distinct branches. The branch which results from high angles of attack (those above L/D maximum) has uniformly better performance.

The individual component ablator weights are seen to be a function primarily of surface area and heating rate when angle of attack is held constant. The nose and leading edge have relatively low ablator requirements (5 and 12 percent) in comparison to the body. The insulation is a large part of the thermal protection system and can be as much as 50 percent of its total weight at high angles of attack.

Modulation of the angle of attack lowered the thermal protection system weight requirement approximately 14 percent in the mid ranges with

only a small improvement at the high ranges. The thermal protection system
weight, using this method, is found to increase approximately linearly with
range at a rate of 190 pounds per 1000 NM above ballistic requirements.

The modulation scheme of using a low angle of attack (that for L/D
maximum) through the large initial heat pulse and then using high angles of
attack to brake aerodynamically is a satisfactory first cut approximation
to a formal optimization technique.

Angle of attack modulation provides optimized trajectories between
the mid-longitudinal range and the maximum longitudinal range and this method
was employed to generate approximately 85 percent of the landing point footprint.

The variation of total stagnation heating with range using angle of
attack modulation shows improvement over constant angle of attack trajectories.
The reduction in heating is about 18 percent throughout most of the upper
ranges. The amount of reduction in total stagnation heating does not
necessarily indicate the amount of weight saving and a complete analysis
should be made to obtain reliable weight trends.

The addition of bank modulation to angle of attack modulation proved
to be advantageous in the lower ranges. This method was used to generate
approximately nine percent of the footprint area.

Although some of the combined bank and angle of attack modulation
trajectories resulted in higher weights for a given second phase angle of
attack, they proved to give lower weights when compared at the same range.
The addition of these optimized trajectories to the optimized angle of attack
modulation only trajectories provides a complete set of optimized trajectories
throughout the attainable range.

159

The total stagnation heating is found to increase as the bank modulation is increased. It is initially lower than the stagnation heating for constant angle of attack trajectories and then increases to values considerably higher than those for constant angle of attack as the amount of bank modulation increases. This occurs even though the total thermal protection system weight continues to decrease, which again indicates the unreliability of total stagnation heating as a guideline for thermal protection system weight.

As the optimized trajectories were expanded into a conformal map by introducing a nominal bank angle, the area of the resulting footprint was 42 million square NM and the maximum cross range was 2612 NM.

The thermal protection system weight varied from 990 pounds at the minimum range (ballistic) to 2810 pounds at the maximum range which is an increase of 183 percent. The payload fraction was reduced from .215 to .114 as the range increased from minimum to maximum.

The weight and payload fraction suffer a severe penalty as cross range increases with a particularly sharp gradient at the lower ranges.

Increasing the initial entry angle reduces the down range, total stagnation heating, and the thermal protection system weight for a given trajectory. The steeper entry angle reduces the attainable landing area coverage, but the thermal protection system weight required to reach a given landing point is essentially the same for the major portion of the footprint as with the nominal entry angle. For the portion of the footprint utilizing bank modulation, the steeper entry angle reduces the thermal protection system weight requirements.

160

The effect of lowering the wing loading while maintaining all other vehicle and initial conditions unchanged was to lower the ablator weight requirement for all components. Although the trajectory ranges were not affected appreciably, the vehicle experienced different velocity and density profiles with a resulting effect on convective heating and dynamic pressure.

The insulation weight at the lower wing loading increases due primarily to the increase in time of flight. This increase was not enough, however, to offset the reduction in ablator weight and the total thermal protection system weight was about 10 percent lower.

The payload fraction does not deteriorate as rapidly for the lower wing loading. The degradation in this parameter is from .221 to .131 at a wing loading of 25 psf and the rate of reduction, which is approximately linear, is about .00138 per million square NM.

An examination of the effect of varying nose radius indicated that the stagnation heating rate decreased as the nose radius increased. The total weight of protection required for the nose, which includes both ablator and insulator, increased due to the increasing area to be protected even though the heating rate and therefore the ablation rate decreased. For example, doubling the nose radius from one to two feet reduces the stagnation heating rate by 29 percent and increases the weight required by 184 percent.

The results of comparing various ablation materials showed that phenolic nylon gives the lowest overall protection system weight over the attainable ranges. An analysis of several low maximum heating rate trajectories utilizing re-radiation cooling on the bottom was made with the result that the radiative-ablation combination is heavier for lower ranges but, above approximately 10,000 miles gives the weight advantage over all the ablators considered except phenolic nylon.

161

The two phase angle of attack modulation procedure developed in this thesis is a satisfactory engineering approximation to the continuous modulation program which results from a formal optimization procedure.

There are several areas of interest in this thesis which are felt to be of sufficient importance to warrant further investigation. These are:

a) A detailed analysis of thermal protection system weights and ranging capability of a low wing loading, glider type reentry vehicle. The hypothetical reduction in wing loading presented in Chapter 6 should be refined to include changes in weight, body shape, and aerodynamic characteristics.

b) Further examination of the two phase angle of attack modulation technique with respect to the time of initiation of Phase II. Several trajectories were noted to have higher stagantion heating rates in later oscillation after the first pull up, and these may serve as motivation for delaying the initiation of Phase II.

c) A formal optimization procedure whereby the thermal protection system weight is minimized rather than the total stagnation heating. A parallel development would be to examine the correlation between total body heating and thermal protection system weight, and the minimization of total body heating (using formal optimization techniques).

d) A comprehensive systems analysis to examine the tradeoffs between weight of equipment required to implement various modulation techniques and the thermal protection system weight reduction realized.

162

REFERENCES

1. Burns, Neal M., "Biologistic Tasks for Rendezvous Vehicles," <u>Advances in the Astronautical Sciences</u>, <u>16</u>, American Astronautical Society (1963).

2. Syvertson, C. A., et. al., "Sone Considerations of the Performance of a Maneuverable, Lifting Body, Entry Vehicle," <u>Advances in the Astronautical Sciences</u>, <u>16</u>, American Astronautical Society (1963).

3. Lees, L., et. al., "The Use of Aerodynamic Lift During Entry into the Earth's Atmosphere,"ARS Paper 785-59.

4. Corning, G., <u>Aerospace Vehicle Design</u>, Braun-Brumfield, Inc. (1964).

5. Truitt, R. W., <u>Hypersonic Aerodynamics</u>, Ronald Press (1959).

6. Cherni, G. G., <u>Introduction to Hypersonic Flow</u>, Academic Press (1961).

7. Wells, W. R. and Armstrong, W. O.,"Tables of Aerodynamic Coefficients Obtained from Developed Newtonian Expressions for Complete and Partial Conic and Spheric Bodies at Combined Angles of Attack and Sideslip with some Comparisons with Hypersonic Experimental Data," NASA TR R-127.

8. Hankey, Wilbur L., et. al., "Design Procedures for Computing Aerodynamic Heating at Hypersonic Speeds," WADC TR 59-610.

9. Adler, Barry K., "A Comparison of Lifting Reentry Vehicles with a Given Payload," Masters Thesis, Massachusetts Institute of Technology, Course XVI, (Aug. 1964).

10. Kelly, Donald L., "Reusable Aerospace Transports," Lockheed Horizons, Issue 4, First Quarter (1966).

11. Konecci, E. B., "Manned Space Cabin Systems," <u>Advances in Space Science</u>, <u>1</u>, Academic Press (1959).

12. Duncan, Robert C., <u>Dynamics of Atmospheric Entry</u>, McGraw-Hill Book Company, Inc. (1962).

13. Hanshaw, Charles E., et. al., "Study of Structural Requirements of Reentry from Outer Space," WADD TR 60-886.

14. Webb., P., "Permissable Heat Transfer Rates for Man During Reentry," ARS Journal, <u>32</u>, 7, 1093-1094 (July, 1962).

15. Eggleston, J. M. and Cheatham, D. C., "Piloted Entries into the Earth's Atmosphere," IAS Paper 59-98.

16. Webber, A. L., "Investigation of the Instrumentation of an Atmospheric Reentry," M.I.T. Instrumentation Lab. Rept. T-218 (Sept, 1959).

17. Danielson, Oliver F., "Materials for Manned Space Flight," AIAA/ASME Seventh Structures and Materials Conference, Cocoa Beach, Florida (April 18-20, 1966).

18. Meltzer, J., et. al., "Structure and Materials Aspects of the PRIME Flight Test Vehicle," AIAA/ASME Seventh Structures and Materials Conference, Cocoa Beach, Florida (April 18-20, 1966).

19. Mathauser, E. E., "Research, Design Considerations, and Technological Problems of Structures for Winged Aerospace Vehicles," Proceedings of NASA University Conference on the Science and Technology of Space Exploration, NASA SP-11, 1 (1-3 November 1962).

20. AF Flight Dynamics Laboratory, "Flight Vehicle Structural Design Criteria, Recovery Phase," ASD-TDR-63-453.

21. Rute, L., "A Study of Aerodynamic Effects of Isothermal and Temperature Gradient Atmospheres on Reentry Trajectories," Polytechnic Institute of Brooklyn, PIBAL Report No. 738, AFOSR 2411 (March 1962).

22. Anonymous, "Military Standard: Climatic Extremes for Military Equipment," MIL-STD-210A (30 November 1958).

23. "Nickel Base Alloys," International Nickel Company, Inc. Phamphlet, Revised Edition (1964).

24. Hermann, Rudolf, "Evaporation Film Cooling at Hypersonic Velocities for Reentry Vehicles," Proceedings of Sixth Symposium on Ballistic Missile and Aerospace Technology, Academic Press (1961).

25. Georgiev, S., et. al., "On Ablating Heat Shields for Satellite Recovery," AVCO Research Rept. 65 (July 1959).

26. Lafazan, S., and Welch, W., "The Charring Ablation Concept; Application to Lifting Orbital and Sub-Orbital Entry," Dynamics of Manned Lifting Planetary Entry, John Wiley & Sons (1963).

27. Yoler, Y. A., "Dyna-Soar, A Review of the Technology," Aerospace Engineering, 20, 8 (August 1961).

28. Bryson, Arthur E., et. al., "Determination of Lift or Drag Programs to Minimize Reentry Heating," Journal of the Aerospace Sciences, 29, 4 (April 1962).

29. Brekka, Lawrence T., "Control and Heat Shield Requirements for Bank-Modulated Supercircular Entry," Engineers Thesis, Massachusetts Institute of Technology, Course XVI, Rept. No. T-403 (February 1965).

30. Baradell, D. L.,"Lateral Range Control by Banking During Initial Phases of Supercircular Reentries," NASA TN D-1511 (November 1962).

31. Lecat, R.,"Grumman Project 330, Aerodynamic Design Evolution of a Lifting Reentry Vehicle - GRV-1, Vol. 1, Design Evolution," Grumman Aircraft Engineering Corp. Rept. PDR 330-00-3 (December 1962).

32. Minzner, R. A. and Ripley, W. S., "The ARDC Model Atmosphere, 1956," Air Force Surveys in Geophysics 86, ARDC (December 1956).

33. Sterne, T. E., et. al., "An Interin Model Atmosphere Fitted to Preliminary Densities Inferred from USSR Satellites," Smithsoniam Contrib. to Astrophysics, 2 (No. 10),"Orbital Data and Preliminary Analyses of Satellites 1957 Alpha and 1957 Beta," (1958).

34. Koelle, Handbook of Astronautical Engineering, McGraw Hill (1961).

35. Baker, R.M.L., Jr. and Makemson, M. W., "An Introduction to Astrodynamics," Academic Press (1960).

36. Clawson, James F., "Thermal Correlation of Heat Protection Systems," AFFDL-TR-65-167.

37. Tietz, T. E. and Wilson, J. W., "Mechanical, Oxidation, and Thermal Property Data for Seven Refractory Metals and Their Alloys," Lockheed Missiles and Space Div., Code 2-36-61-1 (15 September 1961).

38. Wilson, R. Gale (Compiler), "Thermophysical Properties of Six Charring Ablators from $140°K$ to $700°K$ and Two Chars from $800°K$ to $3000°K$," NASA TN D-2991 (October 1965).

39. Love, John A. and Neustadt, L. W., "Derivation of Three Dimensional Trajectory Equations for a Lifting Reentry Vehicle," Space Technology Lab. Rept. 7431.1-107 (9 November 1960).

40. Grimminger, G., et. al., "Lift on Inclined Bodies of Revolution in Hypersonic Flow," Journal of the Aeronautical Sciences, 17, 11 (November 1950).

41. Lees, L., "Laminar Heat Transfer over Blunt-Nosed Bodies at Hypersonic Flight Speeds," Jet Propulsion 26, 4 (April 1956).

42. Roberts, Leonard, "An Analysis of Ablation Shield Requirements for Manned Reentry Vehicles," NASA TR T-62 (1960).

43. Roberts, Leonard, "A Theoretical Study of Stagnation-Point Ablation," NASA TR R-9 (1959).

44. Hedalgo, H., "A Theory of Ablation of Glassy Materials for Laminar and Turbulent Heating," AVCO Everett Research Lab. Rept. 62 (June 1959).

45. Georgiev, S., "Hypersonic Ablation and Interpretation of Test Results, AVCO Everett Research Lab. Rept. 99 (October 1960).

46. Steg, Leo, "Materials for Reentry Heat Protection of Satellites," ARS Journal, 30, 9 (September 1960).

47. Swann, Robert T., "Approximate Analysis of the Performance of Char-Forming Ablators," NASA TR R-195 (June 1964).

48. Walberg, Gerald D., "Analytical Study of Diffusion-Controlled Char Oxidation and its Effects on Steady-State Ablation of Plastic Materials," NASA TR R-242 (July 1966).

APPENDIX A

DERIVATION OF THREE DIMENSIONAL TRAJECTORY
EQUATIONS OF MOTION

The trajectory equations of motion will be derived in a spherical
coordinate system for a vehicle assumed to be a point mass moving over a
spherical, non-rotating earth fixed in inertial space[39]. The coordinate
system is shown in Fig. A-1. R is the radial distance from the center
of the earth to the vehicle, θ_1 is the downrange angle, in the orbital
plane, measured from the initial reentry position. θ_2 is the cross range
angle measured from the orbital plane to the radial line R.

The forces on the vehicle are conveniently written in a coordinate
system centered in the vehicle, but must then be related to an inertial
reference frame. The reference frame for this development will be the x_o,
y_o, z_o frame, shown in Fig. A-1, fixed at the earth's center. A series
of five rotations will now be described, each of which specifies a new
cartesian coordinate system. Finally, the orientation of the body centered
coordinate system with respect to the inertial frame will be specified in
terms of four of these rotation angles.

The first rotation is through the angle θ_1, about the y_o axis,
giving the x_1, y_1, z_1 coordinate system.

The second rotation is through the angle θ_2, about the x_1 axis,
giving the x_2, y_2, z_2 coordinate system. Now z_2 is up along the local
vertical, and x_2, y_2 are in the local horizontal plane.

The third rotation is through the angle θ_3, about z_2, in the local
horizontal plane. Here θ_3 is the "heading angle" such that the x_2 axis

is parallel to the projection of the velocity vector on the local horizontal plane. This rotation specifies the x_3, y_3, z_3 coordinate system. Note here that θ_3 is positive for nose left in the right hand coordinate system shown in Fig. A-1.

The fourth rotation is through an angle γ, about y_3, giving the x_4, y_4, z_4 coordinate system. The x_4 axis is now parallel to the velocity vector, y_4 is parallel to the local horizontal plane, and z_4 is in the local vertical plane described by the velocity vector and the local vertical.

The final rotation is through an angle ϕ, about x_4, giving the x_5, y_5 z_5 coordinate system. Now x_5 is parallel to the velocity vector, y_5 is above the local horizontal by the angle ϕ, and z_5 is parallel to the vehicle's lift vector. The final two rotations are shown in Fig. A-2.

In the x_4, y_4, z_4 coordinate system, the forces on the vehicle may be written

$$F_x = mg \sin \gamma - D = ma_x \tag{A-1}$$

$$F_y = -L \sin \phi = ma_y \tag{A-2}$$

$$F_3 = L \cos \phi - mg \cos \gamma = ma_3 \tag{A-3}$$

Since x_4, y_4, z_4 is a rotating coordinate system, the acceleration in the x_4, y_4, z_4 system must be written with respect to the inertial frame as:

$$\vec{a} = \frac{d\vec{V}}{dt} + (\vec{\omega} \times \vec{V}) \tag{A-4}$$

which may be expanded as:

$$a_x = \frac{dV}{dt} \tag{A-5}$$

168

$$\partial_y = \omega_3 V \tag{A-6}$$

$$\partial_3 = -\omega_y V \tag{A-7}$$

by the specification of the use of the x_4, y_4, z_4 coordinate system.

Now the first four rotations described above may be considered as angular velocities and written in vector form in the x_4, y_4, z_4 coordinate system:

$$\vec{\dot{\Theta}}_1 = \dot{\Theta}_1 \left\{ \left(\cos\Theta_2 \sin\Theta_3 \cos\gamma + \sin\Theta_2 \sin\gamma \right)\vec{e}_x + \cos\Theta_2 \cos\Theta_3 \vec{e}_y \right. \tag{A-8}$$

$$\left. + \left(\cos\Theta_2 \sin\Theta_3 \sin\gamma - \sin\Theta_2 \cos\gamma \right)\vec{e}_3 \right\}$$

$$\vec{\dot{\Theta}}_2 = \dot{\Theta}_2 \left\{ \cos\Theta_3 \cos\gamma \, \vec{e}_x - \sin\Theta_3 \, \vec{e}_y + \cos\Theta_3 \sin\gamma \, \vec{e}_3 \right\} \tag{A-9}$$

$$\vec{\dot{\Theta}}_3 = \dot{\Theta}_3 \left\{ -\sin\gamma \, \vec{e}_x + \cos\gamma \, \vec{e}_3 \right\} \tag{A-10}$$

$$\vec{\dot{\gamma}} = \dot{\gamma} \, \vec{e}_y \tag{A-11}$$

The component angular velocities of the x_4, y_4, z_4 coordinate system with respect to the inertial frame may be written:

$$\omega_x = \dot{\Theta}_1 \left(\cos\Theta_2 \sin\Theta_3 \cos\gamma + \sin\Theta_2 \sin\gamma \right) + \dot{\Theta}_2 \cos\Theta_3 \cos\gamma - \dot{\Theta}_3 \sin\gamma \tag{A-12}$$

$$\omega_y = \dot{\Theta}_1 \cos\Theta_2 \cos\Theta_3 - \dot{\Theta}_2 \sin\Theta_3 + \dot{\gamma} \tag{A-13}$$

$$\omega_3 = \dot{\Theta}_1 \left(\cos\Theta_2 \sin\Theta_3 \sin\gamma - \sin\Theta_2 \cos\gamma \right) + \dot{\Theta}_2 \cos\Theta_3 \sin\gamma + \dot{\Theta}_3 \cos\gamma \tag{A-14}$$

Now from equations (A-1) and (A-5), the acceleration along x_4 may be written:

$$\dot{V} = -\frac{D}{m} + g \sin \gamma \tag{A-15}$$

From equations (A-2), (A-6) and (A-14), the rate of change of the heading angle, θ_3, may be written as:

$$\dot{\theta}_3 = \frac{1}{\cos \gamma} \left\{ -\frac{L \sin \phi}{mV} - \dot{\theta}_2 \cos \theta_3 \sin \gamma - \dot{\theta}_1 (\cos \theta_2 \sin \theta_3 \sin \gamma - \sin \theta_2 \cos \gamma) \right\} \tag{A-16}$$

and from equations (A-3), (A-7) and (A-13) the rate of change of the pitch angle, γ, may be written as:

$$\dot{\gamma} = -\frac{L \cos \phi}{mV} + g\frac{\cos \gamma}{V} + \dot{\theta}_2 \sin \theta_3 - \dot{\theta}_1 \cos \theta_2 \cos \theta_3 \tag{A-17}$$

The development to this point includes the rotation, but not the translation, of the x_4, y_4, z_4 coordinate system with respect to inertial space. This translation can be handled most simply by geometry from Figs. A-1 and A-2, which gives:

$$\dot{\theta}_1 = \frac{V \cos \gamma \cos \theta_3}{R \cos \theta_2} \tag{A-18}$$

$$\dot{\theta}_2 = \frac{-V \cos \gamma \sin \theta_3}{R} \tag{A-19}$$

Substitution of equations (A-18) and (A-19) into equations (A-16) and (A-17) gives:

$$\dot{\theta}_3 = -\frac{L \sin \phi}{mV \cos \gamma} + \frac{V}{R} \cos \gamma \cos \theta_3 \tan \theta_2 \tag{A-20}$$

$$\dot{\gamma} = -\frac{L \cos \phi}{mV} + \left(\frac{g}{V} - \frac{V}{R} \right) \cos \gamma \tag{A-21}$$

170

Equations (A-15), (A-20) and (A-21) comprise the three equations of motion which, with the appropriate initial conditions, were solved numerically to give the reentry trajectory. In addition, the rate of change of altitude, and the downrange and crossrange distance may be expressed as:

$$\mathring{R} = -V \sin \gamma$$

(A-22)

$$DR = R_e \, \Theta_1$$

(A-23)

$$CR = R_e \, \Theta_2$$

(A-24)

where R_e is the radius of the earth.

For the low orbit reentry under consideration, the equations of motion can be simplified by assuming that $R = R_e$, and that the acceleration due to gravity is constant. Note here that the actual altitude must be computed throughout the trajectory since the vehicle's aerodynamic characteristics depend on the air density, which is functionally related to the altitude:

$$\rho = .003 \, e^{-\left(\frac{h}{23000}\right)}$$

(A-25)

The resultant physiological acceleration (that felt by the pilot) may be written in terms of the forces on the vehicle as:

$$R.P.A. = \frac{1}{gm} \left\{ \left(L\cos\phi\cos\gamma + D\sin\gamma \right)^2 + \left[\left(-D\cos\gamma + L\cos\phi\sin\gamma \right)\cos\Theta_3 + L\sin\phi\sin\Theta_3 \right]^2 \right.$$
$$\left. + \left[\left(D\cos\gamma - L\cos\phi\sin\gamma \right)\sin\Theta_3 + L\sin\phi\cos\Theta_3 \right]^2 \right\}^{1/2}$$

(A-26)
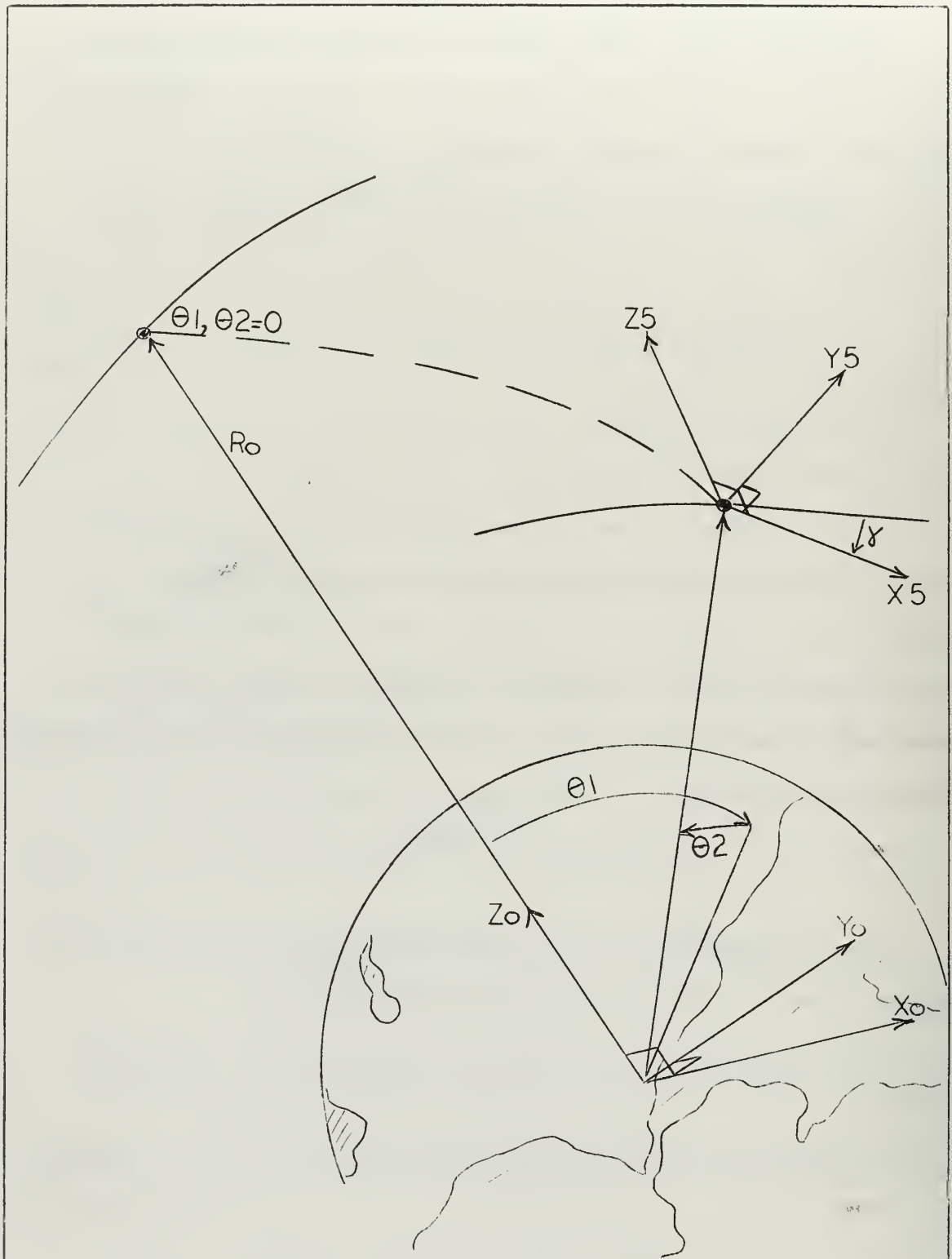
Fig. A-1 Spherical Coordinate System
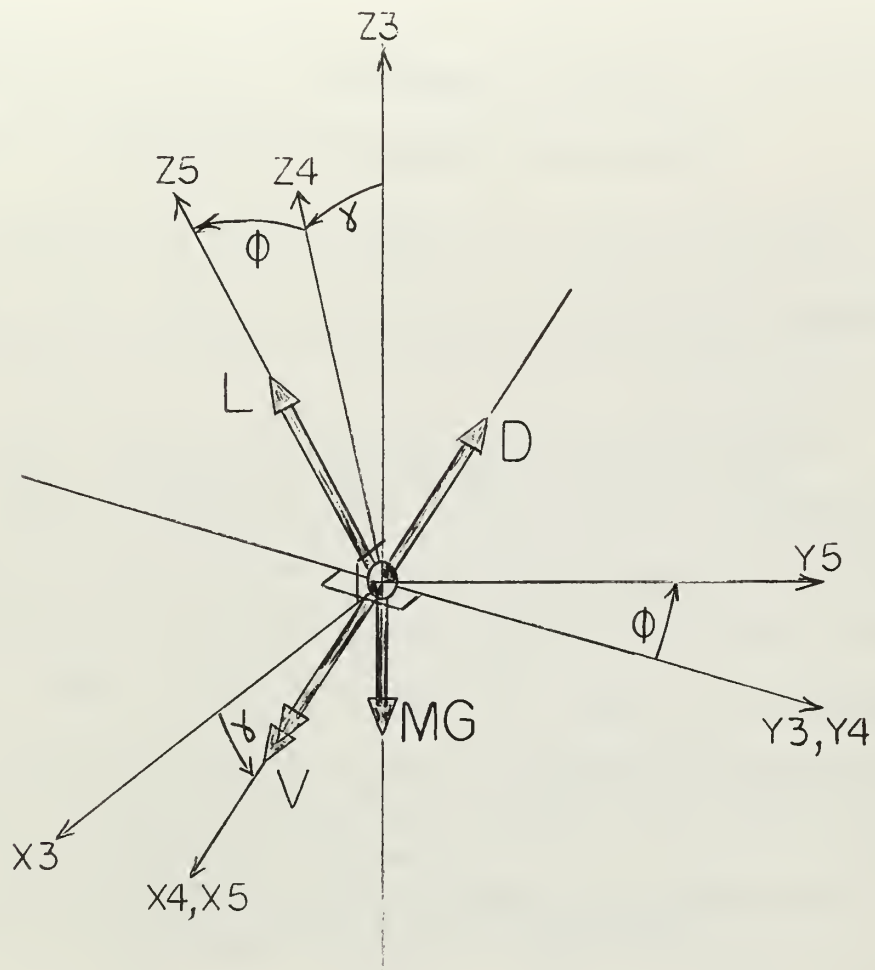
Fig. A-2 Vehicle Coordinate Systems

APPENDIX B

DERIVATION OF AERODYNAMIC COEFFICIENTS

Newtonian theory will be used to derive and calculate the
aerodynamic coefficients of the particular reentry vehicle configuration
under consideration.

In Newtonian flow, it is assumed that the shock layer is
infinitesimally thin and thus the shock wave lies along the surface of
the body. This leads to the further assumption that the component of
momentum normal to the body is reduced to zero and the tangential component
of momentum is unchanged. Consider an elemental surface area, dS. The
rate of mass flow striking the area in the normal direction is $\rho_o V_o \cos\eta \, dS$,
and the component of velocity in the normal direction is $V_o \cos\eta$, where η
is the angle between the velocity vector and the body normal vector[7].
Equating the rate of change of momentum to the force on the surface
element:

$$\rho_o V_o^2 \cos^2\eta \, dS \quad - \quad dF = (p - p_o) \, dS$$

(B-1)

Therefore, the Newtonian pressure coefficient may be defined and
written as:

$$C_p = \frac{(p - p_o)}{p_o} = 2 \cos^2\eta$$

(B-2)

It should be noted that this derivation neglects centrifugal force
effects. In the flow over an actual body, the curvature of the streamlines

174

causes a reduction in the surface pressure coefficient by a factor proportional to the centrifugal force experienced by a particle at that point[40].

Consider a circular cone, as shown in Fig. B-1, at an arbitrary angle of attack and zero side slip angle. The equation of the surface may be written as:

$$S = -x^2 \tan\Theta_c + y^2 + z^2$$

(B-3)

The unit vector normal to the surface is found from vector algebra to be

$$\vec{e}_s = \frac{\nabla S}{|\nabla S|} = \sin\Theta_c \, \vec{e}_x - \sin\beta \cos\Theta_c \, \vec{e}_y - \cos\beta \cos\Theta_c \, \vec{e}_z$$

(B-4)

Similarly the unit velocity vector is found to be

$$\vec{e}_v = -\cos\alpha \, \vec{e}_x - \sin\alpha \, \vec{e}_z$$

(B-5)

The cosine of the angle η may now be expressed as the scalar product of the two unit vectors $\bar{e}_s$ and $\bar{e}_v$:

$$\cos\eta = \vec{e}_s \circ \vec{e}_v = \cos\alpha \sin\Theta_c - \sin\alpha \cos\beta \cos\Theta_c$$

(B-6)

Substituting equation (B-6) into equation (B-2) leads to the expression for the Newtonian pressure coefficient:

$$C_p = 2\left(\cos\alpha \sin\Theta_c - \sin\alpha \cos\beta \cos\Theta_c\right)^2$$

(B-7)

The axial and normal force coefficients may now be determined by appropriate integration of the pressure coefficient found in equation (B-7):

175

$$C_A = \frac{1}{S} \iint\limits_{S_x} C_p \, dS_x$$

(B-8)

$$C_N = \frac{1}{S} \iint\limits_{S_\zeta} C_p \, dS_\zeta$$

(B-9)

In order to determine the limits of integration, recall that the Newtonian pressure coefficient is based on the change of momentum of the normal component of mass flow. Thus, the region downstream of the boundary, $\cos \eta = 0$, does not contribute to the force on the body and the integration is to be performed only over those areas actually exposed to the flow.

Once the axial and normal force coefficients have been determined, the lift and drag coefficients may be calculated from:

$$C_L = C_N \cos \alpha - C_A \sin \alpha$$

(B-10)

$$C_D = C_N \sin \alpha + C_A \cos \alpha$$

(B-11)

Since the local force coefficients determined by this method depend only on the angle between the velocity vector and the surface normal vector, the coefficients of a multicomponent body may be considered as the sum of the individual component coefficients. In particular, for a spherically blunted cone with vertex angle $2\theta_c$, nose radius R_n, and base radius R_b, the lift and drag coefficients may be written as:

$$C_L = C_{L_{cone}} \left[1 - \left(\frac{R_n}{R_b} \right)^2 \right] + C_{L_{sphere}} \left(\frac{R_n}{R_b} \right)^2 \sec^2 \theta_c$$

(B-12)

176

$$C_D = C_{D_{cone}} \left[1 - \left(\frac{R_N}{R_b}\right)^2 \right] + C_{D_{sphere}} \frac{R_n}{R_b} \sec^2 \Theta_c$$

(B-13)

The vehicle configuration shown in Fig. C-1 is an example of a multicomponent body in the above context. For computational purposes, it was assumed that the blunted nose was a spherical cap with an effective nose radius of 1.81 ft., or that radius required to give the same surface area as the actual configuration. Using equations (B-12) and (B-13), the lift and drag coefficients may be written:

$$C_L = 0.955 \, C_{L_{cone}} + 0.0467 \, C_{L_{sphere}}$$

(B-14)

$$C_D = 0.955 \, C_{D_{cone}} + 0.0467 \, C_{D_{sphere}}$$

(B-15)

The coefficients thus determined, corrected from base area to plan form area as the reference, are plotted as a function of the angle of attack in Fig. B-2. Also shown are the closed form approximations determined empirically for use over the angle of attack range of interest. These are:

$$C_L = 0.06 + 0.498 \, \sin 2\alpha \, |\sin 2\alpha|^{0.3}$$

(B-16)

$$C_D = 0.035 + 1.05 \, \sin^2 1.5\alpha \, |\sin 1.5\alpha|^{0.5}$$

(B-17)

177

Fig. B-1 Circular Cone

178

$CL = .06 + .498 \sin 2\alpha \, |\sin 2\alpha^3|$

$CD = .035 + 1.05 \sin^2 1.5\alpha \, |\sin 1.5\alpha^{.5}|$
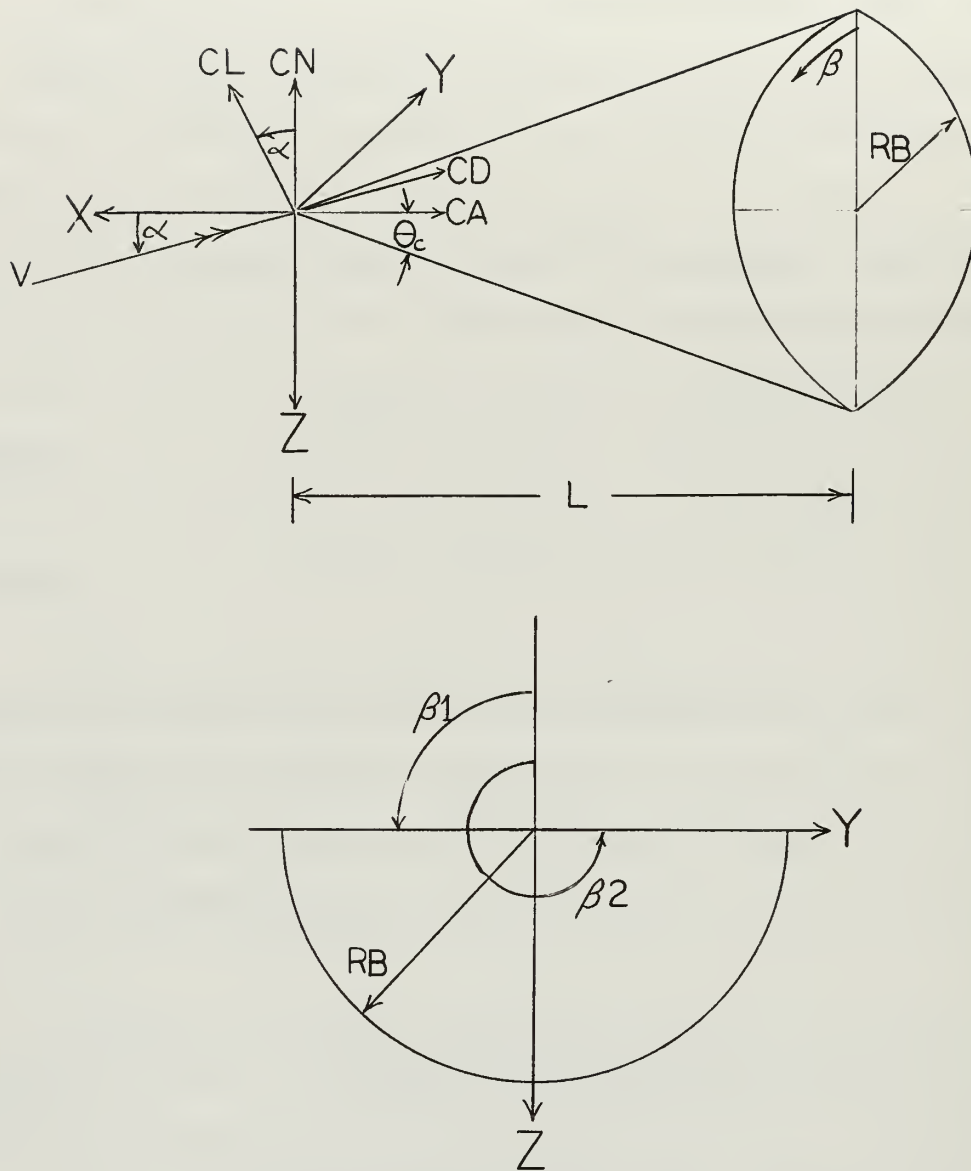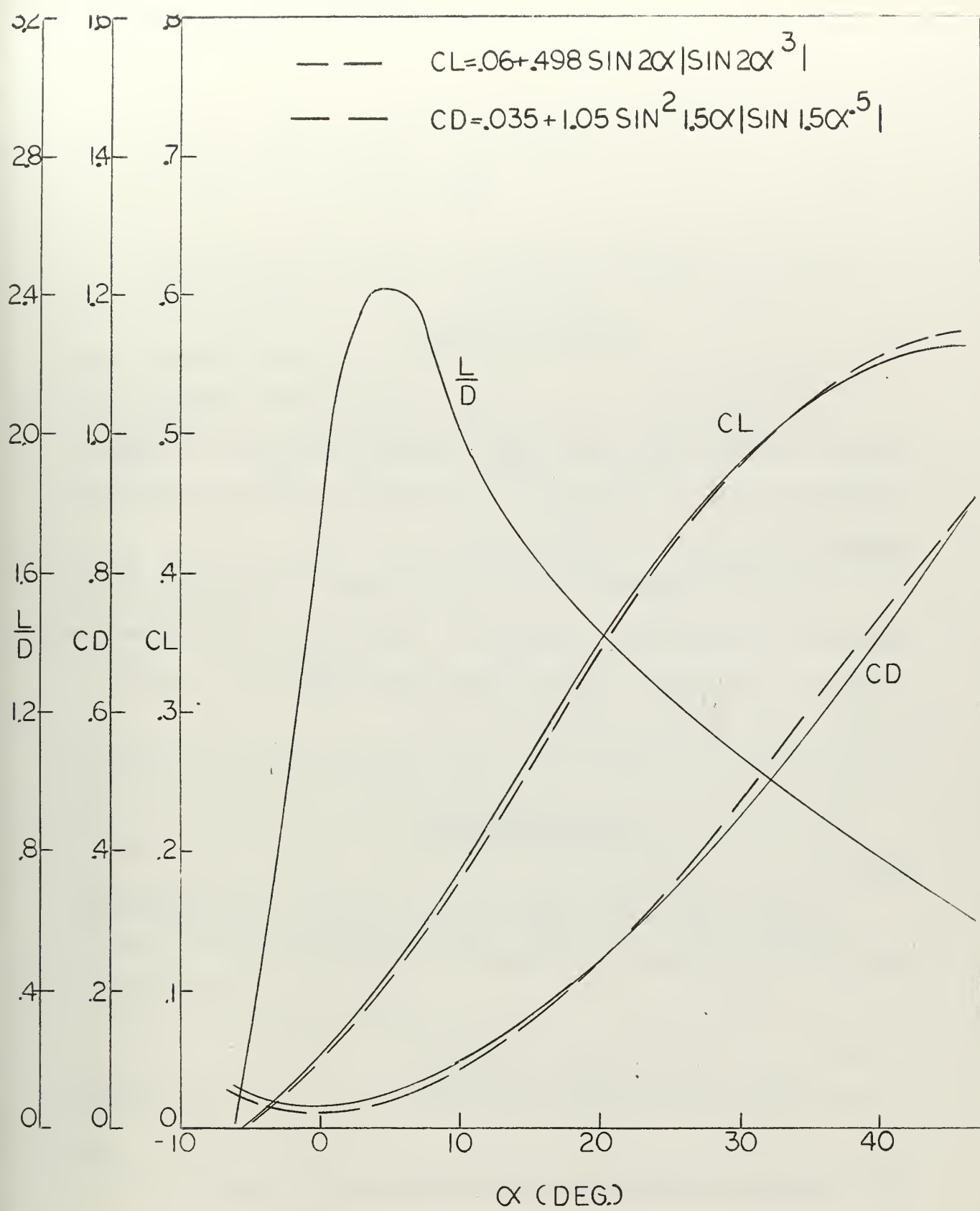
Fig. B-2   Aerodynamic Coefficients

179

APPENDIX C

AERODYNAMIC HEATING

The vehicle under consideration in this analysis is assumed to be composed of four separate components as shown in Fig. C-1. The heating rates over each of the components can be determined from known empirical formulas based on Newtonian flow theory.

The nose is considered to be a quarter sphere of radius R_N. The remainder of the underside of the body is a half right circular cone, which is joined to the top by a rounded leading edge of radius R_{LE}. The top of the vehicle is a delta shaped flat plate.

CONVECTIVE HEATING

Nose:

A quarter sphere was assumed for the round nose. The stagnation point heat transfer rate is approximated by Koelle[34] to be:

$$q_s = 865 \left(\frac{V_\infty}{10^4} \right)^{3.15} \sqrt{\frac{\rho/\rho_{SL}}{R_N}}$$ (C-1)

Using the standard ARDC density relationship,

$$\frac{\rho}{\rho_{SL}} = e^{-\frac{H}{23,500}}$$ (C-2)

Equation (C-1) can be rewritten as a function of velocity and altitude as;

180

$$q_S = 865 \left(\frac{V_\infty}{10^4}\right)^{3.15} \frac{e^{-\frac{H}{47,000}}}{\sqrt{R_N}} \tag{C-3}$$

The heating rate distribution over the hemisphere is a function of the angular distance from the stagnation point and is given for axially symmetric flow in reference[8] as:

$$\frac{q(\theta)}{q_S} = \frac{\cos^{1.5}\theta}{\frac{\sin 2\theta}{2\theta}\left[\cos\theta\left\{1 + \left(\frac{\frac{2\theta}{\sin 2\theta} - \cos 2\theta}{\sin 2\theta}\right)^2\right\}\right]^{0.5}} \tag{C-4}$$

Equation (C-4) may be approximated to an accuracy of 7 percent for values of θ up to $60°$ by:

$$\frac{q(\theta)}{q_S} \approx \cos^{1.5}\theta \tag{C-5}$$

In equation (C-4) and (C-5), the angle θ is measured from the stagnation point. The position of the stagnation point on the nose will vary with the angle of attack and θ could vary from $-90°$ to $+90°$ as shown in Fig. (C-2A). Equation (C-4) is a function of the magnitude of the angle θ as measured from the stagnation point. Therefore, for equation (C-4), θ is defined as:

$$\theta = |\theta' - \alpha| \tag{C-6}$$

where $0 < \theta' < 90° - \theta_v$. θ_v is the cone semi-vertex angle at the virtual apex.

For purposes of determining heat shield weights by numerical integration, the nose is divided into incremental areas, each having an assumed constant heating rate $q(\theta)$ as shown in Fig. (C-2B). The incremental surface area for the quarter sphere is approximated by:

181

$$dS_N = \pi R_N^2 \sin\theta' \, d\theta' \qquad \text{(C-7)}$$

with limits of $0 < \theta' < 90^\circ - \theta_v$.

Body:

The bottom of the vehicle is assumed to be a half right circular cone with a blunted nose. As was assumed by Adler[9], the local heating is a function of the distance from the virtual tip and the angle an element makes with the free stream velocity. As shown in Fig. (C-3), the distance from the virtual tip x' is given by:

$$X' = R_N \left\{ \cot\theta_v + \left[\frac{S}{R_N} - \left(\frac{\pi}{2} - \theta_v \right) \right] \right\} \qquad \text{(C-8)}$$

Lees[41] relates the local heating rate to the stagnation point heating rate for zero angle of attack by:

$$\frac{Q}{\mathring{q}_s} = \frac{A(\theta_v) \, X'/R_N}{\left[B(\theta_v) + \left(X'/R_N \right)^3 \right]^{1/2}} \qquad \text{(C-9)}$$

for x' $R_N \cot\theta_v$. $A(\theta_v)$ relates the two heating rates on a sharp nosed cone as:

$$\left(\frac{Q}{\mathring{q}_s} \right)_{\substack{\text{SHARP} \\ \text{NOSE}}} = \frac{A(\theta_v)\sqrt{R_N'}}{\sqrt{X'}} \qquad \text{(C-10)}$$

$B(\theta_v)$ is a factor which accounts for the effect that the bluntness of the nose has on the after portion of the conical body.

$A(\theta_v)$ and $B(\theta_v)$ are given in reference 41 as:

$$A(\theta_v) = \frac{\sqrt{3}}{2}\left[\left(1 - \frac{1}{\gamma_\infty M_\infty^2}\right)\sin^2\theta_v + \frac{1}{\gamma_\infty M_\infty^2}\right]\sqrt{\frac{\pi}{2} - \theta_v}$$

<div align="right">(C-11)</div>

$$B(\theta_v) = \frac{3/16}{\sin^2\theta_v\left\{\left[1 - \left(\frac{1}{\gamma_\infty M_\infty^2}\right)\right]\sin^2\theta_v + \left(\frac{1}{\gamma_\infty M_\infty^2}\right)\right\}} \times$$

$$\left[\frac{D(\theta)}{\theta}\right]_{\theta=\left(\frac{\pi}{2}-\theta_v\right)} - \cot^3\theta_v \qquad \text{(C-12)}$$

where

$$D(\theta) = \left(1 - \frac{1}{\gamma_\infty M_\infty^2}\right)\left(\theta^2 - \frac{\theta\sin 4\theta}{2} + \frac{1 - \cos 4\theta}{8}\right) +$$

$$\frac{4}{\gamma_\infty M_\infty^2}\left(\theta^2 - \theta\sin 2\theta + \frac{1 - \cos 2\theta}{2}\right) + \dots \qquad \text{(C-13)}$$

The following approximations can be made for $M_\infty \gg 1$:

$$A(\theta_v) \approx \frac{\sqrt{3}}{2}\sin\theta_v\sqrt{\frac{\pi}{2} - \theta_v}$$

<div align="right">(C-11A)</div>

and

$$B(\theta_v) \approx \frac{3/16}{\sin^4 \theta_v} \left[\frac{D(\theta)}{\theta} \right]_{\theta = \left(\frac{\pi}{2} - \theta_v \right)} - \cot^3 \theta_v$$

(C-12A)

Values of $B(\theta_v)$ are tabulated in reference 41 and are shown in the following table.

TABLE C-1

θ_v °	$B(\theta_v)$
10	172.0
20	4.2
30	-0.20
40	-0.26

Introducing (C-11A) and (C-3) into (C-10), the laminar heating rate over a sharp nosed cone at an angle of attack of zero degrees is obtained as:

$$\dot{q} = 750 \left(\frac{V_\infty}{10^4} \right)^{3.15} \frac{e^{-\frac{H}{47,000}}}{\sqrt{x'}} \sin \theta_v \sqrt{\frac{\pi}{2} - \theta_v}$$

(C-13)

For a blunted nose cone at a zero angle of attack:

$$\dot{q} = 750 \left(\frac{V_\infty}{10^4} \right)^{3.15} \frac{e^{-\frac{H}{47,000}}}{R_N^{1.5}} \frac{\sin \theta_v \sqrt{\frac{\pi}{2} - \theta_v} \, x'}{\left[B(\theta_v) + \left(x'/R_N \right)^3 \right]^{1/2}}$$

(C-14)

It can be seen that equations (C-13) and (C-14) for an angle of attack of zero degrees are a function only of the distance back along the body, x',

184

since the heating rate will be constant around the cone due to the axially symmetric flow pattern. When the cone is at an angle of attack, axially symmetric flow no longer exists and the local heating rates become a function of not only x', but also of the angular position, β, around the body. Adler [9] used a method of compensating for angle of attack by defining an effective vertex angle, θ_{EFF}, which is the angle an element makes with the free stream velocity vector. The angle, θ_{EFF}, (see Fig. C-4) is found from the relationship:

$$TAN\ \theta_{EFF} = \sqrt{TAN^2 \eta' + TAN^2 \zeta_o'} \qquad \text{(C-15)}$$

where

$$TAN\ \zeta_o' = R_b\ cos\ \beta / L = TAN\ \theta_v\ cos\ \beta \qquad \text{(C-16)}$$

$$TAN\ \eta_o' = R_b\ sin\ \beta / L = TAN\ \theta_v\ sin\ \beta \qquad \text{(C-17)}$$

and

$$TAN\ \eta' = TAN\ (\eta_o' + \alpha)$$

$$= (TAN^{-1}(TAN\ \theta_v\ sin\ \beta) + \alpha) \qquad \text{(C-18)}$$

Substituting (C-16) and (C-18) into (C-15) and solving for θ_{EFF} gives:

$$\theta_{EFF} = TAN^{-1} \left\{ TAN^2 \left[TAN^{-1}(TAN\ \theta_v\ sin\ \beta) + \alpha \right] + TAN^2 \theta_v\ cos^2 \beta \right\}^{.5} \qquad \text{(C-19)}$$

Assuming that the local heating over a cone at an angle of attack is

185

dependent on the effective vertex angle, the equation for a blunted cone at an angle of attack becomes:

$$\dot{q} = 750 \left(\frac{V_\infty}{10^4} \right)^{3.15} \frac{e^{-\frac{H}{47,000}}}{R_N^{1.5}} \frac{\sqrt{\frac{\pi}{2} - \theta_{EFF}} \; x' \; SIN \; \theta_{EFF}}{\left[B(\theta_v) + \left(\frac{x'}{R_N} \right)^3 \right]^{1/2}} \tag{C-20}$$

To obtain the total heating rate over the cone, it is necessary to integrate this equation numerically over the surface:

$$\int \dot{q} \, ds = 750 \left(\frac{V_\infty}{10^4} \right)^{3.15} \frac{e^{-\frac{H}{47,000}}}{R_N^{1.5}} \int \int \frac{x'^2 \sqrt{\frac{\pi}{2} - \theta_{EFF}} \; SIN^2 \theta_{EFF} \; d\beta \, dx'}{\left[B(\theta_v) + \left(\frac{x'}{R_N} \right)^3 \right]^{1/2}} \tag{C-21}$$

where

$$ds = (x' \; SIN \; \theta_{EFF}) \, d\beta \, dx' \tag{C-22}$$

The double integration is done numerically for $R_N \cot \theta_v \leq x' \leq L$ and $0 \leq \beta \leq \pi$. Since no yaw is assumed, the flow is symmetric on either side of the xz plane, and the angular integration may be made for $0 \leq \beta \leq \pi/2$ and the results multiplied by a factor of 2 to account for the entire body.

Leading Edge:

The leading edges are represented by two quarter cylinders of radius R_{LE} extending back from the nose along the edge joining the body with the top.

The laminar heating rates on a cylinder normal to the flow can be obtained by a coordinate transformation of a three dimensional sphere to two dimensions. Lees[41] states this results in simply multiplying the

186

spherical heating rate by the factor $\frac{\sqrt{2}}{2}$. Therefore, for a cylinder normal to the flow the heating rate is given by:

$$\dot{q} = 610 \left(\frac{V_{\infty}}{10^4} \right)^{3.15} \frac{e^{-\frac{H}{47,000}}}{\sqrt{R_{LE}}} \qquad (C\text{-}23)$$

The local heating rate on a leading edge will be reduced by sweeping the body. This factor for zero angle of attack is approximated by:

$$\frac{\dot{q}_{\Lambda}}{\dot{q}_{\Lambda=0}} = \cos^{1.2} \Lambda \qquad (C\text{-}24)$$

where Λ is the sweep angle.

When the body is pitched to an angle of attack, the effective sweep is decreased and the effective angle of attack of the leading edge is greatly increased. The sweep correction, rewritten to compensate for the angle of attack, is given as:

$$\frac{\dot{q}_{\Lambda}}{\dot{q}_{\Lambda=0}} = \left[1 - \sin^2 \Lambda \, \cos^2 \alpha \right]^{.6} \qquad (C\text{-}25)$$

Combining equations (C-23) and (C-25) gives the relationships for the local heating rate on a swept leading edge at an angle of attack:

$$\dot{q} = 610 \left(\frac{V_{\infty}}{10^4} \right)^{3.15} \frac{e^{-\frac{H}{47,000}}}{\sqrt{R_{LE}}} \left[1 - \sin^2 \Lambda \, \cos^2 \alpha \right]^{.6} \qquad (C\text{-}26)$$

187

<u>Top:</u>

The top surface of the vehicle will be exposed to aerodynamic impact heating for negative angles of attack. The top is assumed to be a delta shaped flat plate. Reference 8 gives the local heating on a flat plate at an angle of attack as:

$$\frac{q_{FP}}{q_s} = 0.0292 \left(\frac{R_N}{X} \right)^{.5} \alpha^{2/3}$$

(C-27)

where α is the angle of attack in degrees. Introducing the relationship for q_s (Eq. C-3) gives the local heating rate on the top as:

$$q = 25.3 \left(\frac{V_\infty}{10^4} \right)^{3.15} \frac{e^{-\frac{H}{47,000}}}{\sqrt{X}} \alpha^{2/3}$$

(C-28)

<div align="center">RADIATIVE HEATING</div>

The heat transfer to the surface due to the high temperature of gas in the shock layer near the stagnation point is usually assumed to be negligible for sub-circular velocities. The gas cap radiative transfer rate for the stagnation point is approximated in reference 34 as:

$$q_r = 7.5 \left(\frac{\rho_\infty}{\rho_{SL}} \right)^{1.5} \left(\frac{V_\infty}{10^4} \right)^{12.5} R_N$$

(C-29)

for velocities greater than approximately 20,000 ft/sec. For lower velocities, the radiative heat transfer rate is:

$$q_r = 100 \left(\frac{\rho_\infty}{\rho_{SL}} \right)^{1.6} \left(\frac{V_\infty}{10^4} \right)^{8.5} R_N$$

(C-30)

188

To determine the exact transition velocity, equation (C-29) and (C-30)
are equated as was done in reference 9 with the resulting transition
velocity being given as:

$$V_T = 1.91 \times 10^4\, e^{-\frac{H}{94,000}}$$

(C-31)

CYLINDRICAL LEADING EDGE

FLAT PLATE TOP

HALF CONE BODY
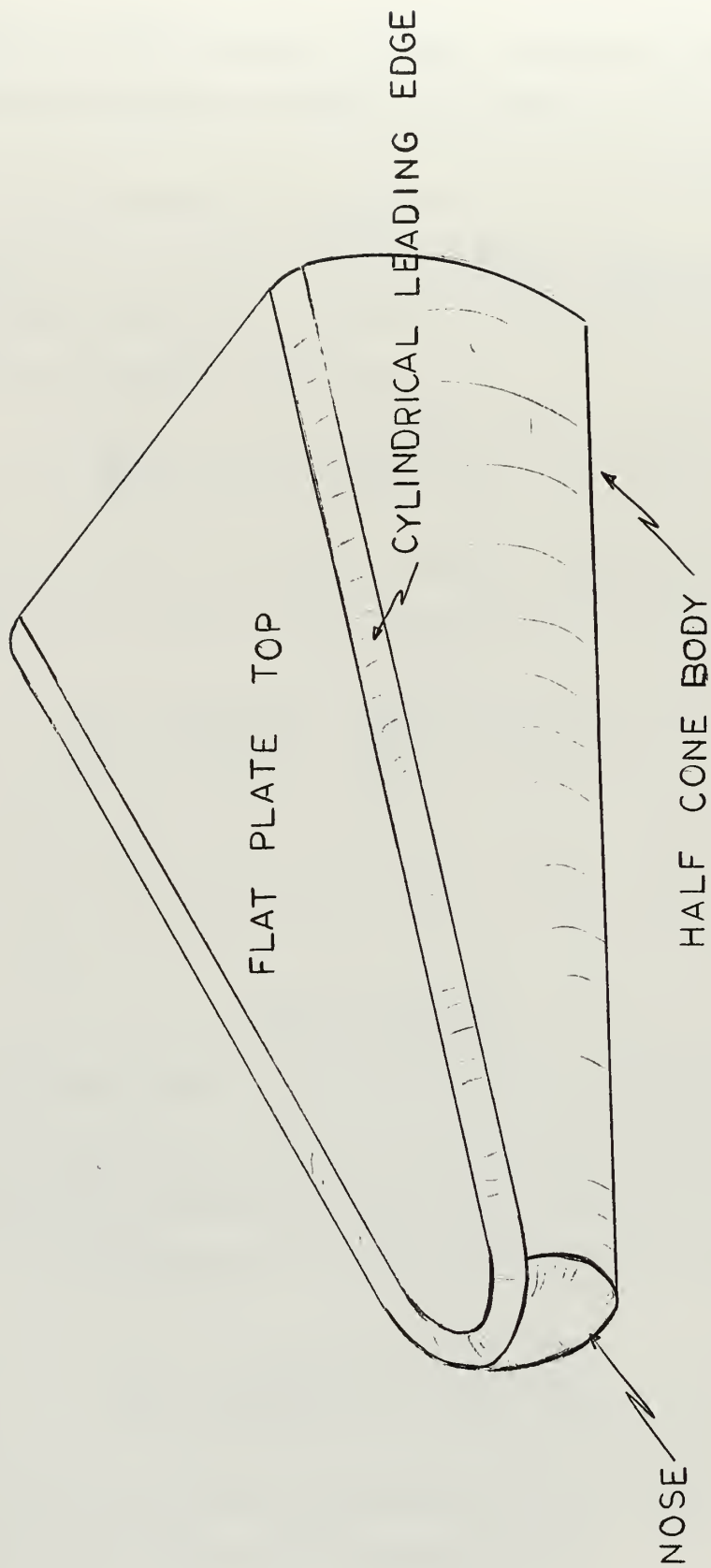
NOSE

Fig. C-1 Composite Vehicle
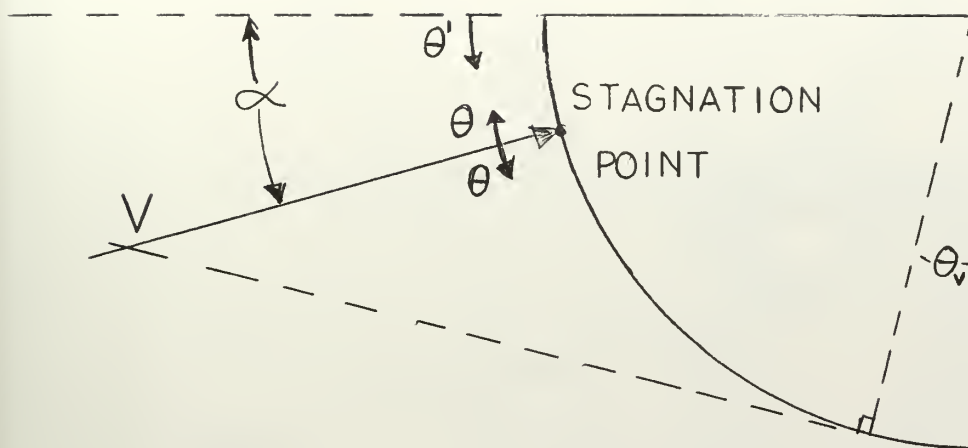
a) Description of Angles Measured on Nose
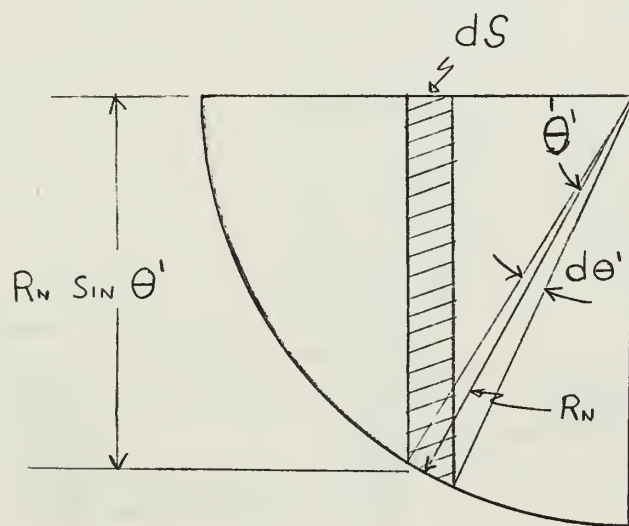
b) Incremental Nose Area

Fig. C-2

191

VIRTUAL
TIP


Fig. C-3 Body Coordinates

Fig. C-4 Cone at an Angle of Attack
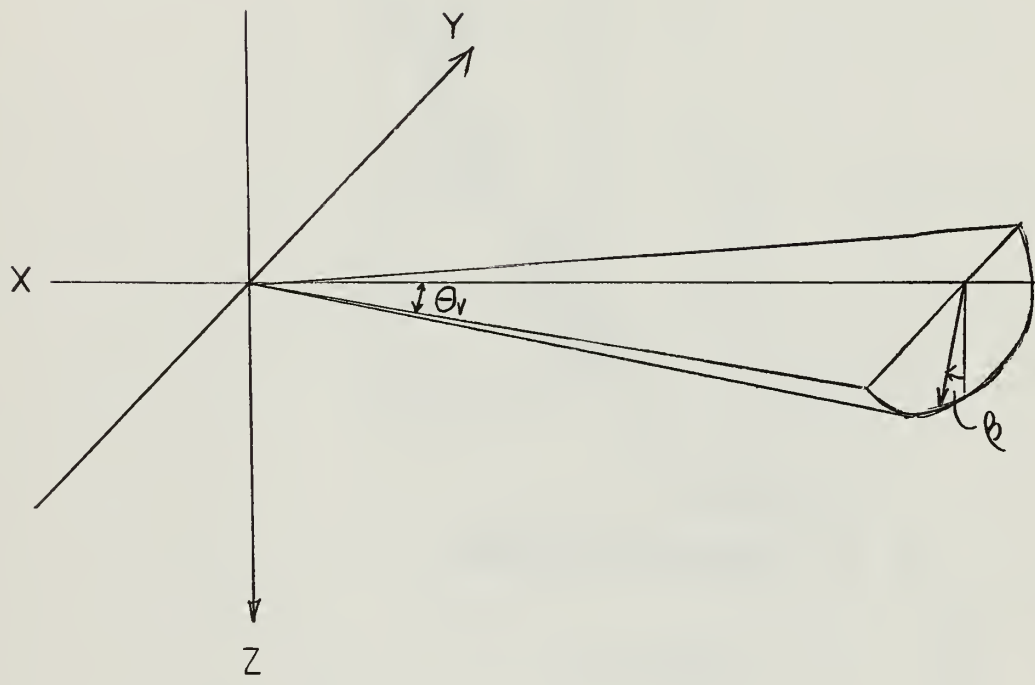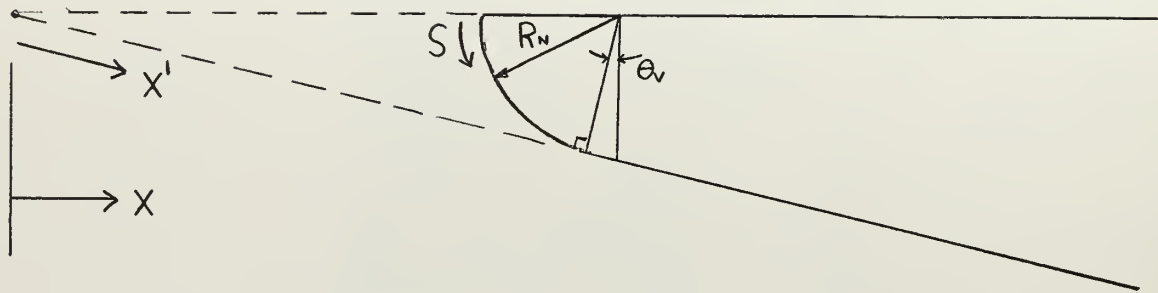
APPENDIX D

ABLATION ANALYSIS

VAPORIZING ABLATOR

The analysis of unsteady sublimation of ablation material from a reentry vehicle is covered by Roberts [42]. The analysis is based on the following assumptions regarding the properties of the material and its behavior during sublimation:

1) the density, ρ, thermal conductivity, k, specific heat, C_p, and latent heat of sublimation, L_v, of the ablating material are constant,

2) the Prandtl number and the Schmidt number of the gas mixture in the boundary layer and the specific heats, C_{p1}, (gas produced by sublimation) and, C_{p2}, (air behind shock wave) are constant,

3) the sublimation temperature, T_A, is constant,

4) sublimation leaves a smooth surface and causes negligible change in the shape of the shield,

5) the boundary layer remains laminar for most of the reentry,

6) the material is sufficiently thick to allow use of the "infinitely thick slab" approximation, and

7) conduction of heat takes place along lines normal to the surface.

Before the vehicle reenters the atmosphere, the ablation shield is assumed to have a uniform temperature $T_o = -100^\circ F$. During the early part of the reentry the shield is heated until the surface temperature reaches the ablation temperature T_A. Once sublimation of the material occurs, the

conduction of heat within the heat shield depends on the rate of mass loss from the surface and the problem becomes non-linear. The following analysis does not obtain an exact solution of the non-linear equations, but determines approximate results which provide estimates for the material required for sublimation and for insulation to maintain a given interior temperature.

A representation of the heat shield during the sublimation process is shown in Fig. D-1. The heat energy balance is given by

$$Q(t) = [C_p(T_A - T_o) + L_v]m + \rho C_p \int_{-\infty}^{0} (T - T_o)\, dz$$

(D-1)

where $Q(t)$ = net heat input at surface

$[C_p(T_A - T_o) + L_v]m$ = heat absorbed by sublimated material

$\rho C_p \int_{-\infty}^{0} (T - T_o)dz$ = heat accumulated by remaining material. When an

integral thickness, θ, defined as

$$\theta(t) = \int_{-\infty}^{0} \frac{T - T_o}{T_S - T_o}\, dz$$

(D-2)

is substituted into equation (D-1) the following equation results:

$$Q(t) = [C_p(T_A - T_o) + L_v]m + \rho C_p (T_S - T_o)\theta$$

(D-3)

Equation (D-3) may also be written in differential form as:

$$q_N(t) = \left[C_p(T_A - T_o) + L_v \right] \frac{dm}{dt} + \rho C_p \frac{d}{dt} \left[(T_S - T_o) \partial \right]$$

(D-4)

where q_N is the net heat transfer rate to the surface. The boundary condition on the surface of sublimation is given by:

$$q_N(t) = L_v \frac{dm}{dt} + \left(k \frac{\partial T}{\partial z} \right)_{z=0}$$

(D-5)

where z is the outward normal distance from the ablation surface. $q_N(t)$ is the heating rate that the shield actually experiences and it is a function of the rate of sublimation. During sublimation the heat transfer rate at the surface of the material is reduced due to the blocking effect of the mass injected into the boundary layer by the vaporizing material. The quasi-steady relationship for the effect is given in Ref. 43 by:

$$q_o(t) - q_N(t) = \alpha \tilde{C}_p (T_e - T_A) \frac{dm}{dt}$$

(D-6)

$q_o(t)$ is the heat transfer rate experienced by a non-ablating body and is equal to the aerodynamic heating rate minus the rate of heat radiation at the surface temperature T_A. $\tilde{C}_p$ is the effective mean specific heat and $\alpha(T_e - T_A)$ is the effective temperature rise of the mass convected in the boundary layer. The expressions for α and $\tilde{C}_p$ derived in reference 43 for a laminar boundary layer are:

$$\alpha = 1 - \frac{1}{3} N_{PR}^{-0.6}$$

(D-7)

and

$$\tilde{C}_P = C_{P_1} \tilde{\omega} + C_{P_2} (1 - \tilde{\omega})$$

(D-8)

where $\tilde{\omega}$ is the effective concentration of the shield material in gaseous form in the boundary layer and is given as a function of the Schmidt number, N_{sc}, in Ref. 43. The specific heat of the gas produced by sublimation is C_{p1}, and C_{p2} the specific heat of the air behind the shock wave. The heating rate, $q_N(t)$, is eliminated from equations (D-4) and (D-5) by use of (D-6) with the resulting relationships:

$$q_0(t) = \left[C_P(T_A - T_0) + L_v + \alpha \tilde{C}_P (T_e - T_A) \right] \frac{dm}{dt} + \rho C_P \frac{d}{dt} \left[(T_S - T_0) \theta \right]$$

(D-9)

and

$$q_0(t) = \left[L_v + \alpha \tilde{C}_P (T_e - T_A) \right] \frac{dm}{dt} + \left(k \frac{\partial T}{\partial z} \right)_{z=0}$$

(D-10)

A comparison of (D-9) and (D-10) show that:

$$\left(k \frac{\partial T}{\partial z} \right)_{z=0} = C_P (T_A - T_0) \frac{dm}{dt} + \rho C_P \frac{d}{dt} \left[(T_S - T_0) \theta \right]$$

(D-11)

197

which when integrated gives:

$$\int_0^t \left(k \frac{\partial T}{\partial z}\right)_{z=0} dt = C_p(T_A - T_0)m + \rho C_p (T_S - T_0)\theta$$

(D-12)

Equation (D-12) shows that only part of the heat transferred from the surface toward the interior is accumulated in the material (an amount $\rho C_p(T_s - T_o)\theta$), the remainder being required to raise the mass of ablator to the ablation temperature.

The purpose of the ablation heat shield is to reduce the heat transfer rate at the surface from the applied heating rate, aerodynamic minus re-radiation, to a value of $(k\frac{\partial T}{\partial z})_{z=0}$ by providing material which absorb heat through sublimation and convects the heat to the gas boundary layer. If this process is successful, then $(k\frac{\partial T}{\partial z})_{z=0} << q_o$ for most of the reentry, and an upper limit to the rate of mass loss can be found by neglecting heat conduction in the solid. Then, from equation (D-10) with $(k\frac{\partial T}{\partial z})_{z=0} = 0$, we get:

$$\dot{m} = \frac{q_o}{L_v + \alpha \tilde{C}_p (T_e - T_A)}$$

(D-13)

If it is assumed that the rate of accumulation of heat

$$\frac{d}{dt} \left[\rho C_p (T_s - T_o) \theta \right]$$

(D-14)

is small compared with the rate of disposal of heat

$$\left[C_p (T_A - T_o) + L_v + \alpha \tilde{C}_p (T_e - T_A) \right] \frac{dm}{dt}$$

(D-15)

198

equation (D-9) becomes

$$\overset{\circ}{m} = \frac{q_o}{C_p(T_A-T_o) + L_v + \alpha \tilde{C}_p(T_e - T_A)} \qquad \text{(D-16)}$$

Equation (D-16) is the quasi-steady expression for the rate of mass loss of ablating material.

The term $\alpha C_p(T_e - T_v)$ in equation (D-16), representing the shielding effect of the vapor being injected into the boundary layer, is a complex term to evaluate. As pointed out previously, it is a function of the Prandtl number, Schmidt number and various specific heats. This term can also be rewritten as a function of the enthalpy change across the boundary layer as $\beta\Delta h$. Δh can be approximated as⁻:

$$\Delta h = \frac{1}{2} \frac{m \Delta v^2}{W J} \approx \frac{v^2}{2gJ} = 20(10)^{-6} v^2 \qquad \text{(D-17)}$$

The transpiration factor, β, accounts for the effect of mass injection into the boundary layer. This factor is reasonably well defined for laminar boundary layer and is given, approximately, by reference (44) as:

$$\beta_L = 0.60 \left(\frac{29}{M_v} \right)^{0.26} \qquad \text{(D-18)}$$

where M_v is the molecular weight of the injected vapor. For mass injection into a turbulent air boundary layer, the value of β is not that well defined since only limited theoretical and experimental results are available. The best estimates made for the transpiration effect of vapors with a molecular weight comparable to or greater than that of air, which is the case for most materials of interest, indicate that:

$$\beta_T = \frac{1}{3} \beta_L \tag{D-19}$$

For this analysis, laminar boundary layer has been assumed as described in Chapter 3. In addition, it is assumed that the molecular weight of the injected vapor is comparable to that of air in which case equation (D-18) reduces to:

$$\beta_L \approx 0.60 \tag{D-20}$$

With these assumptions, equation (D-16) can be rewritten as:

$$\dot{m} = \frac{q_0}{C_p(T_A - T_0) + L_v + \beta \Delta h} \tag{D-21}$$

Another method of computing the mass rate of ablation is by using the effective heat of ablation, Q*. The effective heat of ablation for a subliming material is given by reference (45) as:

$$Q^* = \frac{C_p(T_A - T_0) + L_v + \beta \Delta h}{1 - q_r/q} \tag{D-22}$$

The sublimation temperature of many materials (Teflon, NH_4CL, etc.) is low enough that the energy re-radiated from the surface is usually negligibly small compared to the aerodynamic heat transfer rate. In these cases, the denominator of equation (D-22) becomes unity and Q* is then independent of the heat transfer rate. For a given material, C_p, T_A, L_v, and β are fixed and the effective heat of ablation becomes a function of only the enthalpy

difference across the boundary layer.

If both the heat input in BTU/ft^2-sec, q, and the heat required to ablate the material in BTU/lb, Q*, are known, then the material weight ablated in lb/ft^2-sec, $\dot{m}$, can be found from:

$$\dot{m} = q/Q*$$

(D-23)

or the weight ablated during any differential time in lb/ft^2 is:

$$dm = (q/Q*) \, dt$$

(D-24)

Values for Q* for various ablative materials are shown in Fig. D-2. The effective heat of ablation can be determined by experimental means utilizing the relationship:

$$Q* = q/\dot{m}$$

(D-25)

where q is the total heat rate obtained by applying heat, other than by aerodynamic means, to the specimen of material. The weight of material ablated is then measured and Q* is calculated from equation (D-25). This method assumes a) that regardless of how the Δh is obtained, the resulting Q* is the same, and b) that the flow conditions do not affect the rate at which the heat is carried away by the gas. This method will give the best results near the stagnation point. Some results of an actual flight of an ablation cooled vehicle indicates that the effective heat of ablation obtained from theory and experiment are close enough to yield satisfactory engineering results. Fig. (D-3) shows experimental and theoretical results for Teflon.

Equation (D-21) was used for the calculation of the required

201

mass of Teflon in the comparison of weights for various trajectories described in Chapter 5. In Chapter 6, Teflon is compared with various other materials for a given set of trajectories. In order to compare the materials on a common basis, the effective heat of ablation of the materials considered, as presented in Fig. (D-2), was used to calculate the weights. A comparison was made between the two methods of calculating the weight of Teflon and a 15% difference was found with a Q* method resulting in the higher weights.

The effectiveness of an ablation shield in reducing heat transfer to the vehicle structure is not measured only by the effective heat of ablation. Since the ablation material will be at temperature, T_A, which, in most cases will be well above that which can be tolerated at the structural wall behind the shield, the insulation requirements must be considered when choosing a material. The final measure of the effectiveness of a material is the total mass required to keep the structure below a given temperature. The mass requirements for insulation depend critically on the ablation temperature, and the use of materials with low ablation temperatures will reduce considerably the insulation problem.

The insulation requirements, i.e., the amount of material which should remain when sublimation has ceased in order to maintain the structure at some temperature below the ablation temperature, will depend primarily on the thermal diffusivity of the material, $k/\rho C_p$, the total time of reentry, t_F, and the ablation temperature, T_A. The temperature distribution through the shield at the end of reentry is given by[42]:

$$\frac{T - T_0}{T_A - T_0} = e^{\epsilon_f \xi} \left(1 - \frac{1}{2} \text{erfc} \frac{\epsilon_f + \xi}{2} \right) + \frac{1}{2} \text{erfc} \frac{\epsilon_f - \xi}{2} \tag{D-26}$$

where ξ is the dimensionless distance:

$$\xi = \left(\frac{\rho c_p}{k \, t_f} \right)^{1/2} z \tag{D-27}$$

and ϵ_f is the final dimensionless ablation rate:

$$\epsilon_f = \left(\frac{c_p \, t_f}{\rho k} \right)^{1/2} \left(\frac{d\tilde{m}}{dt} \right)_f \simeq \left(\frac{c_p t_f}{\rho k} \right)^{1/2} \left(\frac{m}{t_f} \right) \tag{D-28}$$

where m is the mass ablated per unit area during the reentry. The heat accumulation is:

$$Q_f = \frac{2}{\pi^{1/2}} \left(\rho c_p \, k \, t_f \right)^{1/2} (T_A - T_0) \, \zeta \tag{D-29}$$

where ζ the dimensionless heat content is given by:

$$\zeta = \frac{1}{2} e^{-\epsilon_f^2/4} - \frac{\pi^{1/2}}{4} \epsilon_f \, \text{erfc} \frac{\epsilon_f}{2} + \frac{\pi^{1/2}}{2 \epsilon_f} \text{erf} \frac{\epsilon_f}{2} \tag{D-30}$$

where the error function, or probability integral, is defined as:

$$erf(x) = \frac{2}{\sqrt{\pi}} \int_0^x exp(-u^2)\, du$$

(D-31)

and its complementary function as:

$$erfc(x) = \frac{2}{\sqrt{\pi}} \int_x^\infty exp(-u^2)\, du$$

(D-32)

The function ζ is shown in Fig. (D-4). For computational simplicity, the curve for ζ has been approximated by two straight lines shown superimposed on the original curve in Fig. (D-4). This provides a much easier method of calculation with a loss of accuracy of less than 3%.

For engineering purposes the temperature distribution, equation (D-26), can be approximated by:

$$\frac{T - T_o}{T_A - T_o} = e^{z/\delta}$$

(D-33)

where ζ is chosen in such a way that the heat content is correct, that is,

$$\rho C_p \int_{-\infty}^0 (T - T_o)\, dz = \frac{2}{\pi^{1/2}} \left(\rho C_p k\, t_f\right)^{1/2} (T_A - T_o)\, \zeta(\epsilon_f)$$

(D-34)

204

Evaluation of the integral using the temperature profile assumed in

equation (D-33) results in

$$\delta = \frac{2}{\pi^{1/2}} \left(\frac{k}{\rho c_p} \right)^{1/2} t_f^{1/2} \zeta(\epsilon_f)$$

<div align="right">(D-35)</div>

The amount of insulation in lbs/ft^2 required ahead of a station at

temperature T is found from (D-33) and (D-35) as:

$$m_{INS} = \frac{2}{\pi^{1/2}} \left(\frac{\rho k}{c_p} \right)^{1/2} t_f^{1/2} \zeta(\epsilon_f) \ln \left(\frac{T_A - T_0}{T - T_0} \right)$$

<div align="right">(D-36)</div>

From equation (D-36) it can be seen that a good insulation should have a

low $k\rho$ product and a high C_p. In addition, the insulation requirements are

seen to be proportional to the square root of the time of flight. It is

dependent upon the ablation process through the temperature of ablation and

the parameter $\zeta(\epsilon_f)$ which is a function of the average mass ablation rate.

CHARRING ABLATOR

The thermal degradation of most charring ablators is characterized by

pyrolytic reactions which yield gaseous products and a highly cross-linked

char matrix. The char matrix consists of the solid residue from a) the thermal

degradation of the plastic, b) material which is condensed out in the char

as the gaseous products traverse the porous char, and c) materials which

result from the chemical reactions between the reinforcement and the char

residue.

Figure D-5 shows a model of a charring ablator. The outer surface is subject to aerodynamic heating. The char provides an insulating layer with the heat which passes through this layer being absorbed by pyrolysis in the reaction layer between the charred and uncharred materials. The surface of the char is at a high temperature and re-radiates a large percentage of the heat input. The gases generated by the pyrolytic reaction pass through the porous char layer and are injected into the boundary layer. The gases are heated as they pass through the char layer and this removal of heat from the char layer reduces the quantity of heat conducted to the reaction layer. When these gases are injected into the boundary layer, the convective heat transfer to the surface is reduced by the same blocking effect as in the case of a simple subliming ablator. In addition to the gases produced by pyrolysis, a residue remains at the interface and adds to the thickness of the char layer. Char removal may occur at the same time as a result of thermal, chemical or mechanical processes and tends to decrease the thickness of the char layer.

Charring ablators are analyzed in references 26, 46, 47 and 48. Ref. 48, one of the latest reports on the subject, deals with the complex chemical reactions which occur during the charring ablation process and gives methods for predicting the ablation rates and effective heat of ablation. Ref. 26 provides a method of determining the thermal conductivity and density of the combined plastic and charred material at any time during the process. Ref. 46 provides a means of approximating the effective heat of ablation of phenolic nylon, which will be considered in this case.

Fig. D-5 shows how a charring ablator may be mathematically zoned. As described in Ref. 26, the three zones of interest are the char residue,

the reaction zone, and the virgin plastic material. In order to make an analysis of the model it is first necessary to determine a set of realistic assumptions regarding the nature of the depolymerization reactions and thermal properties of the material. The following material model is used in Ref. 26 to allow a simplified representation of the phenomena occurring in materials which undergo pyrolysis in depth:

a) the ablation material is divided into three zones: virgin material, material undergoing polymerzation and fully reacted material which remains as a char residue.

b) a single gas constituent is evolved within the reaction zone which flows toward the heat-addition surface instantaneously, without further chemical reactions, and is in thermodynamic equilibrium with the local solid temperature.

c) the rate of depolymerization of the virgin material is dependent on its local density and temperature.

d) the virgin material decomposes to a gas and a solid char residue.

e) the density, specific heat, and thermal conductivity of the two component solid are proportional to the mass fraction of reacted material and the thermal properties of the virgin and char residue solids.

As previously mentioned, if the effective heat of ablation, Q*, is known, the mass rate ablated per square foot of area can be obtained from,

$$\dot{m} = q/Q*$$
(D-37)

Ref. 46 gives the following expression for the effective heat of ablation,

$$Q^* = (\Gamma + \Xi)\left[\left(\frac{\Delta Q}{\Delta \dot{m}}\right)_w + H_{gw}\right] - H_{vp}$$

(D-38)

where Γ = fraction of material ablated which is gaseous

Ξ = fraction of virgin plastic that enters gas phase during surface combustion of char layer.

During hypersonic reentry, oxygen diffuses toward the surface and oxidation reaction occurs. The rate of vaporization is given by $(\Gamma+\Xi)\dot{m}_p$ where $\dot{m}_p$ is the rate of pyrolysis. The instantaneous rate of char formation is $(1-\Gamma-\Xi)\dot{m}_p$. Char is continuously formed at an interface between the virgin plastic and the pyrolyzed layer, and, if sufficient oxygen diffuses to the surface, it is consumed at the outer surface.

For the case of ablation of phenolic nylon, an exact solution for air injection into the boundary layer yields the following expression for the heat blocked due to mass transfer:

$$\left(\frac{\Delta Q}{\Delta \dot{m}}\right)_w = \frac{30}{M_v}\left[240 + 0.48\left(H_e - H_w\right)\right]$$

(D-39)

Since the mean molecular weight of the gas at the surface appears in the denominator, the injection of lightweight gases, such as hydrogen, enhances the blocking term. Nylon and phenolic-resin combined in equal amounts by weight may be represented by the chemical formula $C_{13}H_{18}O_2N$. The behavior of the composite material is such that lightweight gases are released during

pyrolysis. A theoretical analysis of the ablation of phenolic-nylon, utilizing the boundary layer equations, is complicated by the large number of different chemical species which are the original products of pyrolysis and by the subsequent combustion reactions between these species and the components of dissociated air. Experimental data indicate $\Gamma \approx 0.7$ and $0.7 < (\Gamma + \Xi) \leq 1$. If the final products of gaseous dissociation and combustion are primarily hydrogen the heat blocking term can easily be a factor of 2 or 3 larger than the corresponding term for transpiration cooling by air injection. It is also observed that complex hydrocarbons, such as phenolic nylon, have negligible heat of formation per unit mass ($H_{vp} \sim 0$). Combining (D-38) and (D-39) and considering the above discussion, the following approximation can be made for phenolic nylon:

$$Q^* = 1500 + 0.5 \, He \qquad \qquad \text{(D-40)}$$

The analysis from Ref. 26 is used to determine the thermal conductivity and density at a given time of the two component solids composed of virgin material and char residue. The density is given by

$$\rho_s = \rho_{s_1} + \rho_{s_2} \qquad \qquad \text{(D-41)}$$

where s is the two component solid, s_1 is the material undergoing depolymerization and s_2 is the char residue. It is assumed that ρ_{s_2} is a time-variant density and results from a change in ρ_{s_1}. The rate of depolymerization of the material is assumed proportional to the weight of the undepolymerized material

$$\frac{\partial W_p}{\partial t} \sim W_p \qquad \qquad \text{(D-42)}$$

This leads to the density derivative for the reacting material of:

$$\frac{\partial \rho_{s1}}{\partial t} = - k_r \, \rho_{s1}$$

(D-43)

where k_r is a rate constant. For this analysis, k_r, is taken as a first order reaction of the Arrhenuis type;

$$k_r = B_r \, e^{- E/RT}$$

(D-44)

where

b_r = frequency factor, sec^{-1}

E/R = Activation temperature, $^\circ R$

A fraction of the material which depolymerizes remains as a char residue. This fraction is defined as f_c and is equal to the ratio of mass s_2 solid produced to mass of s_1 solid depolymerized. The rate of increase of char density, ρ_{s_2}, is then given by

$$\frac{\partial \rho_{s2}}{\partial t} = - f_c \, \frac{\partial \rho_{s1}}{\partial t}$$

(D-45)

The total rate of density change is given by

$$\frac{\partial \rho_s}{\partial t} = \frac{\partial \rho_{s1}}{\partial t} + \frac{\partial \rho_{s2}}{\partial t}$$

(D-46)

Substituting equation (D-43) and (D-45) the following expression is obtained for the rate of change of total density:

$$\frac{\partial \rho_s}{\partial t} = -(1 - f_c) \, B_r \, \rho_{s1} \, e^{- E/RT}$$

(D-46a)

210

At any instant the densities are given by:

$$\rho_s(t) = \rho_s(0) + \int_0^t \frac{\partial \rho_s}{\partial t} dt$$

(D-47)

and

$$\rho_{s_1}(t) = \rho_{s_1}(0) - B_n \int_0^t \rho_{s_1} e^{-E/RT} dt$$

(D-48)

The thermal conductivity of the two component solid is given by

$$k_s = k_s(0) - \left(\frac{\rho_s(0) - \rho_s(t)}{\rho_s(0) - \rho_{s_2}(c)} \right) \left[k_s(0) - k_{s_2}(c) \right]$$

(D-49)

where 0 indicates initial or virgin material and c indicates final condition
or char. The specific heat of the combined solid is given by:

$$C_{P_s} = \frac{1}{\rho_s} \left(\rho_{s_1} C_{P_{s_1}} + \rho_{s_2} C_{P_{s_2}} \right)$$

(D-50)

Equations (D-46), (D-47) and (D-48) were used to determine the properties of

the material remaining at the end of ablation. Using this result, the thermal

conductivity and specific heat were determined from equation (D-49) and

(D-50). The physical properties of phenolic nylon, a typical charring ablator,

are listed in Table D-1 and were used in this analysis. The resulting values

of k_s, ρ_s and C_{P_s} were used to determine the final insulation thickness utilizing

equation (D-36) described previously for determining the insulation

requirements behind a vaporizing ablator.

211

MATERIAL PROPERTIES

The properties of the ablation and insulating materials used are shown in Table D-1. The effective heat of ablation of the ablation materials except phenolic nylon are shown in Fig. D-2. The effective heat of ablation of phenolic nylon is given in equation (D-40). The properties of some high temperature materials considered for reradiation shields are given in Table D-2. In addition the following properties apply to phenolic nylon[26]:

$$\rho_{vp} = 75 \text{ lb/ft}^3$$

$$k_{vp} = 4 \times 10^{-5} \text{ BTU/ft-sec-}^\circ\text{R}$$

$$C_{P_{vp}} = 0.4 \text{ BTU/lb-}^\circ\text{R}$$

$$f_c = 0.3$$

$$B_r = 1.0 \times 10^9 (\text{sec})^{-1}$$

$$E/R = 3.0 \times 10^4 {}^\circ\text{R}$$

$$\rho_c = 22.5 \text{ lb/ft}^3$$
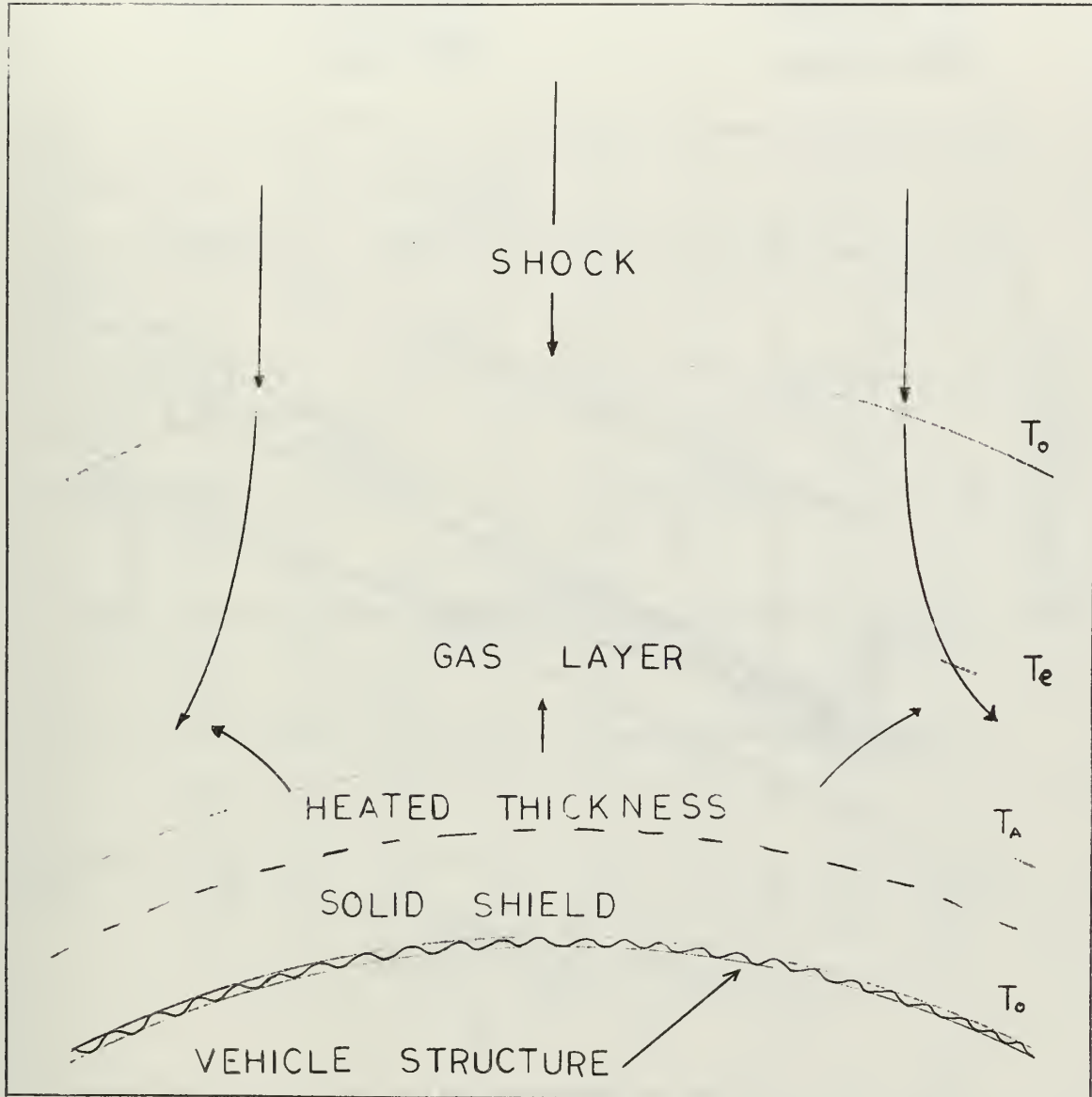
Fig. D-1   Sublimation Heat Shield
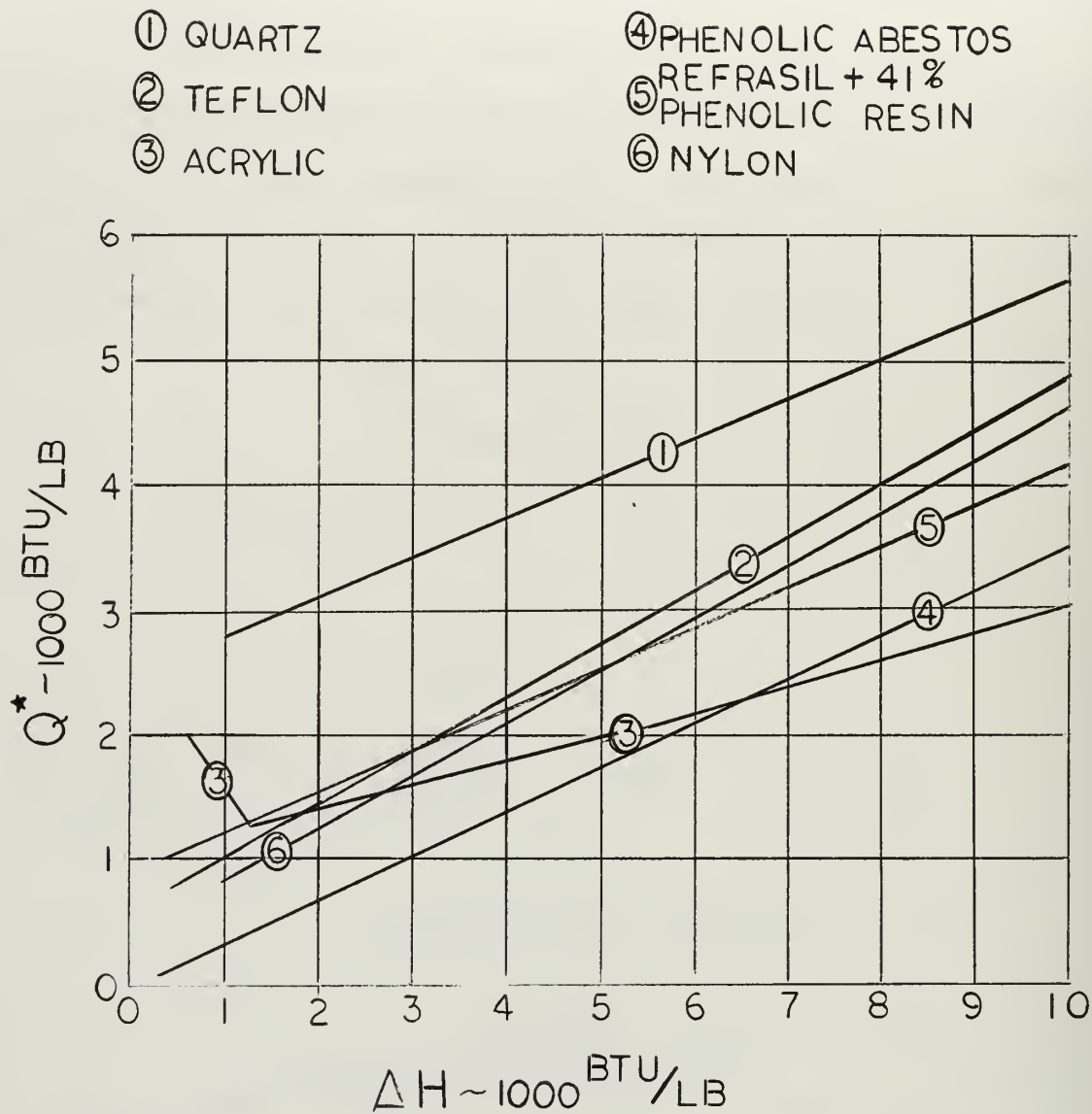
Fig. D-2 Variation of Estimated Effective Heat of Ablation
with Enthalpy Difference Across Boundary Layer

214
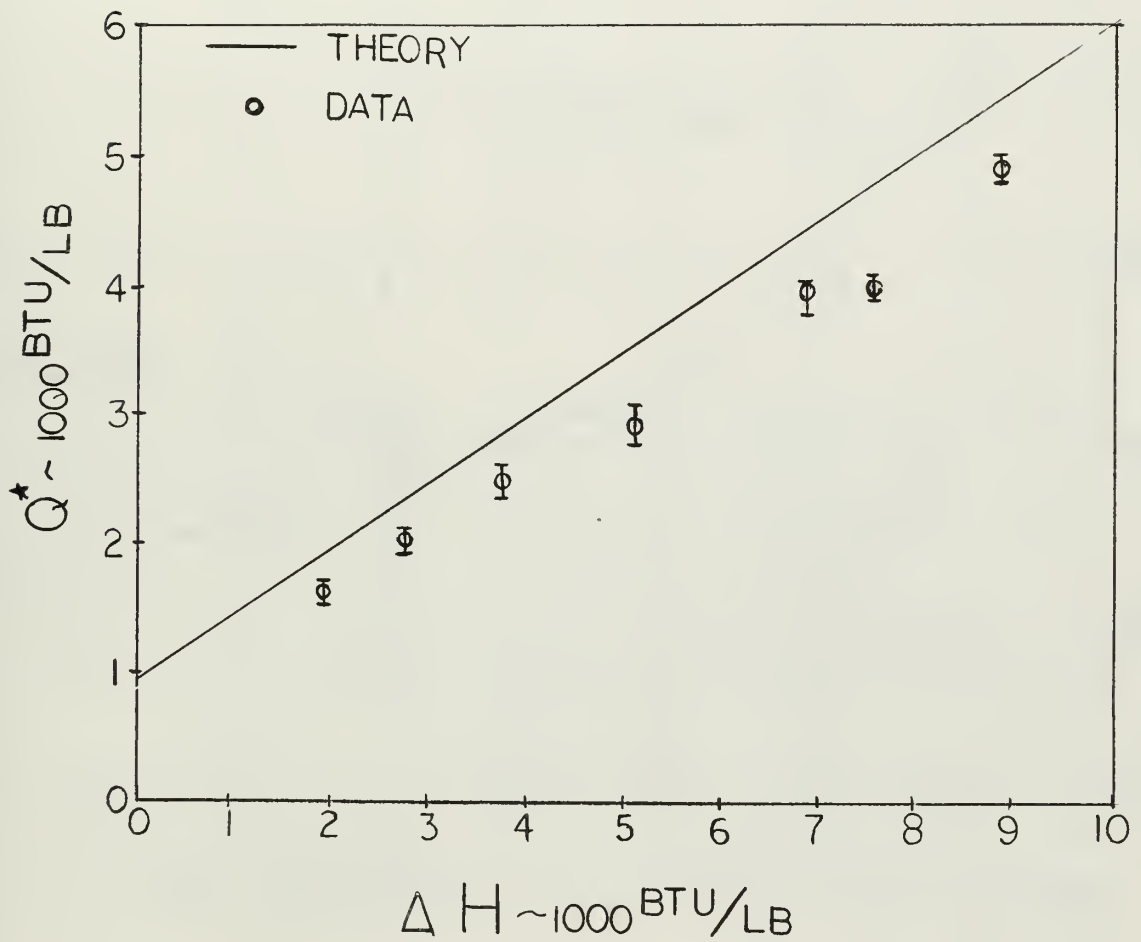
Fig. D-3 Stagnation Point Heat of Ablation Measurements for
Teflon Compared with Theory
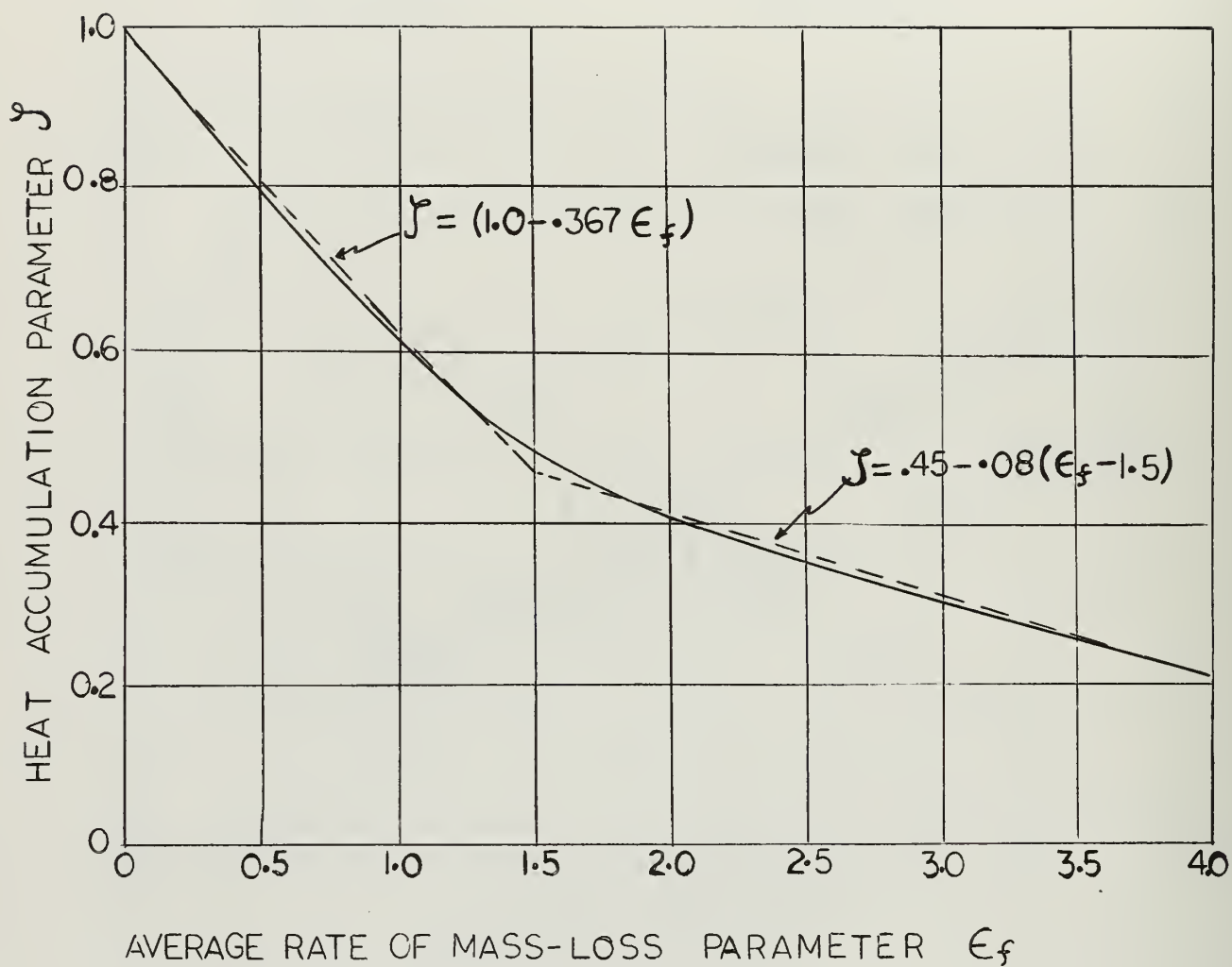
Fig. D-4 Variation of Heat Accumulation Parameter with Average Rate of Mass-Loss Parameter

216
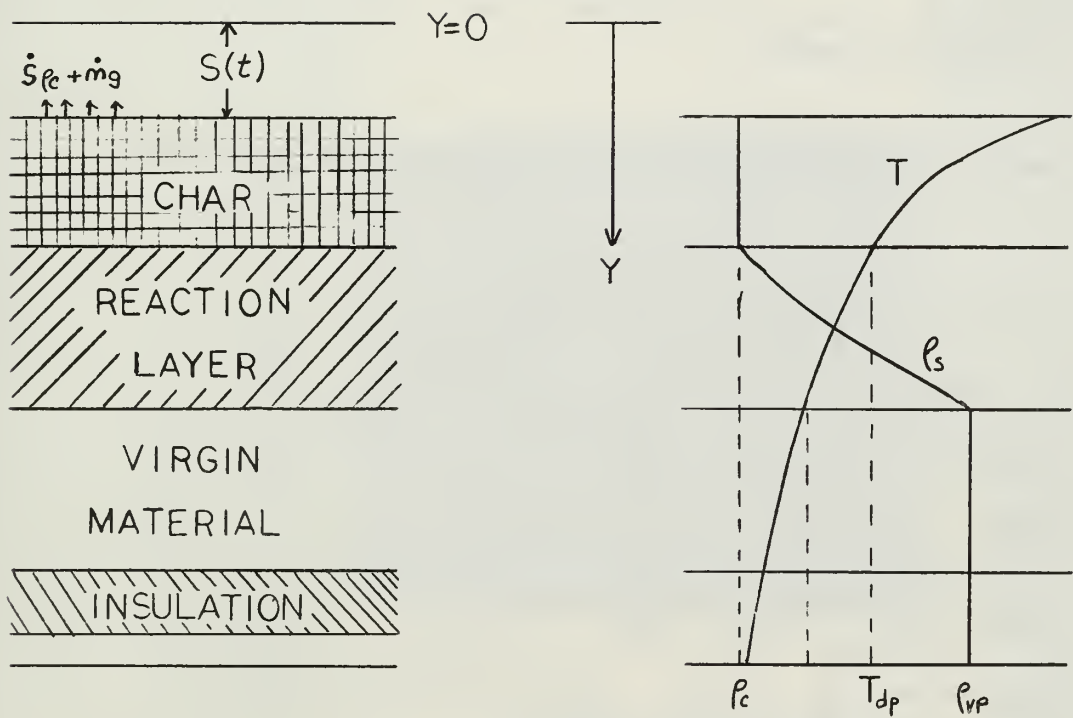
Fig. D-5   Charring Ablator Model Zones

Material	T_A(°F)	k (BTU/FT-SEC°F)	C_p BTU/LB-°F	ρ #/ft^3	EMISSIVITY ϵ
Teflon	1100	$3.48(10)^{-5}$	.25	129.5	.9
Phenolic-Asbestos	2000	$10.1(10)^{-5}$	.23	116.0	.8
Refrasil + 41% Phenolic Resin	2000	$4.2(10)^{-5}$	.23	111.0	.8
Acrylic	475	$3.24(10)^{-5}$	.38	74.6	.8
Phenolic Nylon	1400	$4.0(10^{-5})$ *	.40 *	75.0 *	.8
Q-Felt Insulation	--	$1.2(10)^{-5}$	.278	6.2	--

*Uncharred Material

Table D-1 Material Properties of Ablators and Insulators

Metal	Melting Temp T_M °F	Useable* Temp °F	ρ #/ft^3
René 41	2400 – 2500	1800	513
L605 Nickel Alloy	2425 – 2570	2000	569
UDIMET 700	2200 – 2550	2000	493
Molybdenum	4730	2000+	636
F-48(Columbium +15% T_1+5% M_o)	4474	2000+	583

*Determined from Loss of Strength or Oxidation Properties

Table D-2 High Temperature Metal Properties